UNIVERSITA' DEGLI STUDI DI UDINE

Dipartimento Politecnico di Ingegneria e Architettura

Corso di Dottorato in Ingegneria Industriale e dell'Informazione

Ciclo XXX

Tesi di Dottorato di Ricerca

Architectures and Algorithms for the Signal Processing of Advanced MIMO Radar Systems

Dottorando:

Alexander Rudolf Ganis

Relatore:

Prof. Mirko Loghi

Correlatori:

Dipl.-Ing. Dr. Volker Ziegler

(Airbus Group)

Anno Accademico 2016 - 2017

Abstract (Italiano)

Questa tesi si concentra sulla ricerca, lo sviluppo e l'implementazione di nuovi concetti, architetture, sistemi dimostrativi e algoritmi per l'elaborazione dei segnali in sistemi radar avanzati, basati su tecnologia Multiple Input Multiple Output (MIMO). Il concetto chiave è quello di ottenere sistemi compatti, dalle elevate risoluzioni e in grado di eseguire un'elaborazione del segnale radar veloce, un beam-forming tri-dimensionale (3D) e quadri-dimensionale (4D) per la generazione di immagini radar e la stima delle informazioni dei bersagli, detti target. L'idea è di ottenere una stima completa, che includa la distanza, l'Azimuth e l'elevazione (addizionalmente Doppler come quarta dimensione) dai target nelle acquisizioni radar. La tecnologia radar indagata ha lo scopo di affrontare diverse applicazioni civili e militari, come la sorveglianza e la rilevazione di targets, sia a livello aereo che a terra, e la consapevolezza situazionale, sia nelle auto che nelle piattaforme di volo, dagli elicotteri, agli Unmanned Aerial Vehicels (UAV) e taxi volanti (air-taxis).

Le tematiche affrontante sono molte: Lo sviluppo di sistemi completi e di architetture digitali innovative, basate su tecnologia FPGA, ARM e software, per radar 3D MIMO, che operano in modalità Multiplexing Time Division Multiplexing (TDM) e Multiplexing Frequency Diversion (FDM), con segnali di tipo FMCW (Frequency Modulated Continuous Wave) e Orthogonal Frequency Division Multiplexing (OFDM), rispettivamente; Lo sviluppo di tecniche di elaborazione del segnale radar in tempo reale, algoritmi di beam-forming e di stima della direzione di arrivo, Direction-Of-Arrival (DOA), dei segnali radar, per il rilevamento dei target, con particolare attenzione a processi basati su trasformate di Fourier (FFT); Lo studio e l'implementazione di concetti di sistema avanzati, parametrizzazione e simulazione di radar digitali di prossima generazione, capaci di operare in tempo reale (ad esempio basati su architetture OFDM). La progettazione e lo sviluppo di nuove forme d'onda ortogonali ad inviluppo costante per sistemi radar 3D di tipo OFDM MIMO, operanti in tempo reale.

Le attività di ricerca di questa tesi sono state svolte presso la compagnia Airbus, con sede a Monaco di Baviera (Germania), nell'ambito di un programma di dottorato, svoltosi in maniera congiunta tra Airbus ed il Dipartimento Politecnico di Ingegneria e Architettura dell'Università di Udine, con sede a Udine (Italia).

An investment in knowledge pays the best interest.

Benjamin Franklin

UNIVERSITY OF UDINE

Faculty of Engineering

Polytechnic Department of Engineering and Architecture

In partial fulfillment of the requirements for the degree of

Doctor of Philosophy

Architectures and Algorithms for the Signal Processing of Advanced MIMO Radar Systems

---

Supervisors:

Prof. Mirko Loghi

Dipl.-Ing. Dr. Volker Ziegler

(Airbus Group)

Author:

Alexander Rudolf Ganis

UNIVERSITÀ
DEGLI STUDI
DI UDINE

AIRBUS
GROUP

Abstract

This thesis focuses on the research, development and implementation of novel concepts, architectures, demonstrator systems and algorithms for the signal processing of advanced Multiple Input Multiple Output (MIMO) radar systems. The key concept is to address compact systems, which have high resolutions and are able to perform a fast radar signal processing, three-dimensional (3D) and four-dimensional (4D) beamforming for radar image generation, and target estimation. The idea is to obtain a complete sensing of range, Azimuth and elevation (additionally Doppler as the fourth dimension) from the targets in the radar captures. The radar technology investigated, aims at addressing several civil and military applications, such as surveillance and detection of targets, both air and ground based, and situational awareness, both in cars and in flying platforms, from helicopters, to Unmanned Aerial Vehicles (UAV) and air-taxis.

Several major topics have been targeted. The development of complete systems and innovative FPGA, ARM and software based digital architectures for 3D imaging MIMO radars, which operate in both Time Division Multiplexing (TDM) and Frequency Division Multiplexing (FDM) modes, with Frequency Modulated Continuous Wave (FMCW) and Orthogonal Frequency Division Multiplexing (OFDM) signals, respectively. The development of real-time radar signal processing, beamforming and Direction-Of-Arrival (DOA) algorithms for target detection, with particular focus on FFT based, hardware implementable techniques. The study and implementation of advanced system concepts, parametrisation and simulation of next generation real-time digital radars (e.g. OFDM based). The design and development of novel constant envelope orthogonal waveforms for real-time 3D OFDM MIMO radar systems.

The MIMO architectures presented in this thesis are a collection of system concepts, design and simulations, as well as complete radar demonstrators systems, with indoor and outdoor measurements. Several of the results shown, come in the form of radar images which have been captured in field-test, in different scenarios, which aid in showing the proper functionality of the systems.

The research activities for this thesis, have been carried out on the premises of Airbus, based in Munich (Germany), as part of a Ph.D. candidate joint program between Airbus and the Polytechnic Department of Engineering and Architecture (Dipartimento Politecnico di Ingegneria e Architettura), of the University of Udine, based in Udine (Italy).

Acknowledgements

I would like to express my sincerest gratitude to my advisor Prof. Mirko Loghi for his continuous support throughout my Ph.D studies and related research, for his patience, motivation, and immense knowledge. His guidance helped me throughout my overall academic experience, dating back to my Master's thesis accomplishments. I could not have imagined having a better advisor and mentor.

My deepest gratitude goes to my advisor within Airbus Group, Dr. Volker Ziegler, for providing me an opportunity to join his exceptional team, for his vast expertise, enthusiasm, leadership and unrelenting support throughout my research. He has routinely gone beyond his duties to provide the team with the best projects and all means necessary to accomplish a great work, together with a uniquely great friendship spirit.

Profound gratitude goes to Ulrich Prechtel, Dr. Askold Meusling and Dr. Bernhard Schoenlinner, who have been truly dedicated mentors. I am particularly indebted to them for managing and actively developing the radar projects, for their constant support, inside and outside the lab, and for the countless insightful discussions, concept designs and overall results' analysis throughout the whole Ph.D. experience.

I would like to thank my thesis committee: Prof. Fabrizio Berizzi and Prof. Fabrizio Argenti, for their insightful comments and feedback, which helped me achieve an even better overall thesis' quality.

Special thanks go to my friend and team mate Enric Miralles for the stimulating discussions, for the countless time spent together, for his great work, determination and capabilities, and overall moral support and fun we have had in the last four years.

Sincere thanks go to my friend and team mate Avik Santra, who has always inspired me with his enthusiasm for signal processing and electronics and shared his amazingly wide and profound knowledge with expertise and strong passion, and to Thomas Multerer, Joffrey Lemercier, Pau Panareda-Busto, Peter Heise, Dushan Pamunuwa and all the other friends and colleagues I have met along the way, for all the great experiences and all the fun we had and we keep on having.

Finally, no words in the world could express the feelings and gratitude I have for my family, my parents Afra and Mario, my brother Maximilian, my sister Raffaella, for Farida, Paolo, Sofia, Kimberly and Diego. You are the best gift life has given me and represent the strongest motivation for all of my achievements. I love you all.

Contents

List of Figures

List of Tables

Abbreviations

2D	**2**-Two **D**imensional
3D	**3**-Three **D**imensional
4D	**4**-Four **D**imensional
A/C	**A**ir - **C**raft
ADC	**A**nalog to **D**igital **C**onverter
AF	**A**mbiguity **F**unction
AM	**A**mplitude **M**odulated
ARM	**A**dvanced **R**ISC **M**achines
ASM	**A**lgorithmic **S**tate **M**achine
AWGN	**A**dditive **W**hite **G**aussian **N**oise
CFAR	**C**ostant **F**alse **A**larm **R**ate
COTS	**C**ommercial **O**ff **T**he **S**helf
CP	**C**yclic **P**refix
CPLD	**C**omplex **P**rogrammable **L**ogic **D**evice
CW	**C**ontinuos **W**aveform
DAC	**D**igital to **A**nalog **C**onverter
DBF	**D**igital to **B**eam **F**orming
DC	**D**irect **C**urrent
DDS	**D**irect **D**igital **S**ynthesiser
DDR	**D**ouble **D**ata **R**ate
DFT	**D**iscrete **F**ourier **T**ransform
DMA	**D**irect **M**emory **A**ccess
DOA	**D**irection **O**f **A**rrival
DSP	**D**igital **S**ignal **P**rocessing
FDM	**F**requency **D**ivision **M**ultiplexing

FDM	**F**requency **D**ivision **M**ultiple **A**ccess
FIFO	**F**irst **I**n **F**irst **O**ut
FFT	**F**ast **F**ourier **T**ransform
FM	**F**requency **M**odulated
FM	**F**PGA **M**ezzanine **C**ard
FMCW	**F**requency **M**odulated **C**ontinuos **W**aveform
FOV	**F**ield **O**f **V**iew
FPGA	**F**ield **P**rogrammable **G**ate **A**rray
FSM	**F**inite **S**tate **M**achine
FSPL	**F**ree **S**pace **P**ath **L**oss
FTP	**F**ile **T**ransfer **P**rotocol
GPS	**G**lobal **P**ositioning **S**ystem
GSPS	**G**iga **S**amples **P**er **S**econd
GUI	**G**raphical **U**ser **I**nterface
HDL	**H**ardware **D**escription **L**anguage
HMI	**H**uman **M**achine **I**nterface
ICI	**I**nter **C**arrier **I**nterference
IDFT	**I**nverse **D**iscrete **F**ourier **T**ransform
IEEE	**I**nstitute of **E**lectrical and **E**lectronic **E**ngineers
IF	**I**ntermediate **F**requency
IFFT	**I**nverse **F**ast **F**ourier **T**ransform
IFT	**I**nverse **F**ourier **T**ransform
ISAR	**I**nverse **S**ynthetic **A**perture **A**rray
ISI	**I**nter **S**ymbol **I**nterference
ITU	**I**nternational **T**elecommunication **U**nion
LFM	**L**inear **F**requency **M**odulated
LNA	**L**ow **N**oise **A**mplifier
LO	**L**ocal **O**scillator
LOS	**L**ine **O**f **S**ight
LSB	**L**east **S**ignificant **B**it
MEX	**M**atlab **EX**ecutable
MIMO	**M**ultiple **I**nput **M**ultiple **O**utput
MPC	**M**ulti **P**ath **C**omponent

MSB	**M**ost **S**ignificant **B**it
MSPS	**M**ega **S**amples **P**er **S**econd
MTI	**M**oving **T**arget **I**ndicator
NLFM	**N**on **L**inear **F**requency **M**odulated
NLOS	**N**on **L**ine **O**f **S**ight
OFDM	**O**rthogonal **F**requency **D**ivision **M**ultiplexing
PAPR	**P**eak to **A**average **P**ower **R**atio
PCB	**P**rinted **C**ircuit **B**oard
PLL	**P**hase **L**ocked **L**oop
PRF	**P**ulse **R**epetition **F**requency
RCS	**R**adar **C**ross **S**ection
RF	**R**adio **F**requency
RADAR	**R**adio **D**etection **A**nd **R**anging
RAM	**R**andom **A**ccess **M**emory
ROM	**R**ead **O**nly **M**emory
RSPA	**R**esonant **S**lot **P**atch **A**ntenna
RX	**R**eceiver
SAR	**S**ynthetic **A**perture **A**rray
SDR	**S**oftware **D**efined **R**adio
SFP	**S**mall **F**orm-factor **P**luggable (Transceiver)
SFTP	**S**SH **F**ile **T**ransfer **P**rotocol
SIMO	**S**ingle **I**nput **M**ultiple **O**utput
SNR	**S**ignal to **N**oise **R**atio
SINR	**S**ignal to **I**nterference plus **N**oise **R**atio
SoC	**S**ystem **o**n **C**hip
SPI	**S**erial **P**eriferal **I**nterface
SSH	**S**ecure **SH**ell
STBC	**S**pace **T**ime **B**lock **C**ode
SWAP	**S**ize **W**eigth **a**nd **P**ower
TDL	**T**apped **D**elay **L**ine
TDM	**T**ime **D**ivision **M**ultiplexing
TSA	**T**apered **S**lot **A**ntenna
TX	**T**ransmitter

UAV	**U**nmanned **A**erial **V**ehicle
UART	**U**niversal **A**synchronous **R**eceiver **T**ransmitter
UDP	**U**ser **D**atagram **P**rotocol
USB	**U**niversal **S**erial **B**us
VHDL	**V**HSIC **H**ardware **D**escription **L**anguage
VHSIC	**V**ery **H**igh **S**peed **I**ntegrated **C**ircuits
VTOL	**V**ertical **T**ake **O**ff and **L**anding
WRC	**W**orld **R**adio-communication **C**onference

Symbols

$h(t, \tau)$	Impulse response of the time-varying channel
N_{AZI}	Number of Elements Along the Azimuth's Axis
N_{ELE}	Number of Elements Along the Elevations's Axis
N_{RANGE}	Number of Elements Along the Range's Axis
N_{TX}	Number of Transmit Antenna Elements
N_{RX}	Number of Receive Antenna Elements
$N_{virtual}$	Number of Virtual Antenna Elements
$N_{measures}$	Number of Measurements
$N_{samples}$	Number of Samples
N	Number of Subcarriers in an OFDM Symbol
M	Number of Symbols in an OFDM Frame
N_{FRAME}	Number of Samples in an OFDM Frame
R_n	n-th Receive Antenna
T_n	n-th Transmit Antenna
$x(t)$	Transmitted signal
$y(t)$	Received signal

B	Signal's Bandwidth	Hz
B_{eff}	Effective's Signal's Bandwidth	Hz
c_0	Speed of Light	$c = 2.997\ 924\ 58 \times 10^8\ \mathrm{ms}^{-\mathrm{s}}$
f_C	Carrier's Frequency	Hz
f_D	Doppler Shift	Hz
$f_{D_{max}}$	Maximum Doppler Shift	Hz
f_s	Sampling's Frequency	Hz
G	Antenna Gain	dBi

R	Range	m
R_{max}	Radar's Maximum Range	m
R_u	Radar's Maximum Unambiguous Range	m
RCS	Radar's Cross Section	m^2
S	Speed	m/s
T_c	Signal's Duration	s
T_{chirp}	Chirp Signal's Duration	s
T_{CP}	OFDM Signal's Cyclic Prefix Duration	s
T_S	OFDM Symbols' Duration	s
T_{OFDM}	OFDM Signal's Duration	s
Δf	OFDM's Signal Subcarriers Spacing	Hz
ΔR	Radar's Range Resolution	m
θ	Azimuth Angle	degree
$\Delta\theta$	Azimuth Angle's Resolution	degree
ϕ	Elevation Angle	degree
$\Delta\phi$	Elevation Angle's Resolution	degree
σ	Radar's Cross Section	m^2
Δv	Velocity's Resolution	m/s
Δv_{max}	Maximum Velocity's Resolution	m/s
τ_i	Delay of the i-th path	μs
τ_{max}	Maximum delay spread	μs
λ	Waveform's Length	m

Dedicated to my family...

Chapter 1

Introduction

1.1 Context

A RAdio Detection and Ranging (RADAR), is a system or device which detects the position of an object, or target, by measuring how long radio waves take to travel from the radar transmitter, reflect off the target and travel back to the radar receiver, as shown in Fig. 1.1. The position and bearing of the target can be calculated in the radar processing system, by extracting the time intervals and phase shifts between the received signals [2]. In radar architectures with multiple antennas arranged in particular array configurations, like the ones described in this thesis, a complete estimation of the targets' range, Azimuth and elevation information can be achieved, through radar signal processing. Additionally, from the same received data, some radars are also able to accurately measure the radial velocity of targets, by using the Doppler-effect, named after physicist Christian Doppler. The Doppler-effect describes the apparent change in frequency of a signal emitted or reflected to an observer if an object is moving relative towards or away from its observer.

Since the detection in radar system is based on the reflected energy from a target, if the radar energy passes through or it is absorbed by the target, detection becomes more difficult. The corollary of this is that targets, such as ground, sea and air vehicles or pedestrians and buildings, that reflect radar energy strongly, will be easier to detect using a radar.

Radar originated in the experimental work of Heinrich Hertz in the late 1880s and the first radar was patented in 1904 by Christian Hulsmeyer [3]. It was a pulsed radar, radiating differentiated video pulses, generated by a spark gap, which achieved the detection of the polarisation dependent reflection of electromagnetic waves. The period which follows, is characterized by an improvement in the state of the art of the technology, in both the radar systems and the signal processing. For example, in 1938 the Pulse Radar Patent of Colonel W. R. Blair was published. The first electronically scanning radar was, instead, the German Search Radar FuMG 41/42 Mammut-1, in 1944 [4].

During the Second World War, researchers from Great Britain and the United States of America (U.S.A), developed a high-powered microwave radar system for military use,

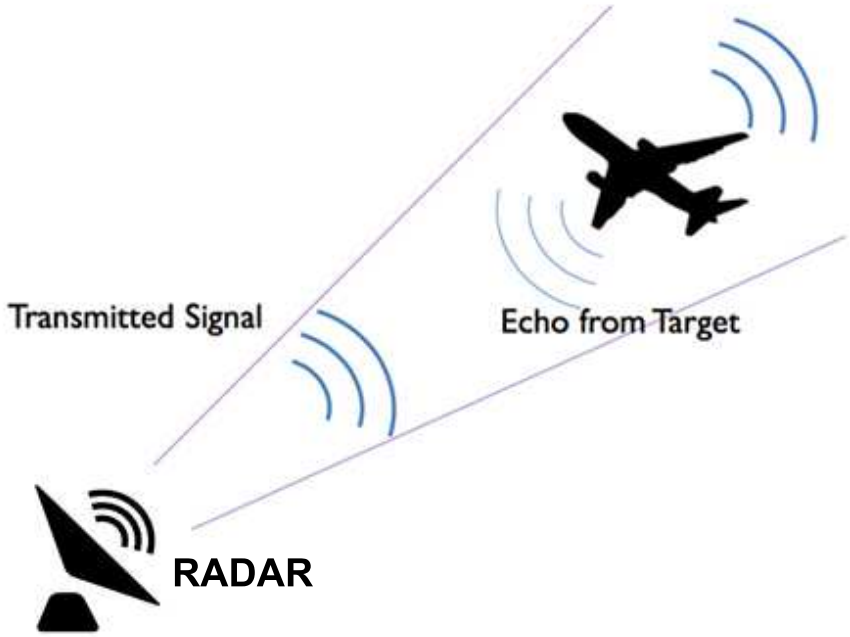

FIGURE 1.1: Principles of a radar device. A radio, i.e. electromagnetic, wave is scattered back from a target.

which represented a breakthrough also due to a much smaller size factor achieved, compared to the previous radars. It was a cavity magnetron designed by John Randall and Harry Boot in 1940 at the University of Birmingham, England [5].
Soon after World War 2, many of the most advanced technologies, still used in modern radar systems, had already emerged and matured: the pulse-Doppler radar [6], the phased array radar [7] and the Synthetic Aperture Radar (SAR) systems [8].
Although until 1990 the radar technology has always been a little ahead of the communications technology, the upcoming spring of wide spread mobile communications of the beginning of the 1990s has changed the world. Only recently, thanks to the increasing demand of radars system, due mainly to the aerospace and automotive industries, a lot of research has been focused on the innovation of the radar technology, in both the hardware and signal processing architectures. [9].

Nowadays, radar systems are used in a wide range of applications within civil, scientific, security and military areas [10],[11]. Some examples are:

- Wide-zone surveillance of open areas and critical infrastructures.
- Automotive collision avoidance and autonomous driving assistance systems.
- Navigational aid and situation awareness for aircrafts, air-taxis, Unmanned Aerial Vehicles (UAV) and flying platforms in general.
- Ship navigation and maritime traffic monitoring.
- Monitoring of local weather systems.

- Vehicle speed detection from law enforcement units.
- Highly-precise position detection for indoors and outdoors applications.
- Military use in fighter aircrafts, missile seekers, fire control and many more.
- UAV detection and tracking.

One of the reason for the adoption of radars, is due to their advantages when compared with other devices, such as electro-optical bases sensors (video and infrared cameras). As a matter of fact, the properties which make radar sensors preferable in many application scenarios are [12],[13], [14], [15] :

- Operability in all weather conditions, especially in the lower GHz range: e.g. dusty, foggy, cold, hot or wet environments.
- Material penetration properties: e.g. revealing of concealed items, underneath clothing or behind walls.
- Possibility to achieve a complete sensing of the targets' range, Azimuth, elevation and speed, with one single device.
- Long-range detection capability.
- Possibility to measure radial velocity of targets.
- Large surveillance area, or volume, capability.
- Possibility to be concealed behind a covering, or protecting, surface.

However, radar sensors, also have some few disadvantages, when compared to electro-optical sensors. Considering only the Azimuth direction, or the direction perpendicularly to the human eye, the so called cross range resolution offered by electro-optical sensors tends to be higher. However, most importantly, radar system tend to be bigger in size, heavier in weight and consume more power than other sensors. Therefore, a good part of the current research on radar technologies, aims at reducing the cost and size of the radar devices, while retaining the 3D high resolution properties.

1.2 Types of Radars

Generally, radars fall into two major categories, referred to as primary radar and secondary radar [16]. Secondary radars operate similarly to a point to point Radio Frequency (RF) communication link. The transmitter broadcasts a message. If a friendly object, such as a friendly aircraft, receives the message, it transmits back a message of its own providing identity and tracking information, such as location, altitude and speed. An example of secondary radars are the Identification Friend or Foe (IFF) radars [17]. These radars respond when they are interrogated by some other radars using encrypted

signals. Ground radars or airborne radars are used for this purpose.
However, conventionally, the main types of radar systems are the primary radars. These involve a transmitter sending out signals, and a receiver, receiving the reflected echoes from the targets. The received signals are then processed to determine various targets' parameters, such as range, Azimuth, elevation and speed. A classification of primary radar systems is quite an intricate task, since there are many aspects that can be considered. One way to characterize the different primary radars, is based on the different system's architectures adopted and the various waveforms used. Several elements affect the architecture of these radars, which can be the combination of one or more of the following concepts:

- **Monostatic/Bistatic**: The difference between a monostatic or bistatic radar architecture can be found in the design of the transmitter and receiver antennas configurations of the system [18], [19]. Radars conventionally operate as a monostatic radar, with the transmitter and the receiver positioned at the same location. On the other side, in the case of a bistatic radar, the transmitter and the receiver are positioned in different locations. Usually, the separation distance between the transmitter and the receiver are in the order of the expected distance to the targets that need to be detected.

- **Mechanically steered**: In these radars, the system involves manually turning the antenna to face the direction of interest, where the targets need to be detected, or where the target has been detected and needs to be tracked. Mechanical steering becomes undesirable and difficult when considering factors such as the antenna size, the weight, the weather conditions and the robustness and wear of the components in such systems. Mechanical steering is often performed by means of electric motors [20], which can limit the steering's speed. Recently, MEMS devices have been used to implement mechanical steering [21], they offer improved speed of scanning compared to manually steered arrays as well as low losses to the system [22].

- **Synthetic Aperture Radar**: The synthetic aperture radar, or SAR, is a coherent radar system often mounted on satellites or aircrafts [23]. It provides very high image resolution, especially along the cross-range domain, by using the flight's path to simulate an extremely large antenna aperture. A technique referred to as Inverse SAR (ISAR) uses the same technique, but utilizes the target's motion rather than that of the emitter, by which the synthetic aperture is then created. The basic principle behind SAR is similar to the one at the base of a phased array antenna. But unlike parallel antenna array elements, SAR systems use parts of the virtual antenna area in a time multiplex mode. The antenna position is known precisely, and moves perpendicularly to the radiation direction over time. All radar echo signals containing their respective amplitude and phase components are stored over time and then later processed. Today's SAR systems apply a signal bandwidth of several GHz in order to achieve a resolution of centimeters or even millimeters. Requirements for successful SAR processing are an extremely stable "fully coherent" transmitter, powerful signal processing and the exact knowledge of the flight's path and ego velocity.

- **Phased-Array Radar**: A phased-array antenna can position its beam rapidly from one direction to another without the need for a mechanical movement of large antenna structures [24]. Agile, rapid beam switching permits the radar to track many targets simultaneously and to perform additional functions, as required. The steering is achieved by means of phase shifters, which are devices that can be controlled electronically, as in the case of the Active Electronically Scanned Array (AESA) [25], [26]. In phased-array radar systems, each of the single isotropic antennas is radiating equally in all directions. This is if no phase shift is applied. The resulting power of the radiated sum beam in forward direction, along the bore-sight of the radar, is very close to the sum of all the transmitted sine signals combined. Additionally, depending on the phase shift between the transmit antenna signals, the beam can be steered into a certain direction of interest. The phase shift of the antenna signals causes the final signal to be reduced in amplitude as compared to a signal being added up in forward direction and without phase shift. However, phased-array radar systems, because of their antennas and RF components, are very costly. Moreover, a large number of antennas is needed, in the case that a large aperture, thus, high cross-range resolution, is required. Therefore, they are used primarily for military and SAR satellite applications.

- **MIMO**: Multiple Input Multiple Output (MIMO) radars can be simply seen as systems with multiple antennas at both the transmitter and receiver side. In the receiver array, the reflected signals belonging to each of the transmitter antennas are detected by the different receiver antennas and jointly processed [27], [28], [29]. The receivers will be able to differentiate among the transmitted radar signals, due to the orthogonality architecture implemented. As it will be later described in this thesis, the signal's orthogonality can, for example, be established in time-domain by employing a Time Division Multiplexing (TDM) based switching scheme between the transmit antenna elements, or in frequency domain. In particular, the orthogonality and MIMO properties, allow the calculation of the amplitude and phase relationships of a large number of points in space, which is the result of the multiplication of the number of transmit by the number of receive antenna elements. This can be seen as a convolution operation and these generated points form the elements of the virtual antenna array. Therefore, the MIMO principle together with an appropriate antenna array arrangement, enables an improvement in the cross-resolution by an artificial increase of the antenna aperture with the so called virtual array concept [30], [31], [32]. The advantages of a MIMO architecture can be summarised as: reduced number of antenna elements and simpler RF distribution structure when compared to a conventional antenna array, compact design through high integration, in particular without complicated mechanics for beam steering, artificially enlarged aperture and thus, improved cross-resolution synthetic image generation [33]. Due to these properties, this will be the architecture chosen for the implementation of the radar demonstrators, presented throughout this thesis.

Additionally to the previously listed architectures, different transmit waveforms, such as Continuous Wave (CW), Frequency Modulated Continuous Wave (FMCW), pulse

or even Orthogonal Frequency Division Multiplexing (OFDM) signals, can be used by radar systems. Following are some of the most commonly used waveforms [34], [35], [36], [37]:

- **Pulse radars**: This type of radar estimates the target's range information, by measuring the time difference between the transmission and reception of a single radar's pulse. While the pulse's width determines the range resolution, the pulse repetition frequency (PRF) determines the range where the measurement results are unambiguous [38], [39]. Typical examples are long-range air and maritime surveillance radars, test range radars, and weather radars. Pulse radars use the Doppler frequency shift of the received signal in order to detect moving targets, such as aircraft, and to reject the large unwanted echoes from stationary clutter that do not have a Doppler shift. Angular information such as elevation and Azimuth is then measured using a narrow transmit antenna beam and by means of a mechanical steering operation. Due to the known position of the antenna's beam, the Azimuth angle is estimated

- **Pulse Doppler Radar**: This radar transmits consecutive pulses and then measures the phase's difference in-between their received echoes to provide radial velocity in addition to range measurement [40]. Additionally, in the case of a coherent operation of the radar transmitter and receiver, the radial velocity is derived from the pulse-to-pulse phase's variations. Pulse Doppler radar systems normally use various pulse repetition frequencies ranging from several hundred Hz up to hundreds of kHz and, in order to solve the range and Doppler ambiguities, the frequencies change during operation. Additional to these measurement parameters, other requirements which need to be met in order to achieve a good performance in pulse Doppler radars, include: the need for a very low LO phase noise, a low receiver noise and a low I/Q gain phase mismatch, in order to avoid a false target indication.

- **Pulse Compression Radar**: Classical pulse and pulse Doppler radar systems, operate by transmitting extremely short radar pulses [41], [42]. On the one hand, by increasing the pulse's width, the radar systems achieve greater ranges. This is due to the fact that there is simply much more power in the pulse. On the other hand, by decreasing the width of the transmitted pulses, a better range resolution can be achieved by the radar system. However, there are also technical boundaries which limit the maximum transmitted power. Pulse compression combines the power-related benefits of very long pulses, thus, long range, with the benefits of very short pulses, thus, high range resolution. With regard to pulse compression, several different modulation techniques can be used: Linear frequency modulation (LFM) [43], Non-linear frequency modulation (NLFM) [44], encoded pulse phase modulation (e.g. Barker code) [45], [46], polyphase modulation [47] and time-frequency coded modulation [47].

- **Continuous Wave Radar**: CW radar systems, which transmit radar signals with a constant frequency, are used to measure the target's radial velocity [48],

[49]. However, they do not provide any range information, due to a missing timing reference. A signal at a certain frequency is transmitted via an antenna. It is then reflected by a target moving with a certain speed relative to the receiver's beam. This causes a Doppler frequency shift in the radar echo signal. Comparing the transmitted frequency with the received frequency, the radial velocity can be determined. However, any tangential component will not be taken into account, hence, a plane traveling at high speed in an exact circle around a rotating radar antenna would result in a zero value in radial velocity captured by the radar. In military applications, CW radars are also used for target "Illumination". The radar beam is kept pointing at a moving target by linking it to a target tracking radar for range, radial velocity and angle information estimation. Due to the fact that CW radars are hard to detect, they are classified as radars with low probability-of-intercept.

- **Frequency Modulated Continuous Wave Radar**: FMCW radars are systems which are able to measure the range and bearing information of the targets [50], [51], [52]. These radars, adopt a signal which frequency increases (up-chirp signal) or decreases (down-chirp signal) with time. The radar range resolution is inversely proportional to the signal's bandwidth. The period of the swept time is longer than the round-trip time of the most distant target. Additionally, the FMCW radar receiver is typically a simple homodyne architecture that mixes the target echo with a replica of the transmit waveform. The received radar signal, reflected from multiple scatterers, is affected by a delay and Doppler frequency shift. Through a beam-forming process, it is possible to resolve the position of the targets, but also, the speed of moving objects, through the use of Fast Fourier Transform (FFT) operations. The FMCW type of radar is also commonly used commercially for measuring distances, e.g. as used in level indicators. Nowadays, automotive radar sensors, as well, apply FMCW radars.
  Furthermore, the FMCW signal model and it's mixing architecture, represent one of the types of radar systems chosen for implementation in this thesis.

- **Moving Target Indicator Radar**: The idea behind a moving target indicator (MTI) radar is to suppress radar echo signals from stationary or slow-moving targets such as buildings, mountains, waves and clouds, and thus, obtain an indication of the moving targets of interest [53], [54], [55]. Unwanted radar echo signals are generally referred to as clutter, which is normally distributed around the zero Doppler's frequency and multiples of the pulse repetition frequency. One possible implementation of a MTI radar, is a delay line canceler, which stores the last radar echo in order to be subtracted from the actual radar echo. In case of a stationary target the difference value becomes zero, while for the remainder represents the moving targets.

- **OFDM Radars**: OFDM radars, as the name suggests, use an OFDM signal, known from communications, as the radar's waveform [56], [57], [58]. An OFDM signal is composed of a set of sub-carriers that are mathematically orthogonal in the time domain, i.e., each carrier has an integer number of cycles over a symbol period. Consequently, the spectrum of each carrier has a null at the center frequency

of the other carriers in the system, and thus a higher level of spectral efficiency can be achieved. The composition from a multitude of orthogonal sub-carriers, makes OFDM radars particularly suitable for real-time MIMO radar applications. The allocation of orthogonal coded waveforms to the different transmit channels of the radar allows the simultaneous operation of all transmit channels in an interference-free manner.
This type of radar's architecture has been implemented in both a simulation environment and one of the radar demonstrators presented in this thesis.

1.3 Radar Frequencies

For the proper functionality and co-existence of various RF applications, which make use of electro-magnetic radiation, like mobile communication, television and radar as well, a regulation on how to use the available frequency spectrum is necessary. This is done officially and worldwide by the International Telecommunication Union (ITU), [59]. It is a special organization within the United Nations, which organizes the World Radio-communication Conference (WRC) [60]. The meetings happen every two to four years, in which issues of radio-communication are decided at an international level. One main topic analysed, is the allocation of frequency bands to certain applications. This allocation is done in a slightly different way, according to three regions in the world: North and South America continents form Region 2, Sub-Asia and Australia continents form Region 3 and Europe, together with Russia and Africa, are part of the designated "Region 1". However, also within one region, the national authorities (e. g. in Germany: the Bundesnetzagentur), individually define the allowed use of the frequency spectrum, taking into account local particularities. An official nomenclature, for the different allocated frequencies [61], has been standardised by the Institute of Electrical and Electronic Engineers (IEEE) and it's presented in Table 1.1.

As it can be seen from Table 1.1, radars can be operated at a wide range of frequencies, ranging from as low as a few MHz, to as high as some hundred GHz, in the millimeter-wave region. Radar applications are frequency dependent. Essentially, the high frequency bands are perfect for applications that need small antennas and, due to the small wavelength, a more efficient antenna design and implementation is possible. The short wavelengths permit the use of high gain antennas with a convenient small size. On the other hand, low frequencies, thus long wavelengths, are better suited for long range applications, considering the higher and easier availability of high power antennas for these bands. Moreover, in this case, the wavelength allows better capabilities in the penetration of obstacles.
Nevertheless, the need for radar signals with a large bandwidth, which can yield very high resolution imaging radar systems, has brought the attention of researcher towards high frequency designs. As it can be seen, higher frequencies are targeted both by military and automotive industries. Millimeter waves open up more spectrum, but until recently, few electronic components were able to generate or receive millimeter waves, so the spectrum remained unused. Generating and receiving millimeter waves is a challenge, but the biggest and most challenging factor with these high frequencies is the

TABLE 1.1: Radar Frequencies, Bands, Wavelength and Applications

Band	Frequency	Wavelength	Applications
HF	3 MHz - 30 MHz	10 m - 100 m	Costal and Over the Horizon (OTH), immune to weather conditions, HF is for High Frequency
P	30 MHz - 300 MHz	1 m - 10 m	Early radars, P is for "Previous" radar systems now for SAR radars for earth observation
UHF	300 MHz - 1 GHz	0.3 m - 1 m	Missile detection, very long-range radar, ground penetrating, UHF is for Ultra High Frequency
L	1 GHz - 2 GHz	15 cm - 30 cm	Long-range air traffic control, Air Route Surveillance Radar (ARSR), L is for "'Long" range radar systems
S	2 GHz - 4 GHz	7.5 cm - 15 cm	Terminal air traffic control, Airport Surveillance Radar (ASR), S is for "Short"
C	4 GHz - 8 GHz	3.75 cm - 7.5 cm	Satellite transponders, weather radar systems, C is for "Compromise", between S and X
X	8 GHz - 12 GHz	2.5 cm - 3.75 cm	Missile guidance, marine radar, mapping and ground surveillance, X band because the frequency was secret
Ku	12 GHz - 18 GHz	1.67 cm - 2.5 cm	High-resolution imaging, surveillance systems, satellite altimetry, frequencies below K band, thus "u"
K	18 GHz - 27 GHz	1.11 cm - 1.67 cm	Police radar for speed enforcement, military airborne radars, Automotive radar is 24 - 26 GHz
Ka	27 GHz - 40 GHz	0.75 cm - 1.11 cm	Mapping, short range radars, airport surface radars, frequencies above K band, thus "a"
mm	40 GHz - 300 GHz	1 mm - 7.5 mm	Millimeter band, limited to short or very short ranges, very high resolution imaging
Q	40 GHz - 60 GHz	5 mm - 7.5 mm	Used for military communications
V	50 GHz - 75 GHz	4 mm - 6 mm	Strong absorption from atmosphere
W	75 GHz - 110 GHz	2.7 mm - 4 mm	76 GHz LRR automotive radar, 79 GHz SRR automotive radar, very high resolution imaging

travelling media [62], [63], [64], [65]. Important effects are introduced by the atmospheric properties. The atmosphere absorbs millimeter waves, as it can be seen from Fig. 1.2 [66], thus attenuating and restricting their transmission range. Rain, fog [67],

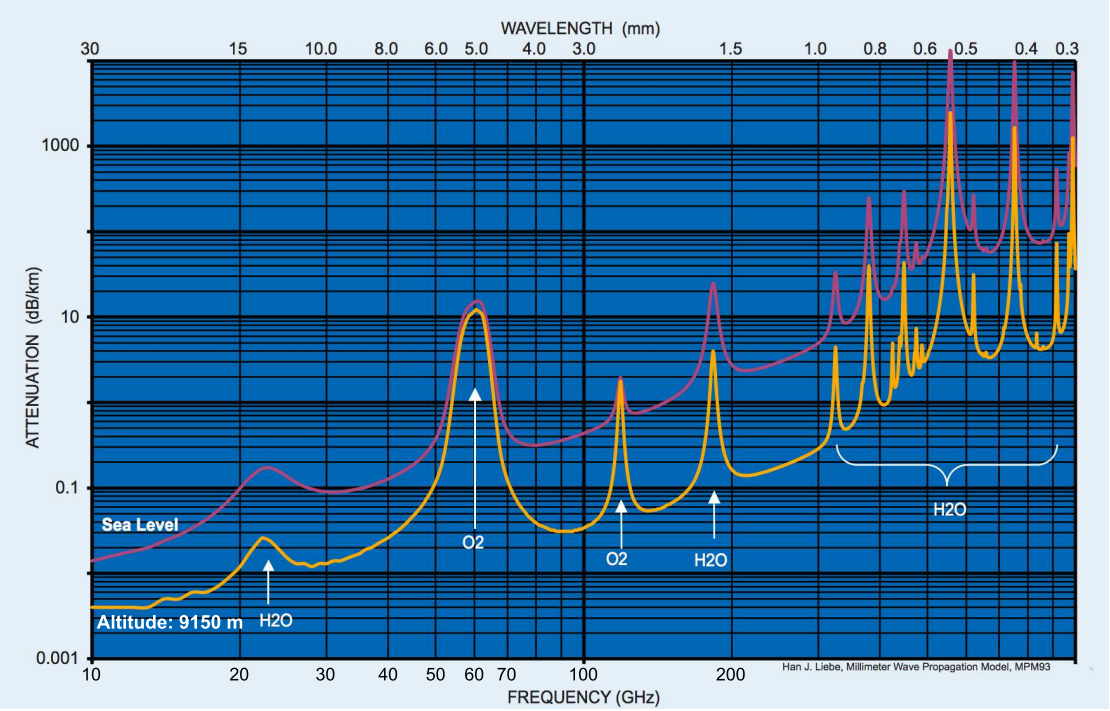

FIGURE 1.2: Average atmospheric absorption of millimeter waves.

and moisture in the air, in the form of water (H20) make the signal attenuation high, especially for frequencies around 25 GHz. Oxygen (O2) absorption instead [68], is especially very high at 60 GHz.
For all of the radar demonstrator systems implemented in this thesis, a radar frequency between 15 GHz and 17 GHz, thus free from any high attenuation factors, has been used.

1.4 Motivation

Radar systems are an important component of both civilian and military operations. Fully autonomous cars may be a decade away, but the sensors they need for collision avoidance, such as the radars, have become a big business already [69], [70], [71]. Global sales of anti-crash sensors will total 9.90 billion Dollars in 2020, up from 3.94 billion Dollars in 2014, predicts IHS Automotive [69]. Radar will account for the lion's share of that revenue, ranging up to 4.38 billion Dollars, according to the forecast, which is almost half of the total [72].
At the same pace as the autonomous cars [73], more than a dozen start-ups backed by deep-pocketed industry figures like Larry Page, a Google founder, along with big aerospace firms like Airbus and their Vahana project, the ride-hailing company Uber and even the government of Dubai, are taking on the dream of a flying car: autonomous flying vehicles or air-taxis, to be precise. Despite promising applications, the industry faces severe challenges that need to be overcome before this comes to fruition. In order for flying cars to be accepted as vehicles for urban mobility, they need to be able to take off and land without the need for a runway amidst the congested urban landscape.

To address this issue, it becomes indispensable for flying cars to have Vertical Take-Off and Landing (VTOL) capabilities. However, safety is also of paramount importance and several levels of fail-safe mechanisms need to be incorporated to inspire confidence in potential customers. An intelligent Air Traffic Control (ATC) system has to be developed to manage flying car traffic to ensure dedicated and safe air corridors for each car. More importantly, however, situational awareness technologies which can sense the surrounding environment have to be implemented. Thus, high resolution sensor architectures and algorithms, particularly for radar systems, are the key topics which are being currently researched, which can address the safety problematics inherent to driving or flying vehicles [74].
Furthermore, radar systems and signal processing techniques have been constantly improving in the last years, in response to increasingly severe threats from military targets. Notably, targets with reduced radar cross sections, slow moving and flying targets, such as UAVs, targets hidden in foliage and under trees, and generally, multiple targets in wide-zones and unknown environments.

The research at the core of this thesis, based on these concepts and problematics, has brought to the development of both novel complete radar demonstrators and innovative radar signal processing techniques, which aim at addressing some of the above mentioned applications.
The research activities for this thesis, have been carried out as the result of the collaboration between Airbus [75], Airbus Group Innovations (AGI), based in Munich (Germany) and the Polytechnic Department of Engineering and Architecture (Dipartimento Politecnico di Ingegneria e Architettura) [76], of the University of Udine (Università degli Studi di Udine) [77], based in Udine (Italy). The research has been performed at the premises of AGI, during a 3 year long period, within the team of Automatic Flight Systems, formerly known as Radio Frequency and Waveforms. During this time, while holding a Ph.D. candidate position, my tasks have been to research, develop and implement novel concepts, architectures, prototype systems and algorithms for the signal processing of advanced MIMO radar systems, together with the study and implementation of novel radar waveforms.
The research activities carried out in AGI were focused on the development of innovative complete prototype systems, based on radar technology, which could address several civil and military applications, such as the surveillance and detection of targets, both air and ground based, and the situational awareness, both in cars and in flying vehicles. Key topic of the work has been the development and analysis of radar system demonstrators, capable of 3D imaging, for a complete sensing of the target's range, Azimuth and elevation information. This has been achieved through the use of a MIMO architecture and fast beam-forming algorithms at the radar signal processing side.
Additionally, in order to cope with the frequency regulations, which vary with region and country, as well as to be adaptable to different requirements, the radar systems are developed to be flexible in achieving wide-band performance. As a matter of fact, most of the installed components are wide-band capable and can cover frequencies between 4 GHz and 40 GHz. With this approach, the radar systems can be used at any location in Europe, or even globally. Most importantly, however, they are able to operate in the Ku band, which as seen in Table 1.1 is between 12 GHz and 18 GHz, which is

the bandwidth allowed for radars to operate in Germany. Nonetheless, all of the tests performed throughout this thesis, have been done in the frequency range of 15 GHz to 17 GHz, with a total operational bandwidth of up to 1 GHz maximum. This band allows for high imaging performance, while still being not affected by tough atmospheric absorption phenomena, as seen from Fig. 1.2.

As previously stated, the chosen architecture for all systems described in this thesis, is that of 3D MIMO imaging radars. Imaging radar systems are crucial solutions for detection, tracking and classification of targets in airborne, surveillance and ground based applications. This is mainly due to their unique and desired properties. Especially, the high performance under various weather conditions, material penetration properties and usability at day and night, compared to other sensors, such as lasers and cameras based systems. Different imaging radar solutions exist. Mechanically steered radars are usually complex systems because of their physically moving components and long term reliability is often compromised [78]. Synthetic aperture radars, or SAR, are a good solution that uses the motion of the radar antenna over a targeted region [79]. This leads to a finer cross-range resolution, but there is a need for a continuously moving platform. Radars need a large effective aperture of the antennas in order to achieve a high resolution. This can be achieved in classical phased array radars [80], with a high number of elements along the transmit and receive paths, which tends to be a relatively large, complex and expensive approach.
Better performance can be achieved by utilizing a MIMO architecture [81],[4]. As it has been previously described, in a MIMO system, orthogonal signals are emitted from the transmit antennas and jointly processed at the receivers.
The signal orthogonality can, for example, be established in:

- **Time Domain**: By employing a time division multiplexing, or TDM, switching scheme between the transmit antenna elements [82]. The typical scheme, usually a round-robin structure, consists in activating only one transmit antenna element at a time, starting from the first one and then progressively sweeping through all transmit antenna elements. Upon reaching the last antenna element, the scheme is repeated from the beginning.

- **Frequency Domain**: This strategy corresponds to Frequency Division Multiple Access (FDMA), in digital communications, and it relates to the case where all transmit signals are sent from all transmit antennas, at different frequencies, simultaneously. One example is the Orthogonal Frequency Division Multiplexing (OFDM) architecture [83], [84], [85].

Independently from how the orthogonality is achieved, a MIMO architecture, based on the MIMO principle together with an appropriate antenna array arrangement, enables an improvement in the cross-resolution by an artificial increase of the antenna aperture with the so called virtual array concept. Therefore, in combination with a signal with a large bandwidth, which determines the resulting resolution in the range direction, high-resolution 3D images of the captured scenario can be achieved in a smaller sized radar. Additionally, together with the reduced number of antenna elements and simpler RF

distribution structure, if compared to a conventional antenna array, the architecture is achieved without complicated mechanics for beam steering.

This thesis focuses on the research, development and implementation of novel concepts, architectures, complete demonstrators and algorithms for the signal processing of advanced MIMO radar systems, which are compact, have high resolutions and are able to perform a fast radar processing and beam-forming for a full 3D target estimation. Additionally, a study and development of OFDM based radars is performed, together with an implementation of novel waveforms for these OFDM radars.
In particular, the major topics investigated are:

- The development of innovative digital architectures for 3D imaging MIMO radar systems, in both TDM and FDM modes, with FMCW and OFDM signals, respectively.
- The development of real-time beam-forming and Direction-Of-Arrival (DOA) algorithms for target detection (e.g. FFT based).
- The generation of advanced system concepts, parametrisation and simulation of the real-time digital radar's of the future (e.g. OFDM based).
- The development and implementation of novel constant envelope orthogonal waveforms for real-time 3D OFDM MIMO radar systems.

1.5 Implementation

One key application targeted with this research, through the collaboration of Airbus and other partners within a European project, named "ZONeSEC" [86], is the surveillance of wide-zones and critical infrastructures within the European Union. A potential failure of critical infrastructures such as nuclear and chemical plants, but also, pipelines, energy lines, transportation routes, etc., can occur at any point and at any unexpected moment across their extended grid spread over wide geographic areas. These wide-zones aim primarily to the strengthening of the infrastructure's robustness by extending in a transboundary fashion for the transport of materials necessary on a daily basis. Failures at critical points (functions, equipment, and controls) can compromise the integrity of the involved installations and the security of energy and resources supply, with adverse socio-economic effects to citizens, customers and the environment (major accidents). Shortcomings in the control of hazards inherent to the safe performance of the infrastructures are strongly linked with the effective implementation and functioning of a Safety Management System (SMS) including appropriate safety and security provisions, emergency planning and other proactive measures such as, surveillance, from detection to alert. Therefore, a key role was taken by AGI and this research, in developing complete radar system prototypes, based on the latest and most appropriate radar technologies available, which could serve the purpose of this European project.

The first achievement aimed at these applications, described in this thesis, has been the development of a complete 3D MIMO imaging radar demonstrator which operates

with a 24x24 MIMO 2D antenna array configuration and a TDM scheme. The radar sensor working frequency range spans between 16 GHz and 17 GHz, transmitting and processing FMCW signals with an operational bandwidth of 1 GHz. A complete system integration of the RF front-end, the digital system and the software architecture for digital signal processing has been accomplished. Moreover, the radar system is intended to be flexible as much in its hardware as it is in its software. A modular approach based on conventional low cost Printed Circuit Board (PCB) is used for the transmit and receive boards, which allows to flexibly add or remove boards.
For the hardware realization of the digital signal processing part, three Field Programmable Gate Array (FPGA) based cards are used, each equipped with an 8 channel Analogue to Digital Converter (ADC) board. A custom built VHSIC-Hardware-Description-Language (VHDL) coded firmware has been implemented into the boards, which works seamlessly with the embedded software on a PowerPC, and performs the radar data processing. The radar's signal generation is controlled from a control graphic Human to Machine Interface (HMI) through a Universal Serial Bus (USB) interface. From the software side, beamforming based on FFT and delay and sum techniques is performed on the raw data acquired via Ethernet, in order to generate complete 3D images of the radar captured scenario.

The second achievement, evolution of the previously described radar prototype, is a radar system which has an antenna board that consists of 16 TX and 16 RX antennas, placed on a single planar PCB with Resonant Slot Patch Antennas (RSPA). Furthermore, the digital hardware architecture used is based on a single proprietary board which has at its core a Xilinx Zynq Z-7020 System on Chip (SoC) unit [87], that combines an Advanced RISC Machines (ARM) Cortex-A9 dual-core processor with an FPGA and 16 ADCs. Additionally, a metallic 3D printed housing, which accomplishes also the task of cooling the electronics, has been built and assembled to house all the components. Thus, a more compact and portable system is achieved, compared to the first radar described. Orthogonality of the TX signals is obtained through TDM. The radar sensor working frequency range spans between 16 GHz and 17 GHz, transmitting a processing FMCW signals with an operational bandwidth of 1 GHz. Compared to the previous radar, this system operates with a faster three-dimensional (3D) FFT based beam-forming at the RX side.
Finally, the system is integrated with additional sensors and actuators, introducing multiple functions, which are integrated in a single system. The rectangular MIMO array used, with two rows of transmit antennas and two rows of receive antennas which are placed opposite to each other, offers an empty space in the center. This allows to integrate additional devices in the unused space, like a camera or a communication system. To show the advantages of the second functionality, the MIMO radar system is combined with a camera and a gimbal for target tracking.

Other crucial applications targeted with this research, through the collaboration of Airbus and other partners within a German project, named "FAST - Fast Actuators Sensors and Transceivers" [88], are the situational awareness, anti-collision, and imaging technologies for flying vehicles, such as airplanes, helicopters, but also air-taxis and UAVs. Additionally, other applications for the security sector (e.g. surveillance of luggage,

borders or buildings, people screening), and the automotive sector, are also targeted. These research activities are partially sponsored by the Federal Ministry of Education and Research (German: Bundesministerium für Bildung und Forschung), abbreviated BMBF, which is a cabinet-level ministry of the Federal Republic of Germany.
In order to target these applications, different architectures and waveforms for MIMO radars have been researched, which can lead towards systems able to operate in an almost real-time manner. However, with the idea of maintaining a small overall system cost and low hardware effort. Helicopters, UAVs and VTOL air-taxis, for example, have unique hover and vertical take-off/landing capabilities which make them ideally suited for transport in difficult access areas, winching operations and take-off and landing at unprepared sites. In these frequently encountered and demanding mission elements, the pilot faces an increase in workload when scanning for obstacles and monitoring the surrounding state. Especially in degraded visual conditions and unknown or confined areas, there's an imminent danger of collision with all kinds of obstacles, which continues to be among the top causes of accidents. If we consider, as an example, civil aircrafts alone, a recent EASA statistic on the accident numbers per cause for Commercial Air Transport (CAT), in the period 2005-2015, can be seen in Fig. 1.3 [89]. The category with the

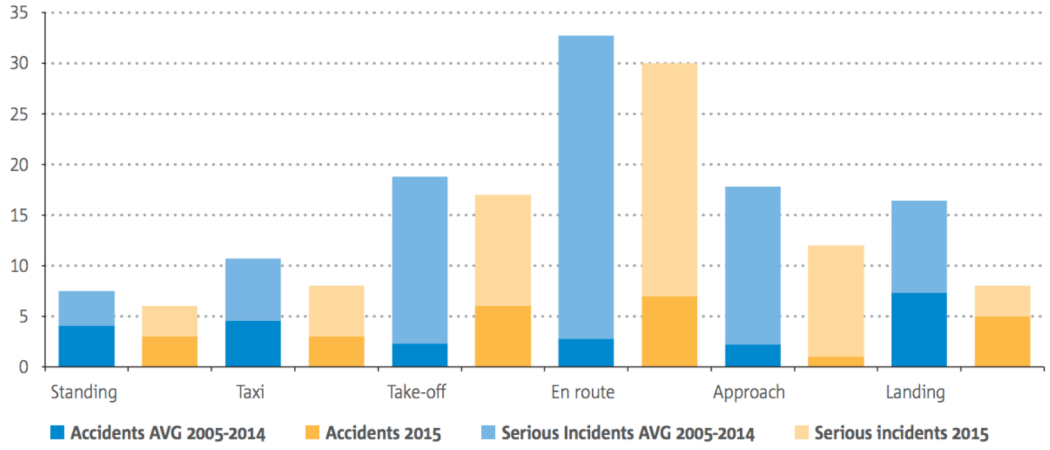

FIGURE 1.3: CAT accidents and serious incidents per phase of flight 2005-2015.

highest number of fatalities assigned is "En route", which encompasses various categories concerned with loss of in-flight control and system component failure. However, if we ignore this, the other categories related to obstacle collisions can be seen to take up most of the numbers. The categories such as "Approach" covers accidents with terrain or objects while intentionally flying close to the surface but excluding take-off and landing phases of flight. The categories "Take-off" and "Landing", instead, comprise the collision with obstacles during take-off and landing phases, respectively. Although the higher number of fatalities can be attributed to the higher speeds in cruise flight, collisions with obstacles during landing and take-off are clearly the main cause for commercial air transport accidents in general.
The main contributions to the above statistics are challenges typical for commercial operations such as Helicopter Emergency Medical Services (HEMS) for which landings in unknown, unprepared environment are part of the daily routine. Additional stress related to the urgency of the situation or deteriorating weather conditions compromises

safety even further.
The aforementioned statistics once more reveal the need for a system, which supports the pilot or crew in the obstacle detection task. For this purpose, various systems have been developed using a wide range of active sensing technologies. The majority of systems, however, come at a high cost often combined with a large physical size and power consumption. These systems are therefore mainly deployed on military platforms. The research project described in this thesis aims at developing a miniaturized, low-cost obstacle detection system specifically for these kind of applications.
Additional applications which are considered, are those aimed at reducing the potential collisions of aircrafts (A/C) during taxi and/or pushback, which are expensive and damaging to the industry in terms of image. As the number of A/C increases, the frequency of collision occurrence is increasing.
Therefore, the radar system to be developed for these primary applications (target detection and obstacle warning), is intended to enhance flight safety in approach, landing and take-off phases of flight by informing the pilot of obstacles in the near vicinity of the aircraft even in degraded visual conditions. The system must not be considered as a primary flight instrument and shall only be relied upon to perform approximation procedures. The system is therefore a flight aid for the pilot operating under visual flight rules (VFR). The following operational use cases can then be identified for the system: landing and take-off in unprepared, unknown or confined areas and in degraded visual conditions.
These use cases, which are characterized by flying at relatively low airspeeds and altitude, are most critical according to the accident statistics in Fig. 1.3. From these use cases, various key design parameters can be derived. The typical low airspeed together with a prescribed warning time for instance, effectively determines the required detection range of the sensing system. To accommodate for the various degrees of freedom and procedures in these flight phases, the field of view (FOV) of the sensor system shall cover every direction in Azimuth as well as below the flying platform. To ensure operations in degraded visual conditions requires an all-weather sensing technology not impaired by any atmospheric conditions.

Taking into account all the above mentioned aspects, the first step of this part of the research, is the study, simulation and implementation of a new system concept for a low cost, miniaturized and imaging radar system for flying platforms. The proposed solution is based on the MIMO radar architecture and on OFDM radar signals for simultaneous transmit operation, and moreover, real-time capabilities.

The OFDM architecture has been chosen for implementation because OFDM signals have been proven to be appropriate as radar signals [56]-[58], whereas their composition from a multitude of orthogonal sub-carriers makes them particularly suitable for real-time MIMO radar applications. For example, the allocation of different, mutually exclusive groups of carriers to the different transmit channels of the radar [57], allows the simultaneous operation of all transmit channels in an interference-free manner. Knowing the carrier allocation scheme, the receivers can unambiguously determine which transmitter the carrier signals were coming from, so that the whole target scenery of the radar can be processed in one run. Compared to time-multiplexed MIMO radars that

have to operate their transmitters sequentially, this is a big advantage of OFDM MIMO radars regarding realtime performance. Digital beam-forming methods for image reconstruction with high angular resolutions can be applied in a similar way as to FMCW MIMO radars. The RF front-end circuitry of OFDM radars, however, differs from the one of other types of radars. OFDM radars are based on the transmission and reception of broadband vector-modulated signals.

The first step in the implementation of OFDM based radar architectures, has been the development of a top-level system concept and a complete OFDM waveform's parametrization. The parametrization is proposed, as an example, for a radar system which is intended for obstacle warning for helicopters and to enhance flight safety in approach, landing and take-off phases of flight, even in degraded visual conditions. The full OFDM MIMO radar system has been implemented and analyzed in a MATLAB [90] based environment and tested with novel OFDM waveforms, which represents the second step.

The second step of the research on OFDM based MIMO radars, is the investigation and development of advanced MIMO OFDM radar's waveforms, coding techniques and architectures, especially with regard to the receiver processing and the beam-forming algorithms for the estimation of the radar targets' parameters. As a matter of fact, another core part of this thesis is, the design and processing of several orthogonal waveforms based on LFM signals for MIMO OFDM radars. The design, implementation and results of the complete system, capable of detection and imaging of radar targets, are here described. The orthogonality of sounding signals is critical for multi-channel radar applications since the interference between signals can significantly limit the radar's ability for observation of weak targets in presence of stronger targets and background clutter. The orthogonal waveforms are designed by coding consecutive complex LFM signals in a frame so that they can be sent to the different transmit channels of the radar, allowing the simultaneous operation of all transmit channels. Unlike other approaches which operate through sub-carrier interleaving or time division duplexing, the orthogonality in the proposed approach is achieved by applying several coding techniques, at a symbol level: Golay complementary, Frank Zadoff Chu, Walsh-Hadamard, Space-Time, Discrete Fourier Transform (DFT) and Costas based sequences. Moreover, a radar receiver processing based on a complex frame based multiplication in frequency domain between transmit and received waveforms is presented, together with a unique 4 dimensional (4D) FFT beam-forming algorithm. This allows for a fast and complete sensing of range, Azimuth, elevation and Doppler in a frame. The performance's analysis of the proposed waveforms are evaluated by their cross ambiguity functions and imaging performance, while the general performance of the radar's receiver processing is shown through the use of multiple radar images. The flexibility of generating such orthogonal coded waveforms and general receiver architecture paves the way for an adaptive radar.

Finally, the last part of the research, is based on the implementation of a complete 3D imaging OFDM MIMO system demonstrator, which uses one of the novel complex waveforms proposed, in particular the Walsh-Hadamard coded LFM based waveform. The system is, again, intended for low cost, miniaturized flying platforms and represents the first step towards the implementation of real-time capable 3D imaging radar systems. The radar architecture is based on the use of OFDM signals which are simultaneously

transmitted from all transmit antennas. Unlike the previous and other approaches which operate through sub-carrier interleaving, the proposed technique relies on the transmission of periodically repeated complex LFM chirps with a coding approach applied at a symbol level. The proposed waveform and radar system is verified through measurements and the results are presented, through radar image captures.

1.6 Outline of the Thesis

The different achievements of this thesis can be categorised into two main branches, which are the research and development of FMCW based 3D MIMO radar and OFDM based 3D MIMO radar architectures and algorithms, together with the design and implementation of novel receiver processing techniques and waveforms. Therefore, in order to fully describe the contributions and results, the thesis is organized as follows:

- Chapter 1: This chapter provides a general introduction to radar concepts, typologies and state of the art, but also the applications and the motivation at the core of the research in this thesis.
- Chapter 2: Here, a theoretical background is introduced, with special focus on radar systems, radar equations and the ways that these systems operate. Additionally the MIMO model and principles, the direction of arrival estimation, the time division multiplexing scheme and concepts regarding FMCW based radar systems are discussed. The information provided in this chapter is essential in order to understand the further two chapters, where complete FMCW based MIMO radar demonstrators are shown.
- Chapter 3: This chapter presents the first complete radar demonstrator which has been achieved: a 3D FMCW MIMO imaging radar system which operates with a 24x24 2D antenna array and integrates three FPGA boards for digital signal processing. The system architecture and an in depth description of the digital hardware and software processing is given. Moreover, the algorithms and techniques for the beam-forming and 3D radar image generation are here described. A calibration, timing and performance analysis on the overall radar system, especially regarding its separation capabilities for the Azimuth angle, elevation angle and range resolution, is carried out. Several resulting radar 2D profiles, proving the high resolution of the reconstructed images, are here presented, for scenarios with static targets. Considering the achieved results, it can be understood that the radar demonstrator presented, is well suited in targeting applications, such as, the ground based surveillance of stationary wide-zones and high security or hazardous infrastructures. The portability and compact size factor aid in this, allowing the radar to be easily and flexibly moved.
- Chapter 4: In this section, the second complete radar demonstrator is shown. The system is a 16x16 2D antenna array based, 3D FMCW MIMO imaging radar, which represents the results of research and studies aimed at improving the architecture of

the radar presented in Chapter 3. A reduction is achieved in the size factor of both the RF front-end, obtaining a single board with TX and RX antennas integrated and a single board based receiver, and the digital hardware architecture, obtaining a single board as well, which is a ZYNQ based proprietary platform with 16 ADCs integrated. Furthermore, an implementation of a faster 3D-FFT based beam-forming processing, is also achieved. The MIMO radar demonstrator is tested and analysed in several scenarios. In an anechoic chamber and in outdoor test fields, for the detection of targets, both static and moving, represented by corner reflectors, UAVs and people. Additional concepts such as the utilization of an added camera sensor, scene imaging capabilities, target tracking algorithms and jamming applications are also discussed. Thanks to its size and fast sensing of 3D information from targets, a new range of applications can be addressed from this compact MIMO radar, as for example, all those situations where high-resolution 3D imaging sensors are required to have a small size factor, such as the situational awareness and autonomous operations in cars and flying platforms.

- Chapter 5: This chapter provides a general introduction to OFDM systems and a description of a new generation of radar system based on an OFDM architecture. Moreover, a description of a system concept architecture for an OFDM based radar is given, together with an in depth analysis of the parametrization of an OFDM radar waveform for a specific application connected to flying platforms.

- Chapter 6: In this chapter, the design, development and analysis of advanced MIMO OFDM waveforms, coding techniques and radar processing architectures is given. Several orthogonal waveforms based on LFM signals for MIMO OFDM radars are presented, in which various coding schemes, for achieving orthogonality, are used: Golay complementary, Frank Zadoff Chu, Walsh-Hadamard, Space-Time, DFT and Costas based sequences. Moreover, a novel radar receiver processing based on a complex frame based multiplication in frequency domain between transmit and received waveforms is presented, together with a unique 4D FFT beam-forming algorithm. The performance of the proposed waveforms is evaluated through the analysis their cross ambiguity functions and imaging capabilities, while the general performance of the radar's receiver processing is shown through the use of multiple radar images, which show a full reconstruction of the range, Azimuth, elevation and speed of the targets. The flexibility in generating such orthogonal coded waveforms, the proposed general receiver's architecture and the fast 4D-FFT beam-forming implemented, pave the way for an adaptive and real-time capable 3D MIMO OFDM radar.

- Chapter 7: In this section, a complete OFDM based 3D MIMO radar demonstrator is shown. The core of the hardware architecture is based on that of the 3D MIMO radar system introduced in Chapter 4. However, the digital processing is completely changed and adapted to be operating with the OFDM radar's architecture described in Chapter 6. The system operates with one of the novel LFM based OFDM waveforms discussed in Chapter 6, where the orthogonality between the transmit elements is achieved by means of a Walsh-Hadamard based coding scheme. The radar system is verified through measurements and the results are

presented, through radar image captures achieved outdoors. The proposed architecture, paves the way for low cost, miniaturized and real-time capable, adaptive OFDM MIMO 3D radar systems.

- Chapter 8: This section summarizes the achieved results and introduces concepts for future works.

Chapter 2

Fundamentals of FMCW MIMO Radars

2.1 Chapter's Introduction

MIMO radar is an emerging technology that is an extension to the classical digital beamforming radar. The main difference compared to a conventional radar is the capability of transmitting different signals on multiple TX antennas while keeping these signals separable at reception. Throughout this chapter, fundamental equations and parameters of radar systems are analysed, before introducing the concepts of MIMO radars, virtual arrays, angle of arrival estimation and, finally, the description of how FMCW MIMO radar systems operate and how the signals can be separated by means of time domain multiplexing.

2.2 The Radar's Equation

The main criterion for the derivation of the radar equation, is the Free-Space Path Loss (FSPL) equation [91]. In telecommunication systems, the FSPL is defined as the loss in signal strength of an electromagnetic wave that would result from a line of sight path through free space, with no obstacles nearby to cause reflection or diffraction. It takes into account several principles. First of all, it is intrinsic the fact that the energy which is emitted by an isotropic radiator, propagates uniformly in all directions [92]. With this in mind, it can be understood that areas which have the same power density, form spheres that have an area of $A = 4\pi R^2$, around the radiating antenna. However, the power density on the surface of a sphere is inversely proportional to the surface area A, or the square of the radius R, of the sphere. Therefore, considering a transmitter and a receiver, the FSPL equation considers how the power loss between the two, is proportional to their distance.
Additionally, the FSPL takes into account the fact that the loss is proportional to the square of the frequency of the radio signal and the effect of the receiving antenna's

aperture, which describes how well an antenna can pick up power from an incoming electromagnetic wave.
From the inverse square law, the spreading out of the electromagnetic energy in free space [93], can be expressed as

$$S = \frac{P_t}{(4\pi R)^2} \tag{2.1}$$

where P_t represents the transmitted power and R is the distance between the transmitter and the receiver. The second aspect, with regard to an isotropic antenna and its aperture [94], is the received power, which is defined as

$$P_r = \frac{S\lambda^2}{4\pi} \tag{2.2}$$

where λ is the transmitted wavelength. All things considered, the expression for the total loss, seen as the ratio between the transmitted and received power, given by the FSPL equation, is

$$FSPL = \frac{P_t}{P_r} = \frac{(4\pi R)^2}{\lambda^2} = \frac{(4\pi Rf)^2}{c^2} \tag{2.3}$$

where f represents the frequency of the signal and c is the speed of light.
The radar equation [95], takes on from the FSPL equation and considers additional factors, such as the directivity of an antenna and the antenna gain [94]. Since a spherical segment emits equal radiation in all direction, at constant transmit power, if the power radiated is redistributed to provide more radiation in one direction, then this eventually leads to an increase of the power density in direction of the radiation. This effect is called the antenna gain [96]. This gain is obtained by directional radiation of the power emitted by the antenna. The directional power density, can be derived from equation (2.1), as

$$S_t = S \cdot G = \frac{P_t}{(4\pi R)^2} \cdot G \tag{2.4}$$

where, here as well, R represents the distance between the transmitter and the target. In a radar system, the target detection isn't only dependent on the power density at the target position, but also on the amount of power which is reflected back towards the radar. In order to determine the useful reflected power, it is necessary to know the so called, radar cross section (RCS) [97], defined as σ. The value of RCS for a target, depends on several elements. Most importantly, the larger the section of a reflecting object, the higher will the be the back reflected power. However, other factors, such as the type of material which the targets is made of, the design and the composition of its surface, will influence the target's RCS value. Thus, all things considered, the reflected power from a target, can be extracted from equation (2.4) as

$$P_{tar} = \frac{P_t}{4\pi R_{tx}^2} \cdot G \cdot \sigma \tag{2.5}$$

where R_{tx} represents the distance from the radar's transmitter to the target. Dually for the receiver, it can be obtained that the power density at the radar receiver is

$$S_r = \frac{P_{tar}}{(4\pi R_{rx})^2} \tag{2.6}$$

where R_{rx} represents the distance between the radar's receiver and the target. Consecutively, considering the effective antenna aperture A_{eff} and the power density, the received power at the radar's receiver is

$$P_r = S_r \cdot A_{eff} = \frac{P_{tar}}{(4\pi R_{rx})^2} \cdot A \cdot K_a \tag{2.7}$$

where A represents the geometric antenna area and K_a denotes its efficiency. Usually, the antennas used for the transmit and receive elements of a radar system are the same. Accordingly, it can be assumed that R_{rx} is equal to R_{tx}. Thus, considering now, both the transmitted and received power, it can be seen that

$$P_r = \frac{P_T \cdot G \cdot \sigma}{(4\pi)^2 \cdot R^4} \cdot A \cdot K_a \tag{2.8}$$

Finally, from antenna theory, the antenna gain can be expressed as [94],

$$G = \frac{4 \cdot \pi \cdot A \cdot K_a}{\lambda^2} \tag{2.9}$$

hence, obtaining the radar's equation expressed for P_r as,

$$P_r = \frac{P_t \cdot G^2 \cdot \lambda^2 \cdot \sigma}{R^4 \cdot (4\pi)^3} \tag{2.10}$$

It is important to notice from this equation, the significant proportional effect of the target's RCS value σ, together with the antenna gain G and transmit power P_t. Additionally, it can be also understood that the distance between the radar and the target, has a inversely proportional effect which evolves with the power of 4 of R. Another way to see the radar's equation is by solving equation (2.10) for the range R, thus, obtaining

$$R = \sqrt[4]{\frac{P_t \cdot G^2 \cdot \lambda^2 \cdot \sigma}{P_r \cdot (4\pi)^3}} \tag{2.11}$$

Furthermore, in a radar system, it is important to calculate the maximum detectable range [98]. Usually, parameters such as P_t, G and λ can be regarded as constants, since these vary in small ranges. However, the radar's cross section plays an important role in influencing the radar's equation, as previously mentioned. The RCS can vary from 1 m^2 to 40 m^2, for a human target or a corner refelctor used as a target, respectively.
The lowest received power that can be detected by the radar is defined as S_{min}. Values which are lower than this, are masked by the receiver's noise. Therefore, calculating equation 2.11, with $P_r = S_{min}$, yields R_{max}, which denotes the maximum detectable range of the radar system, as shown in the graph of Fig. 2.1.
The above mentioned radar's equation is the one used in the characterisation of almost all radar system demonstrators. However, it could be further extended to take into consideration, not only the propagation under ideal conditions, but also all the radar's internal losses, the atmospheric losses and the influence of the earth's surface [99].

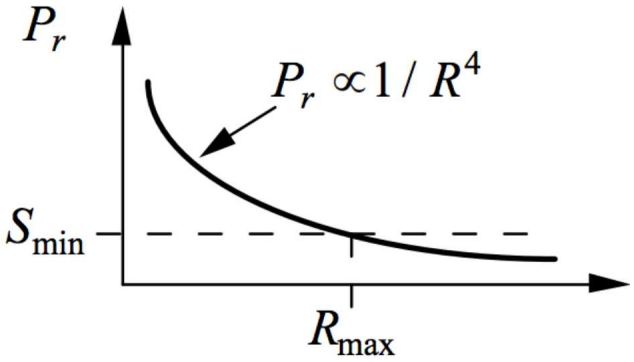

FIGURE 2.1: Maximum range

2.3 Radar's Parameters

Another basic factor in radar's operation is the range resolution. It determines the ability of the radar to distinguish between two targets [100]. Before formulating the range resolution, it is necessary to first introduce and determine the unambiguous range of a radar and its bandwidth.
By considering τ as the two-way propagation delay time, which accounts for the time between the emission of the electromagnetic wave from the radar's transmitter and the reflected wave coming back to the radar's receiver, the maximum unambiguous range of a radar can be written as

$$R_{max} = \frac{c \cdot \tau}{2} \tag{2.12}$$

where c is the speed of light. In this equation, R_{max} represents the maximum range from which a transmitted radar signal, or pulse, can be reflected and received before the next pulse is transmitted. The range is measured by the time delay between pulse transmission and reception, ordinarily assuming that the received pulse is associated

with the most recent transmitted pulse. Therefore, targets at ranges beyond R_{max}, appear at closer ranges because of range folding. Special coding of the pulses permits discrimination between echoes from the most recent transmitted pulse and earlier ones, enabling the measurement of ranges beyond the maximum range.
Additionally, other considerations have to be made regarding the maximum unambiguous range, since a sampling is usually performed at the radar's receiver side, in order to bring the signals from analogue to digital domain. This is mandatory, in order to perform further radar digital signal processing, beam-forming and, therefore, radar image reconstruction.
Considering a sampling frequency f_s, a limit on the maximum resolvable frequencies that can be sampled, is imposed [101], which sets a maximum range of

$$r_{max} = \frac{c0 \cdot \Delta f}{2\frac{B}{dt}} \tag{2.13}$$

where Δf is half the sampling frequency, B is the operational bandwidth of the radar's system and dt is the radar signal duration.

The bandwidth B of a radar's signal, is one of the most important parameters to take into account when designing a radar system. This is due to the fact that the bandwidth is proportional to the range resolution performance of the radar. The larger the bandwidth, the narrower the spectrum peak and the higher performance in the range resolution can be achieve. There are two different bandwidth types that can be defined, the signal's bandwidth, which is regulated by the pulse's width of the signal or by its modulation, and the radar's bandwidth. If the system requires a big resolution in range to differentiate among targets, the bandwidth needs to be large. As a matter of fact, the range resolution is proportional to the inverse of the bandwidth, and it's defined by the relationship

$$\Delta R = \frac{c}{2 \cdot B} \tag{2.14}$$

where, as previously introduced, B denotes the bandwidth of the radar's signal. The range resolution basically defines the ability of a radar system to discriminate between different targets, in the range direction. Equation 2.14 can be linked to previously presented concepts. For a basic pulsed radar, the bandwidth is approximately proportional to the inverse of the pulse width $B = 1/\tau$, where τ corresponds to a distance, as per equation 2.12, which considers that radars deal with round-trip timing measurements. Most modern radars will use a form of pulse compression in order to use longer pulses, hence with more energy, and obtain a Signal to Noise Ratio (SNR) boost while still retaining ideal range resolution. In this instance, the pulse width is no longer proportional to the bandwidth, since a swept frequency is used to increase the bandwidth, like in the case of FMCW radars. However, the above expression is still valid for calculating the range resolution. For CW radars, the ability to measure the range is dependent on using a swept FM modulation on the CW signal, and, again, the range resolution is still dependent on the bandwidth used for that ranging modulation.
Most modern radars are designed to be narrowband. This means that the bandwidth

is very small compared to the operating center's frequency. This allows all of the components to be narrowband components which means that power amplifiers, filters, and other internal components, only have to be linear over a very small frequency range. Implementing wide-band or ultra-wide band signals is not trivial, but today's technology and digital processing is making it more accessible. A wide-band design is more complicated, because all the radar's internal components, including the channel in between the radar and the target, have to be linear over a much wider frequency range. The more wide band the radar is, the better the range resolution achieved, but at the same time, the harder it gets to design and implement such systems. Therefore, if a very high resolution is required, higher carrier frequencies have to be considered. For example, for an FMCW radar operating at a frequency of 16 GHz to 17 GHz, with a 1 GHz bandwidth signal, the range resolution is 15 cm. Factors which could limit the range resolution of a radar systems, are the non linearity of some of the internal components and, especially, the cutting and windowing of the radar signals in the digital processing procedures.

2.4 The MIMO Model

As the name suggests, MIMO radars consists of multiple antenna elements, both for the transmission and the receiving of radar signals. Together with this kind of architecture, another key concept of MIMO systems comes from the idea of diversity [102], [27], [103], [104]. The idea is that an improvement can be achieved in the performance of a system, by combining different informations which have been received by different receivers. For example, in telecommunication's devices, this relates to an improvement in the data rate or quality of the data link, whereas in radars, this translates to better detection and localization properties [105], mainly due to an increase in the angular's resolution properties.

Two categories of MIMO architectures exist: Statistical MIMO radars and coherent MIMO radars. The only one considered throughout this thesis is the coherent type. In this case, the transmit and receive antenna elements are spaced closely together. Here, it is assumed that the target is in the far field of the transmit (and receive) array. Thus, it is assumed that the target's scattering response is the same for each antenna pair, up to some small delay. Whereas, in statistical MIMO radars, the antennas for the transmit of radar signals, are positioned far away from the receive antennas [106].

In a traditional SIMO radar [107], the system can only transmit phase shifted and scaled versions of a single waveform, since the architecture itself is based on multiple receive (RX) antennas, but only a single transmit (TX) antenna.

Moreover, as it will be described later on, the angle resolution of a radar depends on the number of RX antennas [108], [109]. If for example, a device with four RX antennas is considered, the angle resolution is of about 30°, whereas a device with eight RX antennas has an angle resolution of about 15°. Therefore, a direct approach to improving the angle resolution requires increasing the number of RX antennas. This approach has its limits because each additional RX antenna requires a separate RX processing chain on the device, which included a Low Noise Amplifier (LNA), mixer, Intermediate Frequency

(IF) filter, ADC, and many other smaller components.
As previously mentioned, MIMO radar system allows the transmission of orthogonal waveforms from each of its multiple transmit antennas [110]. At the receiver, these waveforms can be extracted by a set of matched filters. Therefore, this allows the calculation of amplitude and phase relationships of a large number of points in space, which, is the result of a multiplication between the number of transmit and the number of receive elements. These points form the elements of the virtual antenna array. This, known as the MIMO principle, together with an appropriate antenna array arrangement enables an improvement in the cross-resolution, thanks to an artificial increase of the antenna aperture with the so called virtual array concept.
For a coherent MIMO radar, with N_{TX} transmit elements and N_{RX} receive elements, there are $N_{TX} \times N_{RX}$ distinct propagation channels from the TX array to the RX array. Therefore, thanks to the possibility of extracting each transmitted signal through orthogonality techniques, a virtual phased array of $N_{TX} \times N_{RX}$ elements can be synthesized with only $N_{TX} + N_{RX}$ antenna elements. Diversity of the TX channels can be achieved by employing time division multiplexing, frequency division multiplexing, spatial coding, and orthogonal waveforms.
Therefore, the angle resolution of a MIMO radar with N_{TX} transmit antennas and N_{TX} receive antennas can be made equivalent to that of a SIMO radar with $N_{TX} \times N_{RX}$ receive antennas. The MIMO radar, therefore, provides a cost-effective way to improve the angular resolution of the radar [111], [112].
The locations of the virtual elements can be obtained by convolving the real transmitters' and receivers' locations. Additionally, by reshaping the antenna array structure, different virtual phased arrays can be obtained.

2.4.1 Phase Delays and Angles of Arrival

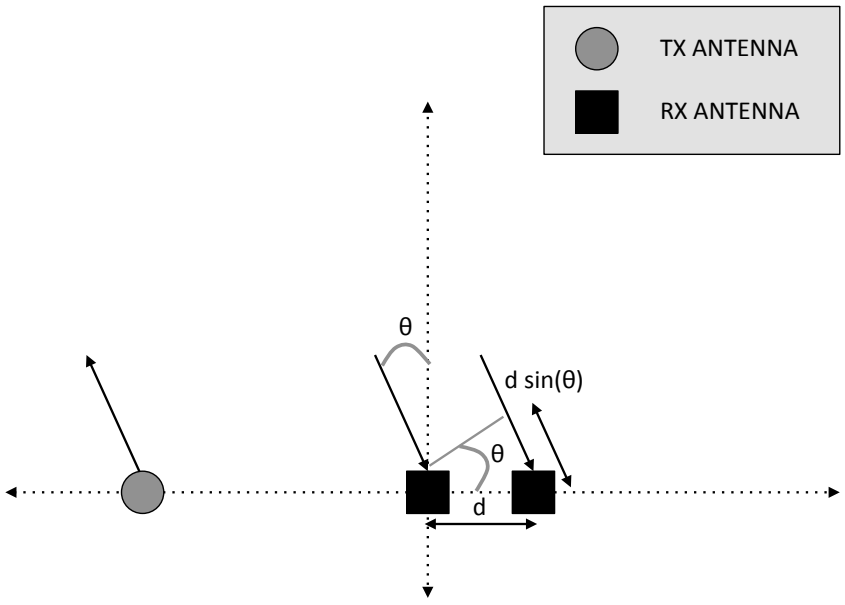

FIGURE 2.2: Angle estimation using 2 RX antennas.

In order to estimate the angle of arrival of a target, the number of RX antenna elements must be $N_{RX} \geq 2$ [113]. For example, in Fig. 2.2, an antenna array which includes two receive antennas, is illustrated. As shown, the RX antennas are separated by a distance d. After being transmitted from the TX antenna, the radar signal gets reflected by an object or target and then reaches all the RX antenna elements. The angle at which the radar signal gets reflected at, with regards to the radar system, is θ. As it can be seen from the picture, the signal must travel an additional distance of $d \cdot \sin(\theta)$, before reaching the second RX antenna (the one on the right). This difference in path length, corresponds to a difference in phase, between the signals which have arrived to the two RX antennas, of

$$\omega = \frac{2 \cdot \pi}{\lambda} \cdot d \sin(\theta) \tag{2.15}$$

Therefore, through a beam-forming operation, such as the delay and sum beam-former or the FFT based beam-forming algorithms later described in this thesis, the angle of arrival of a target can be determined by estimating the phase difference ω, and calculating

$$\theta = \sin^{-1}\left(\frac{\omega\lambda}{2\pi d}\right) \tag{2.16}$$

The Field of View (FOV) of a radar can be determined from this expression. Since, ω can be uniquely estimated only between $-\pi$ and π, then by calculating equation (2.16) with $\omega = \pi$, it can be seen that the unambiguous FOV of a radar is determined by

$$\theta_{FOV} = \pm \sin^{-1}\left(\frac{\lambda}{2d}\right) \tag{2.17}$$

Therefore, it can be understood that the maximum FOV of a radar is obtained by achieving a distance d, between elements, equal to $d = \lambda/2$. With this in mind, equation (2.17) translates to $\theta_{FOV} = \pm 90°$ [113].

Similarly, the same calculations can be done for a system with four receiving antennas, as the depicted in Fig. 2.3. However, in this case, each additional RX element, receives a signal with an additional phase shift ω, as compared to the antenna on its left. This means that, considering N_{RX} elements, for each antenna along the array, there is a linear progression in the phase of the signal of $0, \omega, 2\omega \ldots (N_{RX} - 1)\omega$, compared to the first antenna.
An example of direction of arrival estimation processing, which will be later discussed, is the FFT based beam-forming, which performs an FFT operation along the RX signal sequences, thus, operating on the phase's shifts.

It can be seen, from Fig. 2.4, that by increasing the number of antennas along the RX axis, from four to eight elements for example, a sharper peak can be obtained. Thus, a better angular resolution is obtained. In terms of resolution, the definition usually relates to the beam-width of a peak or lobe, at the 3 dB point. The narrower is the

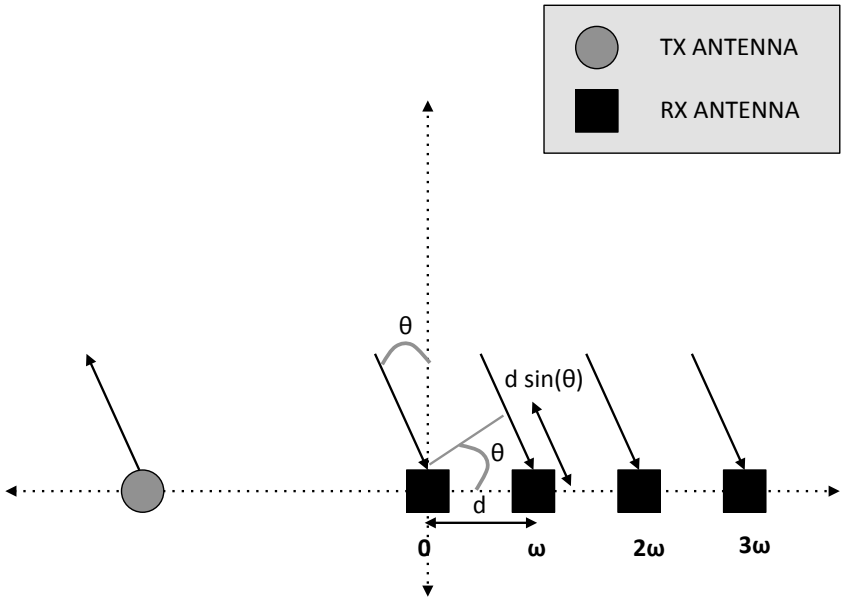

FIGURE 2.3: Angle estimation using 4 RX antennas.

peak, the lower is the resolution's value, and the better is the angular's resolution. In this image, two targets have been placed at $-10°$ and $10°$, and it can be seen that the resolution is half, for the case of eight elements, compared to the case with four. This allows to effectively identify and uniquely distinguish the two targets.

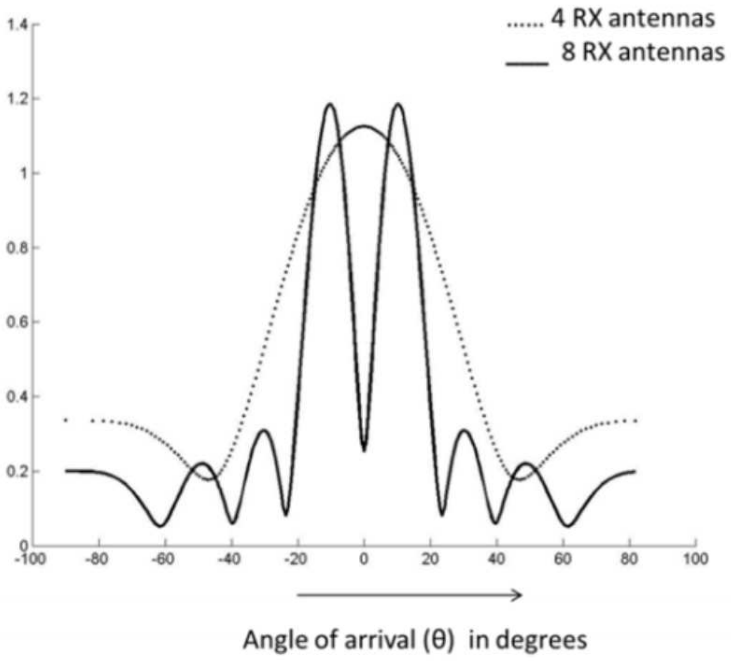

FIGURE 2.4: Angle resolution improves with increasing number of RX antennas.

2.4.2 The MIMO Principle

As a consequence of what has been previously described, it can be understood that, if an even better angular resolution is required or wanted, this can be achieved by increasing the number of RX elements in the antenna array. An example of the effects of doubling the number of RX elements is now presented.
This is depicted in Fig. 2.5, where it can be seen that the consecutive phases for all elements, are $0, \omega, 2\omega, 3\omega, 4\omega, 4\omega, 5\omega, 6\omega, 7\omega$.

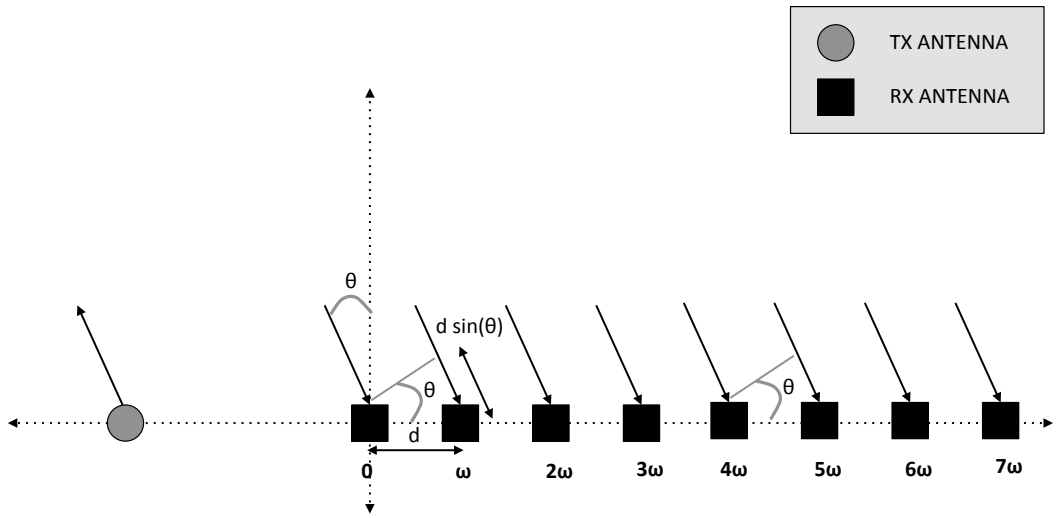

FIGURE 2.5: Angle estimation using 1 TX and 8 RX antennas.

However, the exact same result can be achieved by utilizing a MIMO approach [113]. The idea is that, through the use of an additional TX antenna and only half of the RX elements, as compared to the last example, the same angular resolution can be achieved. Fig. 2.6 shows the array architecture for a 2 TX and 4 RX MIMO radar antenna array. As it can be seen from the schematic, the signals which are transmitted from TX antenna 2, compared to the signals from TX antenna number 1, have to travel an additional path length of $4d\sin(\theta)$.

Therefore, the linear progression in the phase of the signal of $0, \omega, 2\omega, 3\omega, 4\omega$, is still valid for the signals transmitted from TX antenna 1, however it becomes $4\omega, 5\omega, 6\omega, 7\omega$, for the signals from the TX antenna 2. By concatenation of the two sequences, it can be seen that the final results is exactly the same as the one achieved from the architecture shown in Fig. 2.5, which had 4 additional RX antenna elements.
From this simple example, it is understood how the MIMO principle, together with a proper antenna array arrangement, allows to achieve a virtual array of $N_{TX} \times N_{RX}$ elements, thus increasing the radar's angular resolution.
A generalization of the model can be extracted as follows. If p_m denotes the coordinates of the m-th TX antenna, with $m = 0, 1, \ldots N_{TX}$, and q_n denotes the coordinates of the n-th RX antenna, with $n = 0, 1, 2, \ldots N_{RX}$, then the location of the virtual antennas can be computed as $p_m + q_n$, for all possible values of m and n.
If the example in Fig. 2.6 is considered, then $p1 = 0$ and $p2 = 4$, and $q1 = 0$, $q2 = 1$,

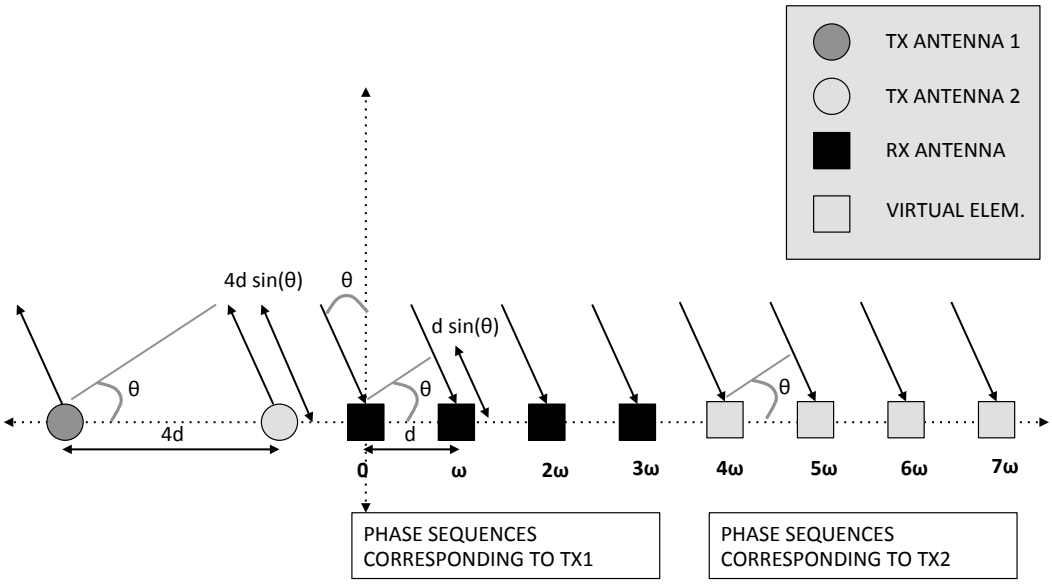

FIGURE 2.6: Angle estimation using 2 TX and 4 RX antennas.

$q3 = 2$, and $q4 = 3$. For simplicity, the coordinates are expressed in units of d, and transmit antenna TX1 and receive antenna RX1 (most left), are assumed to be the origin for the TX and RX antenna arrays, respectively.

The concepts and equations can be easily extended to the case of multidimensional arrays. An example is shown in Fig. 2.7. In this pictures, 4 TX and 4 RX antenna elements are placed in such a way that a virtual antenna array of 16 elements is achieved. Furthermore, this particular multidimensional arrangement, allows for the estimation of both the Azimuth and elevation information from the radar's targets.

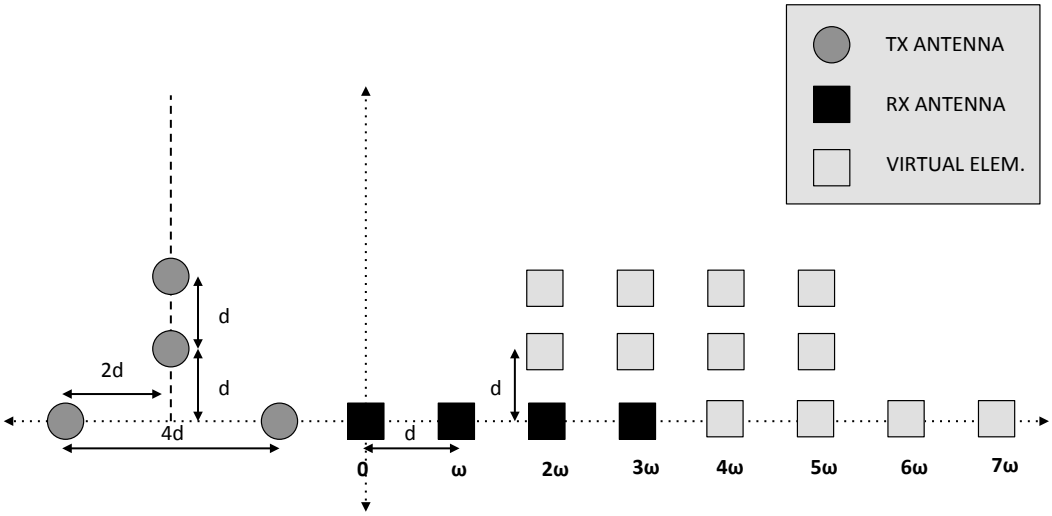

FIGURE 2.7: Two-Dimensional angle estimation using 4 TX and 4 RX antennas.

2.4.3 A Coordinate's System

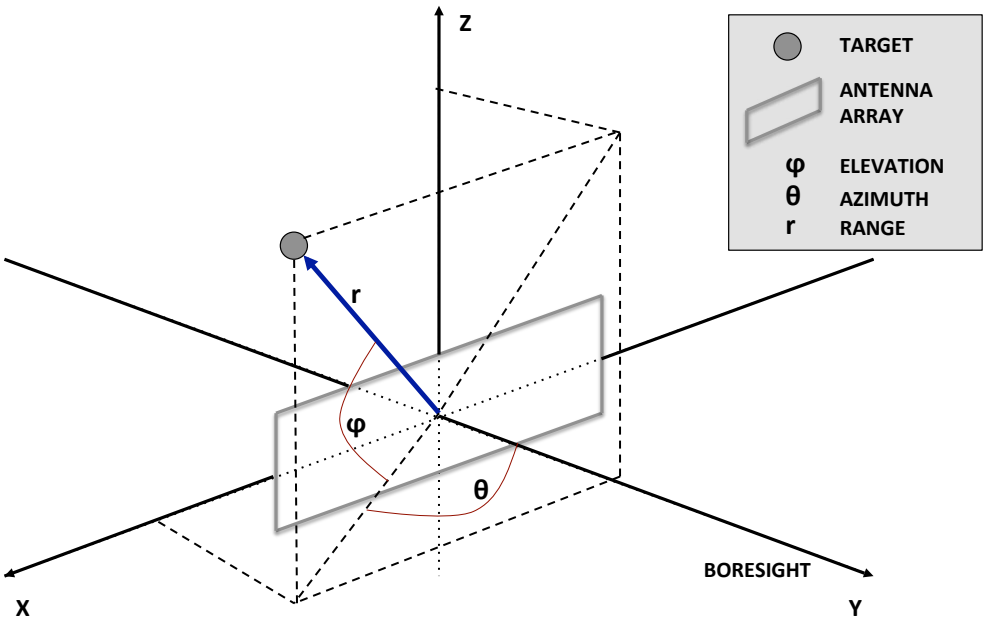

FIGURE 2.8: Radar three-dimensional coordinates system.

Radar measurement data is collected over a surface as a function of position relative to the antenna [114]. The data collection coordinate system directly affects how data is mapped to the surface: planar, cylindrical, spherical or other types. Far-field measurements are usually mapped or converted to spherical surfaces from which directivity, polarization and patterns are calculated and projected. Often the collected coordinate system is not the same as the final-mapped system, requiring special formulas for proper conversion. In addition, projecting this data in two and three-dimensional polar or rectangular plots presents other problems in interpreting data.

Radars in general, and more specifically, the radar systems and algorithms presented in this thesis, make use of particular coordinate transformation's in order to present the radar data in various formats which can be easily interpreted. The radar images from the next chapters, are shown in both three-dimensional or two-dimensional view. However, it is important to introduce the concepts of Azimuth and elevation coordinates, as shown in Fig. 2.8.

The radar is located at the origin of the coordinate system and the Earth's surface lies in the XY plane.

The Azimuth angle of a vector is the angle between the Y-axis and the orthogonal projection of the vector onto the XY plane. The angle is positive in going from the Y axis toward the X axis. Azimuth angles lie between -180 and +180 degrees.

The elevation angle is the angle between the target's vector and its orthogonal projection onto the XY-plane. The angle is positive when going towards the positive Z-axis from the XY plane. These definitions assume the boresight direction is the positive Y-axis.

The radar images presented in this thesis will be various sets of 2D images in the form of Azimuth-range cuts, where the elevation is fixed and constant, elevation-range, where

the Azimuth is fixed and constant, or Azimuth-elevation, where the range is fixed and constant. Additionally, 3D radar images, where all axis are displayed at once, are also shown.

2.5 The FMCW Signal Model

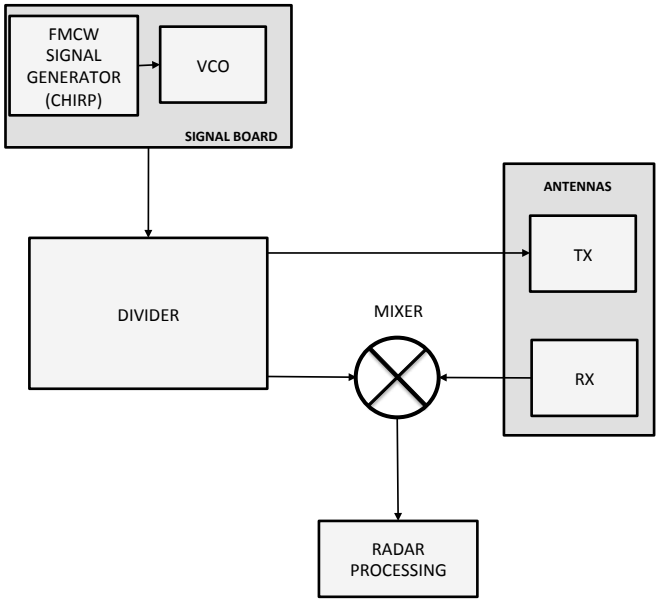

FIGURE 2.9: Basic overview of how an FMCW system operates.

Two of the radar systems implemented through the work of this thesis, are based on an FMCW architecture. Therefore, in order to fully understand the underlying principles of operation, a brief description of the FMCW signal model is here given. The basic operation of an FMCW system, is shown in Fig. 2.9.

FMCW radars differ from pulsed radars, since they operate with electromagnetic signals which are continuously transmitted and use the homodyne principle, i.e., a CW radar in which the oscillator serves as both the transmitter and local oscillator [115]. The advantage obtained by modulating the frequency is the ability to determine range without requiring a short pulse [116]. Modulation of the transmitted signal provides the timing mark which can be used to extract range information. For instance, a frequency modulated signal would have various frequency components [52]. Hence, when a target echo is received, those different frequency components will arrive in different time, thus, creating the option for range measurement. As a matter of fact, the frequency of the FMCW signal changes over time, generally in a sweep across a set bandwidth. The difference in frequency between the transmitted and received (reflected) signal is determined by mixing the two signals, as shown in Fig. 2.9, producing a new signal which can be measured to determine distance, position or velocity. The components of the signals after the mixing operation are commonly referred to as "beat frequencies". The multiplication process will generate two signals: one with a phase equal to the difference of the multiplied signals, and the other one with a phase equal to the sum of the phases. The sum signal will be filtered out and the difference signal will be processed by the

signal processing unit.
The most basic FMCW signal is the chirp signal [117]. It is basically an FM signal where the frequency is increased or decreased with time, just like the chirping noise of birds, or bats. It is simple in concept and easy to generate. A chirp signal can be generated in ascending order (up-chirp signal) or descending order (down-chirp signal). Moreover, the frequency differences can be linear or exponential. In order to maintain simplicity, most radars use a linear chirp signal. An example of FMCW signal, generated as an up chirp, can be seen in Fig. 2.10. This particular signal, represents one of the most commonly used 77 GHz radar signals for automotive driving assistance applications. It can be seen that the signal has a bandwidth of 150 MHz, which is swept in around 7.33 microseconds.
All of the equations which have been previously discussed in this chapter, with regard to the radar and MIMO radar concepts, are still valid for the case of FMCW based MIMO radar architectures.

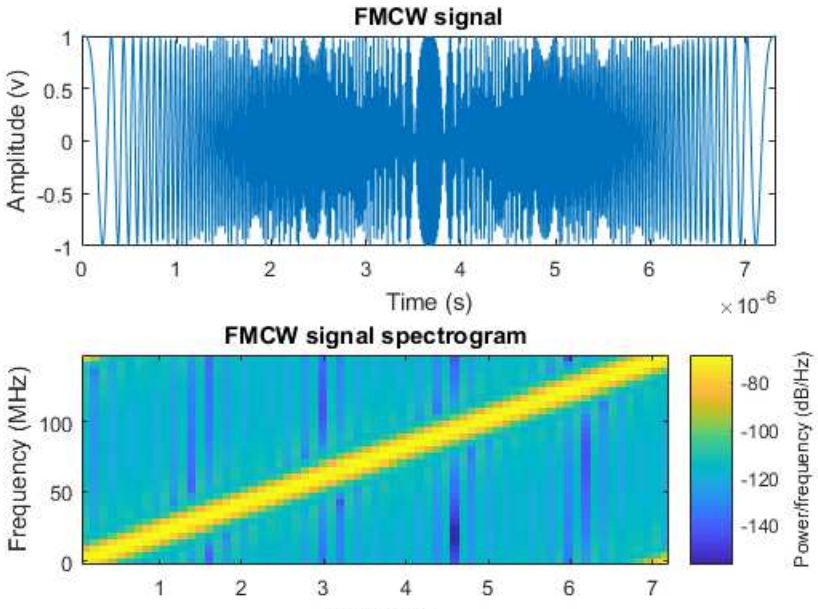

FIGURE 2.10: Example of an FMCW signal, with central frequency of 77 GHz. The time domain and the spectrogram representations are shown in the top and bottom part of the image, respectively. [1]

For the generation of an FMCW radar signal, a Direct Digital Synthesiser (DDS) device in combination with a Phase Locked Loop (PLL) module, can be used. A DDS is a frequency synthesizer that consists of a phase accumulator, phase to sine converter and a DAC. Digitized samples of the time-varying signal are generated and then converted to analogue domain. Possible waveforms include linear up and down chirps.
In an FMCW radar employing a linear up sweep in frequency (up-chirp signal), the radar signal generator produces a phase modulated signal in the form of [118],

$$s(t) = e^{j(2\pi f_c t + \pi k t^2)} \tag{2.18}$$

where t spans between $-T_c < t < T_c$, T_c is the chirp duration, f_c is the carrier frequency, and $k = \pm B/T_c$ is the chirp rate, which is the chirp sweeping bandwidth divided by the chirp duration. The positive sign in the value of k, denotes an up chirp, whereas a negative value, a down chirp, instead.
A target or object is now considered, at a range R and an angle θ, with respect to the radar's bore-sight and, as previously described in Fig. 2.8, considering the elevation $\phi = 0$, for simplicity. With regard to the antenna array of the radar, the coordinates of the TX elements can be defined as x_i, while the coordinates of the RX elements can be defined as x_j. Therefore, through the MIMO principle, by arranging the TX and RX elements, a virtual array is constructed with $N_{TX} \times N_{RX}$ virtual elements, which coordinates can be defined as x_{ij}.
Accordingly, assuming that the far-field condition is fulfilled, the return delay between a virtual element of the radar at a position x_{ij} and the target, can be expressed as

$$\Delta t_{ij} = \frac{2R}{c} + \frac{2x_{ij}\sin(\theta)}{c} \tag{2.19}$$

with c being the speed of light. Therefore, the received signal $r_{ij}(t)$, transmitted from the i-th TX antenna, and received at the virtual element x_{ij}, is a delayed and attenuated version of the transmitted chirp $s(t)$ and can be expressed as

$$r_{ij}(t) = A \cdot s(t - \Delta t_{ij}) \tag{2.20}$$

where A represents the combined effect of propagation loss and antenna gains, assuming time-invariance and equal amplitude at each element.
All the received radar signals are then processed through a de-ramp mixing technique. As shown in Fig. 2.9, the received signals are mixed with the transmitted chirp replica, and then usually low-passed filtered [119]. The result, can be modeled as [118],

$$u_{ij}(t) = r_{ij}^*(t)s(t) = \left[A \cdot s^*\left(t - \Delta t_{ij}\right)\right] \cdot s(t) \tag{2.21}$$

which expands to

$$u_{ij}(t) = A \cdot e^{j(2\pi k \Delta t_{ij} t - \pi k \Delta t_{ij}^2 + 2\pi f_c \Delta t_{ij})} \tag{2.22}$$

It is possible to understand from this equation, that both the range and the bearing information are included in the result from the de-ramp mixing processing.
There are now two important concepts to consider from this equation, one regarding the delay term and one regarding the phase term.
The first one, is that it can be seen how the time delay is effectively converted into the frequency domain through the de-ramping operation of the received signals, as indicated by the frequency term in equation (2.22), $2\pi k \Delta t_{ij} t$. The frequencies of the mixed signals, from the j-th RX element for the i-th TX transmit channel, can be expressed as [118],

$$f_{ij} = k\Delta t_{ij} \approx \frac{2kR}{c} \tag{2.23}$$

As it can be understood, Δt_{ij} is dominated by a factor of $2R/c$, under far field conditions, and thus, it is a constant value along all of the virtual antenna elements. It is also important to notice that, this frequency value is directly proportional to the range R, allowing the possibility in the radar system, to retrieve the range information from a simple FFT analysis. From equation (2.23), it can be seen that each frequency domain sample, represents a specific range bin, which is linearly proportional to its frequency and the term $c/2k$. This can be better understood, by rearranging the equation for R, as

$$R \approx f_{ij} \cdot \frac{c}{2k} = f_{ij} \cdot \frac{cB}{2T_c} \tag{2.24}$$

Accordingly, it can be seen that the range resolution is limited by the frequency resolution, which is inverse to the chirp's duration T_c. Considering what has been previously explained for the calculation of equation (2.14), it is now clear that the range resolution, defined by the bandwidth of the transmitted chirp, is the same even for an FMCW based radar, and expressed as

$$\Delta R = \frac{1}{T_c} \cdot \frac{cT_c}{2B} = \frac{c}{2B} \tag{2.25}$$

which is the same as the expression previously derived in equation (2.14).
The second important concept is linked to the phase term of equation (2.22), which is $\phi = 2\pi f_c \Delta t_{ij} - \pi k \Delta t_{ij}^2$. This term relates to the direction of arrival of the reflected radar signals, which is estimated through beam-forming techniques and adequate steering vectors. It can be noticed, that the phase term contains two components, linked to the delay quantity Δt_{ij}. One is a linear component, $2\pi f_c \Delta t_{ij}$, whereas the second one evolves as a power of two, $\pi k \Delta t_{ij}^2$. A consideration that can be made, is that the component $\pi k \Delta t_{ij}^2$ is nearly constant for all of the signal arriving at the various virtual elements, for all practical cases where targets are within the range of a radar system. Remembering now equation (2.19), it is possible to extract an expression for the phase, as

$$\phi = 2\pi f_c \frac{2x_{ij}\sin(\theta)}{c} + 2\pi f_c \frac{2R}{c} - \pi k \Delta t_{ij}^2 \tag{2.26}$$

which includes components linked to the position of the virtual array elements and a constant quantity, linked to the target's range. Additionally, the second order term is also constant, as previously explained. Therefore, it is possible to write equation (2.26), as

$$\phi = 4\pi \frac{x_{ij}\sin(\theta)}{\lambda} + C \tag{2.27}$$

where f_c has been expressed as $f_c = c/\lambda$ and the quantity $4\pi/\lambda$ is a typical factor of two-way path propagation models.

2.5.1 The Direction of Arrival

The expression obtained in equation (2.22), is representative of $N_{TX} \times N_{RX}$ mixed signals. In order to estimate the target's direction of arrival, weighting vectors have to be considered, which are obtained by the Kronecker product between the TX and RX array's steering vectors. They can be defined, respectively, as

$$a_i = \exp\left(-j2\pi \frac{x_i \sin(\theta)}{\lambda}\right) \tag{2.28}$$

with $i = 1, 2, \ldots, N_{TX}$, and

$$a_j(\theta) = \exp\left(-j2\pi \frac{x_j \sin(\theta)}{\lambda}\right) \tag{2.29}$$

where $j = 1, 2, \ldots, N_{RX}$. In a far-field condition, it can be assumed that $x_{ij} = (x_i + x_j)/2$ and, therefore, it can be seen that the steering vector for the virtual array is obtained as

$$a_{ij}(\theta) = a_i(\theta) \otimes a_j(\theta) = \exp\left(-j2\pi \frac{(x_i + x_j) \sin(\theta)}{\lambda}\right) \tag{2.30}$$

which becomes

$$a_{ij}(\theta) = \exp\left(-j4\pi \frac{(x_{ij}) \sin(\theta)}{\lambda}\right) \tag{2.31}$$

The above expression is the same as the one in equation (2.27), having removed the constant term, just with opposite sign. Consequently, it can be understood that the beam-forming of the MIMO array signals can be regarded as synthesizing the received signals with the two-way steering vector, from equation (2.31), generated from the co-ordinates of the virtual elements. Considering (2.25), the Azimuth profile can be found by

$$A(\theta) = \sum_{i=1}^{N_{TX}} \sum_{j=1}^{N_{RX}} U(f) \cdot a_{ij}(\theta) \tag{2.32}$$

where U_f represents the spectrum of the mixed and de-ramped signals from equation (2.22). Furthermore, the Azimuth's angular resolution $\Delta\theta$ can be obtained, at a given angle θ, from the beam-forming. The Azimuth's angular resolution depends on the

effective aperture of the virtual array along the Azimuth direction, $A_{e_{AZI}}$, and can be defined as

$$\Delta\theta = \frac{\lambda}{2A_{e_{AZI}}} \tag{2.33}$$

The same procedure can be obtained with regard to the elevation axis, in order to calculate $\Delta\phi$. Considering (2.25), the elevation profile can be found by

$$A(\phi) = \sum_{i=1}^{N_{TX}} \sum_{j=1}^{N_{RX}} U(f) \cdot a_{ij}(\phi) \tag{2.34}$$

where ϕ denotes the elevation angle. Similarly to the Azimuth angle, the elevation's angular resolution $\Delta\phi$ can be obtained, at a given angle ϕ, from the beam-forming. The elevation's angular resolution depends on the effective aperture of the virtual array along the elevation direction, $A_{e_{ELE}}$, and can defined as

$$\Delta\phi = \frac{\lambda}{2A_{e_{ELE}}} \tag{2.35}$$

As it has been previously anticipated, various techniques exist in order to operate the beam-forming processing. The techniques which will be used and described in this thesis are based on the conventional delay and sum beam-forming, as well as novel proposed FFT based beam-forming algorithms.

2.5.2 Time Domain Multiplexing

In a MIMO system, which operates with FMCW signals, the most common way to achieve orthogonality is through the use of a time division multiplexing architecture. The idea is that the FMCW signal is transmitted alternately by each transmit antenna. This means that each transmit antenna has exclusive access to the radio channel inside a very small time slot while all other transmit antennas are switched off. Each transmit antenna uses the same waveform, however, in an intertwined way. In this case all transmit signals are mutually orthogonal and no interferences will occur. The radar echo signal is processed in each receive antenna simultaneously. Due to the orthogonality of all transmit signals, each receive antenna can separate perfectly all signals transmitted by different antennas. An example of a FMCW transmission scheme for a TDM MIMO array with 4 TX antennas is shown in Fig. 2.11. By referring to the MIMO case with a TDM approach, the synthesis of an entire MIMO baseline requires N_{TX} effective sweeps that are then equivalent to a single transmission for the virtual array. Therefore, the complete radar data signal structure will comprise, effectively, $N_{TX} \times N_{RX}$ signals. Accordingly, a radar image can be produced only when the reflected signals from all of the TX slots are received.
If the chirp duration is designed to be much longer than the two- way propagation delay

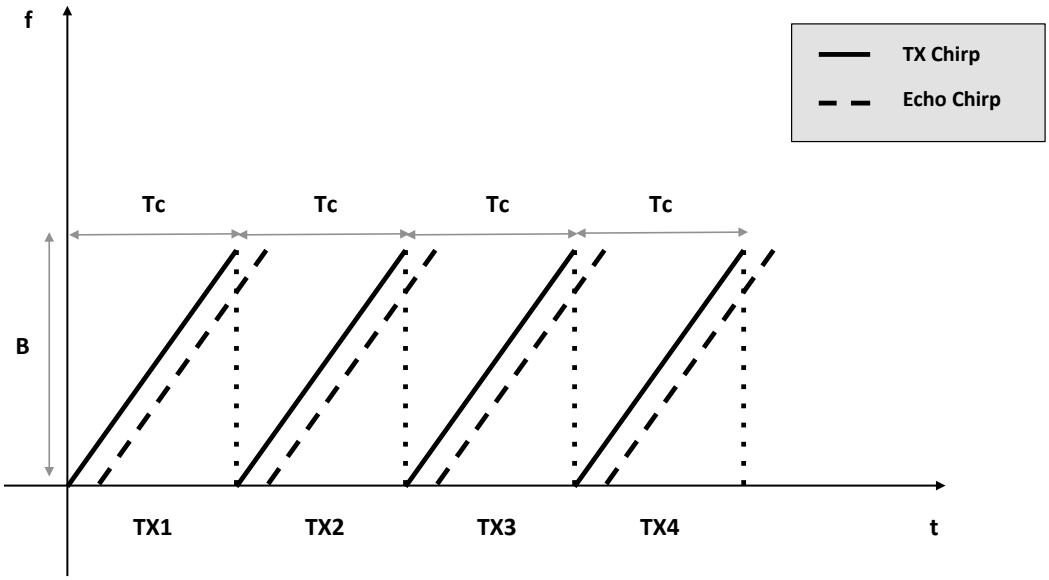

FIGURE 2.11: Example of a FMCW transmission scheme for a TDM MIMO array with 4 TX antennas.

corresponding to the furthest detection range, which is $\tau = 2R_{max}/c < T_c$, the range and angle information carried by the received signals can be retrieved at the resolutions defined by the previously seen equations (2.25), (2.33) and (2.35).

Chapter 3

Portable 3D Imaging FMCW MIMO Radar Demonstrator with a 24x24 Antenna Array

3.1 Chapter's Introduction

In this chapter, the first complete radar demonstrator which has been achieved [120], is presented. As previously discussed, the architecture on which the radar system is built, is the MIMO concept. A MIMO based radar has been investigated, because of its advantages over conventional radar systems, which include an increased antenna aperture, thanks to the virtual array concept [121], [122]. Therefore, this directly translates into an increased cross range resolution, with a reduced number of active antenna elements, which yields a reduced number of electronic components, a reduced overall cost and, finally, a smaller sized factor. Additionally, from [81], the maximum number of targets that can be uniquely identified by a MIMO radar is up to N_{TX} times of its phased-array, counterpart, where N_{TX} is the number of transmit antennas.
Accordingly, these advantages fit perfectly with the applications which are aimed throughout this research, mainly requiring to fit a radar system inside a moving platform, either on the ground or flying. However, the following chapter describes the base for such system, starting from the implementation of a radar demonstrator, which, even though compact and portable, is more suited for the ground based surveillance of stationary wide-zones and high security or hazardous infrastructures like chemical and nuclear plants, fuel transmission and energy pipelines and, more in general, applications in remote areas where a portable platform is highly desired. These applications are in accordance to the ones required by the European project "ZONeSEC", for which part of the research has been focused to.

The result achieved and here presented, is the design, implementation and analysis of a complete MIMO radar demonstrator, follow up of a system concept work, that establishes how all the technological elements work together. The performance results are shown through a series of measurements, from sub-system to system level, in realistic

environments, both indoor and outdoor, and with static targets in the form of corner reflectors.
The radar sensor working frequency range spans between 16 GHz and 17 GHz and the proposed solution is based on a 24 transmitters and 24 receivers MIMO radar architecture, implemented by time division multiplexing of the transmit signals. The radar signals used are FMCW signals, which span through the whole frequency range, therefore achieving a 1 GHz operational bandwidth.
A complete system integration of the RF front-end, the digital system and the software architecture for radar's digital signal processing has been accomplished. Additionally, the demonstrator has been designed to be compact and portable by including its own power unit and cooling system. Moreover, the radar system is intended to be flexible as much in its hardware as it is in its software. A modular approach based on conventional low cost PCB is used for the transmit and receive boards. This modular approach is based on RF multilayer panels with integrated antennas, that are easily stackable in a sandwich configuration. This grants the possibility to vary the number of antennas by removing or adding panels, thus varying the angular resolution and the size of the radar, until the desired values are reached.
Using digital beam-forming (DBF) algorithms and radar processing techniques on the received signals, a high resolution 3D sensing of the range, Azimuth and elevation can be calculated. With the current antenna configuration, an angular resolution of 2.9° can be reached. Furthermore, by taking advantage of the 1 GHz bandwidth of the system, a range resolution of 0.5 m is achieved.
From the software side, the FMCW radar signal parameters can easily be adapted in order to create complete 3D images or only cuts of the complete data for faster radar processing times. The system is flexible, compact and portable, thus a various range of applications can be explored.
The system architecture of the radar system is presented in the following sections together with a description, measurements and pictures of the RF front-end components. Furthermore, an in depth description of the FPGA based digital system architecture, the radar signal processing, the image reconstruction techniques and results analysis is provided. Finally, radar measurements and images taken from field test scenarios are shown together with a comprehensive evaluation of the radar's range and angular resolutions, overall performance and its target detection capabilities.
The provided results, prove the medium range surveillance potential and the high resolution capabilities of the 3D MIMO radar.

The efforts and achievements from the following demonstrator, are a result of a team work. The main contributions given through this work in the Ph.D. program within Airbus, are the MIMO radar system characterization, calibration, operation and control, but more importantly, the complete radar signal processing and results analysis. This includes and it is not only limited to, the implementation of a complete digital hardware and software architecture which, from the receivers, through ADC signal capturing, FPGA implementation, control processing unit integration, radar beam-forming algorithms and image generation software models, yields the radar images and the targets' estimation.

3.1.1 State of the Art

As is has been addressed in the previous chapters, imaging radar systems are crucial solutions for detection, tracking and classification of targets in airborne, surveillance and ground based applications. This is mainly due to their high performance under various weather conditions, material penetration properties and usability at day and night, compared to other sensors, such as lasers and cameras based systems. Different imaging radar solutions exist. Mechanically steered radars are usually complex systems because of their physically moving components and long term reliability is often compromised. SAR systems are a good solution that uses the motion of the radar antenna over a targeted region [79]. This leads to a finer cross-range resolution, but there is a need for a continuously moving platform. Radars need a large effective aperture of the antennas in order to achieve a high resolution. This can be achieved in classical phased array radars [80], with a high number of elements along the transmit and receive paths, which tends to be a relatively large, complex and expensive approach. Better performance can be achieved by utilizing a MIMO architecture [81],[4]. In a MIMO system, orthogonal signals are emitted from the transmit antennas and jointly processed at the receivers. The signal orthogonality can, for example, be established in time-domain by employing a TDM scheme switching between the transmit antenna elements. The typical scheme, usually a round-robin structure, consists in activating only one transmit antenna element at a time, starting from the first one and then progressively sweeping through all. Upon reaching the last antenna element, the scheme is repeated from the beginning. In particular, this allows the calculation of amplitude and phase relationships of a large number of points in space, which is the result of multiplication of the number of transmit by the number of receive elements. These points form the elements of the virtual antenna array. Besides the increase in the number of virtual channels, this leads to a larger virtual array aperture, and therefore, to a higher cross range resolution.

The MIMO principle together with an appropriate antenna array arrangement enables an improvement in the cross-resolution by an artificial increase of the antenna aperture with the so called virtual array concept. Therefore, in combination with a signal with a large bandwidth, which determines the resulting resolution in the range direction, high-resolution 3D images of the captured scenario can be achieved in a smaller sized radar.

Several MIMO radars have been proposed [123]-[124], nevertheless literature shows that a 1 GHz broadband systems, as two of the demonstrator presented in this thesis, the first one of which is presented in this chapter, has been achieved only by few, namely in [123], [125], [126] and [127], with a bandwidth of 8 GHz, 1 GHz, 1 GHz and 1 GHz, respectively. However, a 2D MIMO array granting the ability to reconstruct 3D images with both Azimuth and elevation information has been accomplished in a full imaging demonstrator only in [123] and [128]. Because of insufficient data presented in the papers analyzed, especially regarding the target's RCS considered in the reported measurements, it is difficult to extract a correct range information. Therefore, the devices are analyzed according to their ability to operate in short and medium range applications. The results is that for the above mentioned solutions, in [123] and [128], these are only suitable for

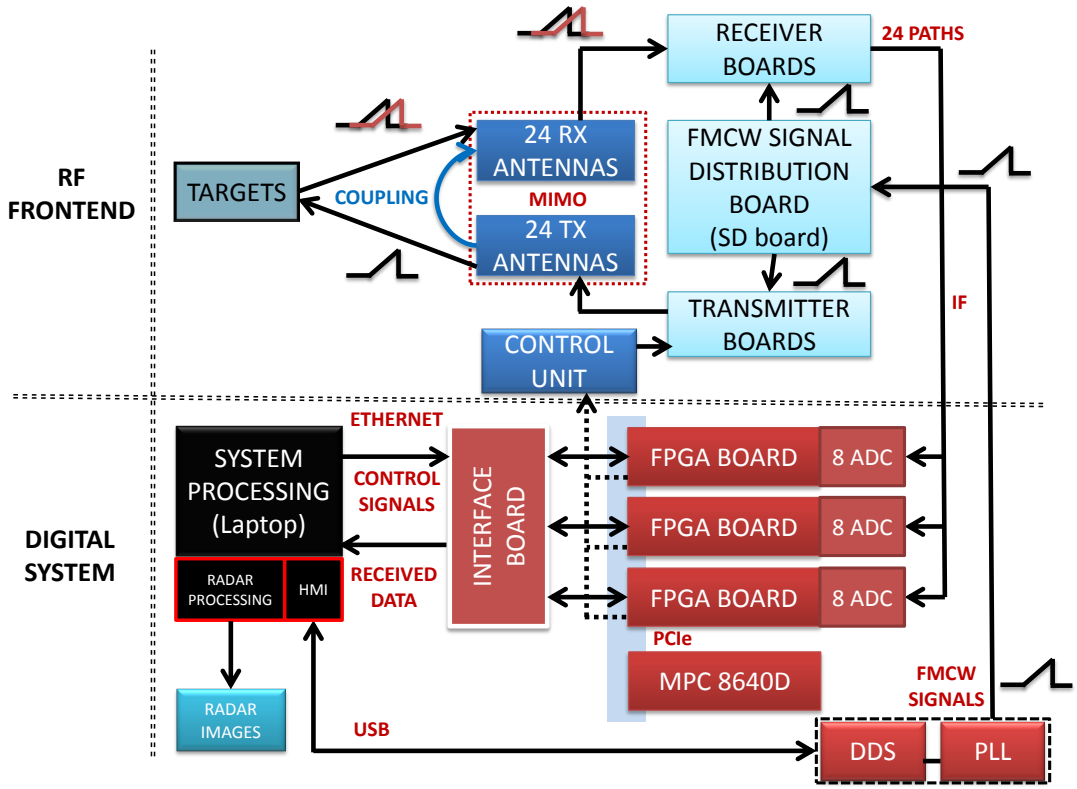

FIGURE 3.1: Block diagram of the 3D Imaging FMCW 24x24 MIMO Radar Demonstrator.

short range applications, i.e. for distances up to 20 meters or less. Additionally, these devices lack an aspect which is important for several of the previously mentioned radar applications, which is the portability and compactness of the radar's device itself.

3.2 The System's Architecture

The top-level system structure of the built MIMO radar demonstrator is presented in the form of a block diagram in Fig. 3.1. Here, the two main building blocks can be seen: the RF front-end and the digital system. In a FMCW radar, operating with a TDM architecture, a sine carrier is swept across the radar bandwidth and sequentially sent through the different transmit antennas. After receiving the chirp signals from the receive antennas, the receivers down-convert the received signal by means of mixing with the transmit chirp signal, so that the signal runtime differences from different reflectors in the scenery translate into different so called beat frequencies. These signals are then sampled and processed in order to generate 3D radar images of the captured scenario. The chirps used in this MIMO radar demonstrator are signals which frequency increases (up-chirps) with time from 16 GHz to 17 GHz, in 100 μs.

The RF front-end system is the essence of the transmit and receive signals analog operations. It consists of the transmit boards, the receive boards, the transmit and receive

antenna arrays and the FMCW Signal Distribution (SD) board. The FMCW SD board provides the chirp signals that are used for transmission and the reference signals for the de-ramp mixing technique used in our radar, where the mixing occurs between the received chirp signals at the RX array and the transmitted chirp replica coming from the FMCW SD board. The FMCW de-ramping technique has been previously described in Chapter 2.5. The comprehensive description of the RF front-end is given in Section 3.3.

The signal processing is at the core of the digital system, which consists of a system processing program on a laptop for radar control and radar signal processing, a combined DDS and PLL system for the generation of the configurable transmit waveforms and three FPGA cards with ADC units for parallel hardware-based signal acquisition, radar signal processing and radar image generation. A complete description of the digital system will be given in Section 3.4. A graphic human to machine interface, or HMI, on the system processing workstation sends the signal generation parameters to the DDS and PLL element and the generated FMCW signals are distributed by the FMCW SD board to the transmitter boards and antennas. The control unit selects individual transmit antenna elements in order to apply TDM. The signals reflected from the targets are received through the receiver antennas with multiple receive paths and are processed in parallel in the digital unit. The pre-processed data is then sent back to the offline software based radar signal processing functions on the workstation that apply digital beam-forming techniques to generate the final radar images.

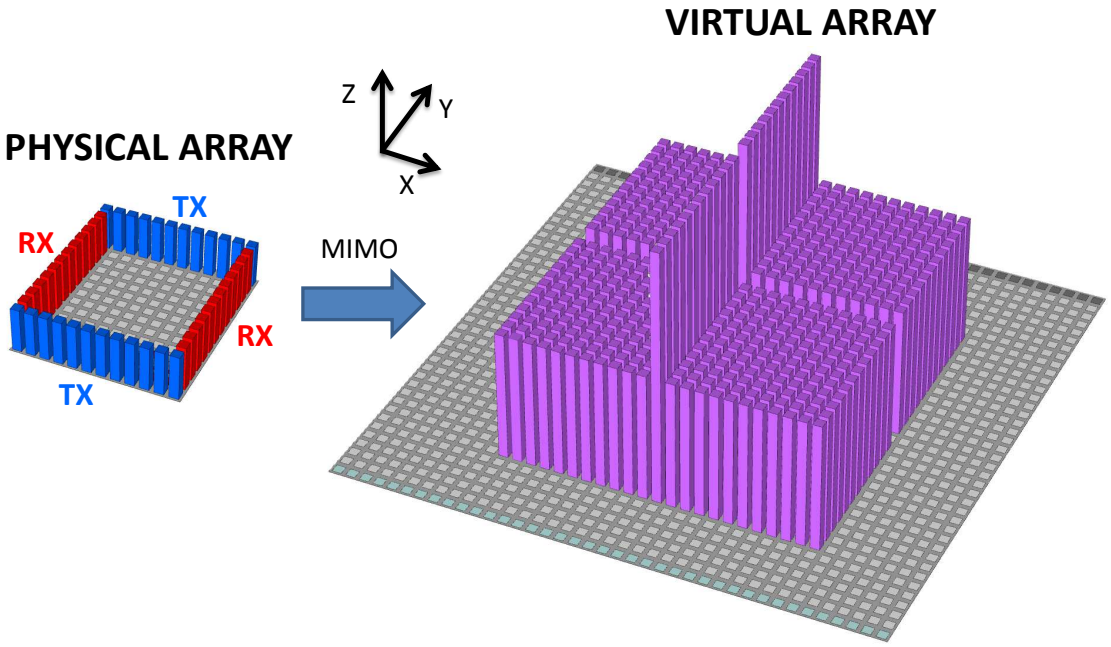

FIGURE 3.2: Schematic representation of the MIMO antenna configuration with the physical array (left) showing the 24 TX antennas in blue, the 24 RX antennas in red and the resulting virtual array (right).

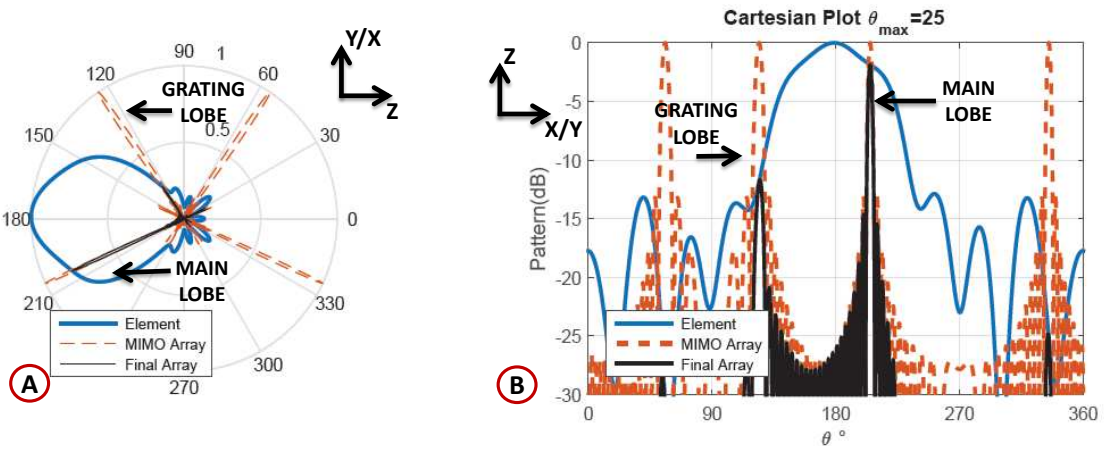

FIGURE 3.3: The graph illustrates a simulation of virtual array pattern with the designed maximum beamsteering of $\theta_0 = 25°$ in red, the single element in blue and the resultant multiplication of both in black. The patterns are displayed in polar (subfigure A) and cartesian (subfigure B) coordinates.

3.3 The RF Front-end

The focus of this section is on the RF front-end. The hardware is optimized for a frequency range of 16 GHz to 17 GHz, which is allocated in Germany for non-navigational radio-location services, as previously discussed in Chapter 1.

3.3.1 MIMO Array Configuration

The presented MIMO radar consist of two sets of multiple transmit and receive antennas. Orthogonality between the transmitted signals of the channels is obtained through the use of a TDM architecture of the transmitters. The equivalent virtual array can be calculated as the discrete convolution of the overall RX and TX element positions, as previously introduced in Chapter 2.4.
In this radar demonstrator, the fabricated antenna elements are based on Tapered Slot Antennas (TSA) [129]. Fig. 3.2 depicts the positions of the antennas' phase centers and the corresponding MIMO virtual array. RX elements (in red) and TX elements (in blue) are placed forming a rectangle. In this manner, the equivalent virtual array has four times the surface of a fully populated array with the same perimeter. This leads to an improvement in the resolution of a factor of two in each axis. Thus, the angular resolution is approximately expressed as [110]

$$\Delta\theta_{3dB} \approx 50° \frac{\lambda_0}{d2N} \approx 2.5° \tag{3.1}$$

with λ_0 being the wavelength, N the number of elements of an equivalent fully populated array with the same perimeter as our physical array and d the distance between elements. The higher purple bars in the right of Fig. 3.2 are redundancy elements. Concerning the redundant elements, there are two important aspects that need to be considered. First, the redundant elements are simply discarded in the beam-forming and image generation

algorithms of the processing unit, therefore not harming the reconstructed radar image. Second, in some fast-moving scenarios the switching time could be slower than the image changes. As a consequence of the redundancy, the same virtual element is calculated at two different times. This can be exploited in order to evaluate if the radar images are fitting the reality. Defining corresponding algorithms will be one important aspect of our future work. Regarding the empty row which appears in the center of Fig. 3.2, an interpolation of the data is performed, according to what has been previously described in [130].

In order to reduce the coupling between radiating elements and to increase the angular resolution, the distance between antennas was chosen greater than $\frac{\lambda_0}{2} = 9.7$ mm. Consequently, grating lobes appear. Since the desired field of view, or FOV, is $\pm 25°$, the system was optimized placing the elements with $d_y = d_x = 15$ mm of spacing. In such a manner, the grating lobes are outside the desired field of view and, based on simulations, an improvement of approximately 10 dB in the coupling is achieved, compared to a spacing of 9.7 mm.

Fig. 3.3 presents a calculation of the resultant antenna pattern. Subfigure A is dedicated to the antenna pattern of the virtual array in polar coordinates (dashed curve) with the maximum beam steering of $\theta_0 = 25°$, single element in blue and the resultant multiplication. As the image shows, the grating lobe remains under -12 dB on the desired FOV. In subfigure B, the same curve is plotted in cartesian coordinates. Since the beam-forming is carried out at the digital signal processing side with a delay-and-sum beamformer algorithm, no phase shifters are needed.

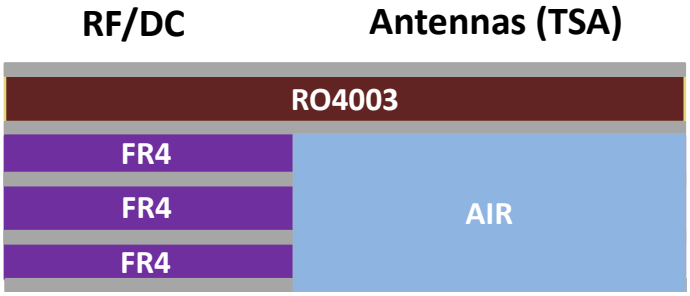

FIGURE 3.4: Representation of the used layer stack-up.

3.3.2 Transmitter

The layer stack-up of the boards used in this demonstrator, is presented in Fig. 3.4. The RO4003 material is a high frequency suitable material from Rogers corporation with $h = 0.203$ mm, $\epsilon_r = 3.55$ and $\tan\delta = 0.0027$. The main function of the Flame Retardant (FR4) ($h = 1$ mm) is to give physical stability. The FR4 also allows to add extra metal layers for routing of Direct Current (DC) signals.

A switch chain with a built-in gain of $G_{TX} = 19$ dB is responsible for the selection of the dedicated antenna at the proper time, according to the employed TDM scheme. The switches are Commercial Off The Shelf Components (COTS) with 1.6 dB insertion loss and 41 dB isolation, at 16.5 Ghz [131]. The switching process is controlled by the firmware's procedures of the digital system by means of setting a Complex Programmable

Logic Device (CPLD).
Fig. 3.5 illustrates the transmitter board and its circuit diagram. The switch chain is located in between the input connector and the antennas. A single path of the switch chain, shown on the right side of Fig. 3.5, which contains two amplifiers, an attenuator, four switches, an antenna and a 20 dB test coupler (only the first and last paths).

Test measurements of the board are performed with a network analyzer, which has 2 ports with its corresponding cables terminated with a K coaxial connector. A through-reflect-line calibration (TRL) is performed at the level of its cables. Fig. 3.6 shows S-Parameters from port IN to C1 and C12, which are the ports of the test coupler shown in Fig. 3.5. A K coaxial to Mini-coaxial transition is included in the measurements but it has a minor impact. A correction factor of 20 dB, due to the test coupler, is also applied. The gain of the board well fits the designed value of $G_{TX} = 19$ dB. A difference in amplitude smaller than 1.25 dB can be observed.

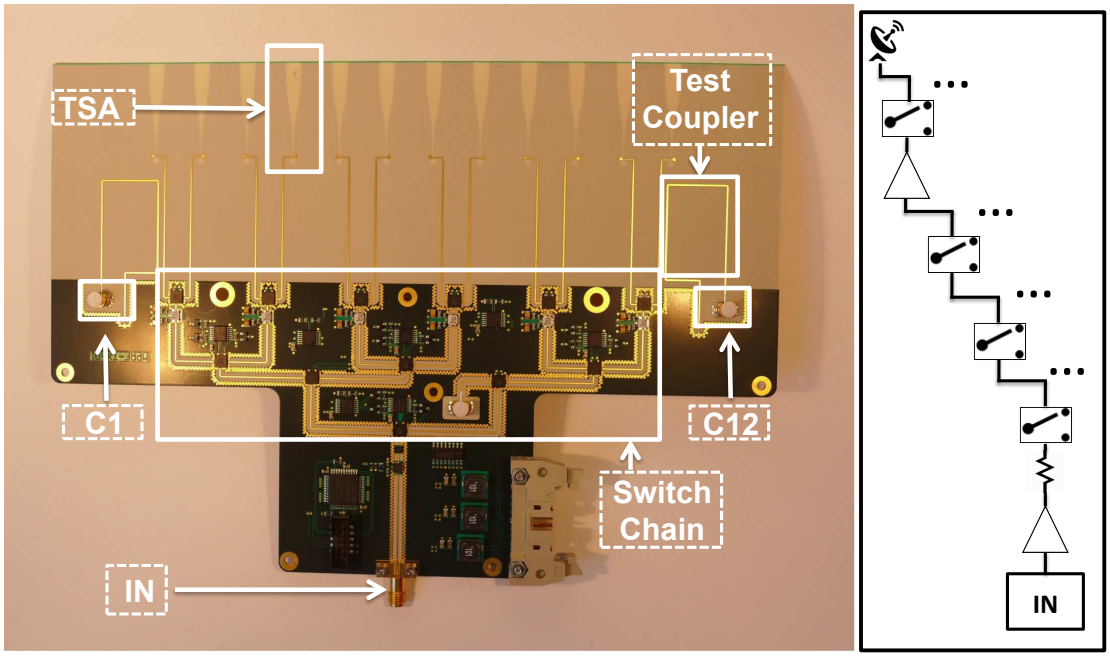

FIGURE 3.5: Photograph of the complete TX panel (left) and the corresponding block diagram (right).

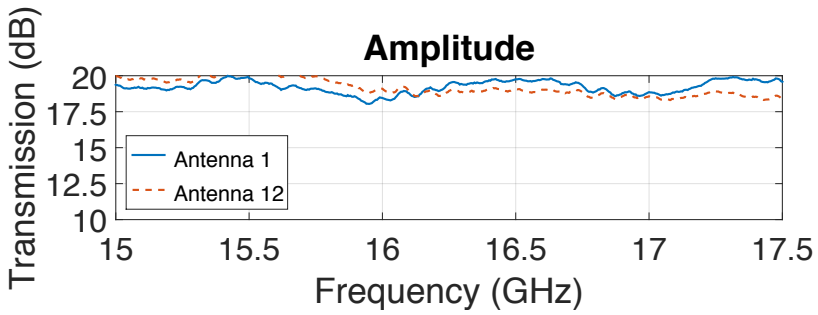

FIGURE 3.6: S-Parameters of the transmission from antenna 1 and 12. The effects of the coupler are compensated.

3.3.3 FMCW Signal Distribution (SD) Board

The FMCW SD board, illustrated in Fig. 3.7, provides a phase-coherent signal from a single input port to 16 output ports (14 for the RX and TX boards and 2 for testing purposes). The output ports are directly connected to the FMCW input ports of each RX and TX board. The FMCW SD board is fabricated with 4 stages of single resistor Wilkinson power splitters and two stages of commercial amplifiers. Fig. 3.7 shows a picture of the fabricated PCB and its corresponding schematic, on the upper part of the image. The substrate described in Fig. 3.4, is also used for this board.

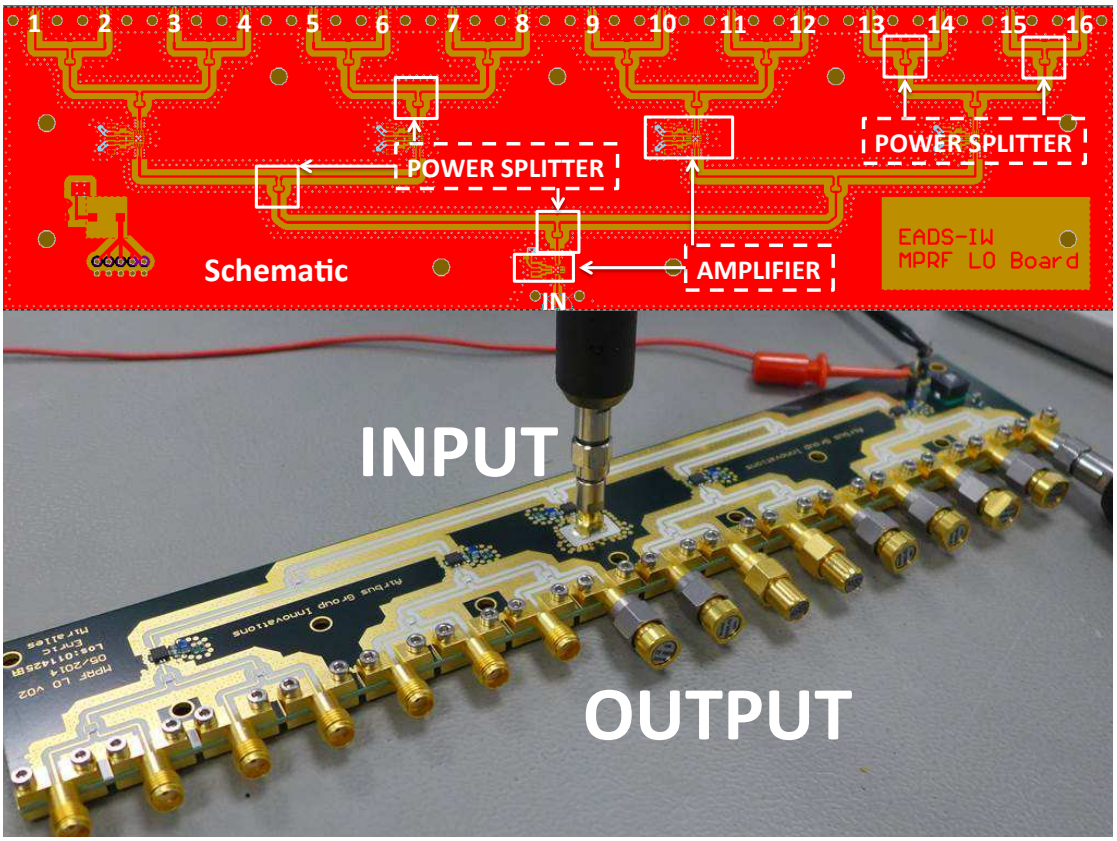

FIGURE 3.7: Photograph of the FMCW signal distribution board with its 16 output ports.

The FMCW SD board is measured with a network analyzer. A TRL calibration is performed at the level of its cables. As it can be observed in Fig. 3.7, a transition from K to mini coaxial connector is needed at the input port. The effects of this transition are minor and are included in the measurements.

The transmission amplitude and phase of all 16 channels belonging to the FMCW SD board are depicted in Fig. 3.8 and Fig. 3.9, respectively. As shown in Fig. 3.8, a maximum difference of 0.5 dB in the amplitude is measured. Moreover, it can be seen from Fig. 3.9, subsection B, that a maximum difference of 13.3° in the phase is also measured. These differences are due to tolerance errors in the PCB fabrication process, its components tolerances and because of soldering inhomogeneities. Nevertheless, these

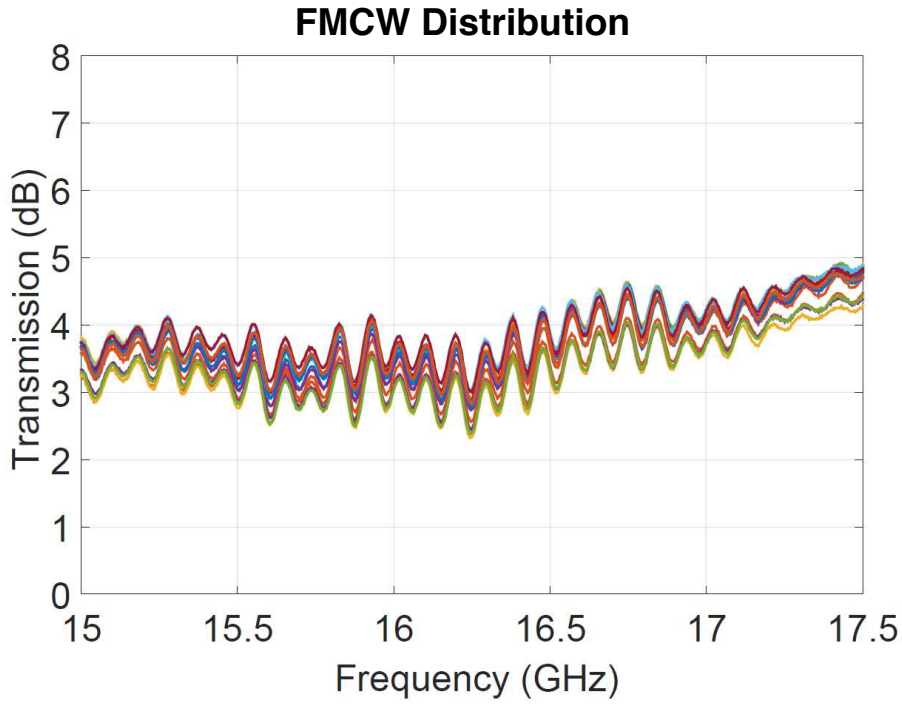

FIGURE 3.8: Amplitude comparison between all channels of the FMCW distribution board.

differences do not affect the performance of the system since a digital processing post calibration is applied in order to overcome the small disparities.

3.3.4 Receiver

The substrate described in Fig. 3.4, is also used for the receiver. A picture of one of the fabricated boards is shown in Fig. 3.10, in which the key components such as the TSA elements, mixer, LNA, FMCW signal path, anti-aliasing filter and equalizer are highlighted. As known from the classic FMCW theory [117], a sine carrier is swept across the radar bandwidth and the receiver down-converts the received signal by means of mixing with the transmit signal, coming from the FMCW signal path, so that the signal runtime differences from different reflectors in the observed radar scenery translate into different Intermediate Frequencies (IF), or beat frequencies.

Over the whole frequency band of operation, the attenuation of the received signal is different, considering that the down-converted signals produced by more distant targets show lower amplitude and higher beat frequency. In order to compensate this, a passive equalizer is incorporated in the receiver design. A measurement setup is created in order to analyze the IF output performance of the RX board, as illustrated in Fig. 3.11. A signal generated from a vector signal generator with a frequency range from 16.51 GHz to 16.61 GHz is fed to a test horn antenna with 15 dB gain, which is placed at a range of 75 cm from the antennas on the RX board. The FMCW input on the RX board is excited with a continuous-wave, or CW, signal at 16.5 GHz and the IF output ports are then connected to a spectrum analyzer. The results are shown in Fig. 3.12, which represents

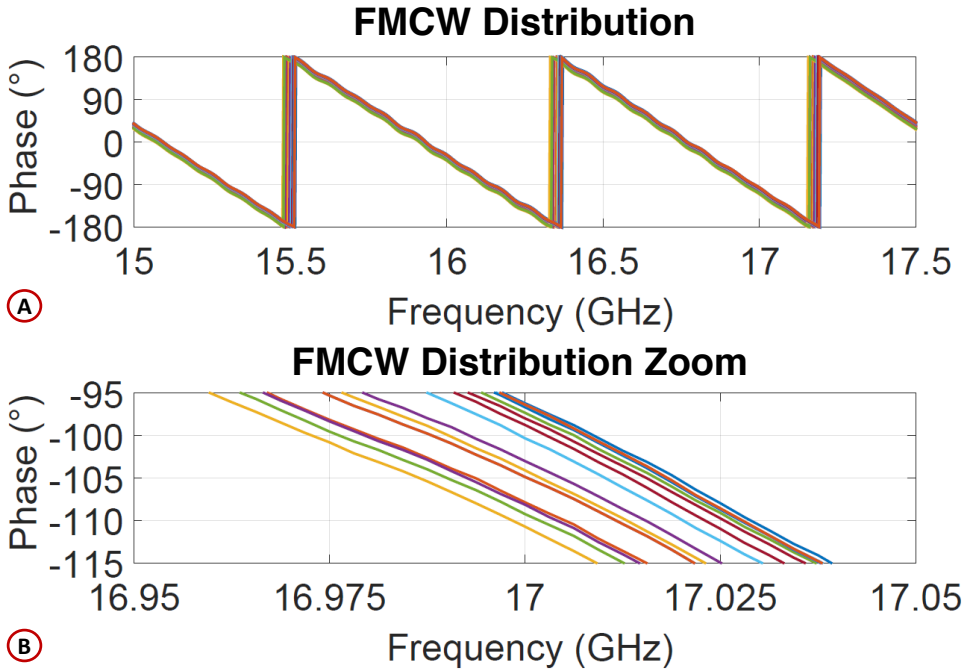

FIGURE 3.9: Phase comparison between all channels of the FMCW distribution board.

a screenshot taken directly from the spectrum analyzer. In this picture, the effects of the equalizer are clearly visible, as an attenuation on the amplitudes of the signal that starts stronger in the lower frequency range and whose effect is linearly decreasing, in order to compensate the higher losses in amplitude for higher frequencies. The low pass filtering effect (beyond 100 MHz at marker number 2 of Fig. 3.12) is instead caused by the anti-aliasing filter.

3.3.5 Coupling Between Antennas

The mutual coupling between antenna elements, in particular between TX and RX elements, is a well known and undesired effect of radar systems, especially for FMCW. When a signal is transmitted from a TX antenna, a part of the signal couples with an adjacent RX antenna and this may compromise the performance of the overall radar system. The maximum coupling between the antennas, with the chosen configuration for our system, is smaller than $C < -23$ dB in the frequency range of operation, as illustrated in Fig. 3.13.

This undesired coupled power can saturate the mixer. In order to avoid this malfunction, the RF power at the mixer must be below $P_{1dB_{MIX}} = 11$ dBm. Considering that the gain of the LNA is $G_{LNA} = 19$ dB and the losses in the line between the receiver antenna and the LNA are $L = 2.5$ dB, the maximum sustainable power at the receiver antenna would be $P_{RX_{MAX}} = -5.5$ dBm. Using the following equation

$$P_{TX_{OUT}} = P_{RX_{MAX}} + C \tag{3.2}$$

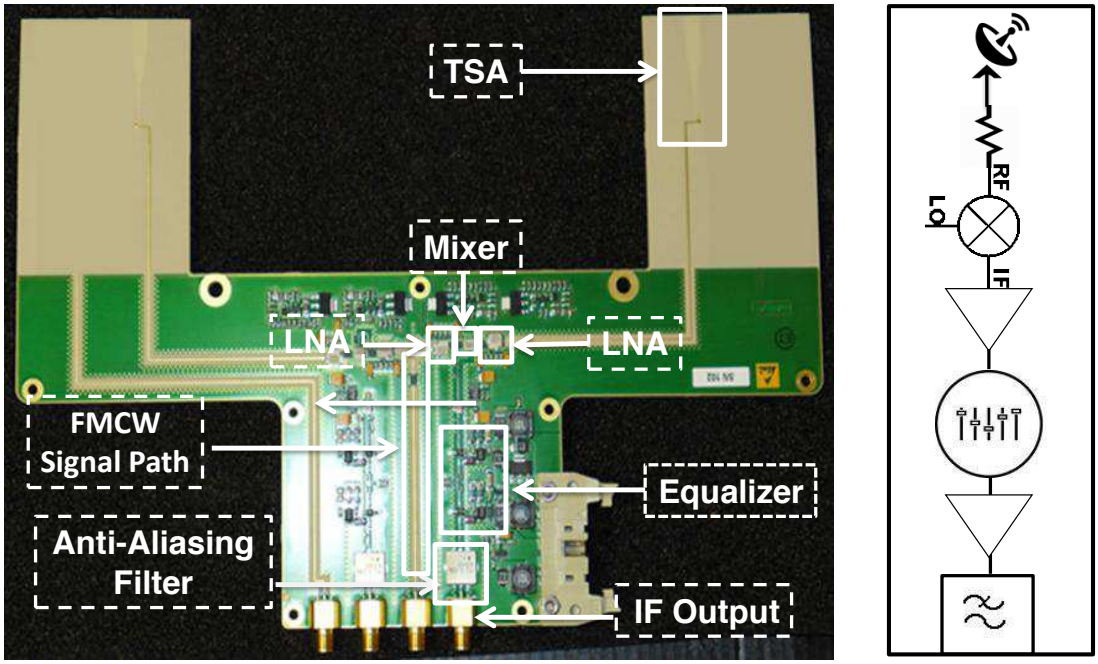

FIGURE 3.10: Photograph of the receiver board, on the left, and corresponding block diagram, on the right.

a maximum transmit power of $P_{TX_{OUT}} = 20.5$ dBm results. Fig. 3.14 shows the measured input power versus output power with compensated effects of the test coupler in the transmitter board. As a conclusion, the coupling does neither damage nor affect the performance of our system because even if a strong signal is sent to the input of the receiver, the amplifiers at the transmit board saturate and will always provide a signal with a power below $P_{TX_{OUT}} < 20.5$ dBm.

3.3.6 Assembly of the RF system

The RX, TX and FMCW signal distribution modules are built on panels, as shown in Fig. 3.15, which are stacked horizontally, in such a way that the desired antenna configuration is achieved. Each RX and TX panel structure is the result of the composition of a multilayer PCB, stacked with a 7 mm thick honeycomb board, a 4 mm Rohacell foam stabilization system and a metal support.

In the upper left part of Fig. 3.16, the complete configuration of the 24x24 MIMO radar demonstrator is illustrated. In this part of the image, it is possible to see the assembled RF front-end and the digital system unit. The lower part of the figure shows the antenna array front view with the radome protection, on the left, and without the radome protection, on the right. In this lower right part of the image, the stacked RX and TX panels configuration can be seen from a front view.
In order to achieve a compact and portable radar, a power unit and cooling system have been integrated into the system, as it can be seen from Fig. 3.15. The system operates with 24 V and a maximum current use of 5.6 A, therefore yielding a maximum power

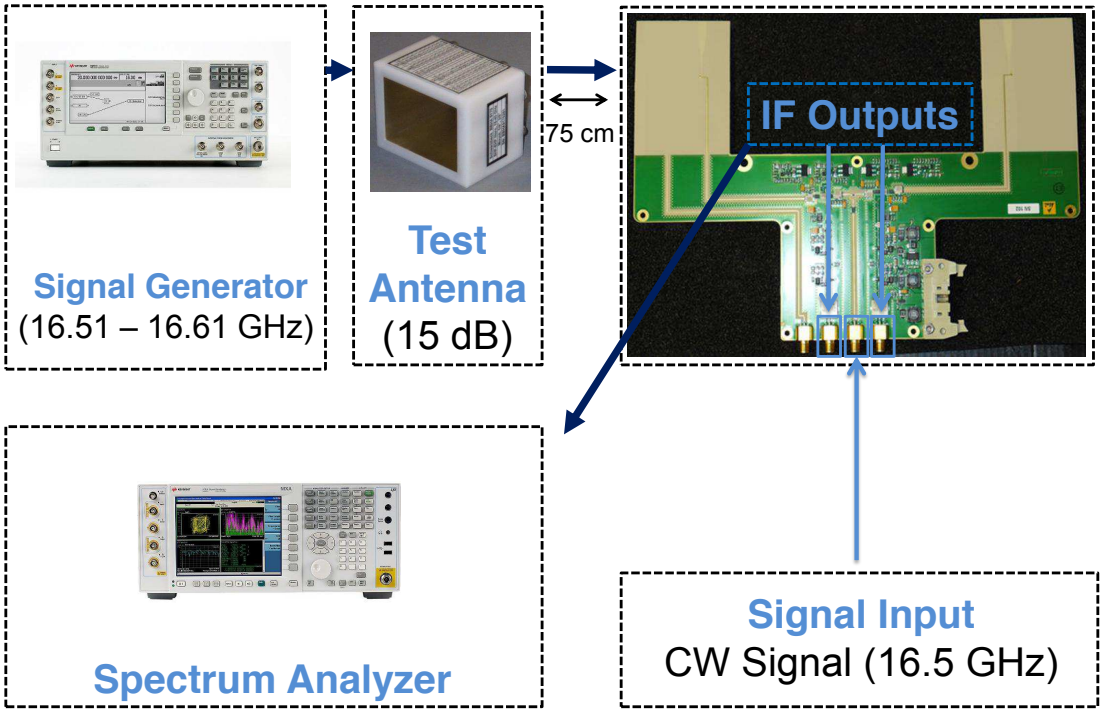

FIGURE 3.11: Measurement setup for testing the performance of the receiver board and the equalizer.

consumption of 134 W. The radar system weights approximately 7 kilograms and has dimensions of 55 cm x 27 cm x 27 cm.

3.4 The Digital System

An overview of operation of the digital processing system is presented in the form of a block diagram in Fig. 3.1. Here, the main units of the digital system are illustrated: the FPGA boards, the ADC units, the PowerPC, the DDS and PLL unit and the offline system processing block. The purpose of the following paragraphs is to describe the digital system hardware and software architecture, its functionalities and the offline radar signal processing software on the laptop workstation for the 3D image reconstruction of the radar captures.

3.4.1 Hardware Architecture

As illustrated in Fig. 3.1, for the hardware realization of the digital signal processing part, three Virtex-5-SX95T [132] FPGA based cards are used. The cards are joined with FPGA Mezzanine Cards (FMC) FMC108 boards by 4DSP [133]. Each of the cards is equipped with an 8 channel ADS62P49 ADC that provides eight analog to digital 14 bit 250 Mega-Samples-Per-Second (MSPS) channels. The sampling clock for the ADCs is supplied externally, directly from the DDS and PLL board. A picture of the digital

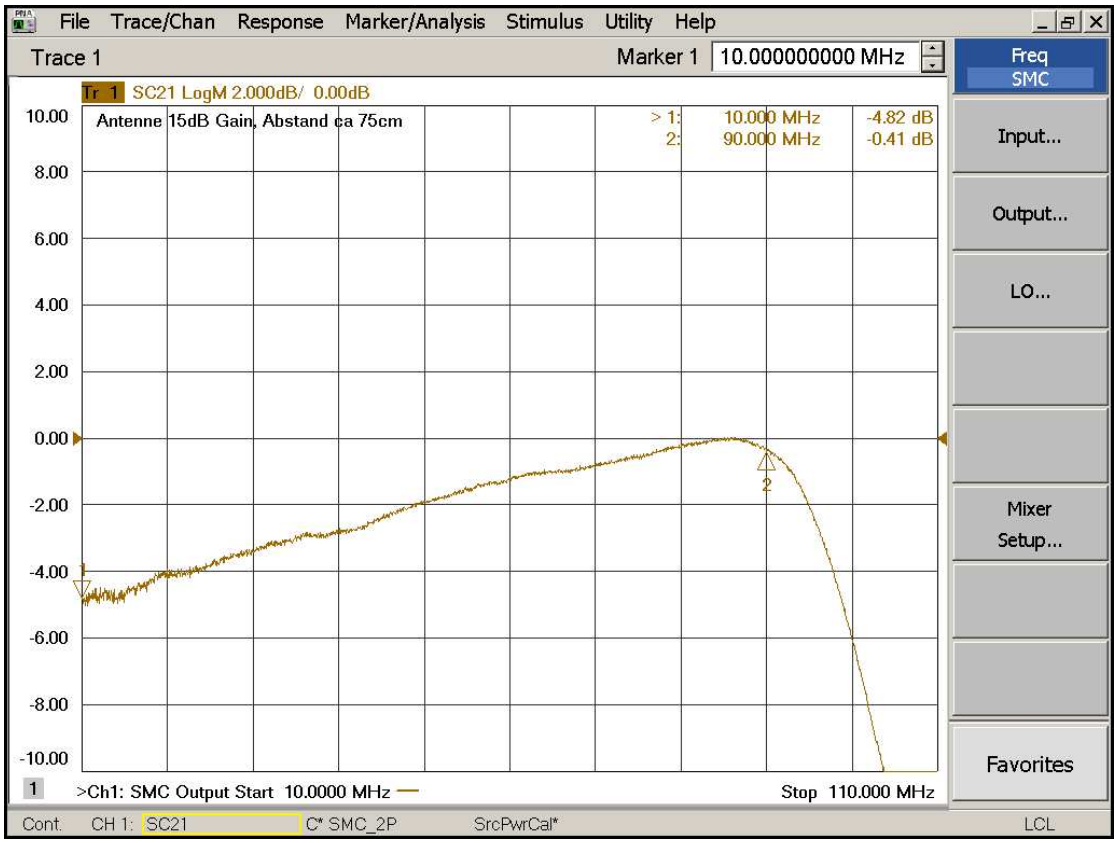

FIGURE 3.12: Screenshot of the measurement of the IF output performance of the RX board, captured by a spectrum analyzer.

system is shown in Fig. 3.17. The available trigger input for customized sampling control is used. This is of high importance since the 24 channels from the 3 boards combined must be perfectly synchronized in order to achieve coherence and perform beam-forming on the received signals. The custom built operational firmware sets all 24 ADC cards to operate with a sampling clock of 204.8 MHz. Additionally, a Freescale MPC8640D [134] dual-core processor for overall data management and transfer is adopted.

3.4.2 FPGA Architecture

A custom built VHDL coded firmware has been implemented, that works seamlessly with the embedded software on the PowerPC through a wishbone architecture and a Peripheral Component Interconnect Express (PCIe) interface. The block diagram of the implemented firmware for the 4DSP FMC108 FMC modules, is shown in Fig. 3.18. As previously discussed, each module provides eight analog to digital converter channels with a sample rate up to 250 MHz. As shown in Fig. 3.18, the eight input channels are synchronized to the internal clocks and fed into a First In First Out (FIFO) architecture. The FIFO is used to pass the radar captured samples from the individual ADC clock domains into the common clock domain for all ADCs, which is run with a 250 MHz clock derived from one of the ADCs. For each ADC data stream, a separate snapshot memory with a capacity of 32768 samples is implemented. The snapshot memories can

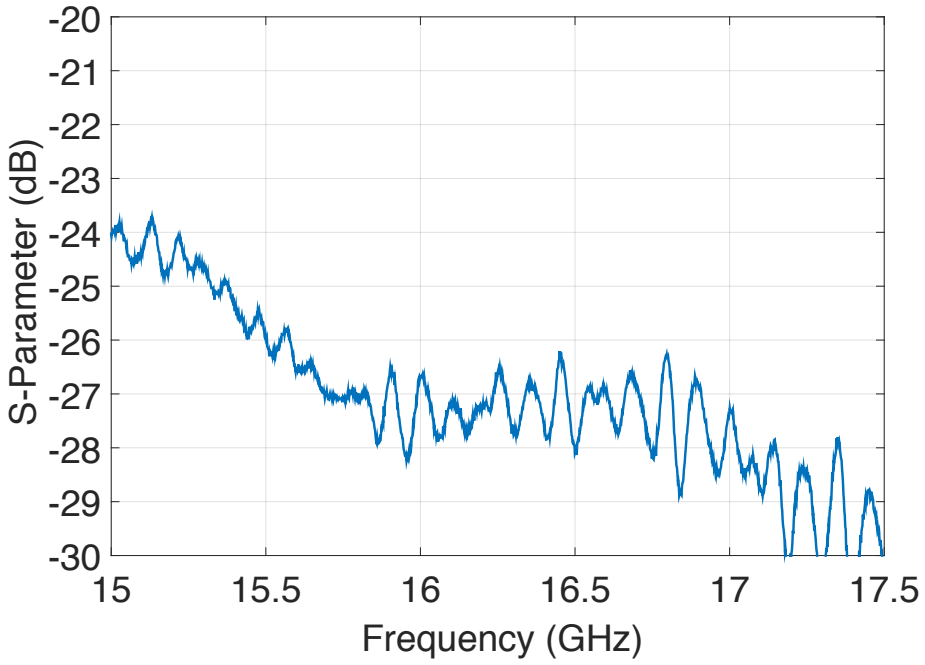

FIGURE 3.13: Measured maximum coupling between one TX and one RX antenna. The chosen elements were adjacent, with a distance (d) of 15 mm.

be started individually or at the same time, and the start may be synchronized to the external trigger signal. Recording stops when the snapshot memory is full, and the appropriate finish bits are set. The sample memories are accessible at any time from the PCIe bus. The finish condition can be used to generate an interrupt on the PCIe bus.

3.4.2.1 Snapshot Memory

The analogue to digital converters are dual channel models, delivering two channels with a single clock. The two channels are synchronized with the appropriate sample clock, fed through a delay pipeline, which can be individually selected between 1 to 16 register stages, and written to a FIFO, using the AD sample clock. Fig. 3.18 shows the schematic of the ADC input block. For channels one to four, and six, the ADC sample clocks are used to run the input circuitry.

There are eight individual snapshot memories, one for each channel. The wishbone access interface is common to all eight memories, providing one wishbone slave interface internally. Each snapshot memory may be individually started by software, or it may be synchronised to the trigger signal. When the trigger signal is used, a trigger mask selects the channels which are started by the trigger signal, allowing a subset of channels to be used. Control of the snapshot is simple: A start bit (or corresponding trigger mask bit) is used for starting the data recording, and when the memory is full, a finish bit is set for each channel. When the start condition is removed (by clearing the start bit and/or resetting the trigger condition), the finish bit is cleared, and the memory is ready to be started again.

The snapshot memory is implemented as fully dual ported memory, and its contents

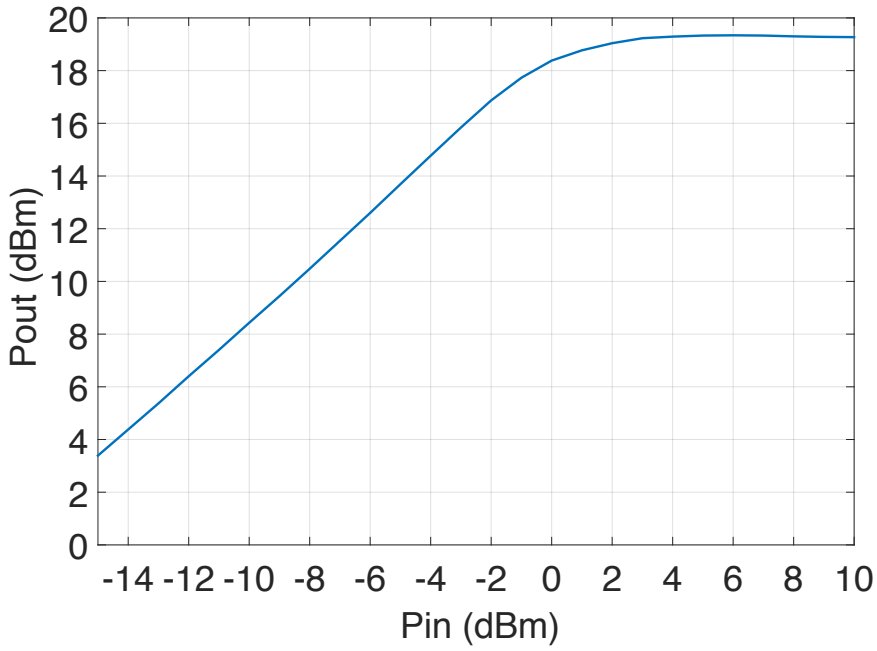

FIGURE 3.14: Measured input power versus output power in the transmitter board. The measurement was performed from the input to the coupler C1 before the antenna. The effects of the coupler are compensated.

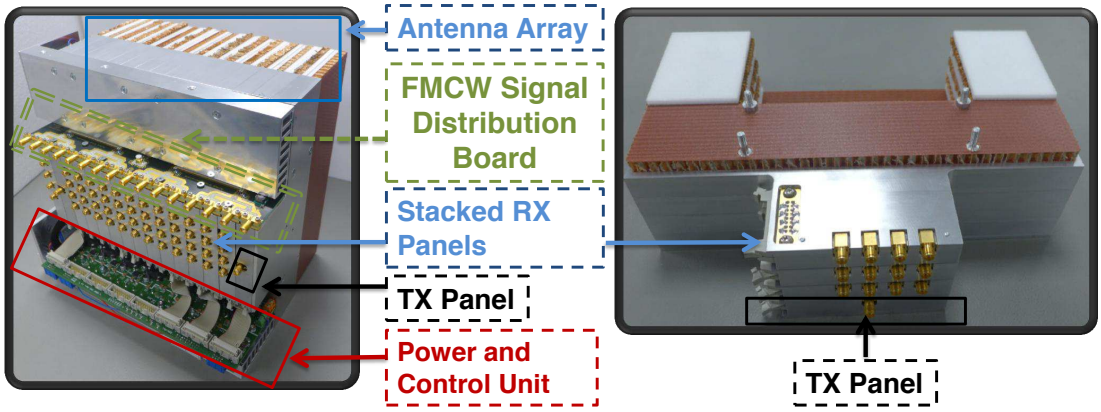

FIGURE 3.15: Photographs of the stacked TX, RX and FMCW signal distribution panels. The left image shows the complete RF front-end unit. The right image is a section view of its structure.

can be read or written at any time. Writing the memory may be used for debugging purposes, during normal operation it is not required or advisable, since it will interfere with the recording of the samples.

Additionally the snapshot memory provides a clock domain transition to the wishbone clock domain. The latter is used for registers and memory accesses, and provides the connection to the PCIe interface block. Each snapshot memory provides space for 32768 samples (32k). The wishbone interface accesses all snapshot memories of all channels consecutively, providing a memory region of 256k samples. Each sample is provided in a

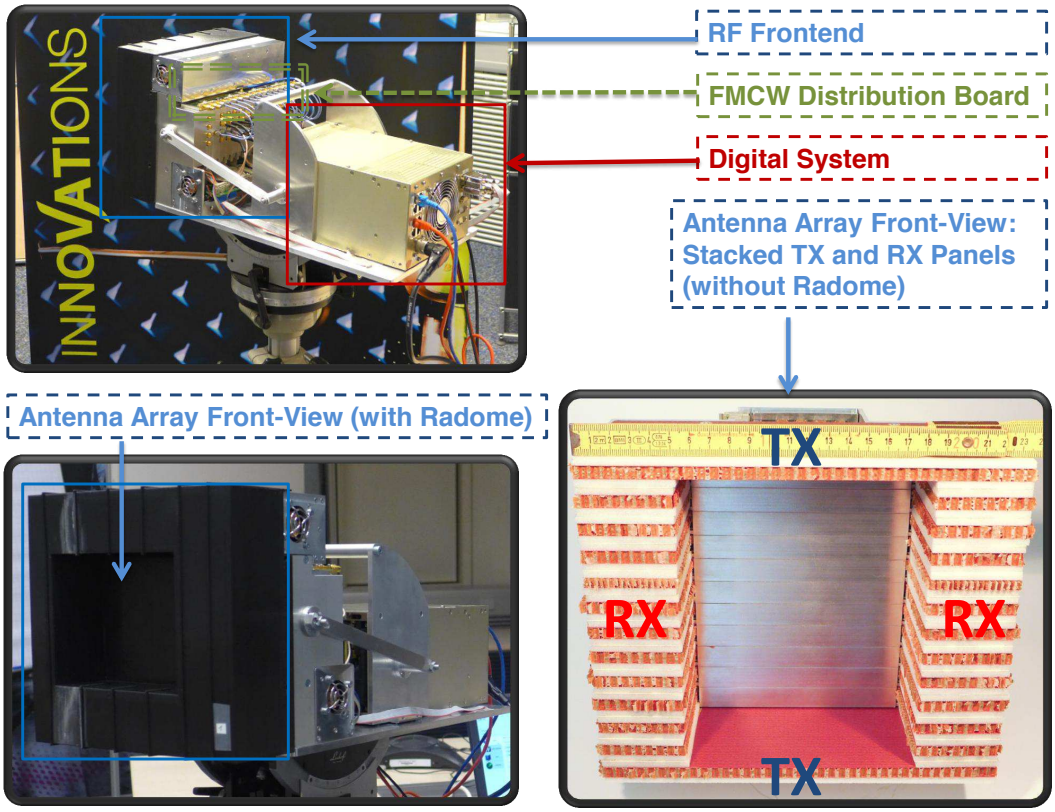

FIGURE 3.16: Photographs of the complete MIMO radar system. In the upper left image, the integrated RF front-end and digital system is presented. On the lower left and right images, a front view of the antenna array is shown.

single four byte sized word, sign extended to the full 32 bits. The entire snapshot memory occupies one megabyte of addressable memory on the wishbone and PCIe busses.

3.4.2.2 Clock Distribution Control and ADC Control

The clock management of the 4DSP FMC108 module is implemented using an AD9510 clock management chip [135]. The chip is controlled using a SPI interface [136]. The registers of the chip are presented in a word array of 256 32-bit words. Each 32-bit word allows read or write access to one of the 256 8-bit registers. The underlying SPI protocol is completely implemented in the FPGA firmware, registers are read or written with simple accesses to the appropriate register locations. A single register write will not stall the accessing processor. A subsequent operation will stall until the write has been finished. Read operations stall until the read data value has been obtained from the SPI interface. For high performance operations, processor accesses to the SPI interface should be carefully timed to prevent long processor stalls.
Each ADC chip provides a SPI interface to access internal registers. Each chip offers an eight bit address to select the registers. The registers are mapped to a 32-bit word each, directly accessible on the Wishbone or PCIe bus, respectively. The SPI accesses are handled internally by the FPGA firmware, stalling the accessing processor as appropriate to achieve the access.

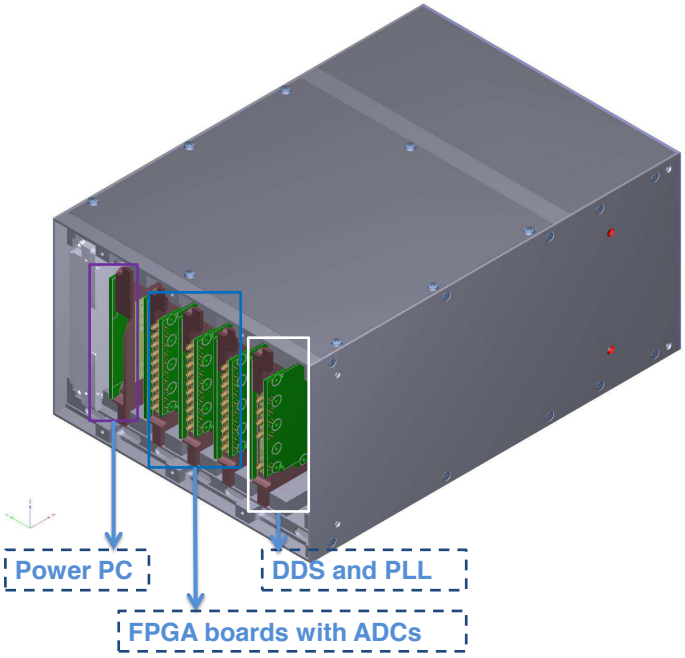

FIGURE 3.17: 3D illustration of the complete digital unit with the 3 FMC-FPGA boards, the PowerPC and the DDS and PLL board.

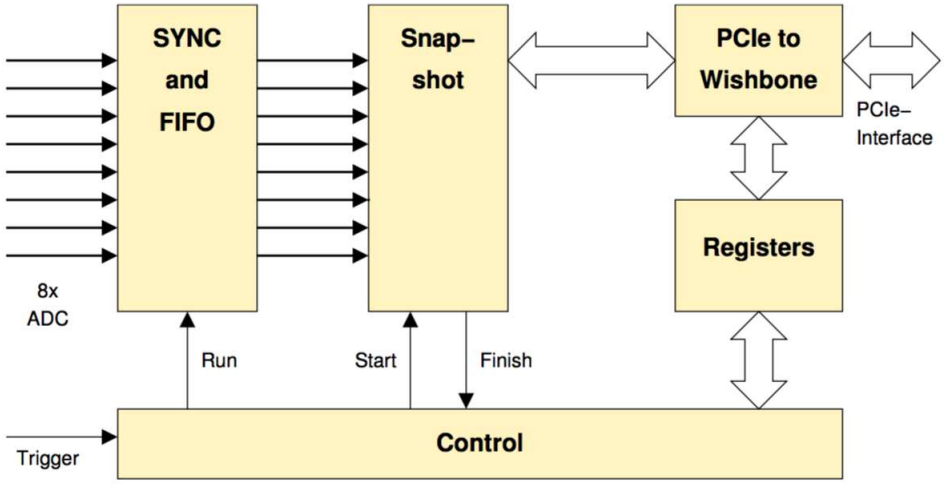

FIGURE 3.18: Schematic overview of the firmware implemented for the 4DSP FMC108 FMC modules.

The access blocks for each ADC are following after each other, and the interface is implemented as a common interface for all four devices. This is necessary since the AD converter chips share the SPI output lines (clock, and data), and only the select and read data lines are separate.

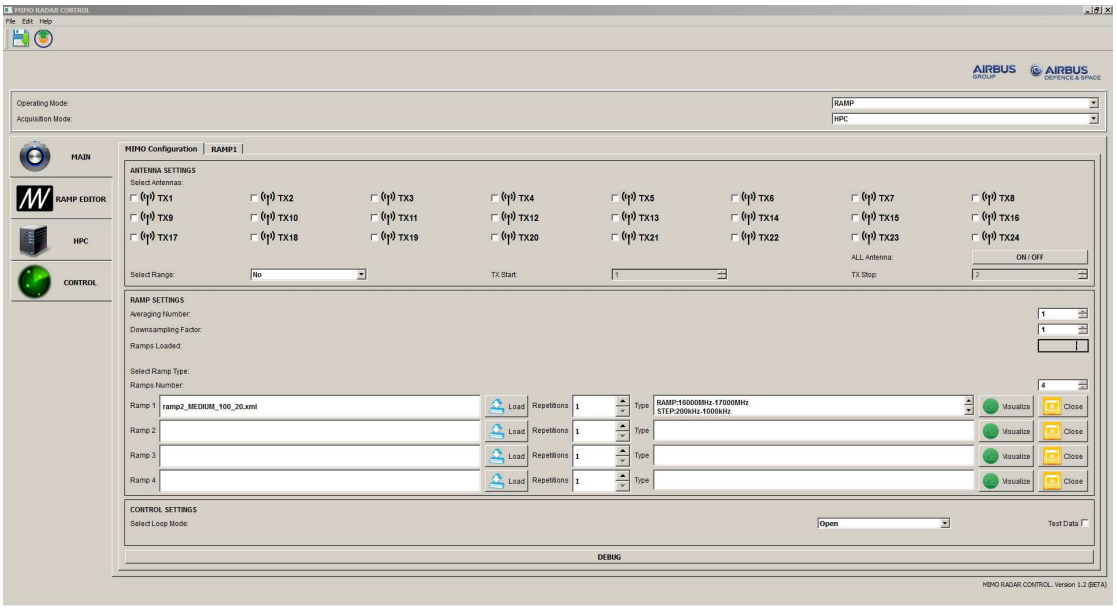

FIGURE 3.19: Picture of the MIMO radar control graphic human machine interface (HMI).

3.4.3 Software Architecture

The signal generation through the DDS and PLL blocks, is controlled from the MIMO radar control graphic HMI, shown in Fig. 3.19, through a USB interface. The data sent from the HMI to the DDS consist of control parameters for the characteristics of the transmitted FMCW radar signals, such as the start and stop frequencies and the duration of the signal. Throughout the measurements, start and stop frequencies of 16 GHz and 17 GHz, respectively, and a signal duration of 100 μs have been used. Therefore, the resulting waveform is an up-chirp signal, generated by a sine carrier which is continuously swept across a 1 GHz radar bandwidth in 100 μs.

Moreover, the HMI exchanges data with the FPGAs directly, interacting with the registers through the wishbone interface, as described previously. The data consist of various register control settings, radar control parameters, number of measurements to be taken and antenna settings, as shown in Fig. 3.19. Taking into consideration the concept of TDM used throughout our radar system [137], there is a need to switch between each transmit antenna within a very small time slot while all other transmit antennas are switched off in order to keep the frequency modulated signals mutually orthogonal so that no interference occurs. Therefore, after initial load of parameters to the DDS and the FPGA, the signal generation is started and the first of the transmit antenna is selected. The up-chirp signal is continuously running and each up-chirp starts matched with a trigger signal.

The next step is the sampling of each received radar signal. The radar echo signal is processed in each receive chain simultaneously. Due to the the TDM architecture used, only one transmit antenna element is active at each time. Therefore each receiver can separate all signals transmitted by the different antennas. The sampling is performed by the 8 ADCs of one board on the received signals and generates sampled signals of

32768 samples that are stored inside Random-Access Memory (RAM) blocks, internally to the FPGA. The FPGAs custom firmware is built in such a way that the sampling is initiated on the rising edge of an up-chirp signal and therefore, is synchronized across the 8 ADCs. Moreover, synchronization is preserved also across FPGAs through a master-slave configuration where an FPGA is selected to be the master and receives the external reference clock provided by the DDS and PLL unit and routes it, together with the trigger signal, to the other FPGAs. The firmware process ends after activating all transmit antennas and capturing the radar signals on all receive paths.

The received samples are then fed through the PCIe interface to a MPC8640D unit that processes the data from the FPGAs and creates a binary file which contains the raw data matrix i.e., the combination of 24 transmit signals by 24 receivers by 32768 samples of 14 bit each. The raw data matrix file is then transferred automatically via Ethernet to the radar processing system realized under MATLAB [90].

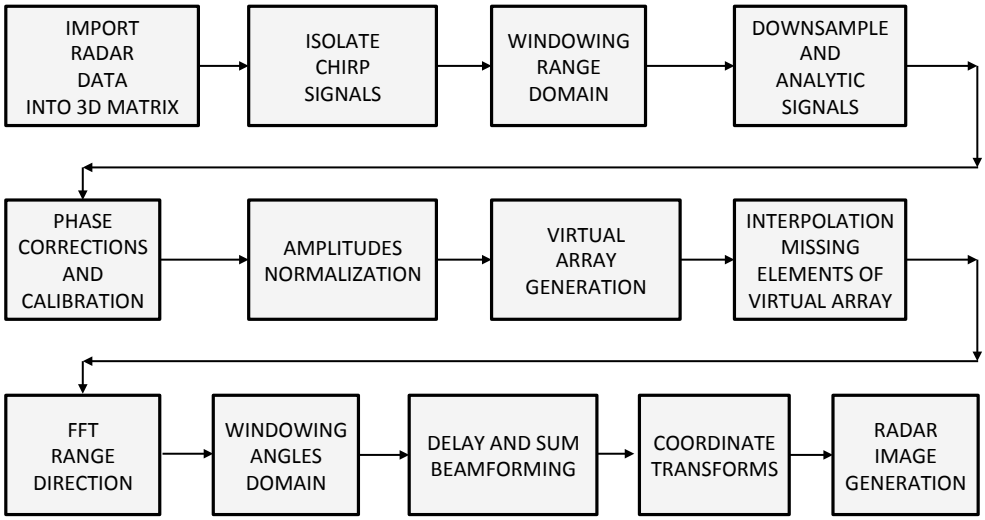

FIGURE 3.20: Radar digital signal processing software architecture.

3.4.4 Radar Digital Signal Processing

The radar digital signal processing software architecture is illustrated in Fig. 3.20. A total of 576 signals are read from the binary file into MATLAB, into a 3D matrix of 24 x 24 x 32768 elements, corresponding to the number of transmit antennas, the number of receive antennas and the total number of samples per signals, respectively. For each subset of transmit and receive elements (T_n, R_n), the 32768 samples represent the transmitted chirp signals from transmit antenna T_n and received at receive antenna R_n. However, of all the 32768 samples acquired, only 20480 samples are of interest. The number of samples for one chirp is given by the chirp duration in time, $t_{chirp} = 100$ μs, multiplied by the sampling frequency, $f_s = 204.8$ MHz. Thus, in a first step, a filtering operation is conducted in order to extract only the information of one chirp signal. The result is a matrix which is now reduced to 24 x 24 x 20480 samples. Subsequently, the 576 signals are windowed through the use of a Hanning window in order to reduce the side

lobes in both range and azimuth direction [138], Hilbert transformed and down converted to baseband. The outcome is a 3D matrix of 576 windowed and complex-valued signals.

3.4.5 Calibration

Considering that certain elements of the matrix show different time delays, due to intolerances and different path lengths of the cables in the system, a calibration was performed in order to reduce the influence of systematic measurement errors on the image reconstruction. Therefore, the first step of the calibration consists in the correction of these constant phase offsets. The corrections are applied to a subset of complex signals of the matrix by means of a multiplication for a complex exponential containing the time correction.

The second step is the creation of a calibration matrix. In order to generate this, a real data measurement of a simple test scenario with one corner reflector at 37 m and at 0° of both azimuth and elevation, is multiplied for the conjugate of the same scenario, simulated idealistically in the MATLAB environment. The resulting calibration matrix is then used, by means of multiplication, with all new radar measurements in order to correct the systematic measurement errors from hardware.

Regarding the sensitivity of the radar to external factors throughout different radar captures, as long as the receiver channels change approximately equally through time, i.e. they are almost equally affected by temperature changes, no recalibration is necessary, considering also that our performed tests have shown that the calibration measure taken is still valid after months of radar operation.

The result is a calibrated 3D matrix where each signal phase is perfectly linear and represents the input for the digital beam-forming algorithm [81]. The complete MIMO matrix can be seen as

$$M_{IF} = [M_{IF}[1], M_{IF}[2], ..., M_{IF}[N_{virtual}]] \tag{3.3}$$

which is a $N \cdot N_{virtual}$ matrix whose columns $M_{IF}[i]$ with $(i = 1, ..., N_{virtual})$ are the complex time domain chirp signals with N sampled points of each virtual element and $N_{virtual} = N_{TX} \cdot N_{RX}$ represents the size of the virtual array, a multiplication of the number of transmit elements by the number of receive elements. The Cartesian position of the virtual elements is obtained by convolution of the real TX and RX antenna elements, as previously shown in Fig. 3.2.

3.4.6 Image Reconstruction

The image processing technique chosen for the proposed radar system is a combination of two core functions. The first one is an FFT in frequency direction in order to determine the range profile of the object, which is contained in the channel impulse response. The second one is a delay-and-sum beam-former function system for Azimuth and elevation processing which is used to reconstruct the scene imaged by the MIMO radar sensor

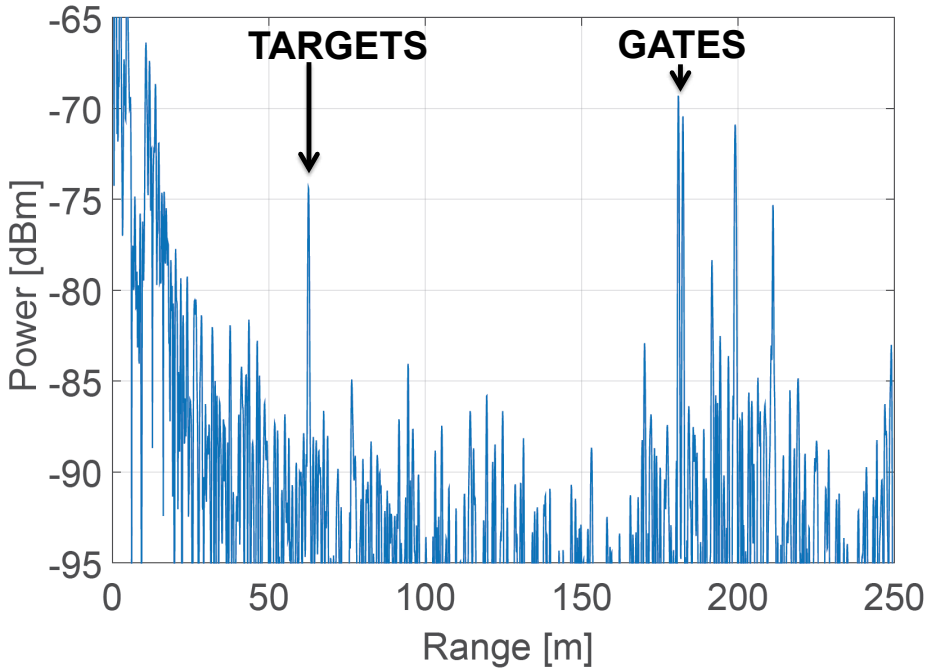

FIGURE 3.21: Range compression through FFT view of the received signal from one of the virtual elements.

[130],[139]. The image processing function operates on the 3D calibrated matrix given in (3.3) and starts with calculating the range compressed data matrix $\widetilde{M}_{IF}$ by means of an FFT transform in time direction. As an example, the result of the FFT operation on one of the received signals of the virtual array is presented in Fig. 3.21, where a distinguishable peak can be seen at 60 m. The position of the peak is the same for the two targets, which are the two corner reflectors at the same distance, in the radar test field used and shown in Fig. 3.23. Other peaks are visible in this image, which represent surrounding objects, such as metal gates which were present in the background of the scene of radar capturing.

The following step is the application of a delay and sum beam-forming algorithm that compensates the phase shift of each virtual element belonging to the virtual array, according to a weighting vector

$$\begin{aligned} w(\theta,\phi) = [&e^{j2\pi\frac{f_0}{c_0}x_v(1)\sin(\theta)\cos(\phi)+y_v(1)\sin(\theta)\sin(\phi)}, \\ &e^{j2\pi\frac{f_0}{c_0}x_v(2)\sin(\theta)\cos(\phi)+y_v(2)\sin(\theta)\sin(\phi)}, ..., \\ &e^{j2\pi\frac{f_0}{c_0}x_v(N_{virtual})\sin(\theta)\cos(\phi)+y_v(N_{virtual})\sin(\theta)\sin(\phi)}] \end{aligned} \tag{3.4}$$

where x_v and y_v are the positions of the virtual elements in the x and y axis, respectively, and θ and ϕ denote the angle of arrival of a given point target in azimuth and elevation, respectively. Therefore, the beam-forming operation can be seen in a vector notation as

$$\hat{m}(\theta,\phi) = \widetilde{M}_{IF} w(\theta,\phi) \tag{3.5}$$

which represents the image of the signal received from angles θ (azimuth) and ϕ (elevation), giving a full 3D representation of the scenario. The angles are expressed with respect to the bore-sight of the radar, for which $\theta = 0°$ and $\phi = 0°$.

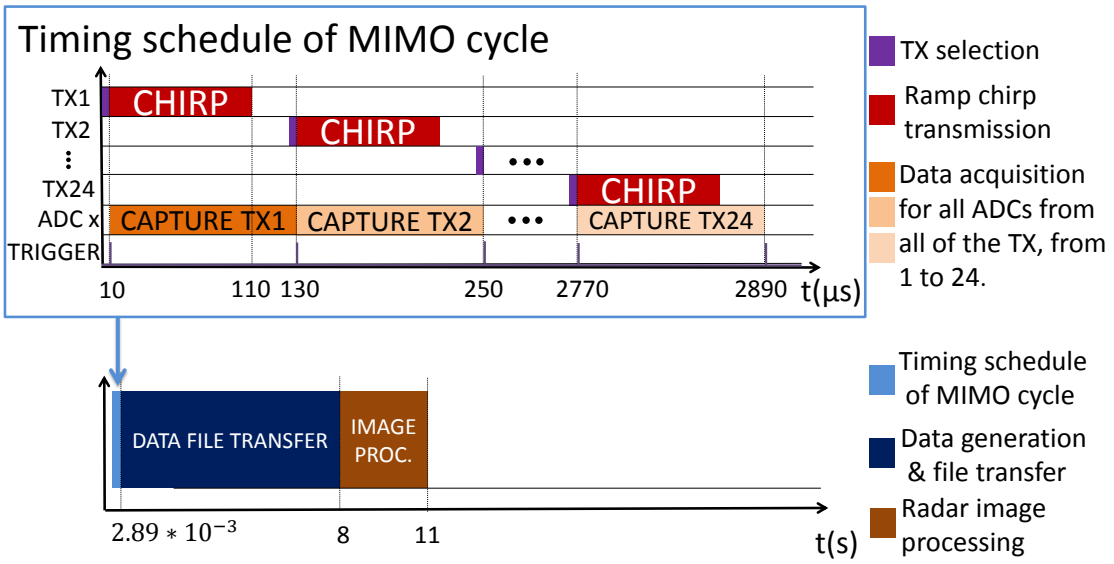

FIGURE 3.22: Illustration of the timings for a complete MIMO cycle: transmission for all 24 TX elements, data acquisition, transfer and radar image processing.

3.4.7 Timings Considerations

The TDM technique used in this radar demonstrator, consisting in the switching between the transmit antenna elements in a round-robin fashion, with only one active at a time starting with TX1 and ending with TX24, is illustrated in Fig. 3.22. In this image, a complete FMCW MIMO cycle is represented from transmission to image generation. As it can be seen from the image, the frequency modulated chirp signals have a duration of 100 μs, a physical switching time of around 10 μs and are sent sequentially with a delay of 20 μs. The received chirp signals at the RX array are then processed in parallel by means of multiplication with the transmitted chirp replica, before reaching the ADCs. The timing schedule for a complete MIMO cycle is, therefore, around 2.9 ms. Additionally, the time to process and transfer the 576 signals inside the digital unit and the radar image processing time itself need to be considered, which are around 8 s and 3 s, respectively for our current configuration. Consequently, as it can be understood, the main bottleneck of the system is the transferring of raw data through Ethernet to the processing system and the time for a single radar capturing and image reconstruction is in total around 11 s. Moreover, in order to speed up the radar image processing time, it is possible to specifically select the number of signals. For example, only 1 TX element and a row of 12 RX elements can be chosen, thus providing the ability to reconstruct the angles in only the azimuth axis, but decreasing the transferring and processing time. As noted and expected, incoming reflections will have modulation from the previous modulation cycle. This imposes a range limit. Considering the timings until transmission of the next chirp, the formula for the two-way propagation delay from the radar to the

target and back, as previously anticipated in equation (2.12), sets a maximum range limit of [110]

$$r_u = t_{chirp}\frac{c_0}{2} = 18\ km \tag{3.6}$$

where t_{chirp} represents the time duration from transmission of one chirp to the next. This value, called maximum unambiguous range, results from the remaining necessarily overlap of the transmission signal with the echo signal, to get enough time to measure a different frequency. Thus, there is always a sufficient time that allows the signals to be uncorrelated for the type of applications aimed with this system, ranging up to only several hundred meters.

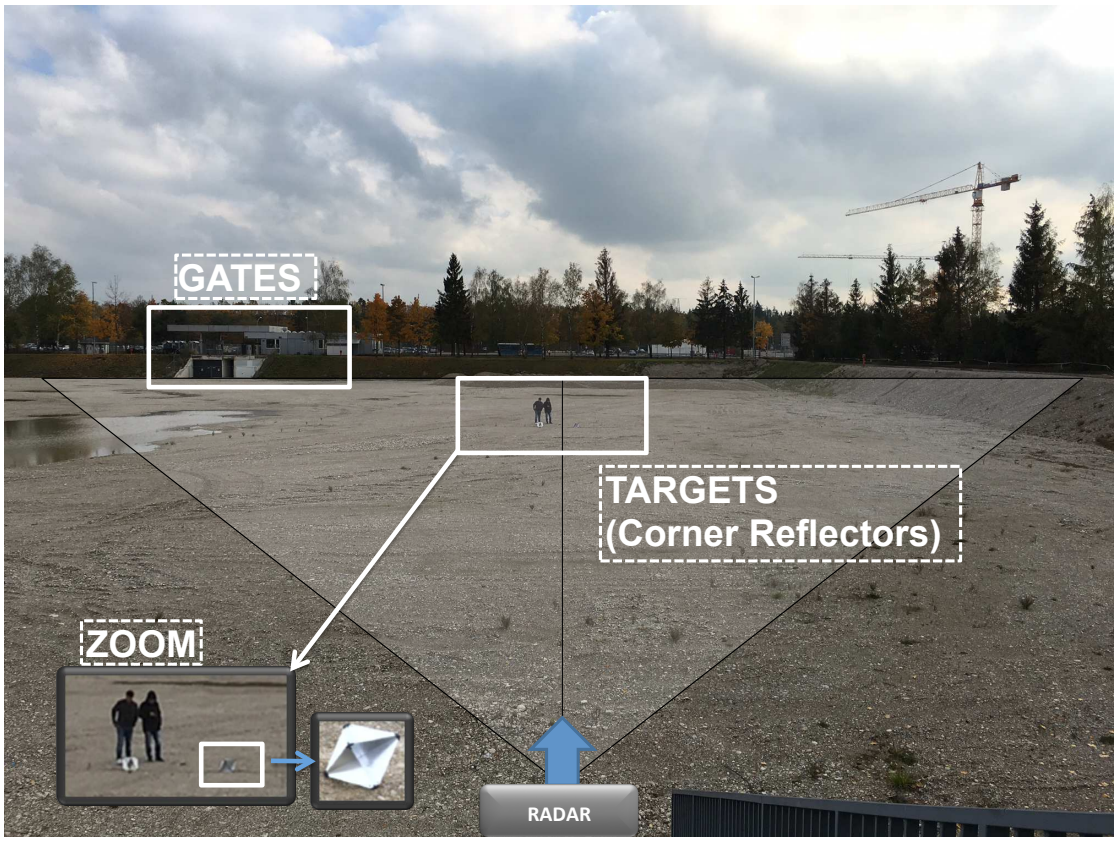

FIGURE 3.23: The MIMO radar test field with two corner reflectors at a range of 60 m with nominal radar cross section (RCS) of 36 m^2.

3.5 System Performance and Results

To demonstrate the radar performance and its capabilities in generating a 3D image in multi-target scenarios, two radar test fields are set up with the use of corner reflectors. Only stationary radar scenarios have been investigated so far. The first test field, used for measuring the range and angular separation capabilities of the demonstrator, is shown in Fig. 3.23. In this test setup, in order to carry out the free space measurements with the FMCW MIMO radar demonstrator, two corner reflectors at a range of 60 m with nominal radar cross section, or RCS, of 36 m^2 are placed in front of the radar at a slightly different orientation leading to differences in the measured RCS and different

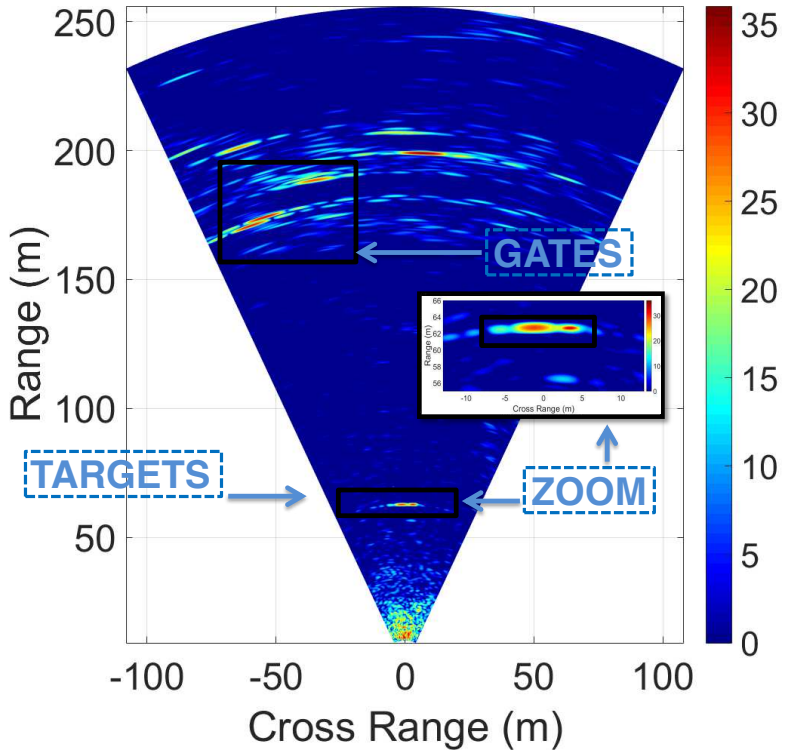

FIGURE 3.24: Range-Azimuth section view of the 3D MIMO radar image capture from the radar setup scenario with two reflectors at a distance of 60 m.

radial and lateral spacings. The people shown behind the reflectors serve the purpose of representing the size of the image compared to the scenario.

Each of the images is generated with 24 up-chirp signals ranging from 16 GHz to 17 GHz and with a duration of 100 μs. For easier understanding of the performance parameters, slices of the 3D images are presented in the following chapters, in the form of 2D images. The range-azimuth and range-elevation 2D section views are obtained by slicing the 3D image at $\phi = 0°$ and $\theta = 0°$, respectively.

3.5.1 Range, Azimuth and Elevation Estimation

A 2D radar image, cut in the azimuth plane, of the complete 3D image produced by the image reconstruction algorithm described in the previous section is shown in Fig. 3.24. In this example, the reflectors are placed within the same range cell at a distance of 60 m and at an angular distance of 4° (about 8 m lateral separation). It is possible to identify the two corner reflectors, together with additional reflections coming from two metal gates that were on the left at around 170 m distance from the radar, as shown in Fig. 3.23 and as it can also be seen from the FFT result presented in Fig. 3.21. The zoom into the targets in this image, makes it easier to clearly identify and separate the 2 corner reflectors at 60 m range. The amplitude of the target on the right is 6 dB lower due to a non identical alignment of the used corner reflectors.

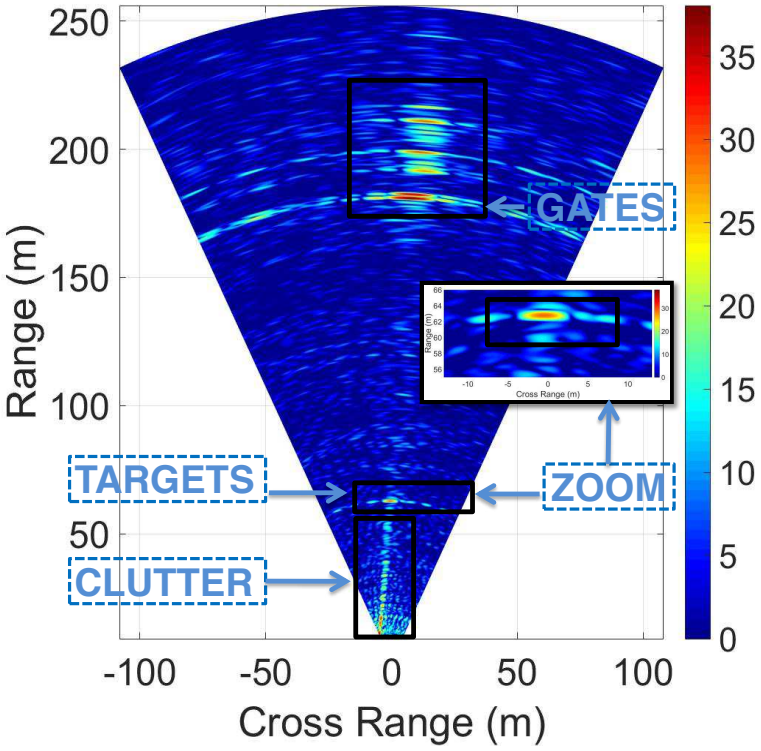

FIGURE 3.25: Range-Elevation section view of the 3D MIMO radar image capture from the radar setup scenario with two reflectors at a distance of 60 m.

A 2D radar image, cut instead in the elevation plane, of the complete 3D image, is depicted in Fig. 3.25. In this image, the two corner reflectors can again clearly be seen. Considering that they are placed at the same elevation of 0° and at the same range, they can't be separated in this view. An important aspect to understand from this view are the clutter effects that can be seen as a line that starts from 0 m up to almost 60 m in range, which is ground clutter produced as reflected signals from the terrain. Since the radar is facing the two corner reflectors directly, but is positioned at an elevated position with respect to the terrain's level where the two corner reflectors are standing, clutter components starting from negative degree values of elevation are perfectly matching. The ground clutter eventually meets the elevation of the reflectors at around 60 m, as expected.

3.5.2 Range Separation Capability

The achievable range resolution of a radar system depends mostly on the total bandwidth covered by the transmitted chirp signal. From equation (2.14), it can be recalled that is is expressed as

$$\Delta r = \frac{c_0}{2B} \tag{3.7}$$

with c_0 being the speed of light and B the signal bandwidth. Considering a bandwidth of 1 GHz, equation (3.7) translates into $\Delta r = 15$ cm. However, because of non linearities in the generated chirp signals, truncation and range windowing, the effective range

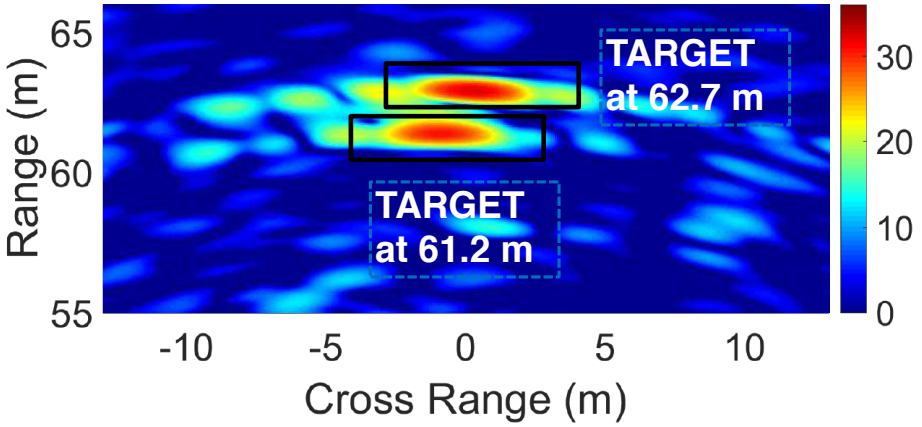

FIGURE 3.26: Range-Azimuth section view of the 3D radar image capture, with DBF and MIMO processing, with the two corner reflectors placed at the same azimuth angle of around 0° and 1.5 m apart.

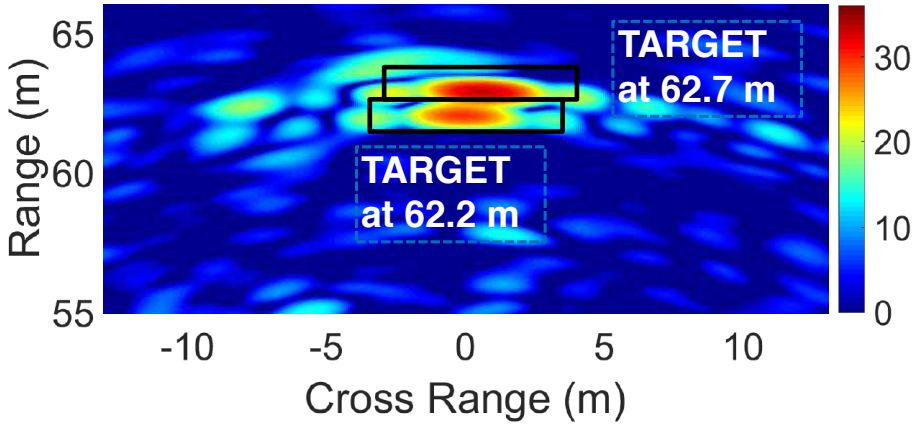

FIGURE 3.27: Range-Azimuth section view of the 3D radar image capture, with DBF and MIMO processing, with the two corner reflectors placed at the same azimuth angle of around 0° and 0.5 m apart.

resolution is different. Considering that the measured bandwidth is $B_{eff} = 830$ MHz and that the Hanning window [138] entails a reduction of resolution by a factor of 1.5, the effective range resolution is $\Delta r = 27$ cm.

For the experimental determination of the range resolution, the corner reflectors are placed at an identical azimuth angle. Fig. 3.26 shows the results of a radar scenario with two targets at a radial distance of 1.5 m. Differently from the previously conducted measurement, by correctly orienting the corner cubes, their RCS has now been adjusted to be almost the same, even though some slight disparities are still to be expected due to fabrication processes of the corner cubes itself. Further reducing the radial distance to 0.5 m, gives instead the results shown in Fig. 3.27. Even though an expansion can be seen in the targets in the image caused by the applied Hanning window, the targets can still be considered uniquely identifiable. This is highlighted in Fig. 3.28, which depicts

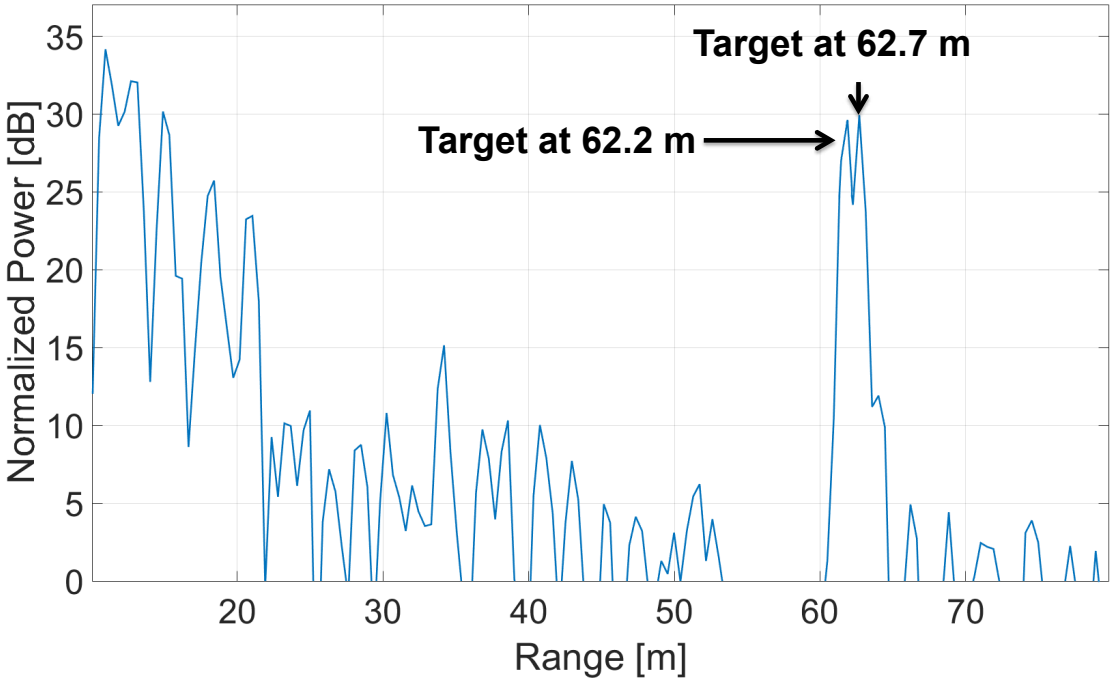

FIGURE 3.28: FFT view of the 3D radar image capture, cut across ranges, with DBF and MIMO processing, with the two corner reflectors placed at the same azimuth angle of around 0° and 0.5 m apart.

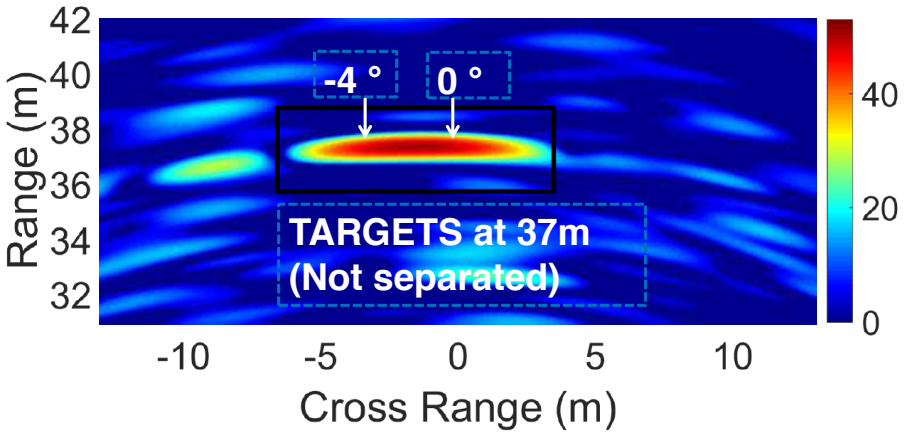

FIGURE 3.29: Range-Azimuth section view of the 3D radar image capture, with conventional DBF and no MIMO processing. The corner reflectors are placed at an identical range cell. The two targets are not uniquely identifiable.

the FFT view of the 3D radar image, cut across the ranges and shows two distinctive peaks. This represents the closest tested distance that can be reached, in order to uniquely identify the targets. The linearity of the chirp signals is minimally affected by the frequency response of the RF front-end boards. This leads to a difference between the theoretical and measured range resolution of 1.48 %. Nevertheless, the achieved resolution is high enough for the intended application of the radar demonstrator, i.e. the surveillance of wide-zone scenarios.

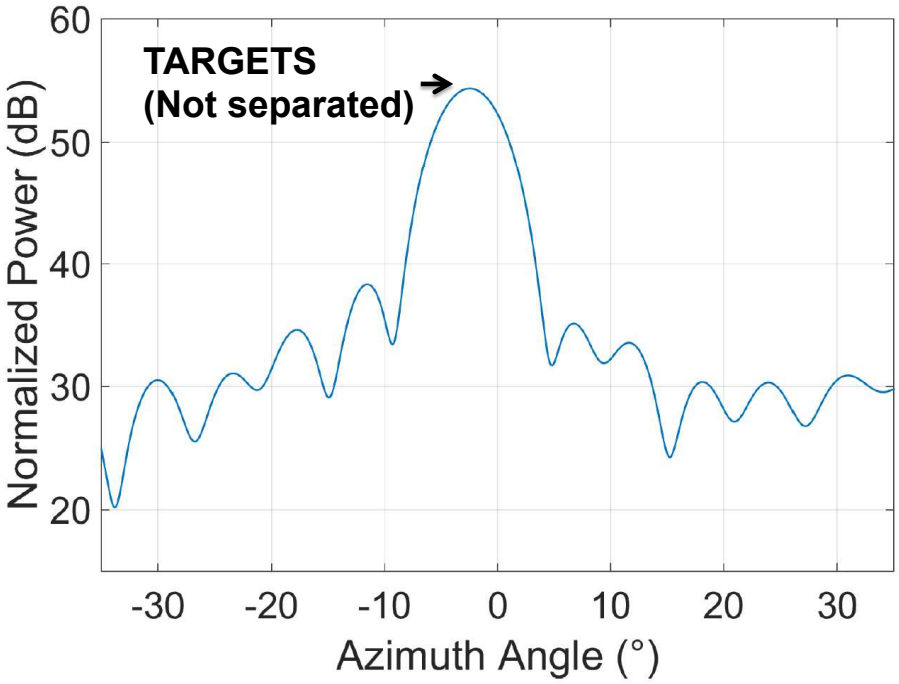

FIGURE 3.30: dB - Angular section view of the 3D radar image capture, with conventional DBF and no MIMO processing. The corner reflectors are placed at an identical range cell. The two targets are not uniquely identifiable.

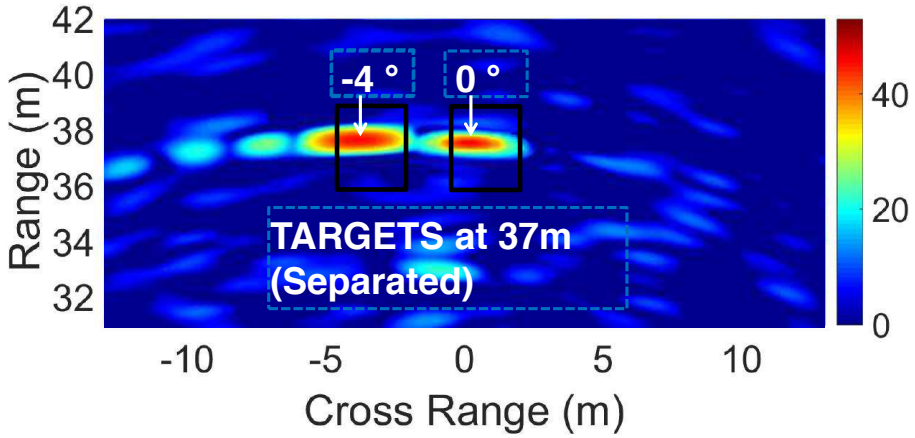

FIGURE 3.31: Range-Azimuth section view of the 3D radar image capture, with DBF and MIMO processing. The corner reflectors are placed at an identical range cell. The two targets are uniquely identifiable.

3.5.3 Angular Separation Capability

The angular separation capability, previously described in Fig. 3.3 and equation (3.1), is now examined within a range cell, in the same scenario used in subchapter V-B, with two corner reflectors correctly oriented with same nominal radar cross section of 36 m^2. However, now the targets are at a distance of 37 m. The system's ability to resolve multiple target scenarios is mainly determined by the width of the main lobe

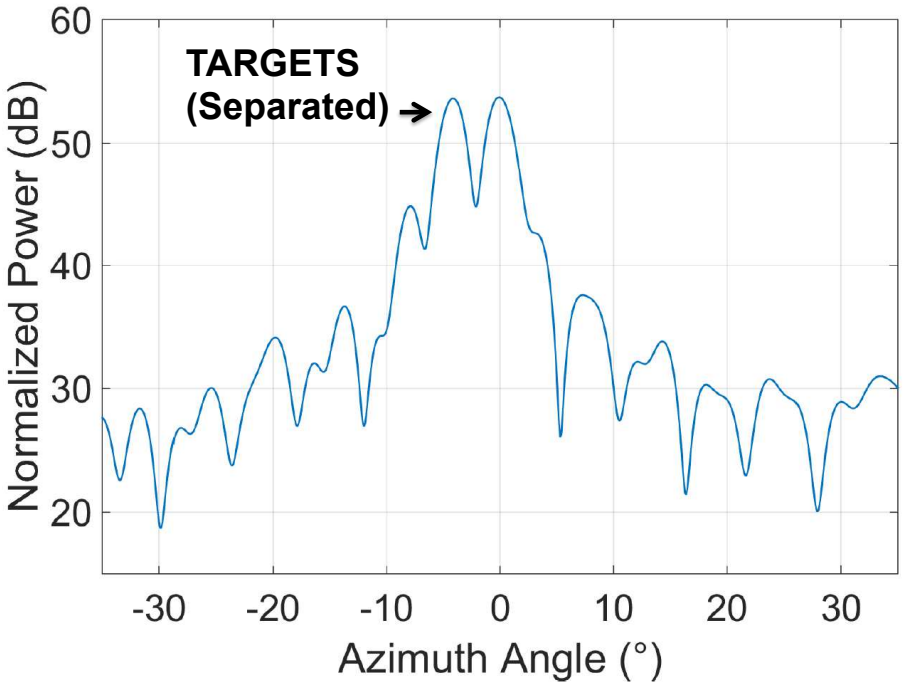

FIGURE 3.32: dB - Angular section view of the 3D radar image capture, with DBF and MIMO processing. The corner reflectors are placed at an identical range cell. The two targets are uniquely identifiable.

of the antenna, after DBF. As a result, the limiting factor for the angle separation capability is solely based on the width of the shaped lobes and the angular resolution is approximately expressed as in equation (3.1). Although interpolation of the missing data is performed in order to address the missing data of the empty row of the virtual array illustrated in Fig. 3.3, which improves the overall resolution, differences between the measured angular resolution and the one given by equation (3.1) are expected to arise. This is due to the fact that the equation is an approximation based on a limited number of antenna elements and, additionally, weighting of antenna elements by means of classical windowing functions like the ones used in this algorithm, allows for better side lobe suppression, but at the expense of a slightly reduced angular resolution [138].

The processing of the collected data is carried out in two different ways. First, through conventional DBF by using only 1 transmit element and no virtual array with a Multiple-Input-Single-Output (MISO) approach and second, by using a MIMO processing approach. To determine the resolution limit, both reflectors are laterally moved toward each other, until the separation of the targets is no longer possible.

In Fig. 3.29 the conventional processing is used. As depicted in this figure, only a single target can clearly be seen in the middle of the detection area of the sensor. A corresponding range cut gives the graph shown in Fig. 3.30. Only one half-width main lobe is clearly visible, of 5.9°, which well matches the theoretical value determined by equation (3.1) of 5.79°. Therefore, since the beam-width is greater than the angular distance of the targets, a separation of the targets is not possible without MIMO processing.

Subsequently, the processing based on the MIMO virtual aperture is applied. The new calculated beam-width now translates into 2.89°. As previously mentioned, compared to the theoretical equation (3.1), this value is expected to be slightly different and in this case it is 0.39° higher. The results of the processing are shown in Fig. 3.31. It can now be seen, with a closer look as shown in Fig. 3.32, that the two close targets become more uniquely identifiable. Both targets are clearly visible at a distance of approximately 4°.

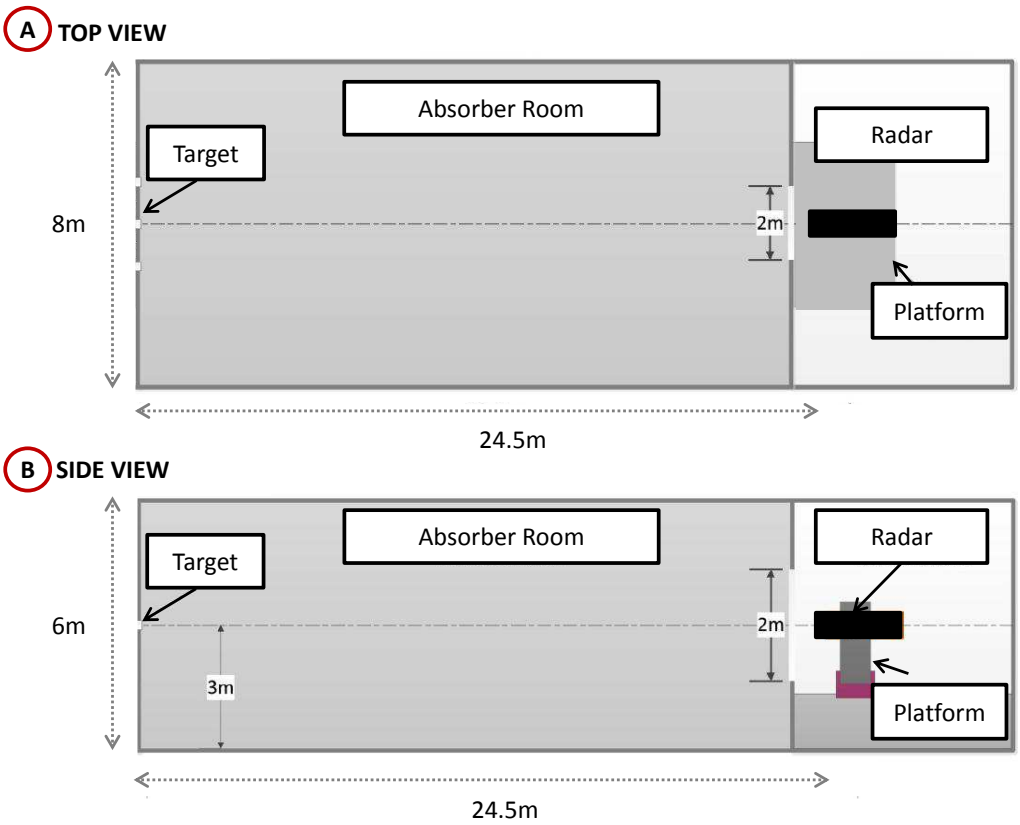

FIGURE 3.33: Procedure for the measurement inside the anechoic chamber. A target is placed at a distance of 24.5 meters and in front of the radar at 0° of both Azimuth and elevation angles.

3.5.4 Measurements in an Anechoic Chamber

In order to verify the results on the angular resolution from the field measurements, a further examination has been made inside an anechoic chamber, according to the procedure depicted in Fig. 3.33. As it can be seen, the radar is placed on a platform and a target is placed on the other side of the anechoic chamber, at the same elevation and Azimuth angle, of 0°. In the image, both a top view and a side view of the experiment scenario are shown, in subfigure A and subfigure B, respectively. A picture of the anechoic chamber used can be seen in Fig. 3.34 and Fig. 3.35, where a view from the radar and from the target are shown, respectively. The target used in this case, is a corner reflector with a nominal radar cross section of 36 m^2, that has been placed at an Azimuth of $\theta = 0°$ and a range of 24.5 m. An azimuth angular section view, cut from the 3D radar image at $\phi = 0°$ and a range of 24.5 m, is shown in Fig. 3.36, subsection

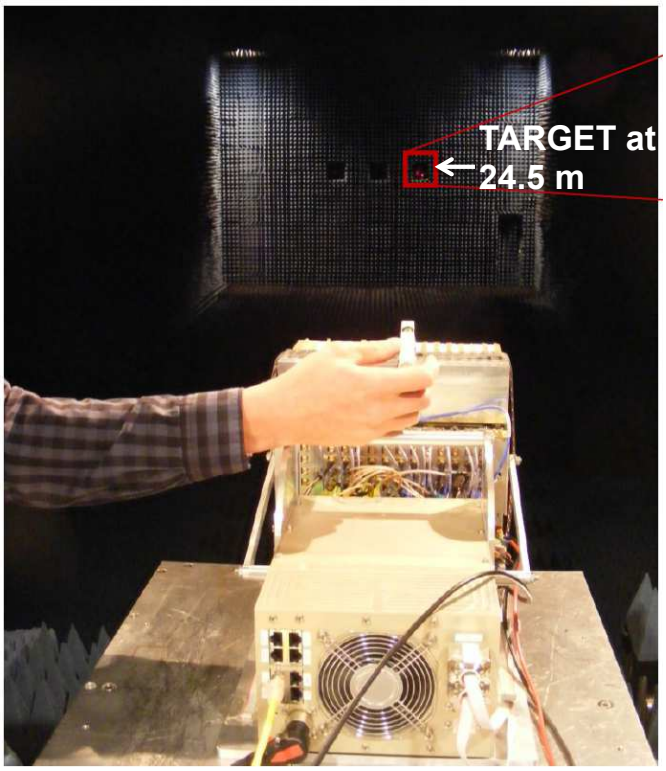

FIGURE 3.34: Picture of the anechoic chamber for the measurement of the angular resolution. The target is placed at a distance of 24.5 meters.

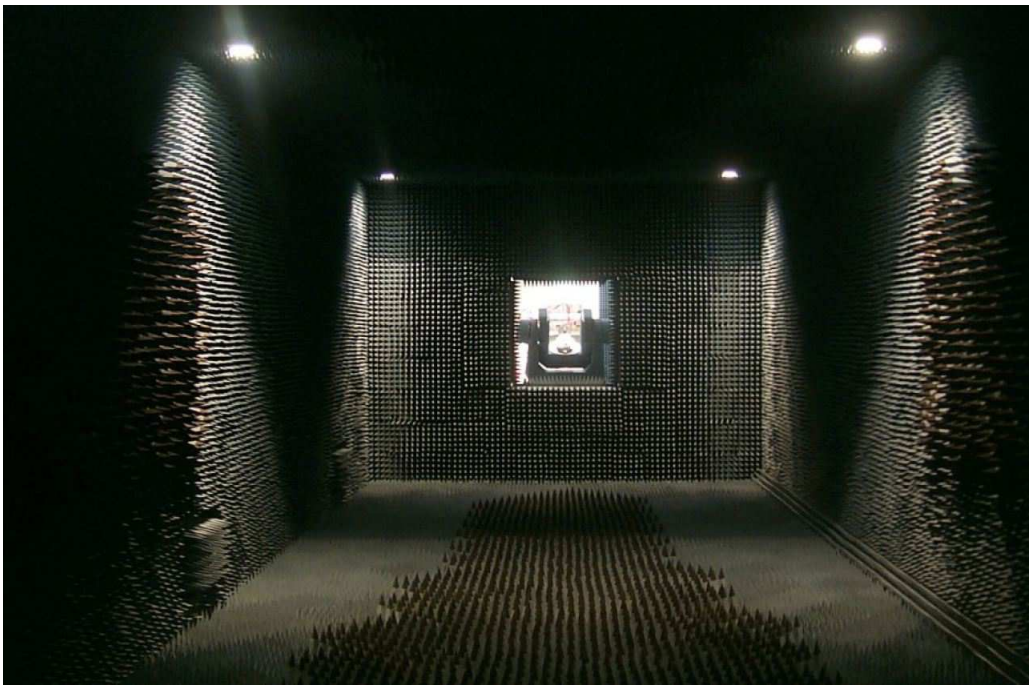

FIGURE 3.35: Picture of the anechoic chamber for the measurement of the angular resolution. View from the position of the target, towards the radar position.

A. The Azimuth angular resolution, calculated with MIMO processing, is taken as the 3 dB bandwidth of the main lobe of the target. In this ideal scenario it becomes 2.7°,

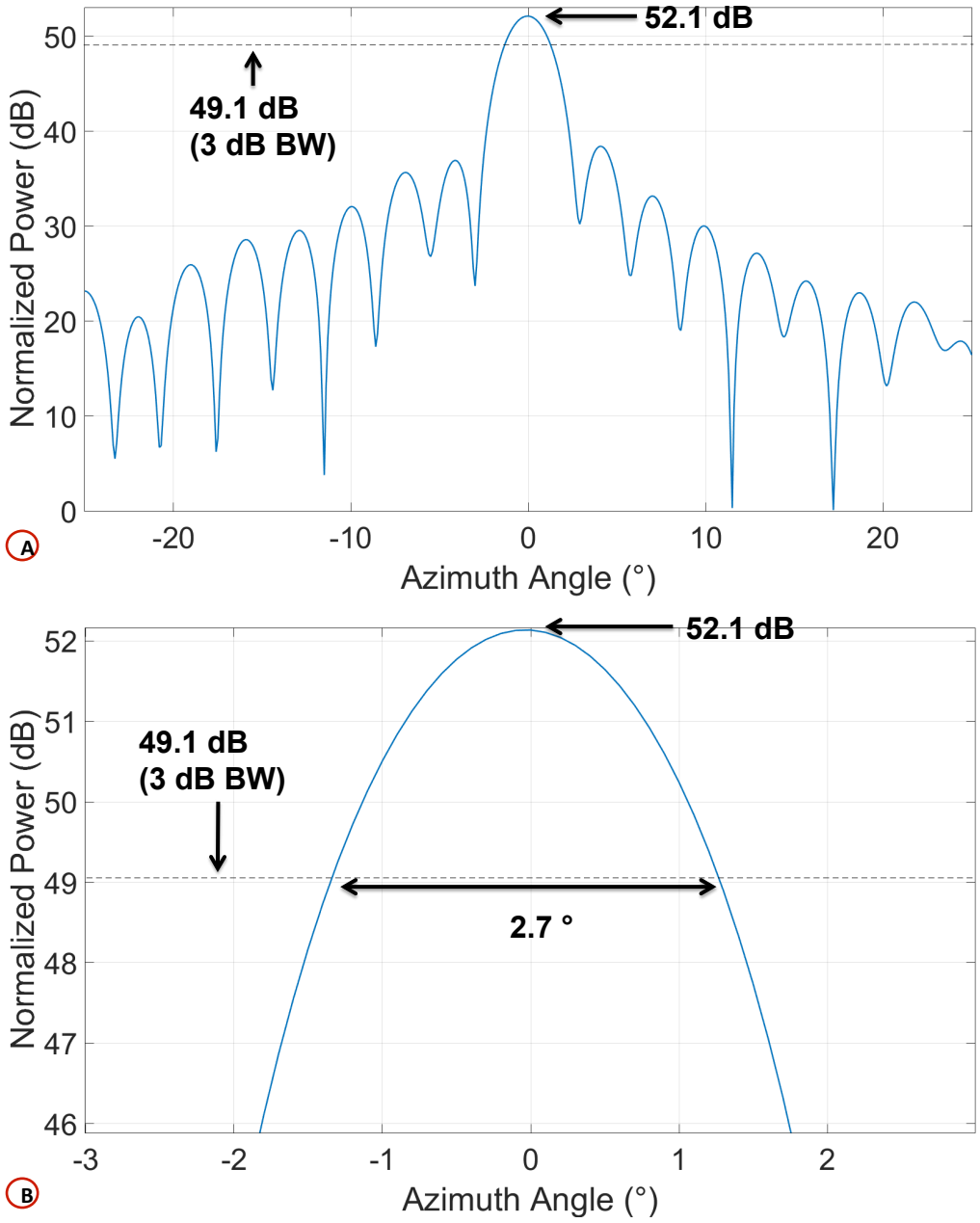

FIGURE 3.36: dB - Azimuth, angular section view of the 3D radar image capture of the target at 24.5 m, in the anechoic chamber.

as shown in Fig. 3.36, subsection B. This value differs now only of 0.2° from the one given in equation (3.1), confirming an influence from the interpolation, the windowing and the fact that the equation is just an approximation.

Additionally, an estimation of the elevation angular resolution is also performed. An elevation angular section view, cut from the 3D radar image at $\theta = 0°$ and a range of 24.5 m, is shown in Fig. 3.37, subsection A. The elevation angular resolution, calculated with MIMO processing, is also taken as the 3 dB bandwidth of the main lobe of the target. In this ideal scenario it is 2.7°, as shown in Fig. 3.37, subsection B, matching with the fact that the radar antenna array is rectangular and the virtual array symmetrical. In Fig. 3.38, an FFT view of the 3D radar image cut across the ranges is shown, where

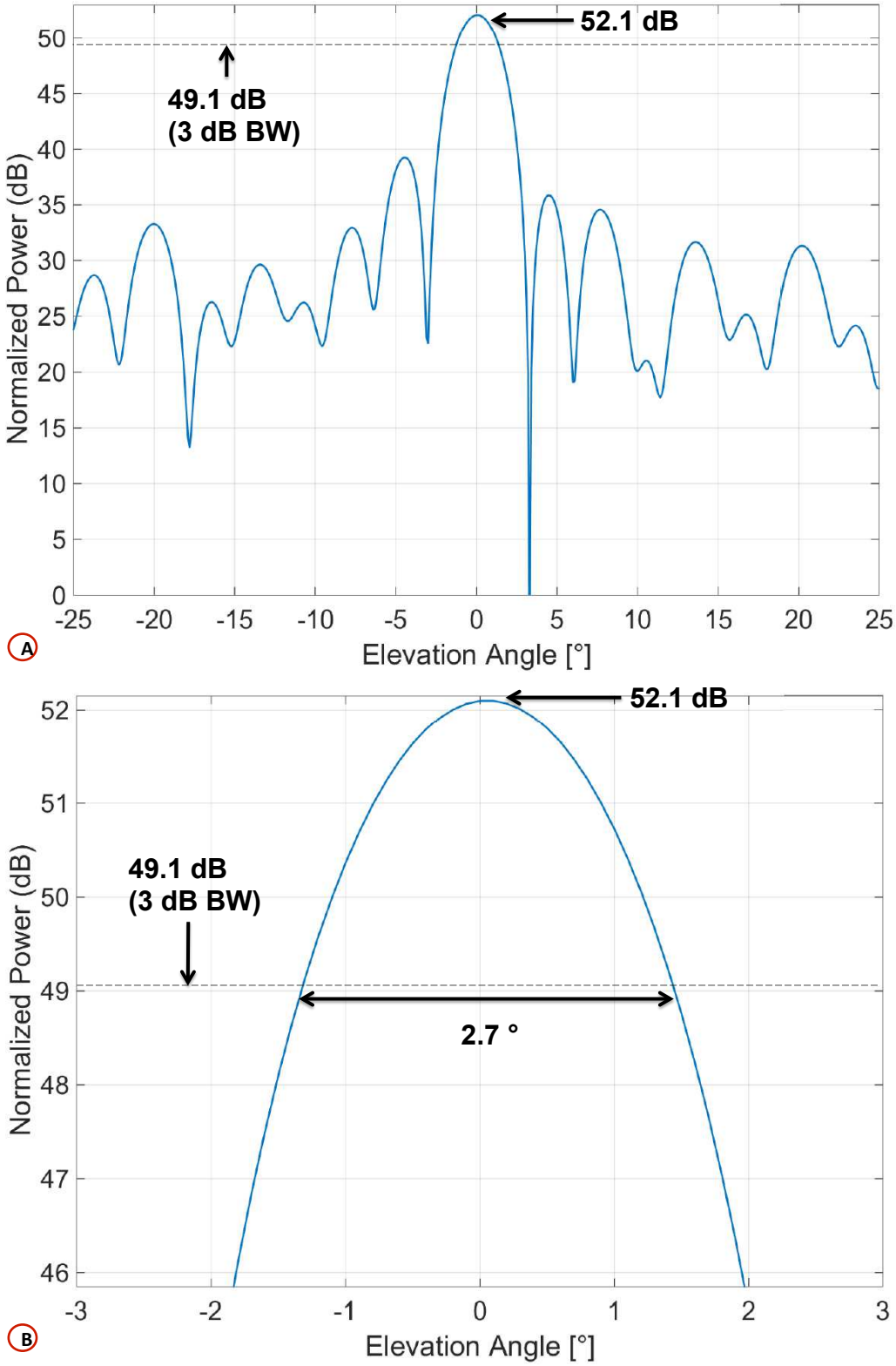

FIGURE 3.37: dB - Elevation, angular section view of the 3D radar image capture of the target at 24.5 m, in the anechoic chamber.

the peak from the corner cube can be distinctively seen, with a distance from the noise floor of around 30 dB.

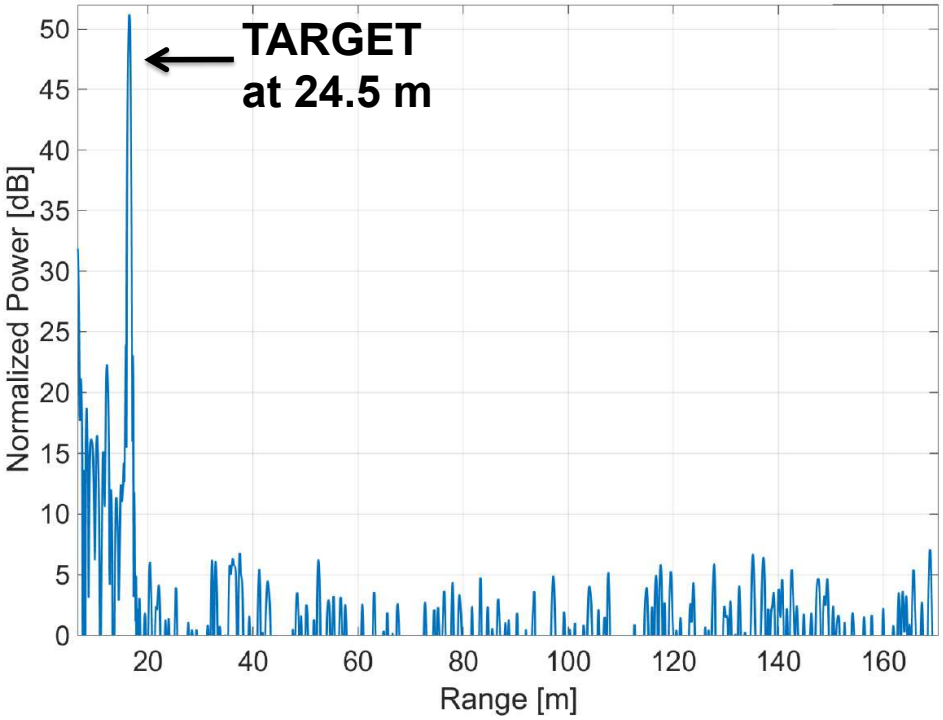

FIGURE 3.38: FFT view of the 3D radar image capture, cut across ranges, for the target at 24.5 m, in the anechoic chamber.

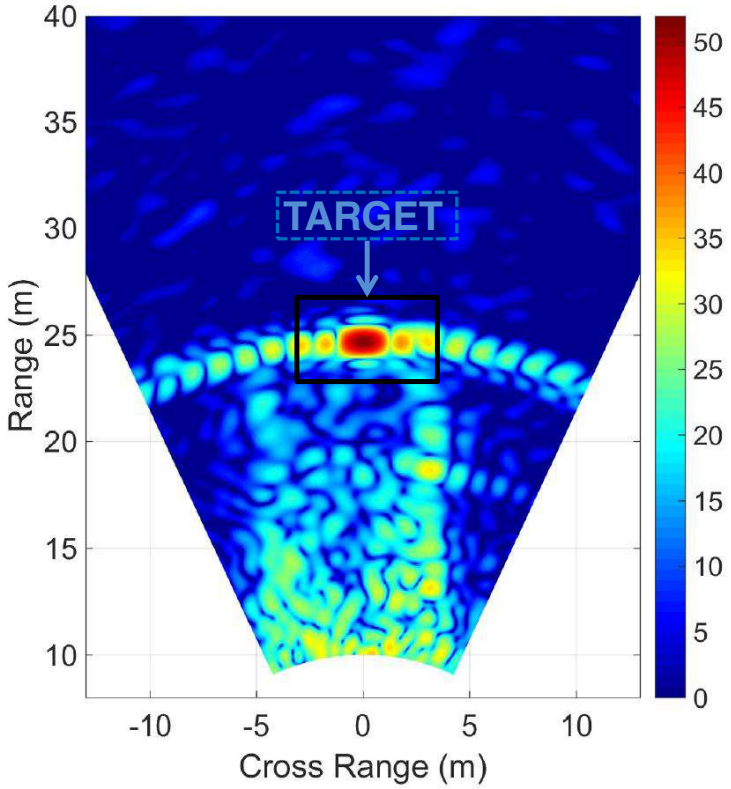

FIGURE 3.39: Azimuth-range section view of the 3D radar image capture of the target at 24.5 m, in the anechoic chamber.

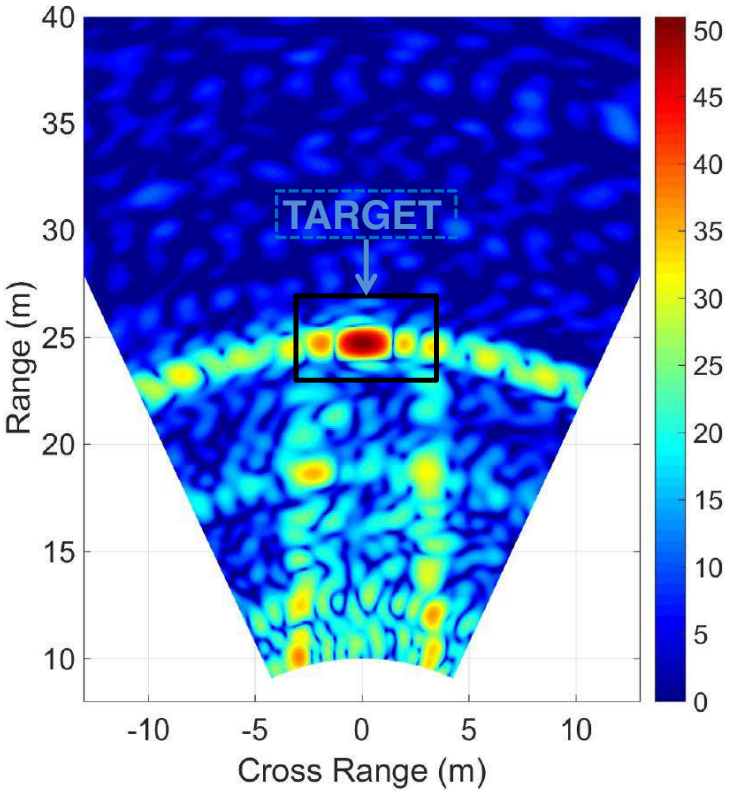

FIGURE 3.40: Elevation-range section view of the 3D radar image capture of the target at 24.5 m, in the anechoic chamber.

A 2D radar image, cut in the Azimuth plane and the elevation plane, of the complete 3D image, is shown in Fig. 3.39 and Fig. 3.40, respectively. The targets, and the side lobes, are clearly visible at a range of 24.5 m.
The overall good imaging performance of the radar is verified as well, by the fact that the walls of the anechoic chamber can also be seen in these images. In Fig. 3.39, the reflections in the picture seem to indicate the presence of a reflecting surface at -4 m and +4 m of cross range and along the range axis, therefore for a total span of 8 m, in accordance to dimensions of the anechoic chamber shown in Fig. 3.33, subsection A. Similarly, in Fig. 3.40, the reflections are at -3 m and +3 m of cross range and along the range axis, therefore for total span of 6 m, in accordance to dimensions of the anechoic chamber shown in Fig. 3.33, subsection B.

3.5.5 Multiple Targets Identification Capability

TABLE 3.1: Targets' Parameters for the Four Target Scenario

Target Number	Range	Azimuth	Elevation
1	14 m	0°	-3°
2	18.5 m	-4°	-3°
3	22 m	-9°	-1°
4	24 m	8°	-1°

Finally, a test scenario comprising four targets has been set-up, in order to analyse the performance of the radar device in detecting multiple targets, at different ranges, Azimuth and elevation values, as described in Table 3.1. In Fig. 3.41, the test field is shown, with the four corner reflectors at ranges of 14 m, 18.5 m, 22 m and 24 m, spaced both in Azimuth and in elevation, and having a nominal radar cross section of 36 m^2.
A 2D radar image, cut in the azimuth plane, of the complete 3D image produced by the image reconstruction algorithm described in the previous section, is shown in Fig. 3.42. As it can be seen from the image, all corner reflector are uniquely identifiable, at the exact same positions in range and Azimuth given in Table 3.1: one target centrally spaced in Azimuth and at 14 m of range; two targets on the left of the radar, at 18.5 m, with $\theta = -4°$ and 22 m, with $\theta = -9°$; one target on the right side, at 24 m distance, with $\theta = 8°$. Additionally, two important things to notice from the picture are, the sidelobes of each and every target which are present on the sides of it, and the reflected amplitude of the targets, decreasing with the range, in accordance with the theory.
A 2D radar image, cut instead in the elevation plane, of the complete 3D image, is depicted in Fig. 3.43. In this image, the four corner reflectors can, again, clearly be identified at the exact same positions in range and elevation given in Table 3.1: two corner reflectors which are below the bore-sight of the radar, at the level of the ground clutter, with $\phi = -3°$, at 14 m and 18.5 m of range; two corner reflectors which are elevated from ground and almost at the same level of the bore-sight of the radar, at a distance of 22 m and 24 m, with $\phi = -1°$. In Fig. 3.44, an FFT view of the 3D radar image cut across the ranges is shown, where the peaks from all four targets can be distinctively seen.
An estimation of both Angular and elevation capabilities is now presented for each target in this scenario. An Azimuth angular section view, cut from the 3D radar image at $\phi = 0°$ and ranges of 4 m, 18.5 m, 22 m and 24 m, is shown in Figures 3.45, 3.46, 3.47 and 3.48, respectively. It can be noticed that the identification of the targets is performed in a correct manner, with the main lobe of the target positioned at $\theta = 0°$, $\theta = -4°$, $\theta = -9°$ and $\theta = 8°$, for Figures 3.45, 3.46, 3.47 and 3.48, respectively.
An elevation angular section view, cut from the 3D radar image at $\theta = 0°$ and ranges of 4 m, 18.5 m, 22 m and 24 m, is shown in Figures 3.49, 3.50, 3.51 and 3.52, respectively. Here as well, it can be seen that the identification of the targets is performed in a correct manner, with the main lobe of the target positioned at $\phi = -3°$, $\phi = -3°$, $\phi = -1°$ and $\phi = -1°$, for Figures 3.49, 3.50, 3.51 and 3.52, respectively.

3.5.6 Maximum Tested Range

In order to measure the maximum range at which the radar demonstrator can identify a target, a corner reflector with nominal radar cross section of 36 m^2 has been used and placed in an open field test scenario, at a distance of 315 m, as shown in Fig. 3.53. As previously described and shown in Fig. 3.14, the transmit output power and the antenna gain of the radar are close to 20 dBm and 7 dB, respectively. A radar image, cut in the azimuth plane, of the complete 3D image, is shown in Fig. 3.54. A zoom into the picture, shows that the target is clearly visible at a distance of 315 m, thus determining the maximum tested range of the radar system.

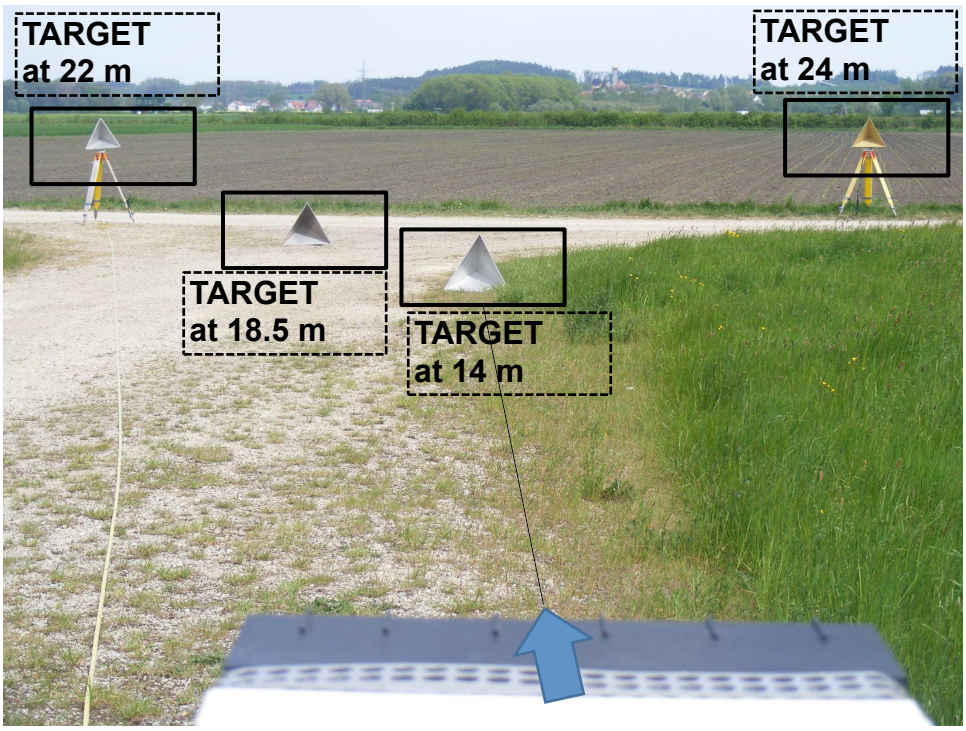

FIGURE 3.41: The MIMO radar test field with four corner reflectors at ranges of 14 m, 18.5 m, 22 m and 24 m with nominal radar cross section of 36 m^2.

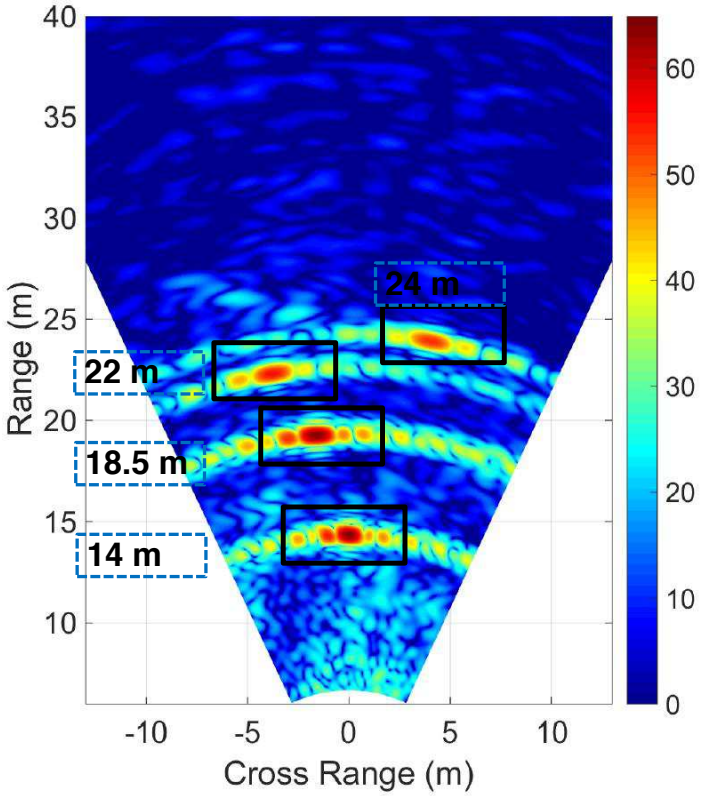

FIGURE 3.42: Azimuth-range section view of the 3D radar image capture of four targets at 14 m, 18.5 m, 22 m and 24 m, spaced both in Azimuth and in elevation.

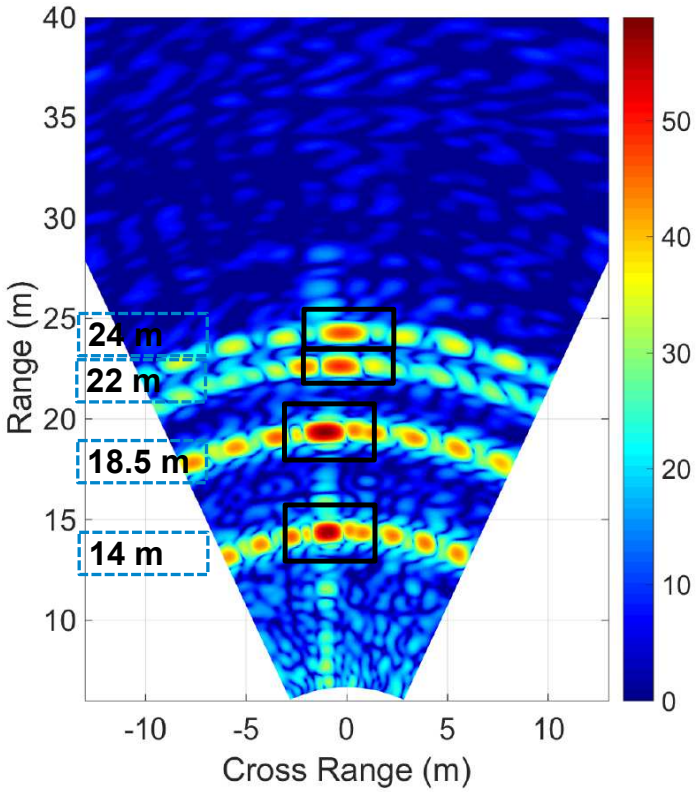

FIGURE 3.43: Elevation-range section view of the 3D radar image capture of four targets at 14 m, 18.5 m, 22 m and 24 m, spaced both in Azimuth and in elevation.

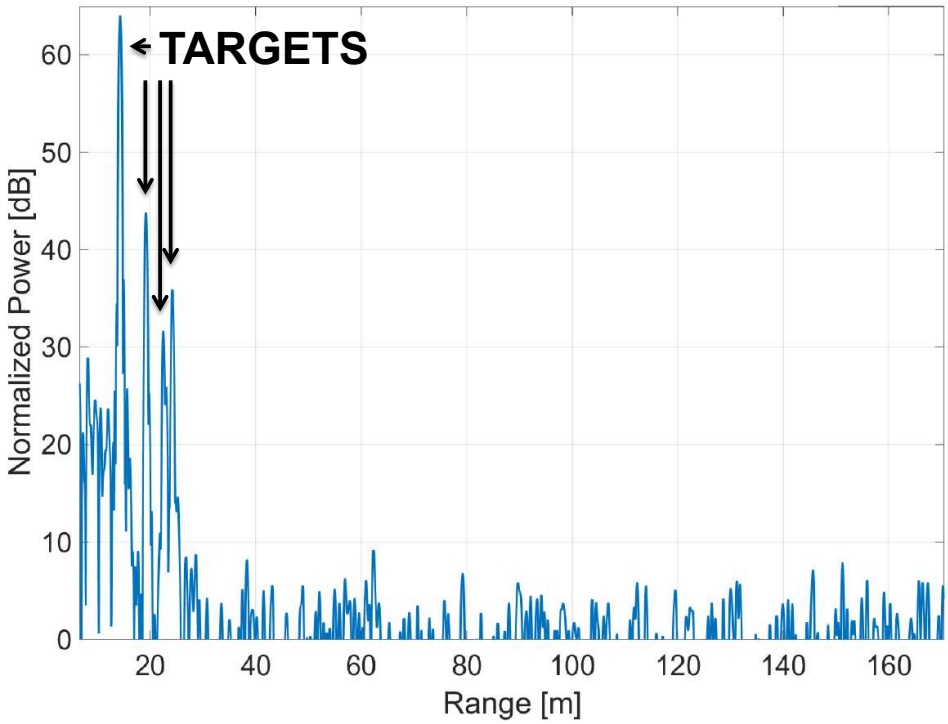

FIGURE 3.44: FFT view of the 3D radar image capture, cut across ranges, of four targets at 14 m, 18.5 m, 22 m and 24 m.

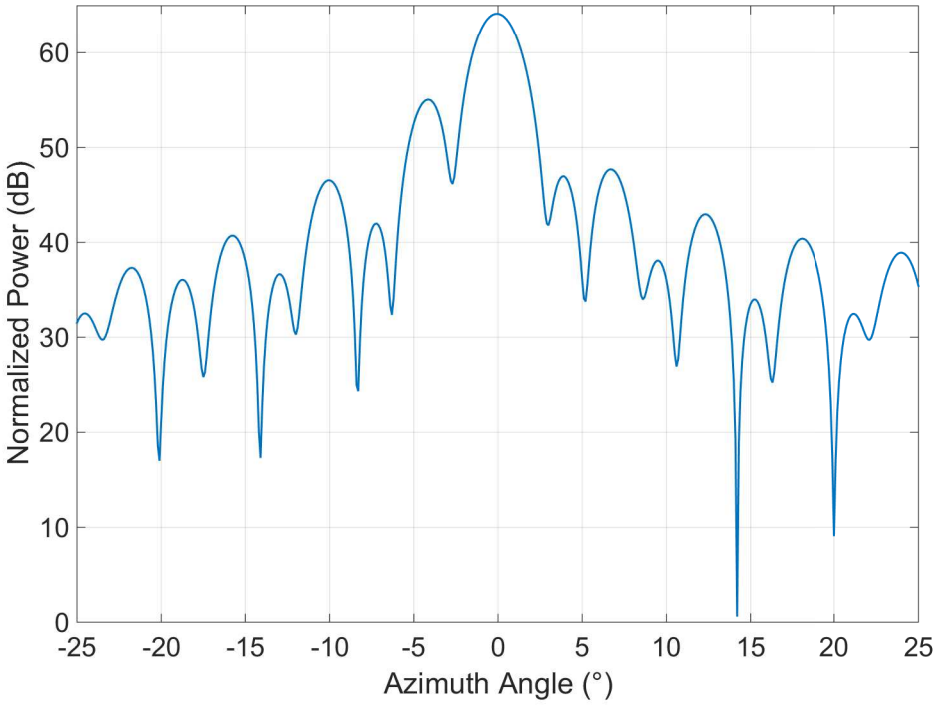

FIGURE 3.45: dB - Azimuth, angular section view of the 3D radar image capture of the target at 14 m and $\theta = 0°$.

3.6 Comparison with the State of the Art

A comparative research has been performed on the demonstrator structure and performance of other imaging radars already published. The results are presented in Table 3.2. To the best of my knowledge, there is currently only one device capable of generating a 3D image out of a 2D MIMO array configuration, described in [123]. Because of insufficient data presented in the papers analyzed regarding the target's RCS, it is difficult to extract a correct range information. Therefore, the devices are analyzed according to their ability to operate in short and medium range applications. From the first column of the table, it can be seen that it is intended for short range capturing, as observed from the high range and angular resolution but limited maximum range of the device of 1.5 m. Furthermore, limited by its large size, it is not portable. The high performance of the 3D imaging proposed in this radar demonstrator, instead, can be seen in the last column of the table. This demonstrator is capable of operating in medium range radar scenarios, higher compared to the other 2D MIMO radar device analyzed in the table, nevertheless still maintaining a relatively high angular and range resolution of 2.9° and 0.5 m, respectively, thanks to its 1 GHz bandwidth. Moreover, a comparison study has been made considering the size of the devices. Considering medium sized portable devices, the radar demonstrator here proposed is the best in terms of resolutions. Additionally, the possibility of other devices of being modular and flexibly changeable in terms of MIMO array configuration has been investigated. The result is that there are currently no other 3D MIMO FMCW radar which have the capability of being modular.

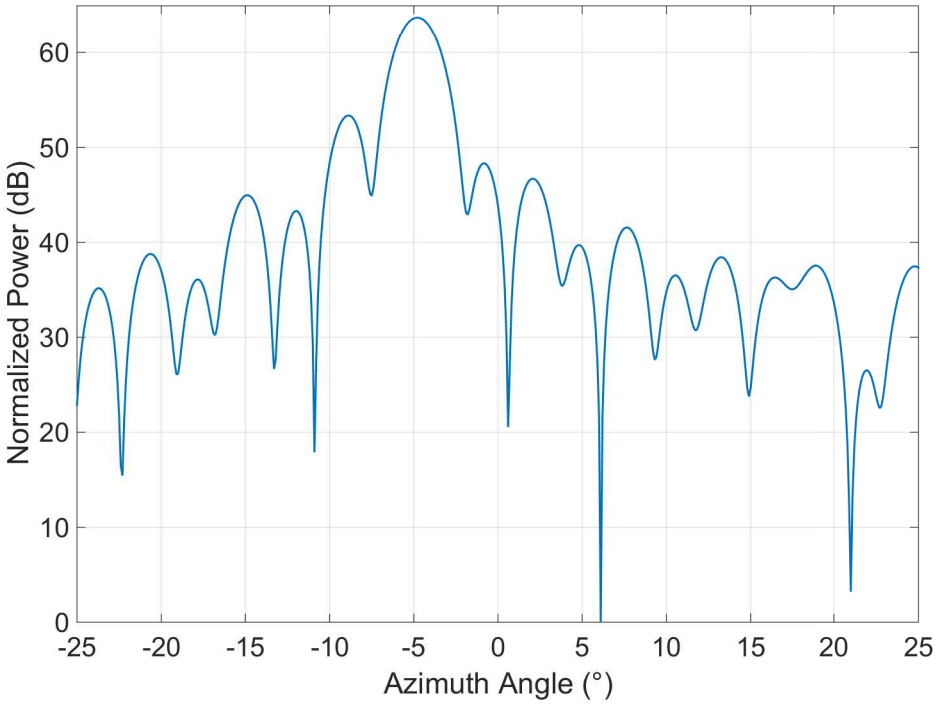

FIGURE 3.46: dB - Azimuth, angular section view of the 3D radar image capture of the target at 18.5 m and $\theta = -4°$.

TABLE 3.2: Structure and Performance Comparison of Different Imaging Radars.

	[123]	[118]	[125]	[126]	[127]	This Work
MIMO Array	YES	YES	YES	YES	YES	YES
2D MIMO Array	YES	NO	NO	NO	NO	YES
Freq. Ini. [GHz]	72	9.15	18	8.95	24	16
Freq. Fin. [GHz]	80	9.35	19	9.95	25	17
Bandwidth [GHz]	8	0.1	0.75	1	1	1
Max. Range	Short	Med.	Med.	Med.	Med.	Med.
Range Res. [m]	0.02	1.5	0.2	0.15	0.15	0.5
Angular Res. [°]	2.3	1.8	0.06	0.45	3	2.9
Modular	NO	NO	NO	NO	NO	YES
Size	Large	Med.	Large	Med.	Med.	Med.

3.7 Chapter's Conclusions

An innovative and successful implementation of a complete 3D imaging MIMO radar based on a 24x24 array architecture has been presented. The radar operates with a working frequency range between 16 GHz and 17 GHz and FMCW signals with 1GHz of bandwidth. The individual transmit signals are separated at the receiver using TDM and are digitally processed in hardware before applying the radar processing algorithms

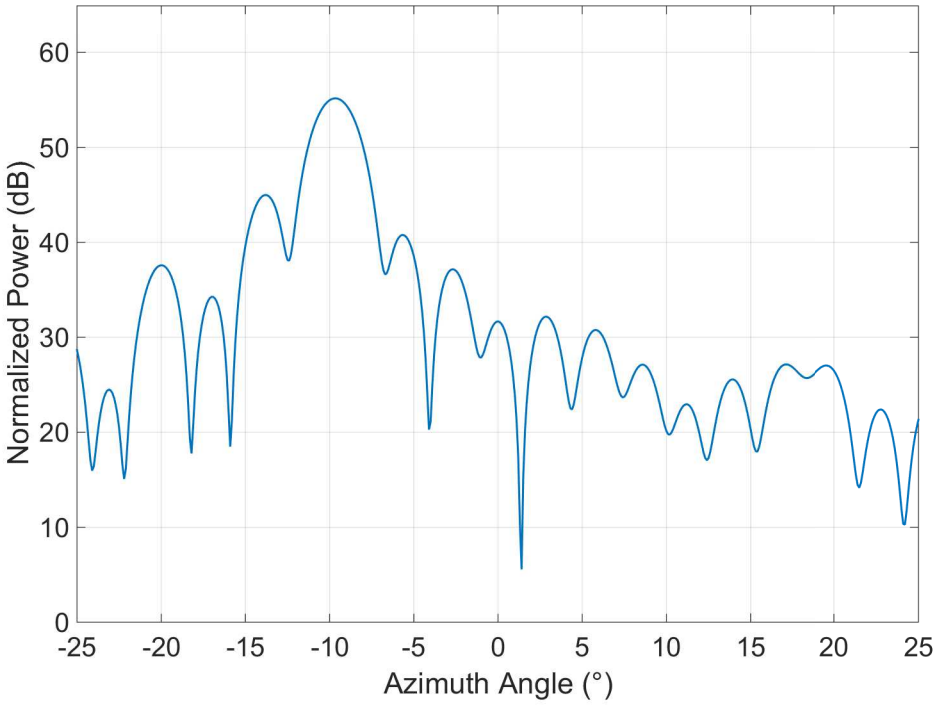

FIGURE 3.47: dB - Azimuth, angular section view of the 3D radar image capture of the target at 22 m and $\theta = -9°$.

that generate the 3D radar images by means of digital beamforming techniques. A complete radar image can be generated in around 11 s, with the current configuration.
Furthermore, the demonstrator has been designed to be compact and portable by including its own power unit and cooling system. Since the radar system is intended to be flexible, a modular approach based on conventional low cost PCB is used for the transmit and receive boards. This modular approach is based on RF multilayer panels with integrated antennas, that are easily stackable in a sandwich configuration which grants the possibility to vary the number of antennas by removing or adding panels. This gives the ability to vary the angular resolution and the size of the radar.
In the proposed demonstrator, measurements of the components in both the TX and RX boards have been performed in order to ensure the proper operation of the system. Additionally, measurements of the coupling and its overall effect on system performance have been analyzed with satisfactory outcomes. Moreover, calibration, timing and performance analysis on the overall radar performance, especially regarding its separation capabilities for both, angle and range, have been carried out. Several resulting 2D profiles, proving the high resolution of the reconstructed images, have been presented. Based on the shown results, it can be seen that the full advantages brought by the use of a MIMO architecture have been achieved so far, which can be summarized as follows: reduced number of antenna elements and simpler RF distribution structure when compared to a conventional antenna array, compact design through high integration, in particular without complicated mechanics for beam steering and artificially enlarged aperture and thus, improved cross-resolution synthetic image generation.

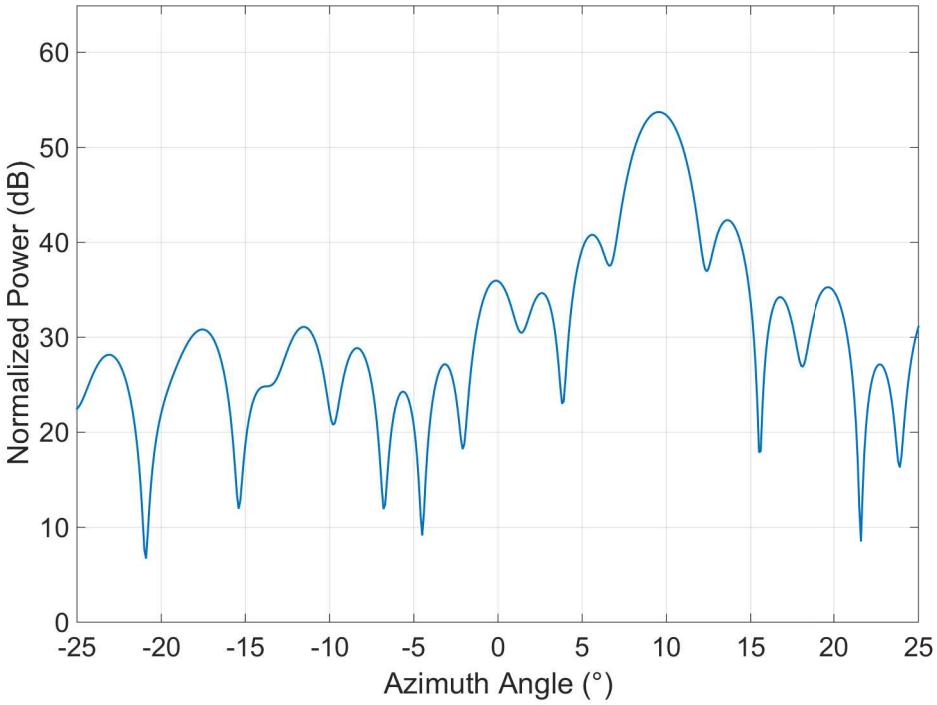

FIGURE 3.48: dB - Azimuth, angular section view of the 3D radar image capture of the target at 24 m and $\theta = 8°$.

3.7.1 Improvements

Considering the achieved results, it can be understood that the radar demonstrator here presented, is well suited in targeting applications, such as, the ground based surveillance of stationary wide-zones and high security or hazardous infrastructures. The portability and compact size factor aid in this, allowing the radar to be easily and flexibly moved. The 24 channel, three-board FPGA based digital architecture, in conjunction with the MPC8640D based dual-core processor board, allows to easily process raw radar data, digitize it and transfer it to the software for the radar image processing. Additionally, the results from the radar digital signal processing and the delay and sum beam-forming, show good resolution and overall image reconstruction performance. The timing from capturing of a radar's scenario to the generation of a radar image, is in total around 11 s, which does not allow the capturing of scenarios in the presence of moving targets. The main bottleneck of the system is the transferring of raw data through Ethernet to a binary file, which is consequently read into the radar beam-forming scripts. Additionally, the beam-forming is based on a delay and sum beam-former. All these aspects can be improved.

A study on this radar demonstrator, allowed to research the stages where improvements could be made, in order to address applications which require an even more compact and faster device, such as those linked to the detection of targets in flying platforms. Especially important, is the achievement of a system able to sense a complete 3D information of range, Azimuth and elevation of targets, even when these are moving.

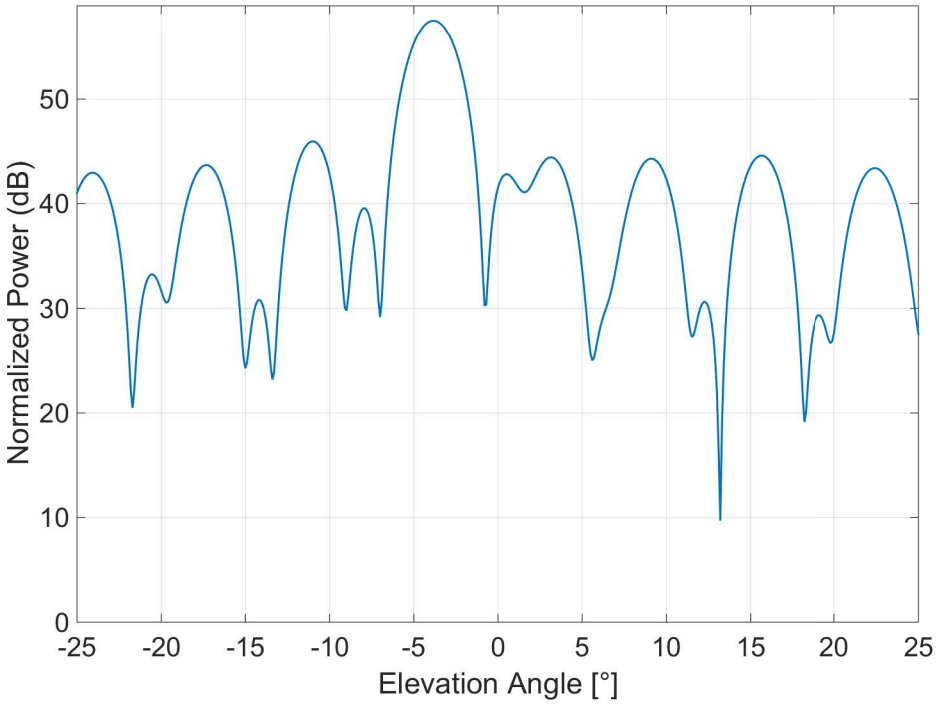

FIGURE 3.49: dB - elevation, angular section view of the 3D radar image capture of the target at 14 m and $\phi = -3°$.

The ideas conceptualized into a reduction of the size factor of both the RF frontend, obtaining a single board with TX and RX antennas integrated, and the digital hardware architecture, obtaining a single board as well, which integrates a powerful ZYNQ based proprietary platform with all the ADCs. Furthermore, an implementation of a faster 3D-FFT based beam-forming processing is also achieved. These concepts will be seen in the next chapter.

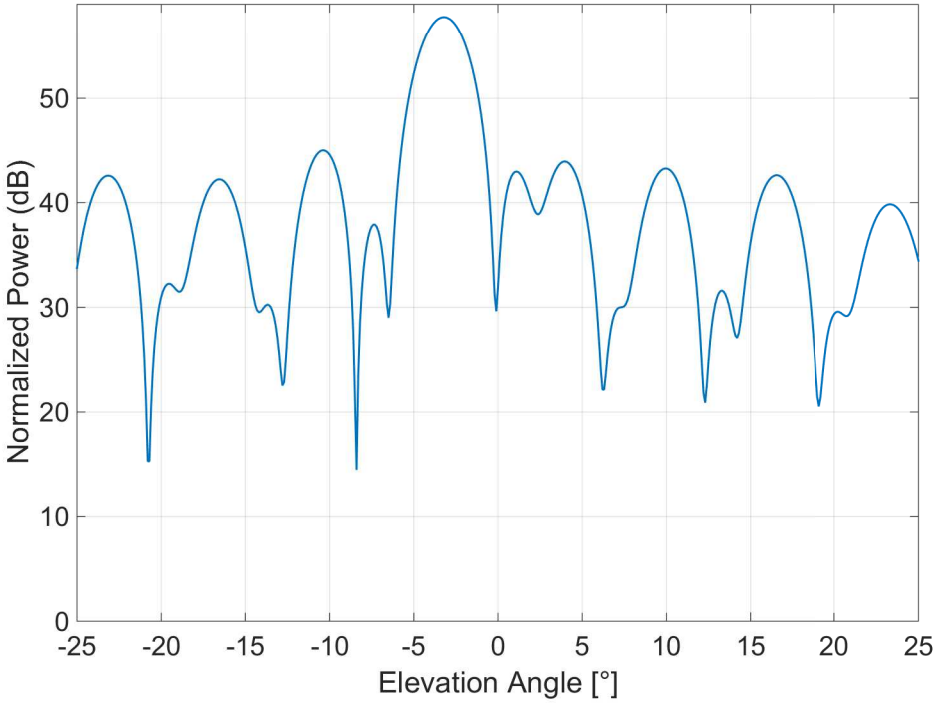

FIGURE 3.50: dB - elevation, angular section view of the 3D radar image capture of the target at 18.5 m and $\phi = -3°$.

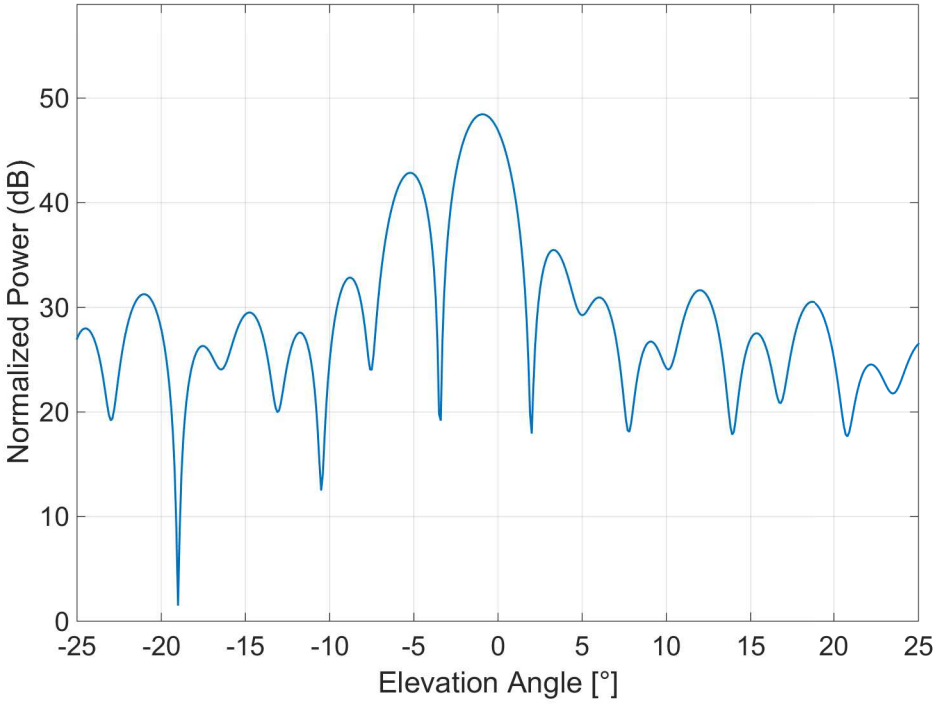

FIGURE 3.51: dB - elevation, angular section view of the 3D radar image capture of the target at 22 m and $\phi = -1°$.

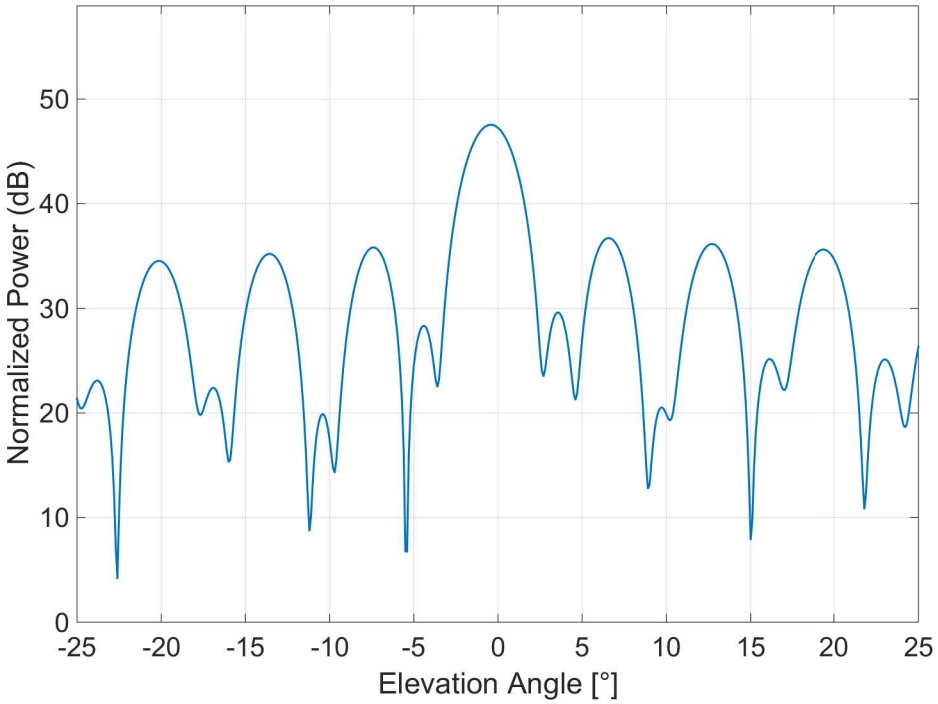

FIGURE 3.52: dB - elevation, angular section view of the 3D radar image capture of the target at 24 m and $\phi = -1°$.

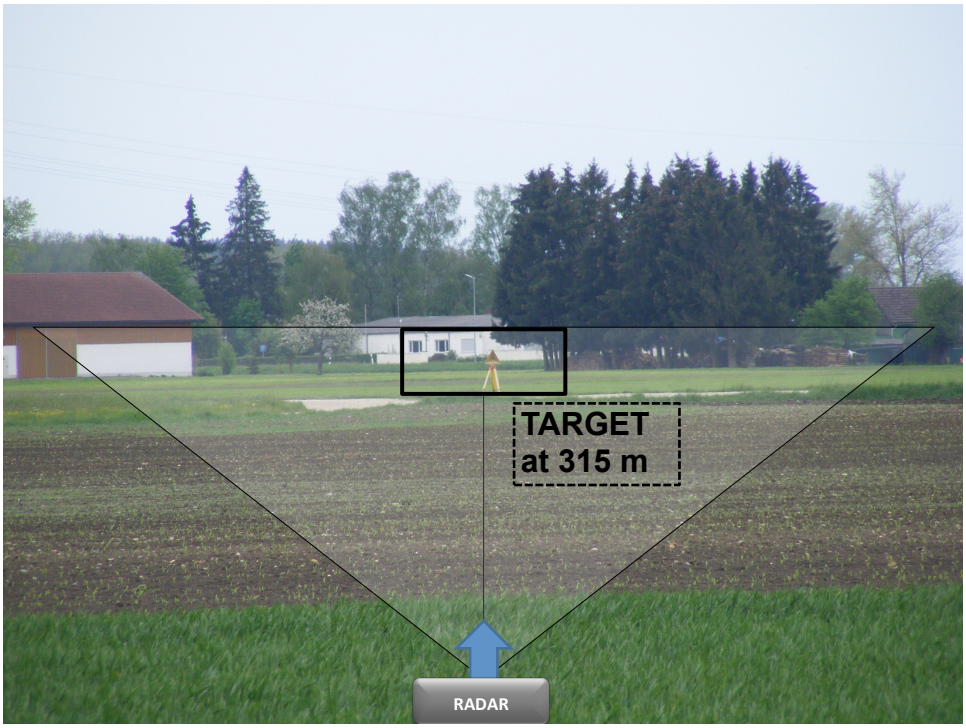

FIGURE 3.53: The MIMO radar test field with one corner reflector at ranges of 315 m, with nominal radar cross section of 36 m^2.

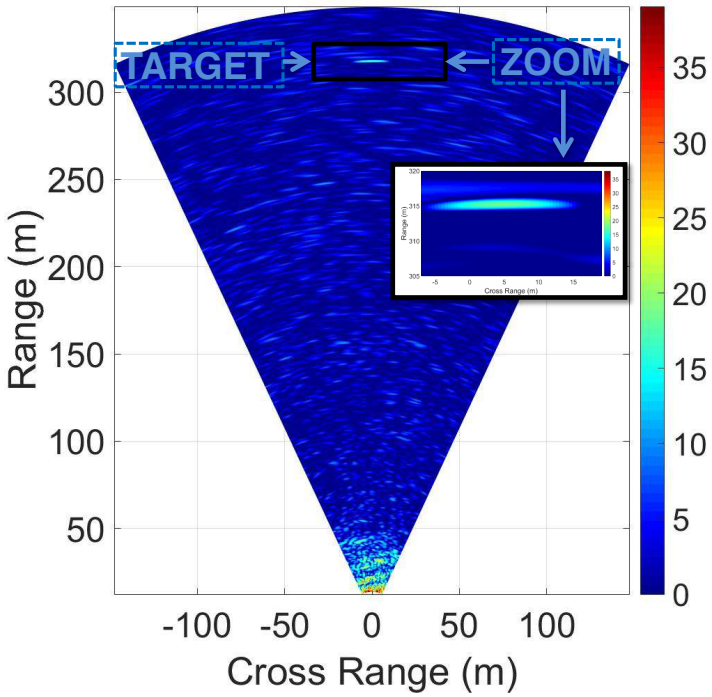

FIGURE 3.54: Range-Azimuth section view of the 3D radar image capture, with 1 corner reflector visible at 315 meters.

Chapter 4

Multifunctional and Compact 3D Imaging FMCW MIMO Radar Demonstrator with 16x16 Antenna Array

4.1 Chapter's Introduction

The previous chapter presented a successful implementation of a complete 3D imaging MIMO radar demonstrator, based on the transmit of FMCW signals from 16 GHz to 17 GHz with 1 GHz of bandwidth, multi-stacked PCB RF front-end, a TDM architecture, three FPGA boards plus a PowerPC enabled digital processing with a delay and sum beam-forming image generation.
In this chapter, a new MIMO radar system [140], result of a miniaturization and overall improvement in all aspects of the previous demonstrator, from the RF front-end, to the digital architecture and radar processing algorithms, is presented.
The idea is to obtain a system which can address applications linked, not only to the ground-based surveillance of stationary wide-zones and infrastructures, but also to the situational awareness and detection of targets in flying platforms, UAVs and helicopters. Therefore, the device has to be even more compact and have a faster and more performant radar processing. Especially important, is the implementation of a system able to detect targets even in moving environments and platforms and even when the targets themselves are moving, while still obtaining a complete 3D estimation of range, Azimuth and elevation of the targets. This leads to the development of a different architecture which is a first step towards the creation of a MIMO radar able to operate in an almost real-time manner, while still maintaining a small overall system cost and low hardware effort.
Moreover, an approach to combine an FMCW MIMO radar system with additional sensors and/or actuators, like a camera or a tracking system, introducing multiple functions, which are integrated in a single system, is also studied and analyzed. Therefore, the

term "multifunctional" is used throughout this chapter, in order to address the fact that the system is able to perform more than just radar sensing.
The first step, is the achievement of a much smaller RF front-end, with a smarter antenna array configuration. Instead of multi-stacked PCBs and a modular approach, in the MIMO system presented in this chapter, a single planar PCB is used, which integrates 16 TX and 16 RX antennas, together with all the circuitry needed, from the amplifiers to the filters and mixers. The antennas used in the system presented in Chapter 3, were TSA, which have now been replaced by narrow band patch antennas. A rectangular MIMO array with two rows of TX antennas and two rows of RX antennas, which are placed opposite to each other, offers an empty space in the center. This allows to integrate additional devices in the unused space, like a camera or a tracking system. Furthermore, a metallic 3D printed housing, which accomplishes also the task of cooling the electronics, has been built and assembled. Similarly to the previously presented MIMO radar system of Chapter 3, the orthogonality of the TX signals is obtained through TDM and the radar sensor working frequency range spans between 16 GHz and 17 GHz, using FMCW signals with 1 GHz bandwidth.
Additionally, a lot of research effort concretized into an achievement of a much faster digital architecture and signal processing, with yields a better performance. This is achieved due to the implementation of a new proprietary digital board, which integrates a lot of different functions, into a single device.
The board is based on a Xilinx ZYNQ Z-7045 SoC, a chip comprising two ARM CPU cores and FPGA fabric compatible to a Xilinx Kintex-7 FPGA [141]. Additionally, it is equipped with 16 ADC channels for the acquisition of the received radar signals. This SoC approach gives some degree of freedom to implement parts of the signal processing routines in hardware using the FPGA fabric and other parts in software using the ARM cores, as this way the computation of the radar data stream and the radar processing can be shared between domains.
An additional aspect where the system differs from the predecessor, is the new beamforming and radar image processing. The system operates with a new 3D FFT based beam-forming at the RX side, which enables to capture radar images with a faster refresh rate, thus opening up the demonstrator to a multitude of additional radar applications, with moving scenarios or targets. The targeted applications are in accordance to the ones required by both the European project "ZONeSEC" and the German project "FAST", for which part of the research has been focused to.

For this multifunctional system, a detailed descriptions of the hardware and software architecture, measurements, performance and resolution's analysis, and 3D radar images are presented in this chapter.
The MIMO radar demonstrator is tested and analysed in several scenarios. In an anechoic chamber and in outdoor test fields, for the detection of targets, both static and moving, represented by corner reflectors, UAVs and people.
Additionally, to show the advantages of a second functionality, the MIMO radar system is combined with a camera and a gimbal for target tracking. The imaging capabilities of the radar, integrated with the camera imaging capabilities, are presented for an outdoor test comprising trees and hills.
Moreover, specific algorithms are proposed for the detection and tracking of moving

targets, and the target tracking capabilities of the system are analyzed. The detection is performed in the presence of UAVs and people.
Finally, a scenario where a jamming system, based on the MIMO radar demonstrator here discussed, is used against small UAVs, is also shown.

4.2 State of the Art and Applications

Ever since the era of autonomous systems started, multi-sensor platforms have become a key topic in aerospace, automotive and robotics industries. Multifunctional systems integrate more than one sensor and/or actuator in one device and are capable of creating synergies between them. As a consequence, their performance is superior compared to single-sensor systems, for different reasons [142] [143] [144].

First of all, these systems can capture, process and merge information from different perspectives that can complement each other. Second, a more compact approach is possible, because the hardware required for additional functionalities can be integrated in unoccupied spaces of the main system. Third, a reduction of the costs is possible in a multifunctional architecture, since part of the hardware can be shared. For instance, the signal processing unit (ARM and FPGA) or the power supply unit. Sharing hardware components can also lead to a reduction in both power consumption and weight. To summarize, Size, Weight and Power (SWaP) optimization can be achieved with a proper design of a multifunctional system. This is of vital importance and highly profitable for many applications.

One of the most popular sensors technologies is radar [110], due to its all-weather capabilities, its ability to penetrate material and to provide a 3D sensing of range, azimuth and elevation. A radar sensor can be combined with additional functionalities, depending on the task, for example: a light source (torch or laser pointer), a weapon, antennas for communication and a (thermo-) camera. The system demonstrator that is here described, combines a MIMO radar [118], and a camera mounted on a gimbal. This combination of sensors can ease the task of change detection and classification of targets [145] [146].

Some work has already been done in this field. For example, a 2D FMCW [147] MIMO radar combined with a camera is presented in [148]. In this architecture, the camera and the radar are not integrated into one single system. It is rather multiple systems operating together than one multifunctional system. Furthermore, the used radar sensor is not able to generate elevation information. In addition, the presented device is bulky and not portable, which is highly required for the targeted application. Another approach is shown in [149]. Here, the system is intended for indoor use and short range applications. Like the previous system, it cannot estimate the elevation of the target. Nevertheless, an increase in tracking performance is shown by the combination of radar and camera capabilities through data fusion. Another system which deals with the advantages of having a radar and a camera for object classification is presented in [145]. This system,

as well as the others, does not create a full 3D reconstruction of the observed scene. Moreover, the chosen camera has a low resolution, which can be appropriate in an automotive context, but not for medium range applications. The advantages of having a multifunctional system in a naval environment are well described in [150].

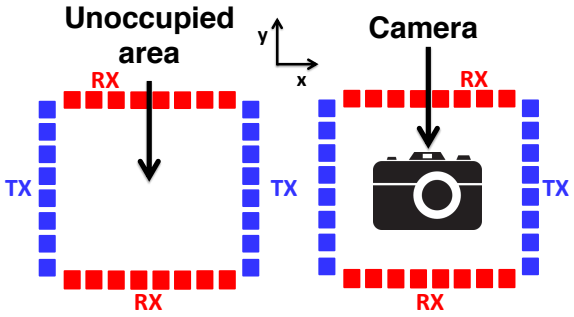

FIGURE 4.1: Visualization of a rectangular MIMO array with unoccupied space in the center (left) and a camera (right).

The 3D FMCW MIMO radar here presented, as anticipated, is integrated with a camera and a two axis gimbal, placed in the center of the MIMO array. For a determined number of TX and RX modules, a MIMO radar offers a higher angular resolution compared to a conventional phased array radar [80]. Consequently, it is smaller, lighter and costs less. The MIMO architecture uses the spatial separation of the antennas to create a so called virtual array, which can be calculated via a discrete convolution [81]. The size of the resulting virtual array, and not the physical array, determines the angular resolution of the MIMO radar system. If the TX and RX antennas of the array are placed in a rectangular configuration, the center of the antenna aperture is unoccupied. This area is used to place the camera and the gimbal, as illustrated in Fig. 4.1. With the gimbal it is possible to steer the camera to the target detected by the radar. The same procedures can be easily adapted and extended to a configuration where a gimbal is used for target detection and jamming, instead, as it will be shown later in the chapter.

4.3 The System's Architecture

The top-level system architecture of the MIMO radar demonstrator is presented in the form of a block diagram in Fig. 4.2. The main components are the antenna board, the digital board, the DDS board, the receiver, the laptop and the camera. The modular approach of the 3D printed housing, easily allows to add and change hardware components. The following part describes the block diagram and explains how the system works.

From the laptop, the DDS board and hence the PLL can be configured to create the desired FMCW chirp. The most important parameters are the chirp length in time and the bandwidth. The chirp is then transmitted to the antenna board, where it is distributed to two switch chains and the receiver board using a 3-way Wilkinson divider, as it can be seen in Fig. 4.3. For the measurements carried with the proposed radar demonstrator, an FMCW signal with a duration of $t_{chirp} = 100\ \mu$s, has been selected.

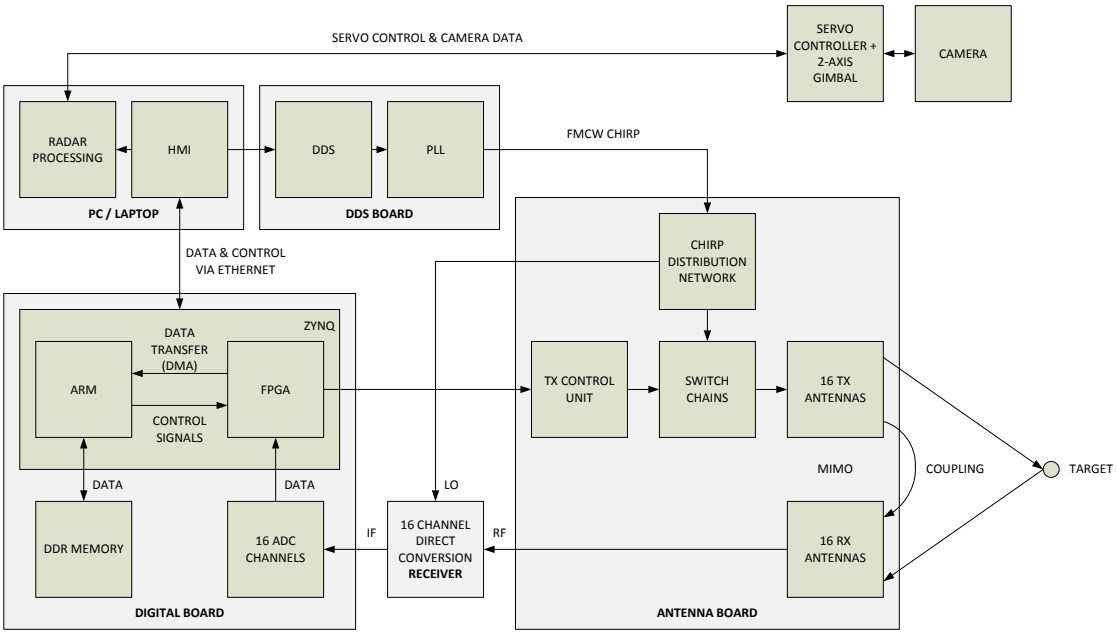

FIGURE 4.2: Block diagram of the 3D imaging FMCW 16x16 MIMO radar demonstrator. The main components are the antenna board, the digital board, the DDS board, the receiver, the laptop and the camera.

First, each switch chain can select between eight TX antennas or a matched load, enabling a TDM configuration and thus orthogonality of the signals. This means that all TX antennas are switched consecutively within one MIMO cycle. Second, the receiver uses the originally sent chirp as LO signal to down-convert the 16 received delayed chirps. This way, the beat frequencies (associated with the range information) of the target can be extracted.

A proprietary ZYNQ based platform, which includes an FPGA and an ARM processor, serves as the interface between the ADC and the laptop performing the acquisition of digital data. The resulting signals are digitized by 16 ADC, which are interfaced to the FPGA. The sampling frequency of the ADCs is $f_s = 100$ MHz.

The data is first stored in the FPGA and then transferred to the DDR memory of the system via DMA. From the digital board, the data is transferred to the laptop via Ethernet. The whole process of the data capturing is triggered by the HMI. Once started, the TX control unit is commanded by the ZYNQ which runs a program on the ARM processor. The TX control unit sets the proper bit combination for the switch matrices in order to select the TX antenna.

The radar processing is carried out on the laptop, where FFT based digital beamforming techniques are applied in order to extract the target position in range, Azimuth and elevation. Consequently, the target position is sent to the servo controller, which creates the steering signals for a two axis gimbal, where the (zoom-) camera, or the antenna, is mounted. The camera can then take a close-up picture or video of the target and send it back to the HMI. The image can then be possibly used to classify the target or to do further image processing. If an antenna is chosen, instead, it can be used to send jamming signals towards a UAV.

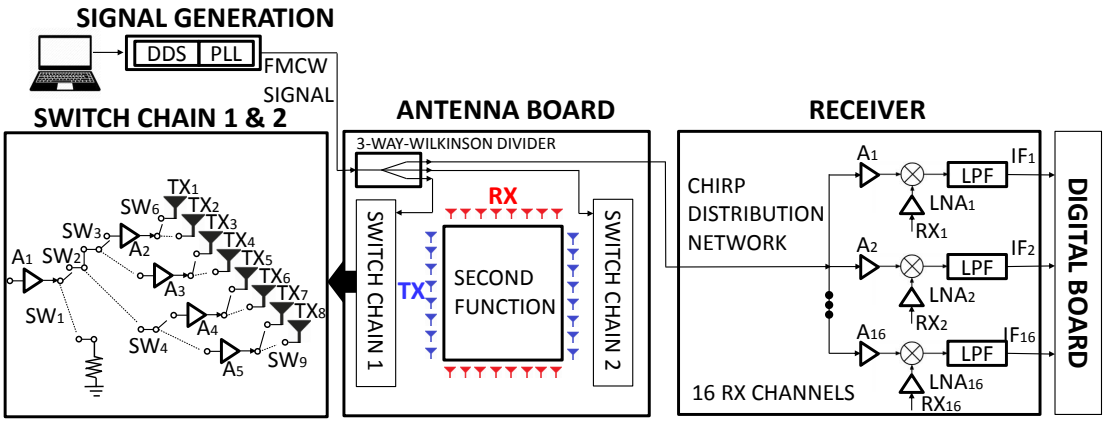

FIGURE 4.3: Component level block diagrams of the antenna board and the receiver with schematic of the switch chains.

4.4 The RF Front-end

This section introduces the main blocks of the radar's hardware including the antenna board and the receiver board. The circuit level block diagrams are shown in Fig. 4.3.

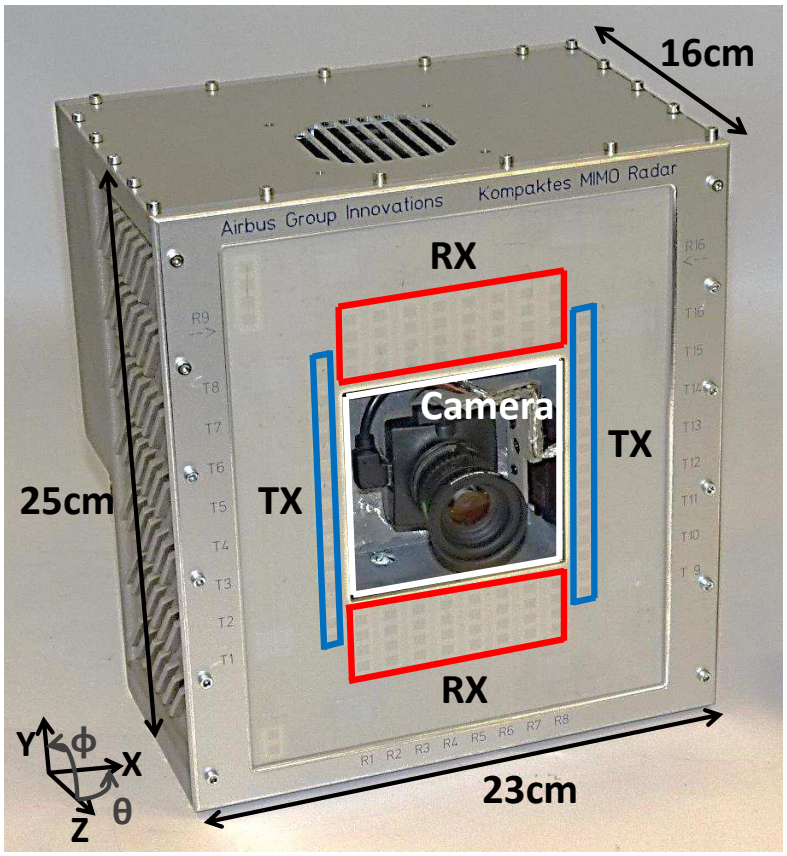

FIGURE 4.4: Picture of the 3D printed housing with antenna board and camera mounted in the middle. The markers show where the TX and RX antennas, and the camera are placed.

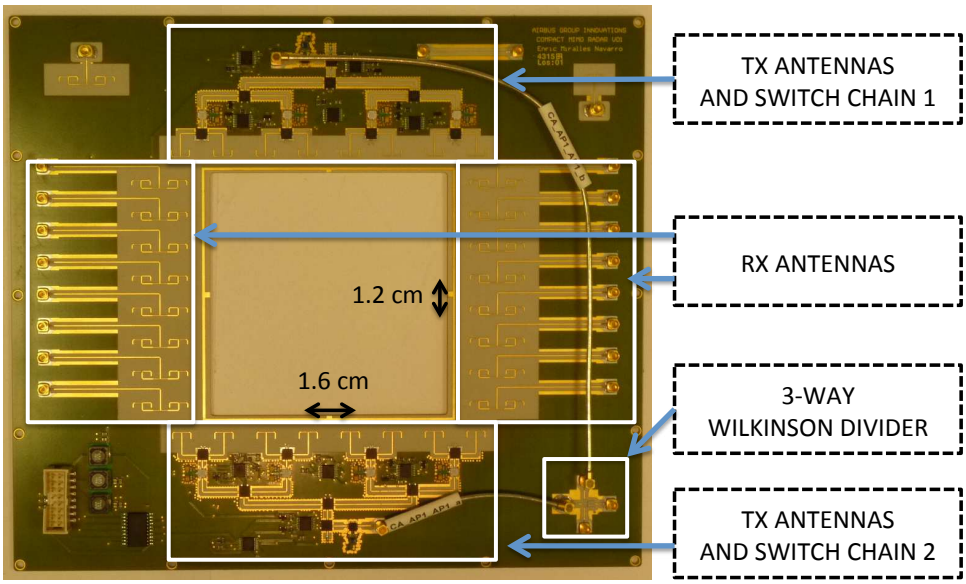

FIGURE 4.5: Picture of the back of the RF front-end antenna board, with 16 TX and 16 RX antenna elements, switch matrixes and a 3-way wilkinson divider.

As shown in Fig. 4.5 [151], the antenna board includes in a single planar PCB, 32 radiating elements, 16 for transmit TX (in blue) and 16 for receive RX (in red). The TX antenna element is a 2 patch array, whereas the RX antenna element, is 4 patch array [152]. The distance between each TX antenna and each RX antenna element, is 16 mm and 12 mm, respectively. In this manner, 8 TX element fit in a row and 8 RX elements plus 2 TX elements fit in a column covering 160×120 mm for the antennas. The antennas are placed in a rectangular configuration, in such a manner, that an unoccupied surface at the center of the array arises. In order to achieve the desired operational bandwidth and the desired range resolution, RSPA instead of traditional patch antennas are incorporated [153]. As it can be seen from Fig. 4.5, a three way Wilkinson divider is present. This equally distributes the FMCW ramp, that is generated by the DDS and PLL, to the two independent switch chains and the receiver. The two switch chains are able to select the proper antenna at the right time or to lead the signal to a terminated port (50 Ω resistor) in order to accomplish a orthogonality of the received data streams under a TDM paradigm. A more detailed description of the antenna board can be found in [151].

The receiver board consists of 16 direct-conversion receivers. A picture of the receiver board can be seen in Fig. 4.6. A common input to all 16 paths, comes from the LO signal input port, where the FMCW chirp signal is fed, created from the DSS and PLL unit. As it can be seen, an FMCW chirp signal distribution network splits up the chirp signal and distributes it coherently to all 16 stages. Each stage has its own amplifier in order to drive the LO input port of the mixer. The RX signals, fed via 16 MiniSMP input jacks [154], are amplified by the LNA and then fed to the mixers, for the de-ramping and generation of the IF signals. The FMCW de-ramping technique has been previously described in Chapter 2.5. Therefore, the RX signal are mixed with the originally sent FMCW chirp and low-pass filtered. From the output of the receiver, the IF signals go

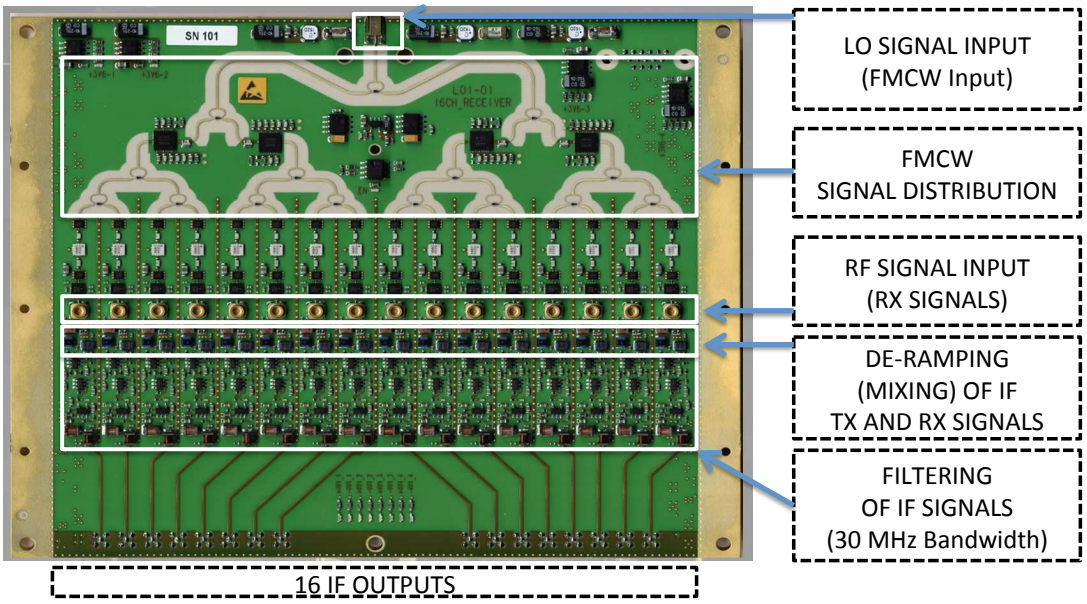

FIGURE 4.6: Picture of the receiver board, with the 16 channel paths to intermediate frequency (IF), with the FMCW signal distribution for de-ramping, the RX inputs, the mixers and the filters.

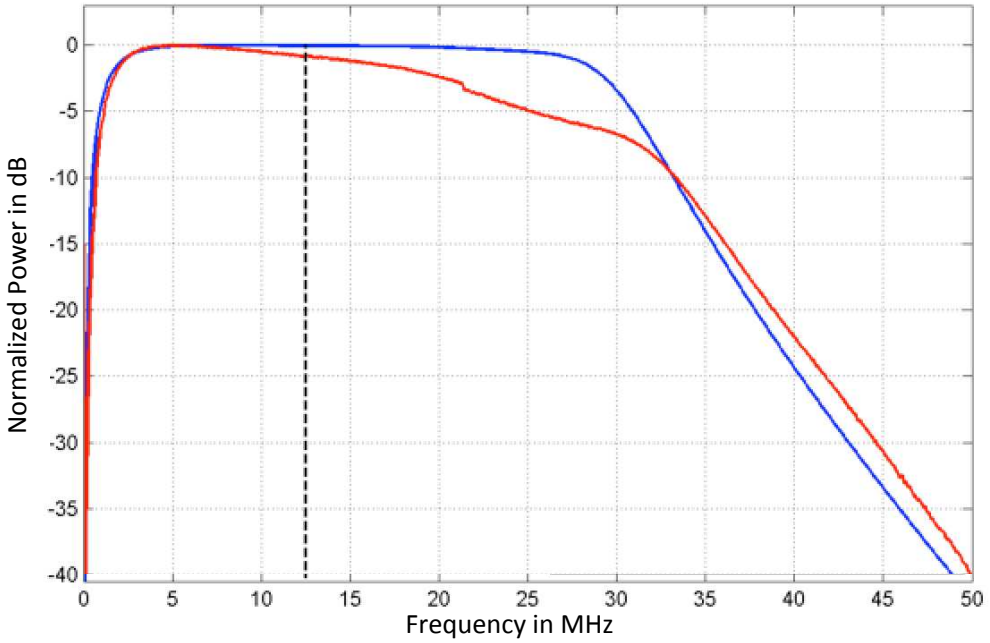

FIGURE 4.7: Frequency response of the receiver board.

directly to the 16 ADC input ports on the digital board.
The frequency response of the 16-channel RX board in the frequency range 0 . . . 50 MHz, is shown in Fig. 4.7. In this image, the blue curve shows a simulation and the red curve shows a measurement (exemplary for one channel). As it can be seen, the measured spectrum in the range 0 . . . 12.5 MHz is very close to the simulated waveform. For higher frequencies, however, the plot decreases, and an attenuation of about 4-5 dB can

be noticed, at about 25 MHz. However, this is not relevant because the maximum beat frequency is 12.5 MHz, for the current demonstrator and FMCW signal used.
Finally, for the radar system to be compact and multifunctional, a lightweight, robust and adaptable housing is needed. To fulfil these requirements, a special housing was designed and 3D printed in aluminium. Additionally to the protection of the components, the housing is used as a heat sink. All boards are thermally linked to the housing and two cooling channels which are connected to a fan enhance the heat dissipation of the system. Fig. 4.4 shows a photograph of the overall system with 3D printed housing. The boxes show the TX and RX elements, the camera and the two axis gimbal, which is mounted in the middle of the rectangular array. The size of the housing is 23 cm×25 cm×16 cm. On the top of the housing, the opening of the cooling system can be seen.

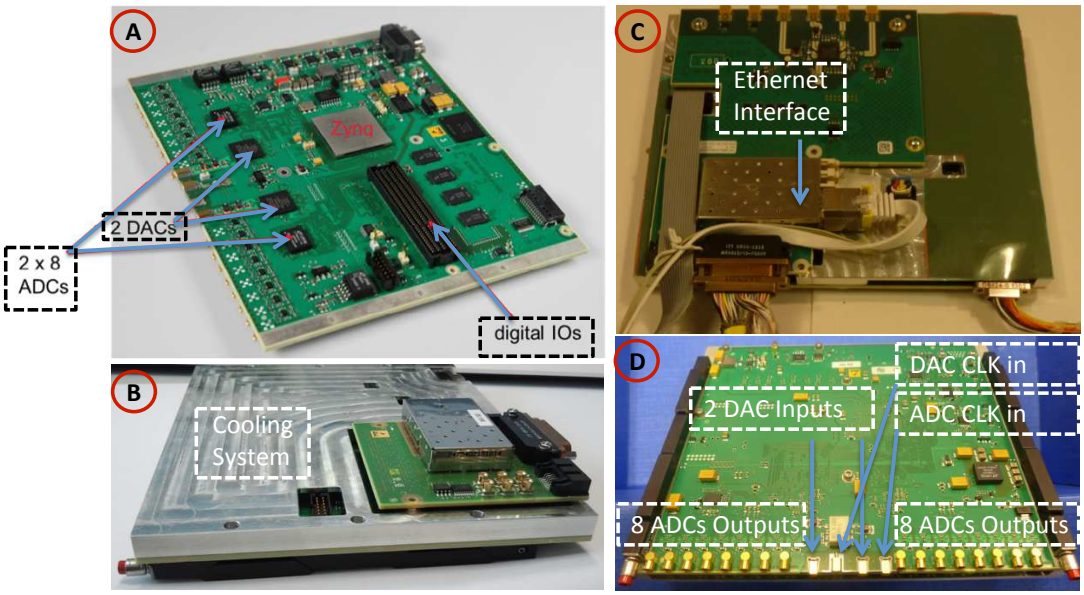

FIGURE 4.8: Pictures of the digital board, based on a ZYNQ SoC, with ARM and FPGA, and integrated ADCs.

4.5 The Digital System

One of the main elements of the Airbus' proprietary digital board, is the ZYNQ SoC, which integrates the software programmability of an ARM-based processor with the hardware programmability of an FPGA, enabling key hardware acceleration on a single device. Additionally, the digital board includes two LTM9011 8-channel 14-bit ADC elements running at 100 MHz [155], which yield a total 16 ADC inputs, and an Ethernet interface. Furthermore, the board provides two AD9129 14-bit DAC units [156], which are not necessary for the MIMO radar system here presented in this chapter. However, they are used for the generation of digital waveforms, as later described in this thesis, in Chapter 7. Pictures of the digital board are shown in Fig. 4.8. The ZYNQ unit is visible in subfigure A, together with the two ADC chips. In subfigure B, the cooling system, which is necessary to provide the cooling for all internal components, can be seen. The

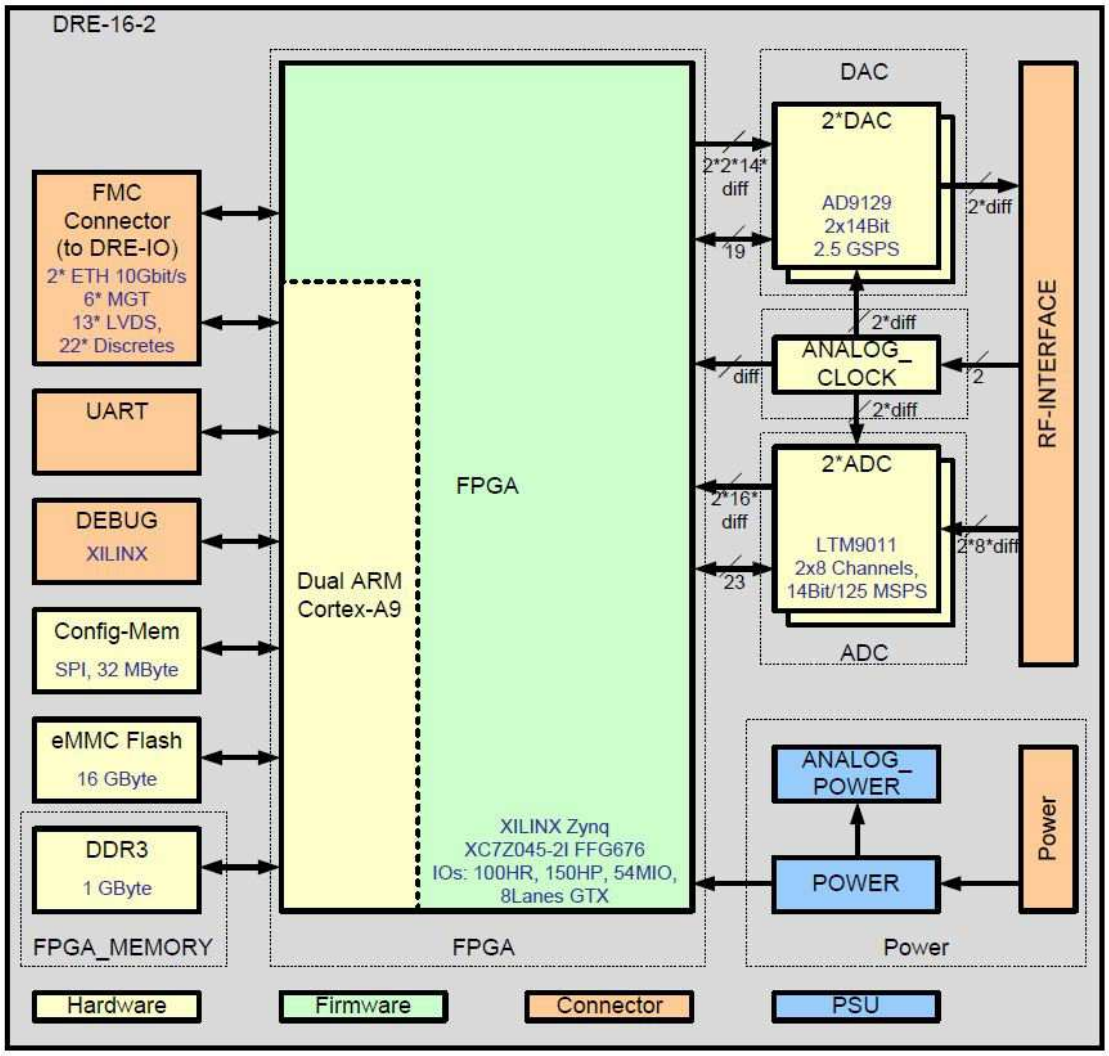

FIGURE 4.9: Schematic view of the main components and functionalities of the digital board.

Ethernet interface, is integrated in a Small Form-factor Pluggable (SFP) module, which is a compact, hot-pluggable transceiver, and it is shown in subfigure B and C. The 16 ADC inputs are shown, instead, in subfigure D, together with the ADC clock inputs. Additionally, in this subfigure, the 2 DAC outputs and the DAC clock input can also be seen. The 16 ADC input ports on the digital board, are directly connected to the 16 IF output ports of the receiver board, shown in Fig. 4.6. A 100 MHz reference clock signal is fed through the ADC clock in connector. This clock is generated using the DDS board, responsible for generating the FMCW signals and, additionally, providing a trigger for each start of the FMCW chirp. The connection is made with a female mini-SMP connector. The clock signal is necessary for the two ADCs, as it provides the sampling frequency of the ADC input channels. In addition, the FPGA is also dependent on the clock signal for synchronization purposes.
Finally, the digital board is equipped with a power connector, also shown in Fig. 4.8, subfigure C, to which two supply voltages must be applied within a tolerance range in order to initiate the boot process of the ZYNQ chip. The supply voltages are fed to the

board via a Micro-D power connector.

The internal architecture of the digital board is illustrated in Fig. 4.9. Additionally to the previously described components, it can be seen that the digital board integrates a Universal Asynchronous Receiver/Transmitter (UART) module, which is a computer hardware device for asynchronous serial communication, a serial peripheral interface bus, or SPI, communication capabilities, a 32 MB configurable memory, an embedded Multi-Media Controller (eMMC) with 16 GB of flash memory available, 1 GB of Dual Data Rate (DDR) memory, several debug interfaces, connectors and Power Supply Unit (PSU). The flash memory allows to have the FPGA firmware always inside the board, in order to load it at every boot of the system. However, the operating system for the ARM units is loaded at each boot of the system, from an FTP server, running on a PC or laptop, which provides always the most up to date version of the kernel drivers and user applications.

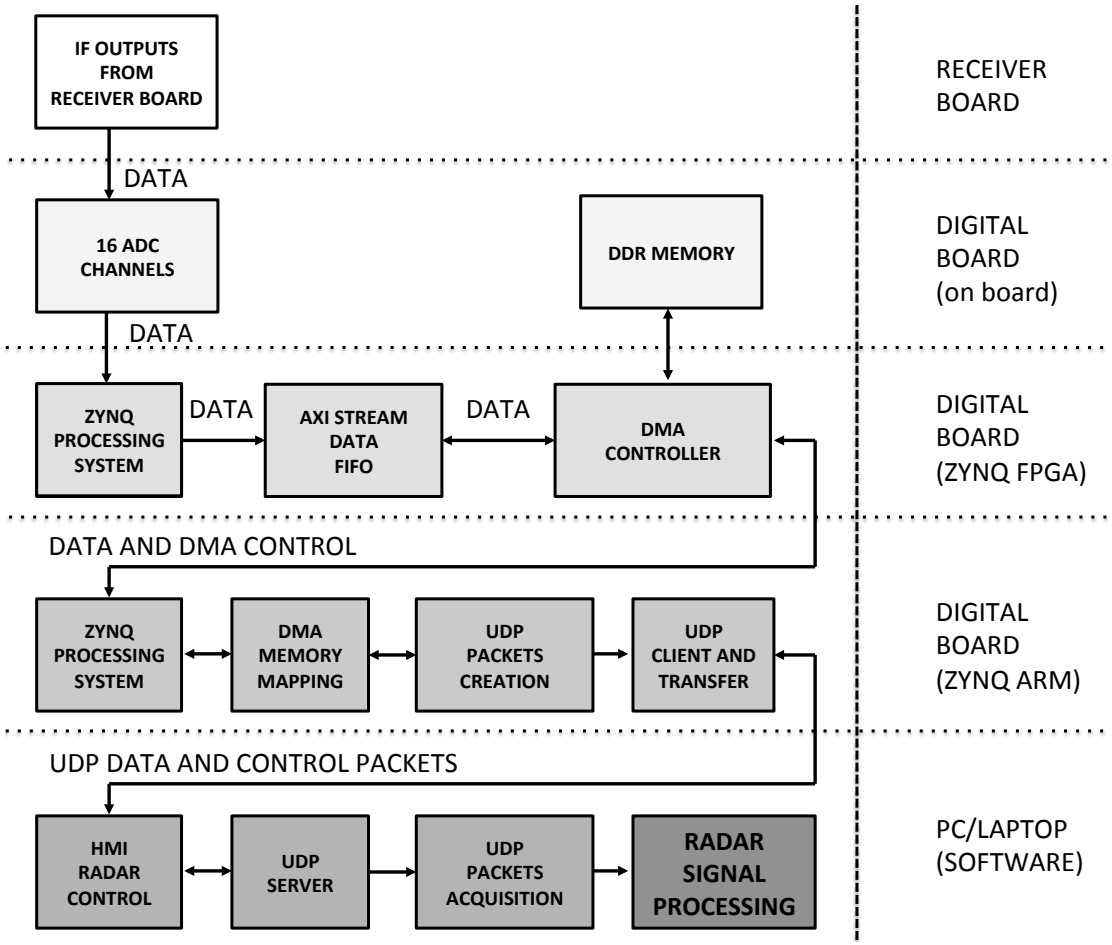

FIGURE 4.10: Schematic view of the digital architecture for the radar processing, from the sampling of the radar signals, to the radar image generation.

4.6 The Digital Architecture

A schematic view of the implemented digital architecture for the signal processing of the radar signals, from sampling to radar image generation, is presented in Fig. 4.10. As it can be seen, the complex architecture consists of several interfaces and domains, which are continuously crossed with a flow of both data and control signals. The architecture is a fusion between physical interfaces, VHDL firmware components, ARM drivers and applications, C code blocks and applications, MEX functions and MATLAB code programs.
From the HMI radar control interface, a user can start the processing of the radar signals. However, in order to understand how the radar data and control signals flow, throughout the design, it is important to start from the basic concepts of time domain multiplexing and data sampling.

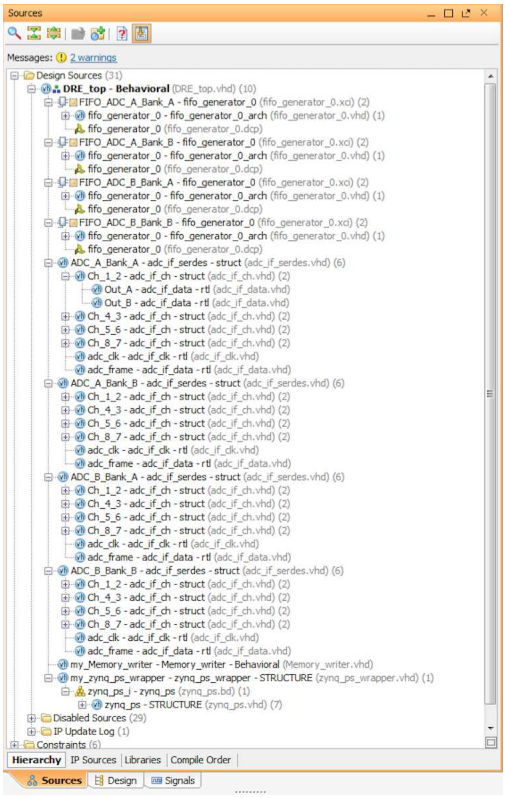

FIGURE 4.11: Picture from the Xilinx Vivado tool, depicting the main blocks implemented in the VHDL firmware for the radar processing.

4.6.1 The FPGA Processing

The first step is to establish an interface between the two LTM9011 ADC chips on the digital board and, therefore, with the 16 ADC inputs, which stream the radar signals data, sampled from the signals arriving from the receiver board. This, among other functionalities, is achieved in the implemented firmware for the ZYNQ board, as it can be seen from Fig. 4.11, which depicts the main components of the VHDL based firmware,

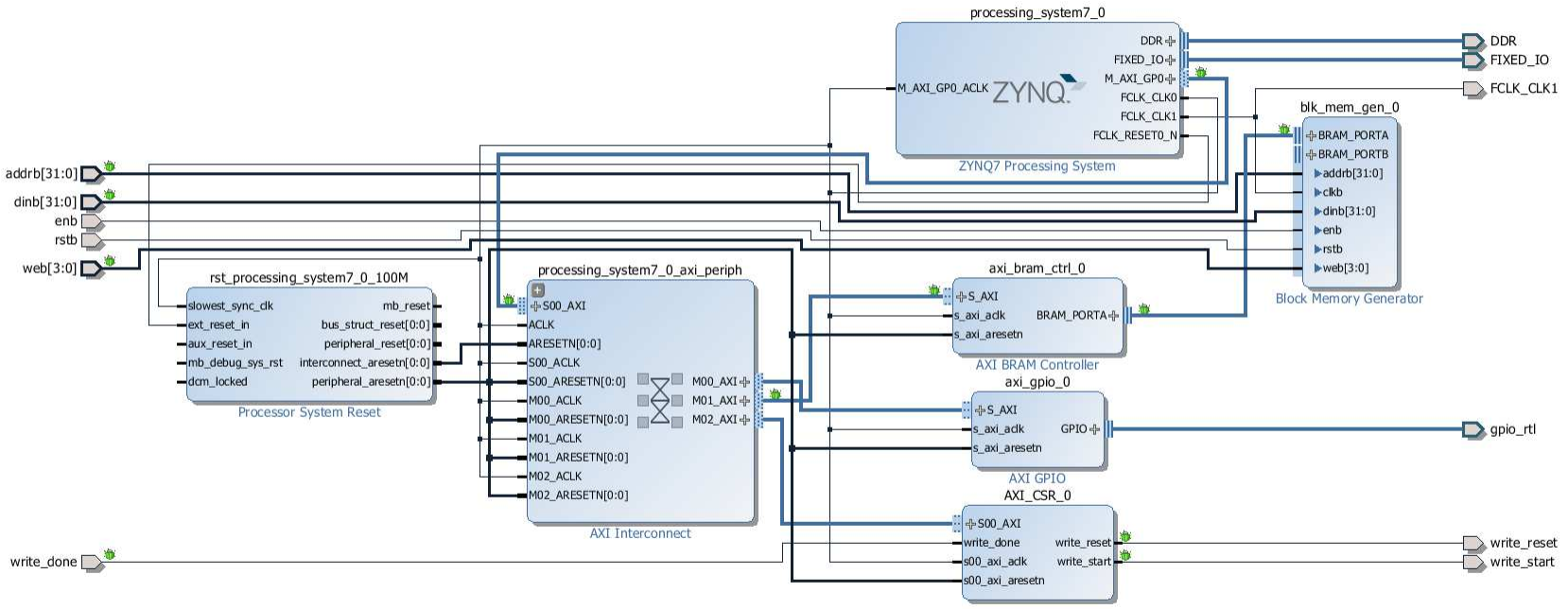

FIGURE 4.12: Schematic view of the VHDL firmware for the radar processing, implemented in the Xilinx Vivado tool.

and Fig. 4.12, which illustrates a schematic view of the complete firmware architecture, from a top level view. The main components which can be seen from these images are the ADCs, the FIFOs, the ZYNQ processing system, the RAMs and the AXI components and peripherals.
After initial setup of the ADC chips' interfaces and serial/deserializer operations, the 16 ADC channels are connected to LogiCORE IP AXI4-Stream FIFO cores [157], which allow a memory mapped access to a AXI4 stream interface. For the storing of the ADC samples, a Direct Memory Access (DMA) module is used [158]. A DMA unit allows the transferring of data from the ADCs to the external DDR memory. The AXI-lite bus [159], allows the ZYNQ processor to communicate with the AXI DMA controller to setup, initiate and monitor data transfers. This is done through master-to-slave (AXI_MM2S) and slave-to-master (AXI_S2MM) buses, which are memory-mapped AXI4 buses, which provide the DMA access to the DDR memory.
Therefore, the above mentioned operations allow to store the samples of the radar signals inside an external DDR memory, which is necessary due to the size of the transferred data, which would not, otherwise, fit inside the internal FPGA memory. This, also in consideration of the fact that the same procedures is repeated for each and every TX antenna, for a total of $N_{TX} \times N_{RX} = 256$ times, since there are 16 transmit and 16 receive antenna elements and a TDM scheme is adopted. As a matter of fact, once the radar capture is triggered from the HMI radar control program, as shown in Fig. 4.10, a first TX antenna is selected, from the FPGA, which initializes on a high levelled dedicated register value, which is connected with the switch matrixes from Fig. 4.3. The above mentioned operations are then inizialized and the data from the 16 receivers is transferred to the DDR memory. Consequently, a second value is set on that register, the second TX antenna is selected through assertion of the switch matrix and the operations are repeated, therefore, storing the additional data from the 16 receivers. This is repeated until the 16-th TX antenna has been reached. The content of 256 radar signals is, therefore, present inside the DDR memory and ready to be transferred to the ARM processor and, consequently, through an Ethernet interface to the PC.

4.6.2 The ARM Processing

The data is managed inside the ARM core, through the use of kernel drivers and user applications, which are written in *C* code, for a Linux operating system. As a matter of fact, the ARM core runs a light version of a Linux based operating system, provided by Xilinx directly through the PetaLinux Software Development Kit (SDK) [160], which is a Xilinx development tool that contains everything necessary to build, develop, test and deploy embedded Linux systems. The operating system is loaded at each boot, from a PC or laptop, through a Dropbear [161] based Secure File Transfer Protocol (SFTP) server interface. This allows to have always the most up to date version of the kernel drivers and user applications.
Two main functionalities which the ARM system is responsible for, are the reading of the data from the DDR memory and the transferring of the data, through User Datagram Protocall (UDP), to the PC or laptop, for further processing.

The reading of the data is achieved through a combination of a *mmapsystem* call [162], which allows the mapping of the DMA device memory directly into the user process's address space, a kernel *kiobuf* mechanism, which provides direct access to user memory from kernel space, and various DMA I/O operations. This allows to effectively access the 256 radar signals inside the DDR memory, from the Linux operating system.
Consequently, from another kernel based driver which acts as a UDP client, the DDR accessed data is read and encapsulated into UDP packets. After the creation of the socket, a binding is done with a socket opened on the same network, from a UDP server running on the PC, connected through Ethernet connection, which is listening for incoming UDP packets. Therefore, a series of send and receive operations between UDP server and client are initialized, in order to transfer the full content of the radar data stored in the DDR, through UDP packets, to the PC.
The whole procedure is repeated in the case that multiple measurements have been requested. In this case, the content of the DDR memory is transferred to the PC, an acknowledgment packet is received, the content is cleared, the FPGA and ARM routines are re-launched and a new transfer is initialized.

4.6.3 The Software Processing

The PC or laptop, has a MATLAB based radar processing program running at all times, which includes both the HMI radar control system and the UDP server, as shown in Fig. 4.10. The UDP server is implemented through the use of MATLAB executable (MEX) files [163], which are files that provide an interface between MATLAB and functions written in C, $C++$ or Fortran. The UDP server is, in fact, a program which has been implemented in C code and it is a dynamically linked subroutine that the MATLAB interpreter loads and executes. The main functions of the server are to send commands, through UDP packets, to the digital board, and also to receive the radar data which is sent from the UDP client running on the ARM unit.
The commands are given from the HMI radar control system, which can be the start or stop of the radar capture, which TX antennas to select and how many measurements to take. After the data has been completely received, an acknowledgment UDP packet is sent to the ARM unit, which redirects the signal to the FPGA. Everything is reset, all registers and memories, including the DDR memory, are cleared. In the case that multiple measurements have been selected, a new radar capture is initialized and a new transfer is done towards the PC, process which is repeated until all measurements have been correctly transferred.
Once the UDP server acquires the radar data, it saves it into a 3D radar data matrix, which has dimensions $N_{TX} \times N_{RX} \times N_{Samples}$, which correspond to the number of TX antennas, the number of RX antennas and the number of samples for each signal. This is repeated a number $N_{Measures}$ of times, corresponding to the number of measurements taken.
The 3D radar data matrix is then passed to the MATLAB based radar processing routines, which apply various signal processing and FFT based digital beam-forming procedures, in order to generate radar images of the captured scenario and targets.

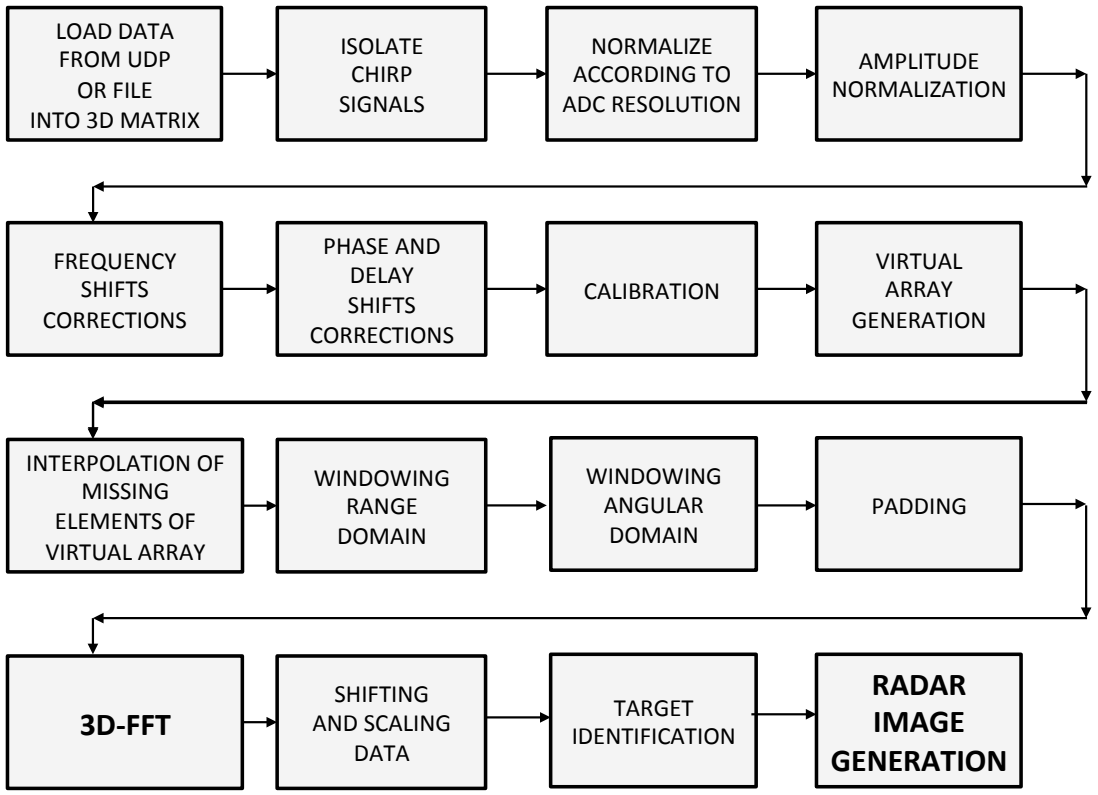

FIGURE 4.13: Radar digital signal processing software architecture, based on the 3D-FFT beam-forming.

4.6.4 The Radar Processing

The radar digital signal processing software architecture is illustrated in Fig. 4.13. A total of 256 signals are read from the UDP server, or optionally loaded from a previous file measurement, into a 3D matrix of 16 x 16 x 10000 elements, corresponding to the number of transmit antennas, the number of receive antennas and the total number of samples per signals, respectively. For each subset of transmit and receive elements (T_n, R_n), the 10000 samples represent the transmitted chirp signals from transmit antenna T_n and received at receive antenna R_n. The number of samples for one chirp is given by the chirp duration in time, $t_{chirp} = 100$ μs, multiplied by the sampling frequency, $f_s = 100$ MHz. As a first step, a filtering operation is conducted in order to extract only the information of one chirp signal, since at the beginning and at the end of the acquired samples, there could be unwanted or spurious components which can affect some of the samples. The samples are then normalized according to the ADC resolution of 14 bits, which corresponds to dividing each sample by 2^{14-1}. After this, the samples are normalized once more, but now according to their amplitudes.

Considering that the length of the cables from the Wilkinson divider to the TX antenna switch matrixes is different, as it can be seen from the antenna board shown in Fig. 4.5, a correction in the data needs to be applied to the 256 signals linked to the transmit components 1 to 8. Due to the large difference in length, not only a phase delay, but also

a frequency delay needs to be accounted for. This is achieved through the implementation of a fractional delay filter, which is a filter of digital type having as main function to delay the processed input signal a fractional of the sampling period time. Additionally, several other phase and delay shift corrections, due to intolerances and different path lengths of the cables in the system, are performed. The final step of the calibration process, consists in the use of a calibration matrix acquired from a measurement in an anechoic chamber, which is multiplied with each new radar measurement.
Subsequently, the 256 signals, organized into a 3D calibrated matrix, are aligned according to the virtual array.

4.7 The 3D-FFT Based Digital Beamforming

The main starting point of the digital beam-forming architecture implemented, is the the concept of the MIMO virtual array, as previously introduced in Chapter 2.4. The MIMO radar has 16 TX (N_{TX}) and 16 RX (N_{RX}) antennas, leading to a total number of $N_{TX} + N_{RX} = 32$ antennas and $N_{vir} = N_{TX}N_{RX} = 256$ virtual elements. The physical antenna placement and the resulting virtual array are shown in Fig. 4.14. It can be seen that the antenna elements are placed along a rectangle with 8 antennas per edge [152]. The virtual array (in purple) can be calculated as the discrete convolution of all RX (in red) and TX (in blue) antenna element positions. To achieve the same angular resolution with a conventional mechanically or electronically scanning radar, 256 RX antennas (16 x 16) and one TX antenna are needed. With a rectangular MIMO array configuration, the size of the antenna array can be reduced by a factor of two in both, x- and y-dimension, compared to a conventional phased array radar. Due to physical placement constraints, there is one additional column in y-direction, which is unoccupied. For the empty column which appears in the center of Fig. 4.14, an interpolation of the data is performed, according to what has previously been described in [130]. This results in a virtual array, which has 16 elements in x-direction ($N_{vir,x}$) and 17 elements in y-direction ($N_{vir,y}$). Therefore, the data structure can be seen as a real-valued 3D data matrix $M \in \mathbb{R}^{N_{vir,x} \times N_{vir,y} \times N_{Samples}}$, where $N_{vir,x} \times N_{vir,y}$ is the dimension of the resulting virtual array which represents all TX-RX-combinations. The elements in the first two dimensions have to be ordered in the same way as they result from the convolution. The third dimension $N_{Samples}$, results from the chirp length (100 ms) and the sampling frequency (100 MHz) of the ADC, which results in $N_{Samples} = 10000$ samples for each TX-RX-combination.
The angular resolution defined as the 3-dB-beamwidth of the main lobe for this particular MIMO array can be calculated as follows:

$$\Delta\theta_{3dB_x} \approx 50^\circ \frac{\lambda_0}{N_{vir,x} d_x} = 50^\circ \frac{\lambda_0}{(2N_{pop}+1) d_x} \approx \ 4.5^\circ \tag{4.1}$$

$$\Delta\phi_{3dB_y} \approx 50^\circ \frac{\lambda_0}{N_{vir,y} d_y} = 50^\circ \frac{\lambda_0}{2N_{pop} d_y} \approx \ 3.5^\circ \tag{4.2}$$

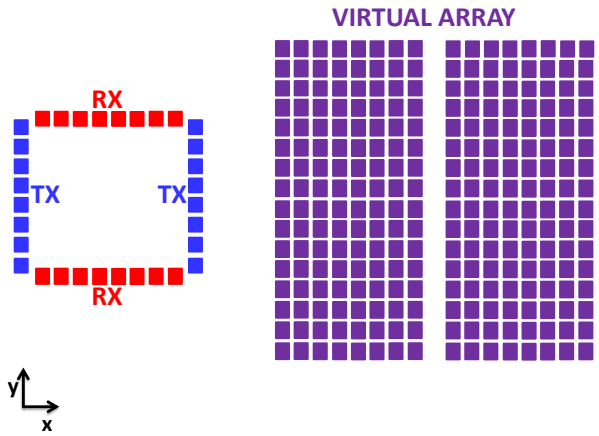

FIGURE 4.14: Schematic representation of the MIMO antenna configuration with the physical array (left) showing the 16 TX antennas in blue, the 16 RX antennas in red and the resulting virtual array (right). A unit in the graph is equivalent to $\frac{d_x}{2}$ and $\frac{d_y}{2}$ respectively.

with $\lambda_0 \approx 18$ mm being the wavelength, $d_x = 12$ mm and $d_y = 16$ mm the spacings between elements along the corresponding axis and $N_{pop} = 8$ the number of antenna elements which are used along each edge of the rectangle.
Various windowing functions can be applied before the FFT, as described in [138]. According to which matrix dimension the window is applied to, it might affect the resolution. One of the most commonly selected window functions, and used throughout our simulations, is the Hamming window, which has a minimal influence on the resolutions.
The zero padding operation is introduced just after the application of the window function and consists, as the name suggests, into the concatenation, or padding, of zeros at the end of the radar signals, in time domain. Taking advantage of the fact that at the end of a windowed signal, the signal itself smoothly goes to zero, it can be understood that zero padding must be applied after windowing, in order to avoid a sharp transitioning of the signal to zero.
After the padding operation, the size of the 3D data matrix scales according to the padding factor which has been chosen in the previous step. Therefore, a 3D data matrix of size $N_{ELE} \times N_{AZI} \times N_{RANGE}$ is obtained and will be used throughout the rest of the processing, where $N_{ELE} = N_{vir,y} \times PAD_{ELE}$, $N_{AZI} = N_{vir,x} \times PAD_{AZI}$ and $N_{RANGE} = N_{Samples} \times PAD_{RANGE}$. The terms PAD_{ELE}, PAD_{AZI} and PAD_{RANGE} represent the padding factor for the elevation, Azimuth and range respectively. For optimum performance, each dimension's length should be a power of two, in order to make use of the efficiency of the FFT algorithms.
Therefore, the data structure for the MIMO processing is a real-valued three-dimensional data matrix $D \in \mathbb{R}^{N_{AZI} \times N_{ELE} \times N_{RANGE}}$.

As shown in Fig. 4.13, the 3D reconstruction of the radar scenario is done with a three-dimensional FFT on the data matrix described before. The FFT processing is very fast on the one hand, but requires a plane wavefront on the other hand. The 3D-FFT can be

seen as an operation that computes in-place the one-dimensional fast Fourier transform along each dimension of the 3D radar signals matrix D, in this order:

1. The first FFT goes along the third dimension (N_{RANGE}) of the 3D matrix D, which represents the range components of the virtual array. The result (D_1) is a complex-valued range-compressed matrix for every element of the virtual array. Now the DOA of the targets can be estimated with two additional FFT.
2. The second FFT goes along the second dimension (N_{AZI}) of the previously calculated 3D matrix (D_1), resulting from the operation in step 1, which represents the azimuth components of the virtual array, and yields the azimuth information of the targets. The resulting matrix is D_2.
3. The third FFT goes along the third dimension (N_{ELE}) of the previously calculated 3D matrix (D_2), resulting from the operation in step 2, which represents the elevation components and yields the elevation information of the targets.

The next paragraph explains the link between the result of the FFT and the DOA estimation. Here, just the calculations for the Azimuth angles are presented, but the same principle applies for the elevation direction. Moreover, for simplicity of understanding, PAD_{ELE}, PAD_{AZI} and PAD_{RANGE} are considered equal to 1. For complex input samples (D_1), the FFT results in a complex spectrum (two-sided). These complex points are sampled at the virtual element positions which leads to a sampling frequency in space of

$$f_{s,space_{AZI}} = \frac{1}{d_x} \approx 83.3\ m^{-1} \tag{4.3}$$

and a frequency spacing for the FFT of

$$df_{space_{AZI}} = \frac{f_{s,space_{AZI}}}{N_{vir,x}} \approx 4.9\ m^{-1} \tag{4.4}$$

The FFT will give $N_{vir,x}$ bins equally distributed from $f = 0$ to $f = f_{s,space_{AZI}}$. Let α be the angle between the incident wavefront and the antennas, spanning between -90° to 90°. This means that the first sample is the component which belongs to a straight incident wave $\alpha = 0$. The samples above $\frac{f_{s,space_{AZI}}}{2}$ represent negative angles and have to be shifted according to Tab. 4.1. The reordering of the FFT leads to a representation with $\alpha = 0°$ in the center.
For each frequency sample n of the FFT, the corresponding angle can be calculated as:

$$\alpha = \arcsin(n \cdot df_{space_{AZI}} \cdot \lambda_0) \tag{4.5}$$

with

$$\left\{ n \in \mathbb{N} \middle| -\frac{N_{vir,x}-1}{2} \leq n \leq \frac{N_{vir,x}-1}{2} \right\} \tag{4.6}$$

This leads to Azimuth angles from $-45°$ to $45°$, for this system demonstrator. The FFT's original and reordered, indexes and corresponding DOA angles are shown in Table 4.1, for the case of the Azimuth angles.

TABLE 4.1: FFT's Original and Reordered, Indexes and Corresponding DOA Angles, for the Azimuth Angles.

Original	1	2	...	8	9	10	...	16	17
Reordered	10	11	...	17	1	2	...	8	9
Index n	-8	-7	...	-1	0	1	...	7	8
Angle in deg	-45	-39	...	-5	0	5	...	39	45

Similarly, the values for the elevation angles can be obtained, considering

$$f_{s,space_{ELE}} = \frac{1}{d_y} \approx 62.5 \ m^{-1} \tag{4.7}$$

and

$$df_{space_{ELE}} = \frac{f_{s,space_{ELE}}}{N_{vir,y}} \approx 3.9 \ m^{-1} \tag{4.8}$$

This leads to elevation angles from $-30°$ to $30°$, for this system demonstrator. The FFT's original and reordered, indexes and corresponding DOA angles are shown in Table 4.2, for the case of the Elevation angles. The 16-th element corresponds to half the sampling frequency and, thus, is the repetition of element 0 and can be discarded.

TABLE 4.2: FFT's Original and Reordered, Indexes and Corresponding DOA Angles, for the Elevation Angles.

Original	1	2	...	8	9	10	...	14	15
Reordered	9	10	...	15	1	2	...	7	8
Index n	-7	-6	...	-1	0	1	...	6	7
Angle in deg	-30	-25	...	-4	0	4	...	25	30

Hence, a complete sensing of range, Azimuth and elevation of the targets is achieved in this manner, which represent the 3 dimensions of the resulting 3D data matrix, after the 3D-FFT. Moreover, it is important to understand that in this way, the compensate and integrate properties of the N-Dimensional FFT are exploited to yield better target estimates.
Finally, as illustrated in the scheme of Fig. 4.13, the last three steps of the algorithm

are the shifting and scaling of the resulting data matrix, after the 3D-FFT processing, the target identification and, at last, the radar image generation. The shifting and scaling procedures consists of various mathematical operation, among which coordinates transformations, for the plotting of the 3D radar images into a 2D metric coordinates system, with respect to the radar defined as origin. Z and X are the axis used to represent the range and the cross-range in meters, respectively, in the case of range-Azimuth radar images. Similarly, Z and Y are the axis used to represent the range and the cross-range, in the case of range-Elevation radar images. The target identification consists in peak analysis functions which yield the most significant targets in a radar's image, based on thresholding. The radar image generation block, includes all the 2D and 3D plotting functionalities, for the generation of the radar images.

4.8 Waveform and Timing

This section describes the waveform and the timing of the MIMO radar. The system uses linear FMCW signals from 16 GHz to 17 GHz. The up-ramp chirp has a duration of $t_{up} = 100$ μs and a bandwidth B = 1 GHz. Considering c_0 as the speed of light and recalling equation (2.14), a range resolution of

$$\Delta R = \frac{c_0}{2B} = 0.15\ m \tag{4.9}$$

is obtained. The maximum range of the system can be calculated using the sampling frequency of the ADC ($f_s = 100$ MHz) which determines the maximum difference frequency due to the sampling theorem. In this case, recalling equation (2.13), the maximum range can be obtained as

$$R_{max} = \frac{c_0 \frac{f_s}{2}}{2\frac{B}{t_{up}}} = 750\ m \tag{4.10}$$

Here, a MIMO cycle is composed of 16 up-ramps, where each ramp is sent via a different TX antenna. In order to avoid interferences between the TX signals and then achieve orthogonality, TDM is used. With TDM it is possible to assign the TX antenna to the RX signal according to the timing scheme.

The timing of a MIMO cycle is shown in Fig. 4.15. At the beginning, the system waits for a start command from the HMI. After that, the first TX antenna is activated and sends the FMCW chirp. The RX signals are captured by the ADC and stored in the FPGA. After that, the data is transferred from the FPGA to the DDR memory of the system via DMA. This procedure is repeated for all 16 TX antennas and lasts, altogether, approximately 20 ms. Currently, the radar beamforming algorithms are carried out in a MATLAB environment. For this reason, the data of the complete MIMO cycle is transferred via Ethernet to a workstation. After the transfer, the radar processing is launched. With the current configuration the system has an update rate of less than 3 s.

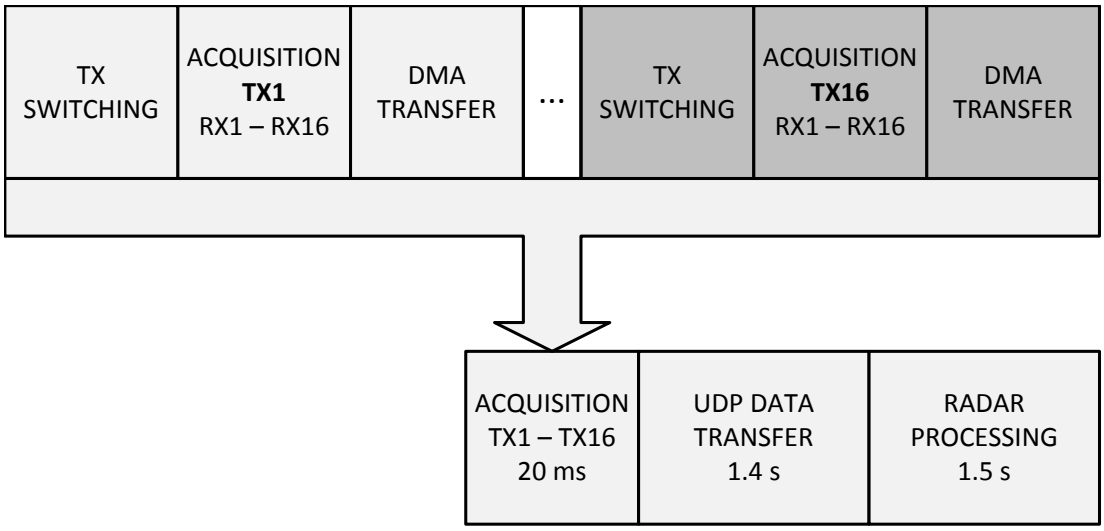

FIGURE 4.15: Exemplary timing of a MIMO cycle.

This is mainly determined by the UDP data transfer (1.4 s) and the MATLAB radar processing, which represent the current bottleneck of the system. These processes can be accelerated by implementing the radar processing directly in the FPGA.

As it can be understood, an improvement has been obtained, as compared to the timings shown in Chapter 3.4.7 for the previously presented MIMO radar demonstrator. Specifically, the timing from a radar capture to the radar's image generation, thanks to the new digital architecture and the much faster 3D-FFT based beam-forming implemented, has gone from 11 s to less than 3 s. This, compared to before, allows to capture moving targets and not only static targets represented by corner reflectors.

4.9 System's Performance

This section presents an analysis of the radar system's performance and resolutions, together with several radar captures. Additionally, the field of view and the maximum range of the device are also characterized. The angular variables are θ for Azimuth and ϕ for elevation. The coordinate system is displayed in Fig. 4.4. The following radar captures have been processed according to the 3D-FFT beam-forming radar processing previously described and shown in Fig. 4.13.

4.9.1 Radar's Resolutions

In order to measure the 3-dB-beamwidth of the system, as shown in Fig. 4.16, a corner reflector with a nominal radar cross section of $\sigma_0 = 150\ m^2$, is placed in an anechoic chamber, at a range $R = 23.5$ m, with Azimuth and elevation angles of $\phi = 0°$ and $\theta = 0°$, respectively. With the FFT processing and FMCW waveforms's parameters presented in the former sections, a three-dimensional radar image, which contains the information of range, Azimuth and elevation, is calculated.

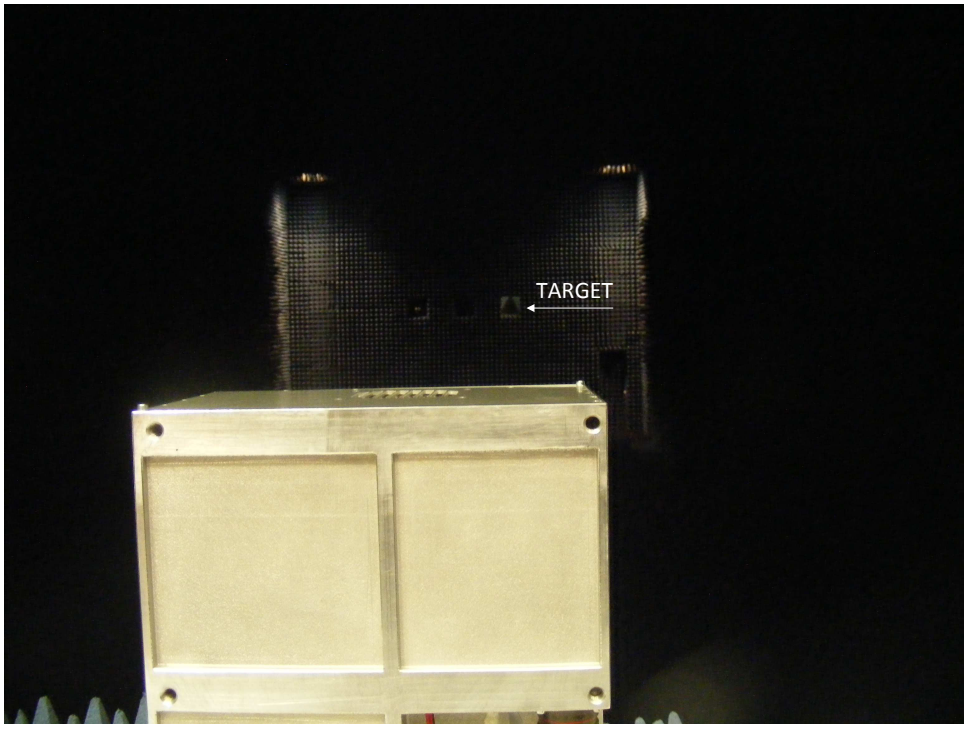

FIGURE 4.16: Picture of the anechoic chamber for the measurement of the angular resolution. The target is placed at a distance of 23.5 meters.

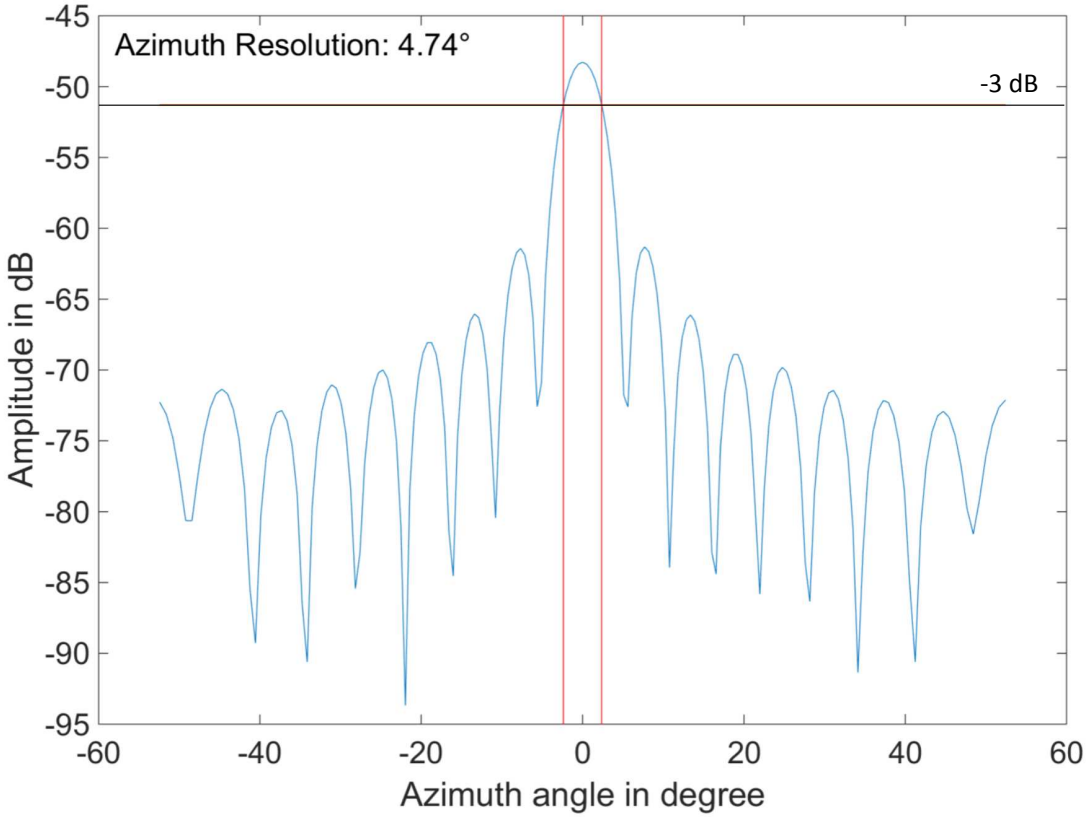

FIGURE 4.17: Azimuth profile, angular section view of the 3D radar image capture of the target at 23.5 m, in the anechoic chamber.

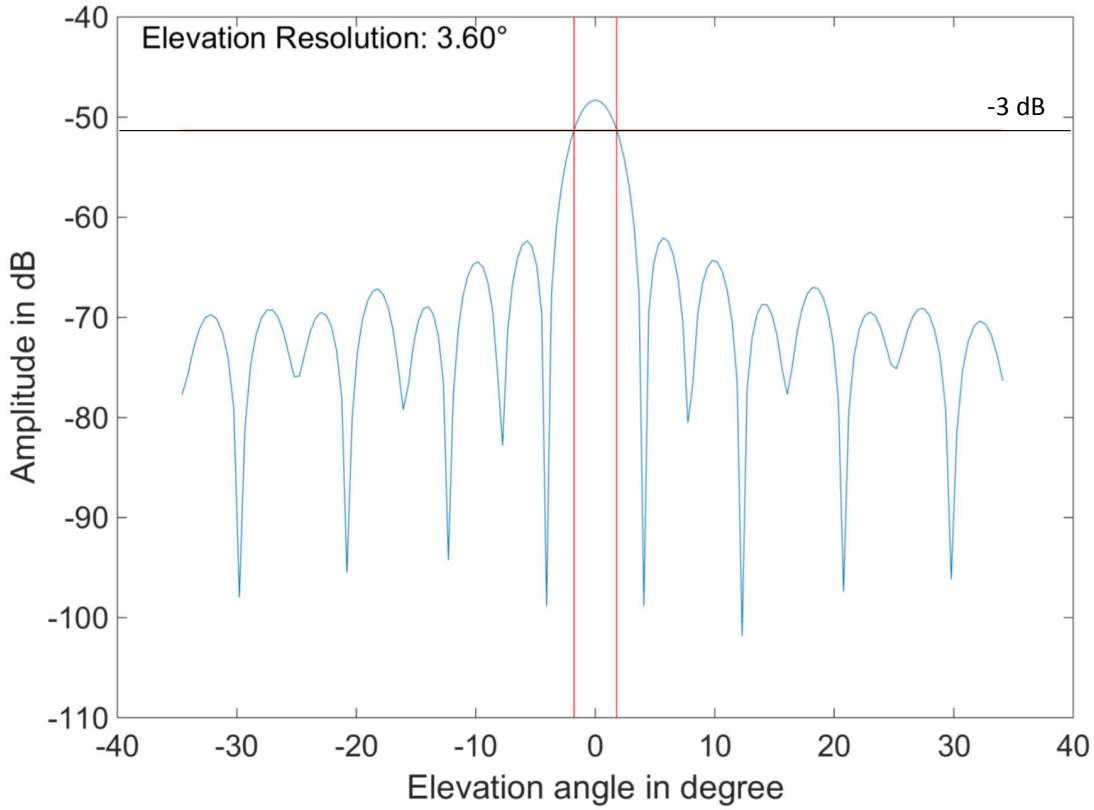

FIGURE 4.18: Elevation profile, angular section view of the 3D radar image capture of the target at 23.5 m, in the anechoic chamber.

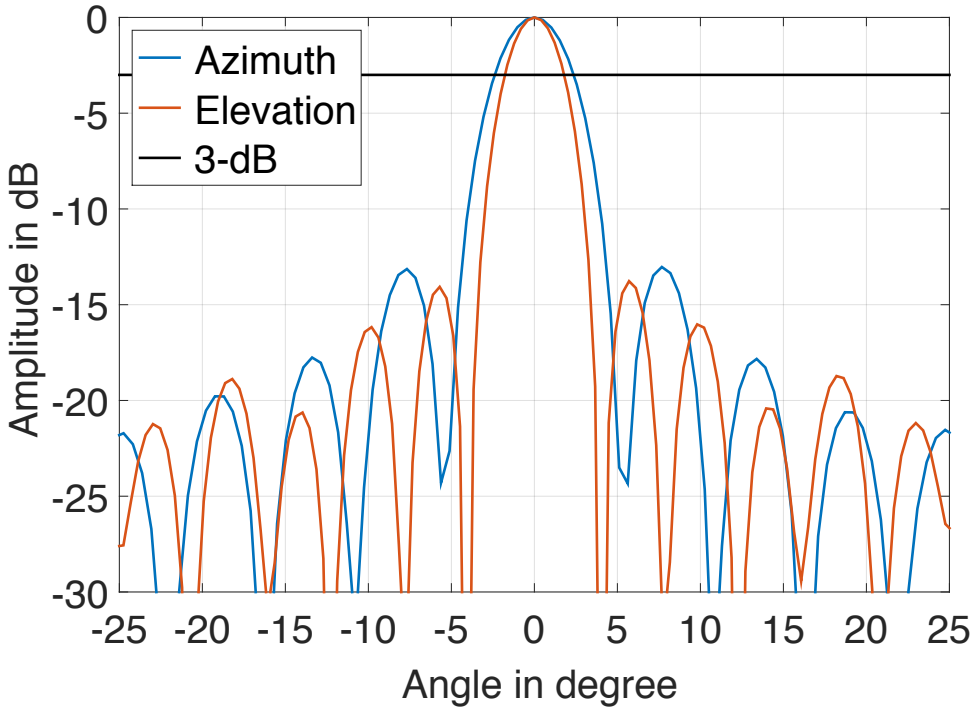

FIGURE 4.19: Superposition of Azimuth and elevation profiles, angular section views of the 3D radar image capture of the target at 23.5 m, in the anechoic chamber.

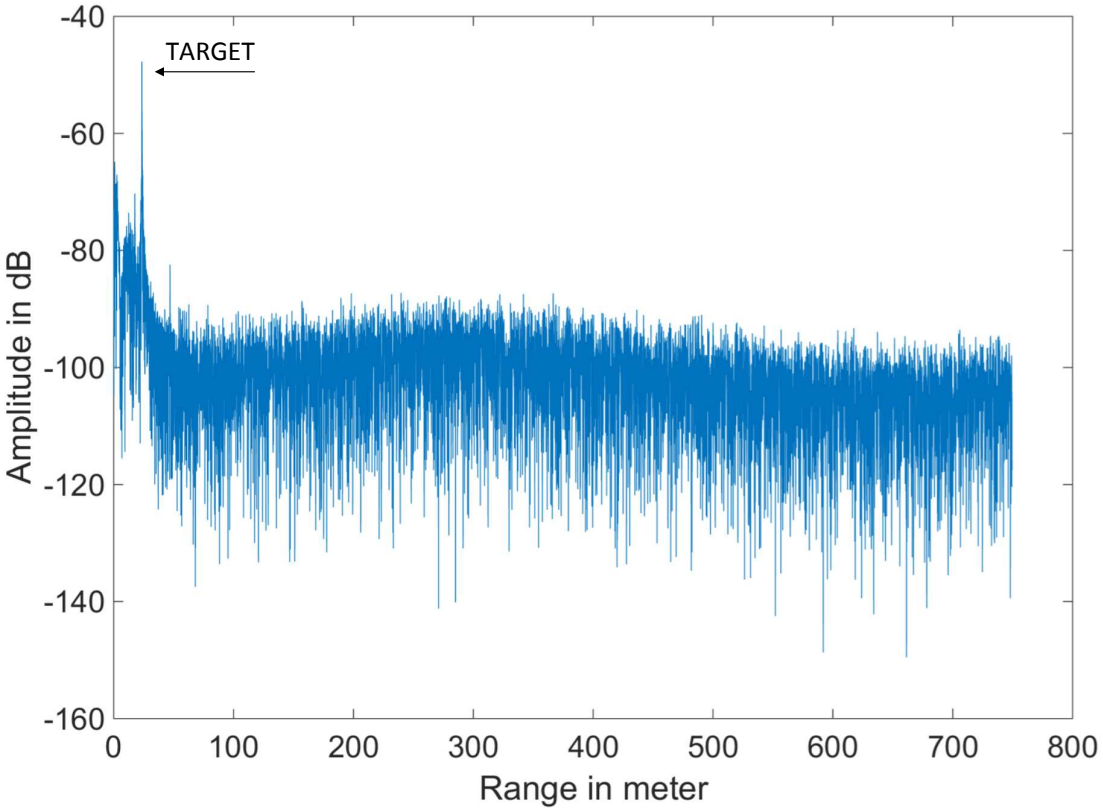

FIGURE 4.20: FFT across range plot, section view of the 3D radar image capture of the target at 23.5 m, in the anechoic chamber.

Fig. 4.17 shows the Azimuth ($\phi = 0°$) profile taken at the range cell of the central target, whereas Fig. 4.18 shows the elevation ($\theta = 0°$) profile. Under the assumption that the corner reflector represents a point target and that the distance is big enough to be in the far-field region, the theoretical values of the angular resolution of the MIMO virtual array, calculated in Section 4.7, should match with the measured 3-dB beam-width of the target's main lobe. The measured Azimuth resolution is $\Delta\theta_{3dB_x} = 4.7°$ and the elevation resolution is $\Delta\phi_{3dB_y} = 3.6°$ whereas the calculated is $\Delta\theta_{3dB_x} = 4.5°$ and the elevation resolution is $\Delta\phi_{3dB_y} = 3.5°$. As it can be seen, the measured and calculated angular resolutions match very well and a difference between the two is expected to arise. This is due to the fact that the equations are an approximation based on a limited number of antenna elements and, additionally, weighting of antenna elements by means of classical windowing functions like the ones used in this algorithm, allows for better side lobe suppression, but at the expense of a slightly reduced angular resolution, due to an enlargement of the width of the main lobe. Additionally, it is important to notice that, in the estimation along the Azimuth direction, the missing element is included, while in the radar beam-forming process, this missing element is calculated as the average of its neighbouring elements. An image, showing the superimposed angular profiles is illustrated in Fig. 4.19, where it can be noticed how the elevation resolution, due to a larger aperture in the Y-direction, is finer, thus resulting in a finer main lobe's beam-width at 3 dB.

Additionally, the range resolution is estimated, by calculating an FFT across ranges,

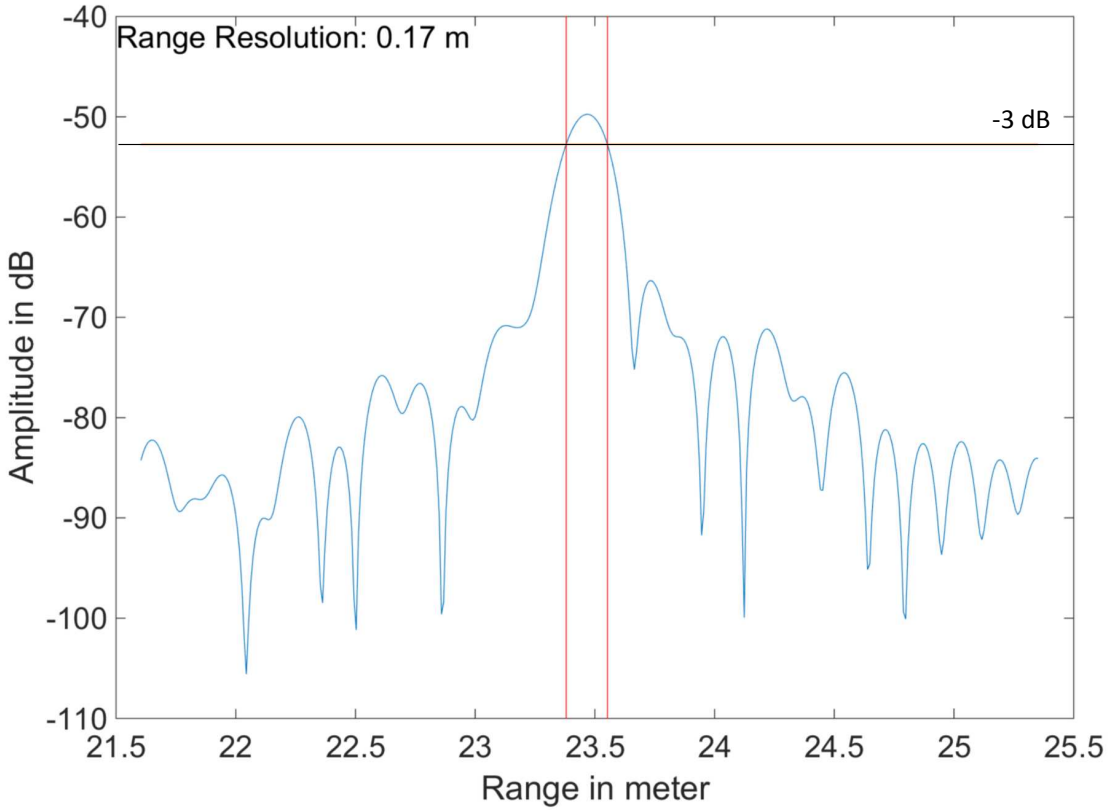

FIGURE 4.21: Range profile, zoom in of the plot in Fig. 4.20.

for a capture of the same target at 23.5 m, in the anechoic chamber. The FFT plot is shown in Fig. 4.20, whereas a zoom in of the same plot is shown in Fig. 4.21. As it can be noticed, the effective range resolution is of $\Delta R = 0.17$ m, which is slightly different from the theoretical value calculated in equation (4.9). For the same reason as above, by adopting classical windowing functions like the ones used in this algorithm, a slight increase in the main lobe is expected.

A 2D radar image, cut in the Azimuth plane and the elevation plane, of the complete 3D image obtained through the 3D-FFT beam-forming radar processing, is shown in Fig. 4.22 and Fig. 4.23, respectively. The targets, and the side lobes, are clearly visible at a range of 23.5 m.
The overall good imaging performance of the radar is verified as well, by the fact that the walls of the anechoic chamber can also be seen in these images. In Fig. 4.22, the reflections in the picture seem to indicate the presence of a reflecting surface at -4 m and +4 m of cross range (X-Position) and along the range axis (Z-Position), therefore for a total span of 8 m, in accordance to the dimensions of the anechoic chamber shown in Fig. 3.33, subsection A, presented previously. Similarly, in Fig. 4.23, the reflections are at -3 m and +3 m of cross range (Y-Position) and along the range axis (Z-Position), therefore for total span of 6 m, in accordance to the dimensions of the anechoic chamber shown in Fig. 3.33, subsection B.
Finally, a 2D radar image, cut in the range bin of the target, from the complete 3D image obtained through the 3D-FFT beam-forming radar processing, is shown in Fig.

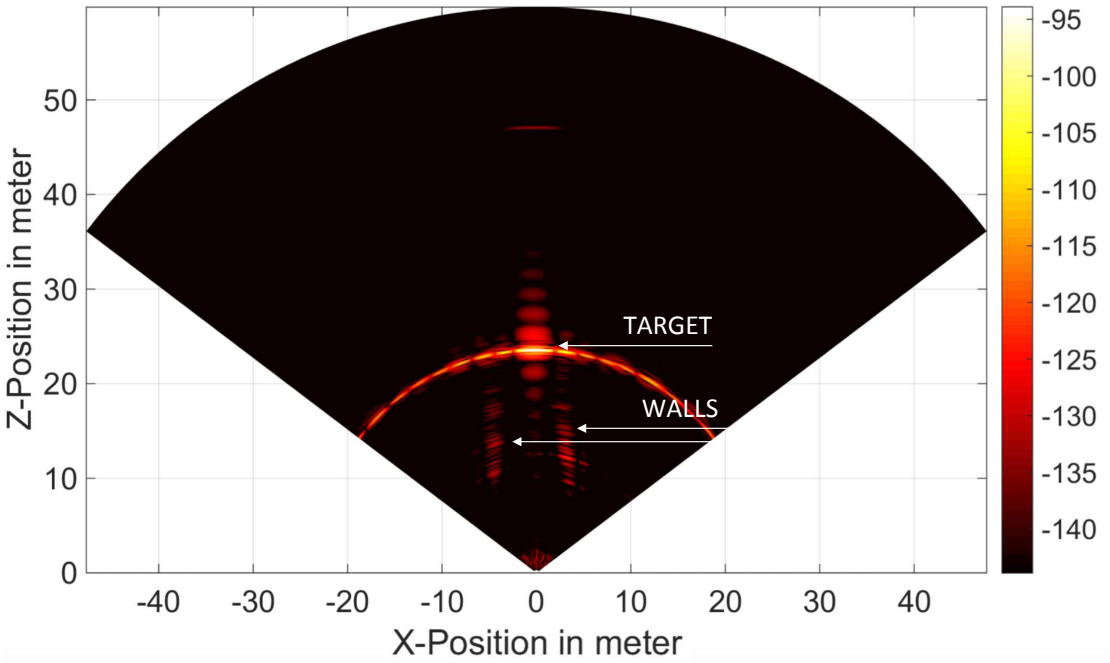

FIGURE 4.22: Azimuth-range section view of the 3D radar image capture of the target at 23.5 m, in the anechoic chamber.

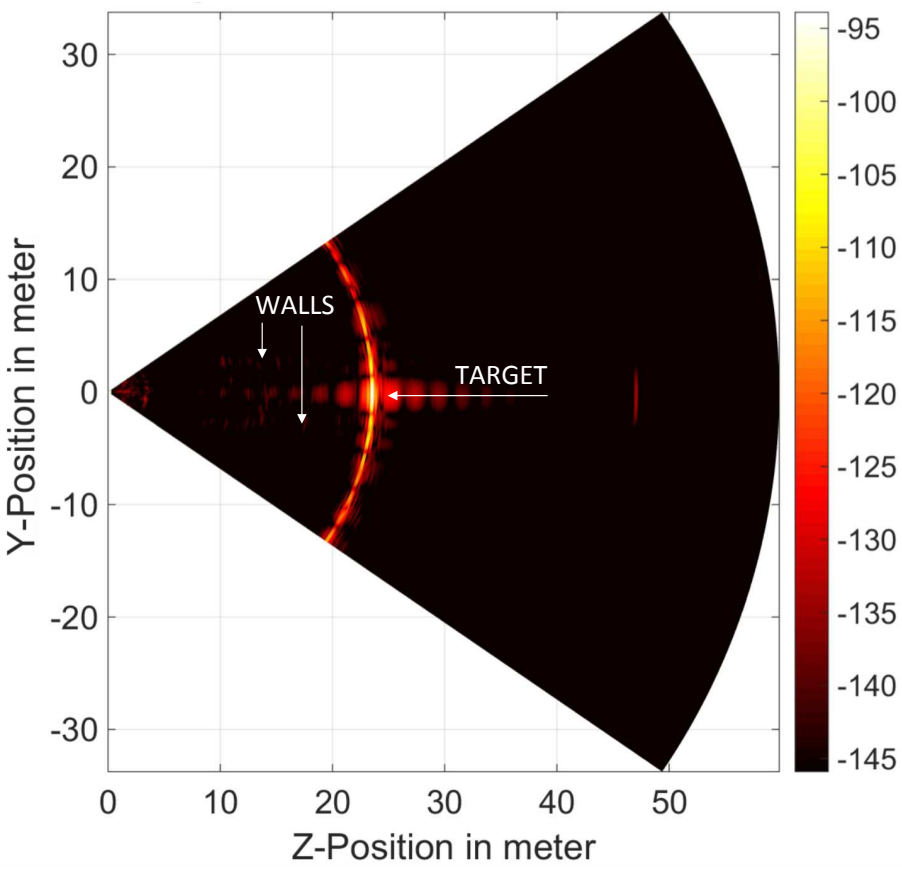

FIGURE 4.23: Range-elevation section view of the 3D radar image capture of the target at 23.5 m, in the anechoic chamber.

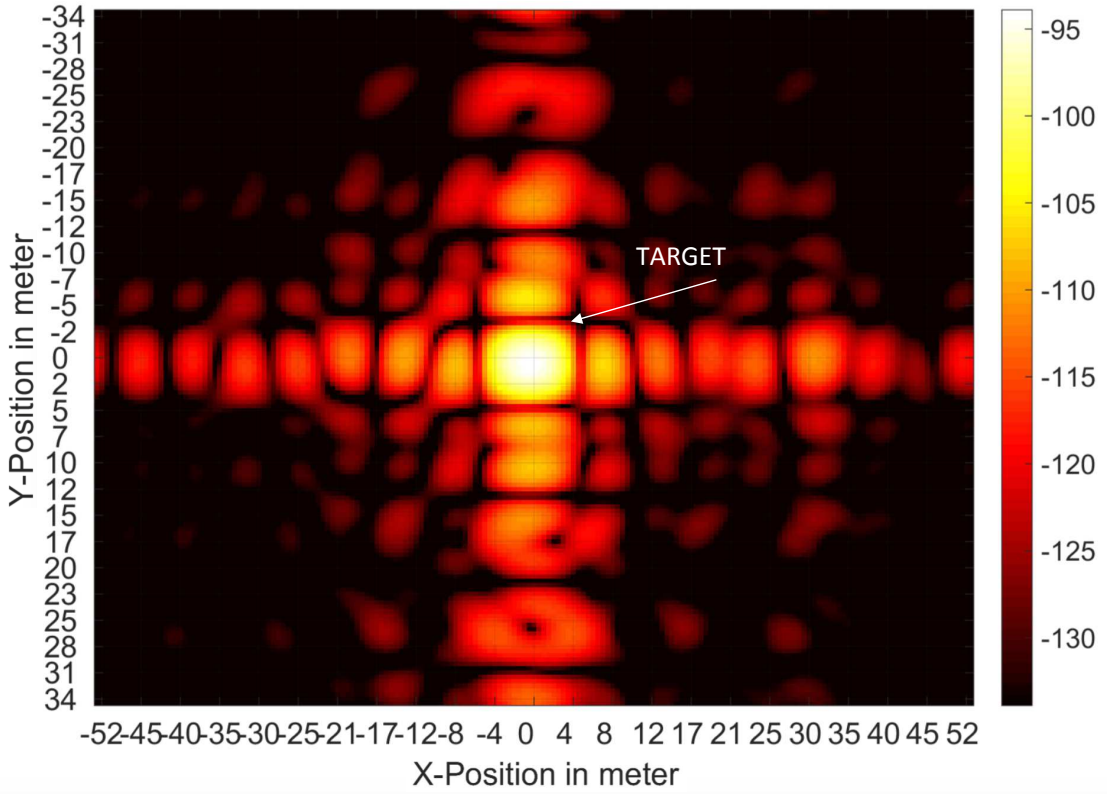

FIGURE 4.24: Azimuth-elevation section view of the 3D radar image capture of the target at 23.5 m, in the anechoic chamber.

4.24. As it can be noticed, the target is perfectly identifiable at an elevation of $\phi = 0°$ and Azimuth of $\theta = 0°$, together with its side lobes, along both dimensions.

4.9.2 Radar's Field of View

The aim of this sub-chapter is to show the dependency between a target's received power, at a certain distance R, and its angle, in both Azimuth and elevation directions.
A corner reflector with a nominal radar cross section of $\sigma_0 = 150\ m^2$ is placed at $R = 23.5$ m, $\phi = 0°$ and $\theta = 0°$, in an anechoic chamber. Then, the radar is rotated by $\phi = -60°$ in elevation direction, without moving the target. At this point, a radar capture is started. This process is repeated following an angular sweep from $\phi = -60°$, $\theta = 0°$ to $\phi = 60°$, $\theta = 0°$, with a constant step of 1°. Since the RX (array of 4 patches along y) and TX (array of 2 patches along y) antennas are not isotropic, a relatively pronounced dependency of the received power with the angle is expected.

Fig. 4.25 illustrates the measured curves for different angles $\phi = \phi_i$, $\theta = 0°$. The simulated curve, dotted curve in the figure, is the multiplication of the simulated RX antenna pattern and the TX antenna pattern. As it can be seen, the amplitude decays approximately by ± 10 dB at 30°. The simulation matches very well with the envelope of the complete set of performed measurements.

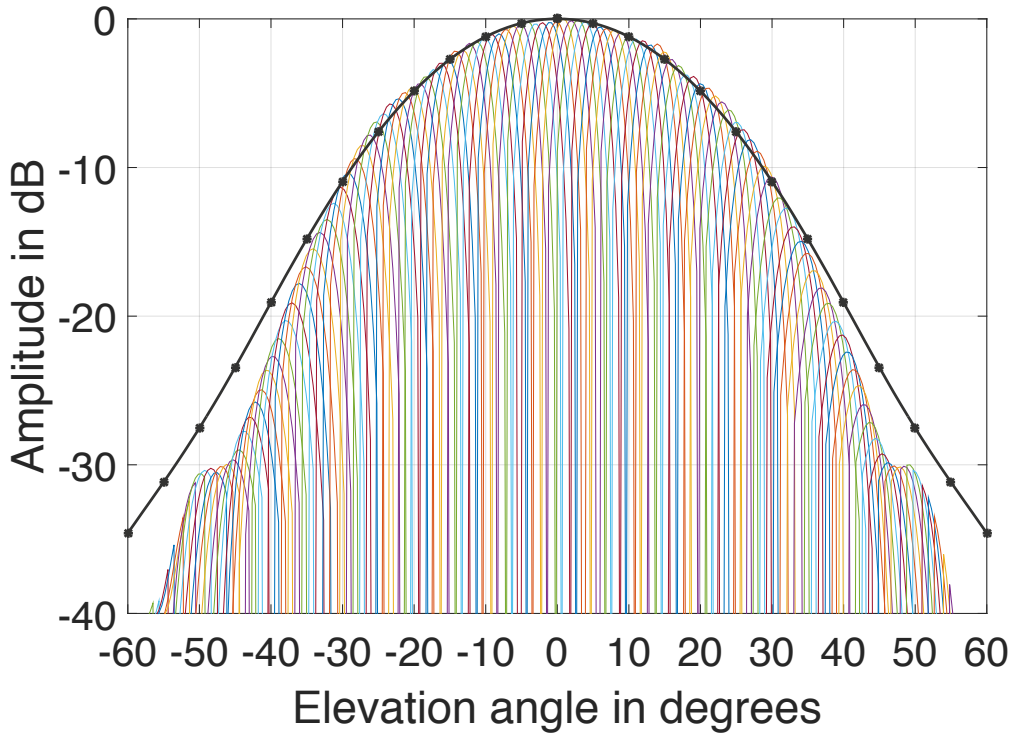

FIGURE 4.25: Normalized dependence of the received power in the elevation direction with the angle due to the antenna element pattern.

Similarly, the measurement has been performed in the azimuth direction. This time the angular sweep is from $\phi = 0°$, $\theta = -60°$ to $\phi = 0°$, $\theta = 60°$, with a constant step of 1°. Since the RX (single patch along x) and TX (single patch along x) antennas are not isotropic, a corresponding angular dependence of the power is expected. In this axis, the antennas are single patches Therefore, the characteristic dependence of the received power with the angle is expected to be rather wide.

Fig. 4.26 illustrates the measured curves for different angles ($\phi = \phi_i$, $\theta = 0°$). Considering the TDM architecture implemented, each TX radiating element is connected to a switch, in such a manner that only the TX antenna which sends the FMCW ramp is matched to 50 Ω, while the rest of the TX antennas are connected to a open-circuit. Consequently, a ripple appears in the azimuth dimension. The simulated curve, dotted curve in the figure, is the multiplication of the simulated RX antenna pattern and the TX antenna pattern (considering the whole antenna array with the corresponding open circuits in the proper TX elements). The amplitude decays approximately by 10 dB at ± 50°. The simulation matches rather well with the envelope of the complete set of performed measurements. As a summary, the fields of view of the radar are $FOV_\theta = 100°$ and $FOV_\phi = 60°$, respectively.

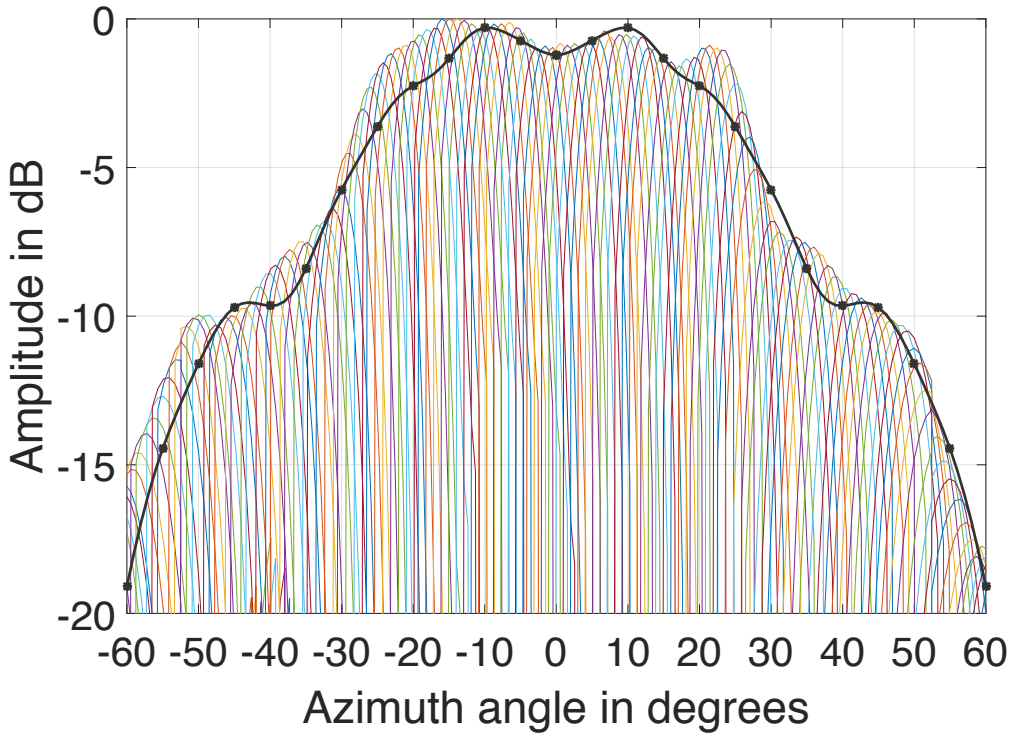

FIGURE 4.26: Normalized dependence of the received power in the azimuth direction with the angle due to the antenna element pattern.

4.9.3 Maximum Range

In order to measure the maximum range at which the radar demonstrator can detect a target, a corner reflector with a nominal radar cross section of $\sigma_3 \approx 169\ m^2$ has been used and placed in an open field test scenario, at a distance of 197 m. A radar image, cut in the Azimuth plane, of the complete 3D image, is shown in Fig. 4.27. As it can be seen, the target is clearly visible at a distance of 197 m, thus determining the maximum tested range of the radar system. Additionally, a radar image, cut in the elevation plane, of the complete 3D image, is shown in Fig. 4.28. It can be noticed from this picture, that the target lays on the ground, at 197 m. Finally, it is also important to see from this image, how the ground clutter is captured by the radar as well. This can be noticed on the left side of the image and it is represented by the reflections which are visible, at ground level, up to 25 m along the range dimension (Z-Position).
In real radar scenarios, the maximum range represents one of the most critical parameters of a radar system and particular considerations have to be given to the analysis and suppression of the ground clutter, in order to discriminate a target. For this purpose, statistical properties of the clutter have to be investigated and Constant False Alarm Rate (CFAR) based models have to be implemented, which will form part of the future works which will derive from this thesis.

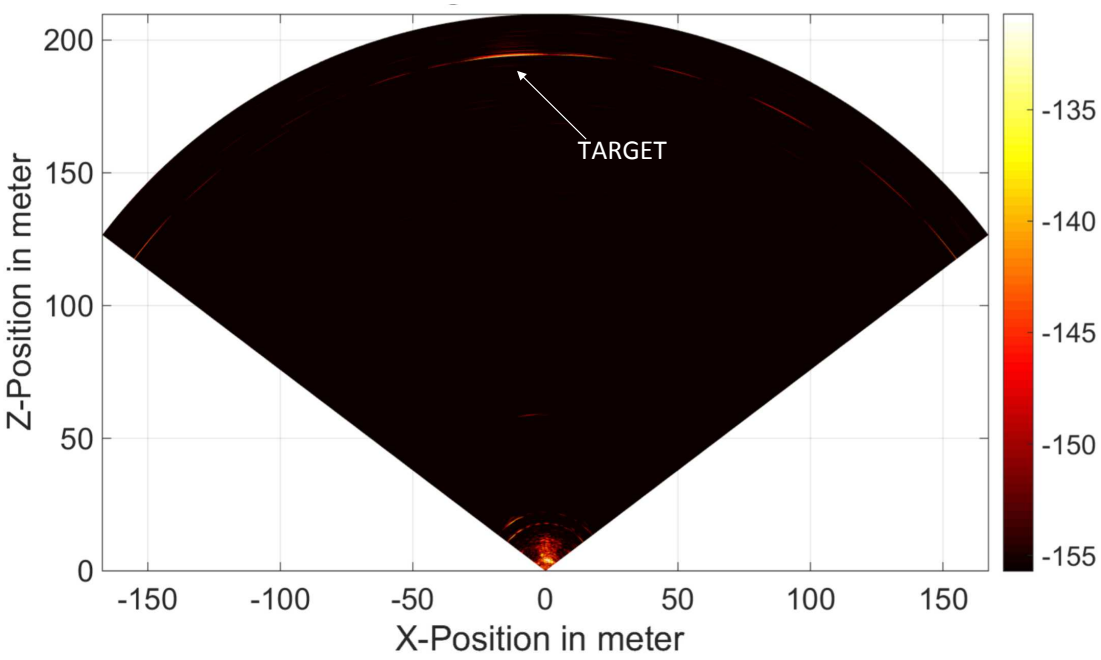

FIGURE 4.27: Azimuth-elevation section view of the 3D radar image capture of the target at 197 m.

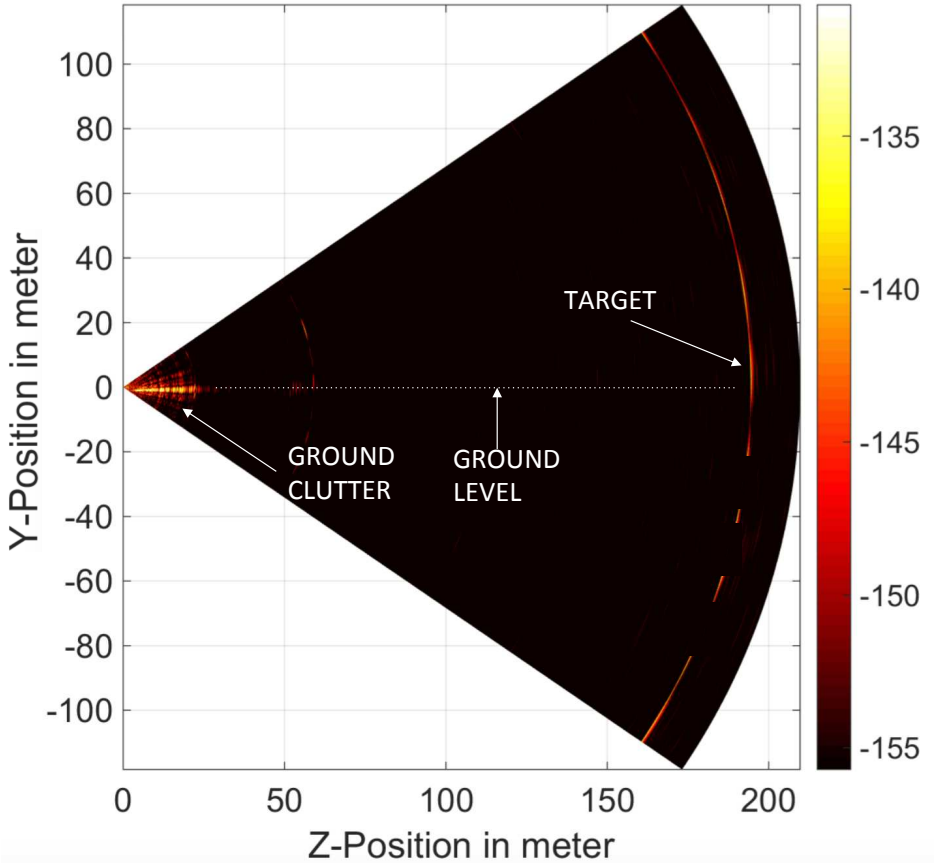

FIGURE 4.28: Range-elevation section view of the 3D radar image capture of the target at 197 m.

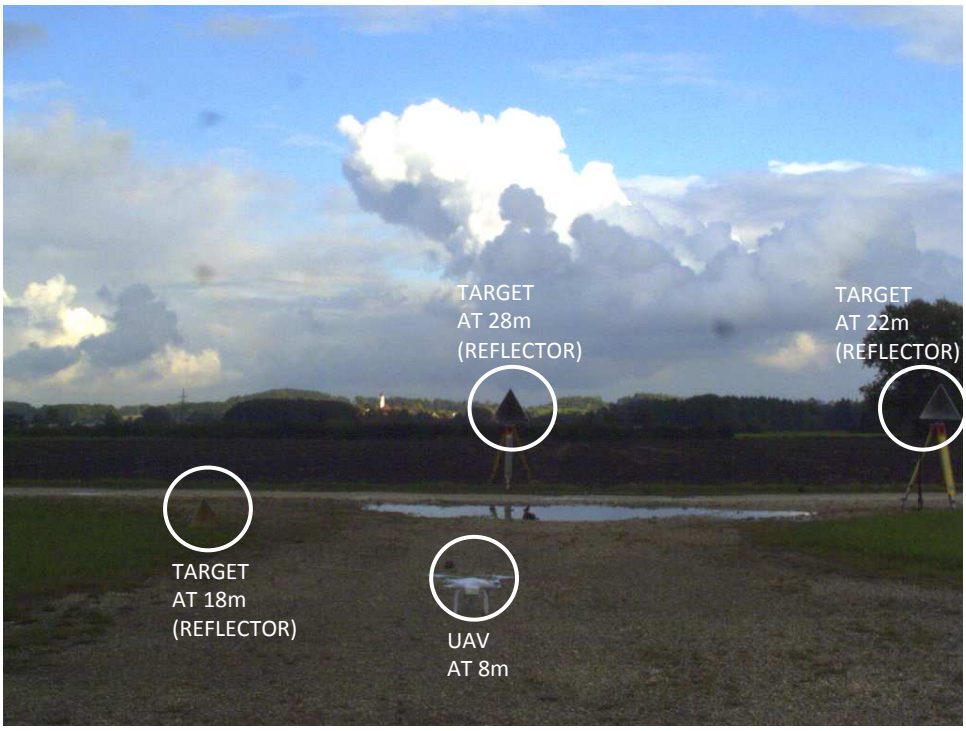

FIGURE 4.29: Image of the scene with three corner reflectors at 18 m, 28 m and 22 m, and a UAV at 8 m, marked with white circles.

4.10 Radar Demonstrator Results and Applications

The results shown in this section, demonstrate the capabilities of the radar's architecture and 3D-FFT beam-forming processing algorithm in several different applications, such as for the detection and tracking of targets in the form of static corner reflectors, flying UAVs and people walking. The purpose is to verify the performance of the MIMO radar in real scenarios and to show the advantages of a multifunctional system.

4.10.1 Surveillance Applications

In this test, the MIMO radar is combined with a camera which is placed in the middle of the antenna array, as originally shown in Fig. 4.4. In Fig. 4.29, the scene of the measurement as seen by the camera, is presented. A commercial camera, with $n_{pix,h} = 2048$ pixels horizontally and $n_{pix,v} = 1536$ pixels vertically is used. The pixel size is 3.2°. With an objective with a focal length of $f = 12$ mm, a field of view of

$$FOV_h = \frac{n \cdot p}{f} \cdot \frac{360^\circ}{2\pi} = 31.3^\circ \tag{4.11}$$

horizontally and $FOV_v = 23.5^\circ$ vertically is obtained. The field of view of the radar have been calculated in the previous sub-section to be $FOV_\phi = 60^\circ$ and $FOV_\theta = 100^\circ$. Since the FOV of the radar is greater than the FOV of the camera, the gimbals can be used to point the camera to the right direction. A field test measurement has been

performed, in order to simulate a detectable change in the surveillance area. For this purpose, three corner cubes with nominal cross-sections $\sigma_1 \approx 49\ m^2$, $\sigma_2 \approx 422\ m^2$ and $\sigma_3 \approx 169\ m^2$ are placed at ranges of 18 m, 28 m and 22 m, respectively. Additionally, a UAV is placed at 8 m, in order to show the importance of a correct amplitude scaling in the radar images here presented. It is safe to assume that the nominal RCS of the UAV is in the order of $\sigma_4 \approx 0.15\ m^2$. Determining the accurate position of the objects in a medium range, is a computationally intensive task for pure image processing algorithms, as it can be understood from Fig. 4.29, where the target on the most left, at 18 m, is hardly visible.

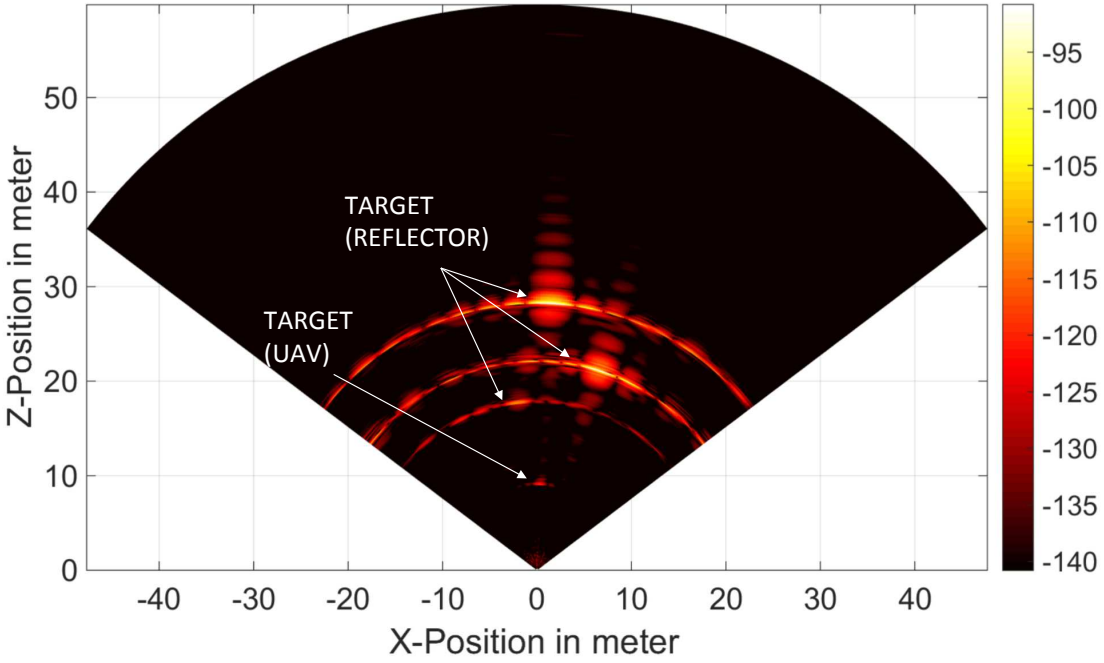

FIGURE 4.30: Azimuth-elevation section view of the 3D radar image capture of the 3 targets at 18 m, 28 m and 22 m, and the UAV at 8 m.

The results of the 3D-FFT beam-forming radar processing, in this kind of scenario, are now shown. In Fig. 4.30 a 2D radar image, cut in the Azimuth plane, of the complete 3D image, is shown. As it can be seen, all of the three corner reflectors are correctly identified at a distance of 18 m, 22 m and 28 m, and at their respective angles, as shown in Fig. 4.29. Additionally, at the bottom of the picture, it can be noticed that the UAV is also identified, at a distance of 8 m and at a central Azimuth angle. It is important to understand that the UAV, having a much lower RCS, has a peak reflectivity which is 30-40 dB lower than that of the corner reflectors, as shown in this image. By applying a threshold on the amplitudes and a different scaling, the UAV can either be more or less emphasized. However, a direct relationship between the thresholding and the enhancement of the target's side-lobes exists, and therefore needs to be taken into account. The same scenario is depicted in Fig. 4.31, where a 2D radar image, cut in the elevation plane, of the complete 3D image, is shown. Here as well, all four objects can be identified. It is important to notice how the UAV at 8 m and the first corner reflector at 18 m are correctly displayed laying on the ground, whereas the other two corner reflectors, at 22 m and 28 m, are displayed elevated from the ground, as in Fig.

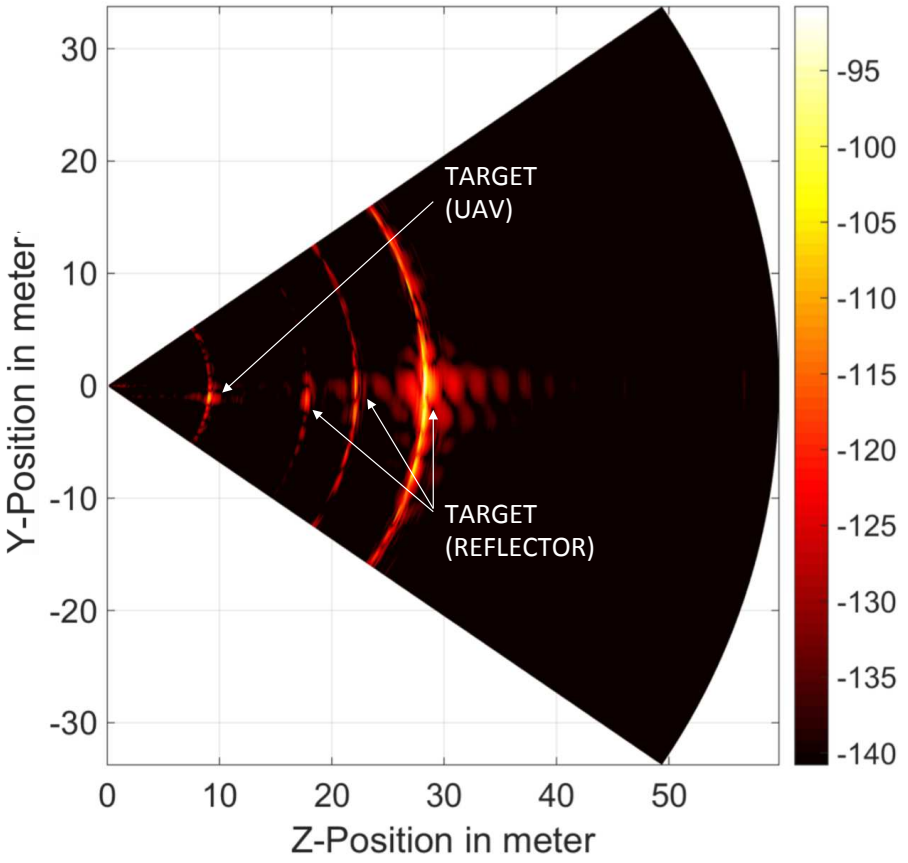

FIGURE 4.31: Range-elevation section view of the 3D radar image capture of the 3 targets at 18 m, 28 m and 22 m, and the UAV at 8 m.

4.29.

Finally, from these results, it can be understood that one of the advantages of MIMO radar systems, which is to identify objects independently from day, weather and light conditions (in the correct operational frequencies), is fully exploited. This is clearly seen from the fact that the target on the most left, at 18 m, is correctly displayed in all radar images presented, even though it is hardly visible in the picture captured from the camera, shown in Fig. 4.29.

A full 3D reconstruction of the scene, where all three dimensions (range, Azimuth and elevation) are shown in the same image, is presented in Fig. 4.32. This depicts the complete information which is sensed, from the raw radar data, by the 3D-FFT beam-forming processing algorithm. As it can be seen, a correct estimation of the range, azimuth and elevation, for all three targets used in the measurement is achieved. For simplicity of understanding, the UAV is not displayed in this picture, as it would be necessary to reduce the thresholding to a value where the side-lobes of the main targets are too strong, corrupting the visualization.

An additional and more intuitively understandable image, fusion of the camera image and the radar data is presented in Fig. 4.33. Here, the camera image is superimposed with the radar data. In order to still see the scene, the amplitude of the reflection is used to define the transparency level and the color of the radar cell. With this method,

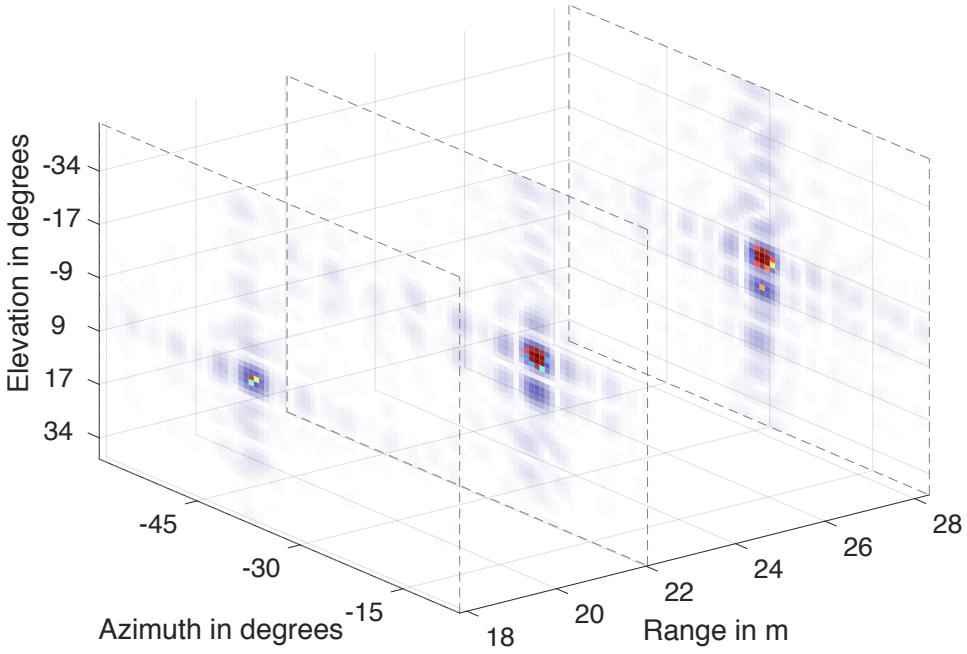

FIGURE 4.32: 3D reconstruction of the scene with radar data. The three targets are spaced in range and have different positions in azimuth and elevation.

strong reflections occur as opaque areas in the image. In this case, the evaluation is done for the four most significant targets in amplitude. According to the distance, a red, a yellow and a green tag are placed close to the targets, where the red tag shows the closest, and usually most important, targets. This way of displaying the information is very intuitive since a strong target within the monitored scene is highlighted in the camera image. Hence, a higher degree of automation is achieved.

Another application is the detection and classification based on image processing. In this case the radar can be combined with a zoom camera pointed to the objects previously detected by the radar. Therefore, a different camera objective is needed, e.g. with a focal length of $f = 75\ mm$, which leads to a field of view of $FOV_h = 5.0°$. This is comparable to the azimuth resolution of the radar, which makes it possible to observe each azimuth sector separately. To point the camera, the two axis gimbal, shown in Fig. 4.3, can be used. The servos of the camera gimbal are linked to the radar processing and receive the azimuth and elevation angles of the most significant target. This could be the one with the highest amplitude or the one which is closest to the radar. The gimbal then moves to the target's direction and offers a much more confined area to be processed by the image processing. The zoom increases the resolution of the target. Object detectors in image processing need a certain minimum number of pixels, on which they can operate. When using a wide-angle objective, the resolution of a target in medium distance would be too low. With a zoom objective the resolution is increased and the probability of detection is higher and a better classification can be performed. Object classification algorithms are not presented here, because they go beyond the scope of this thesis.

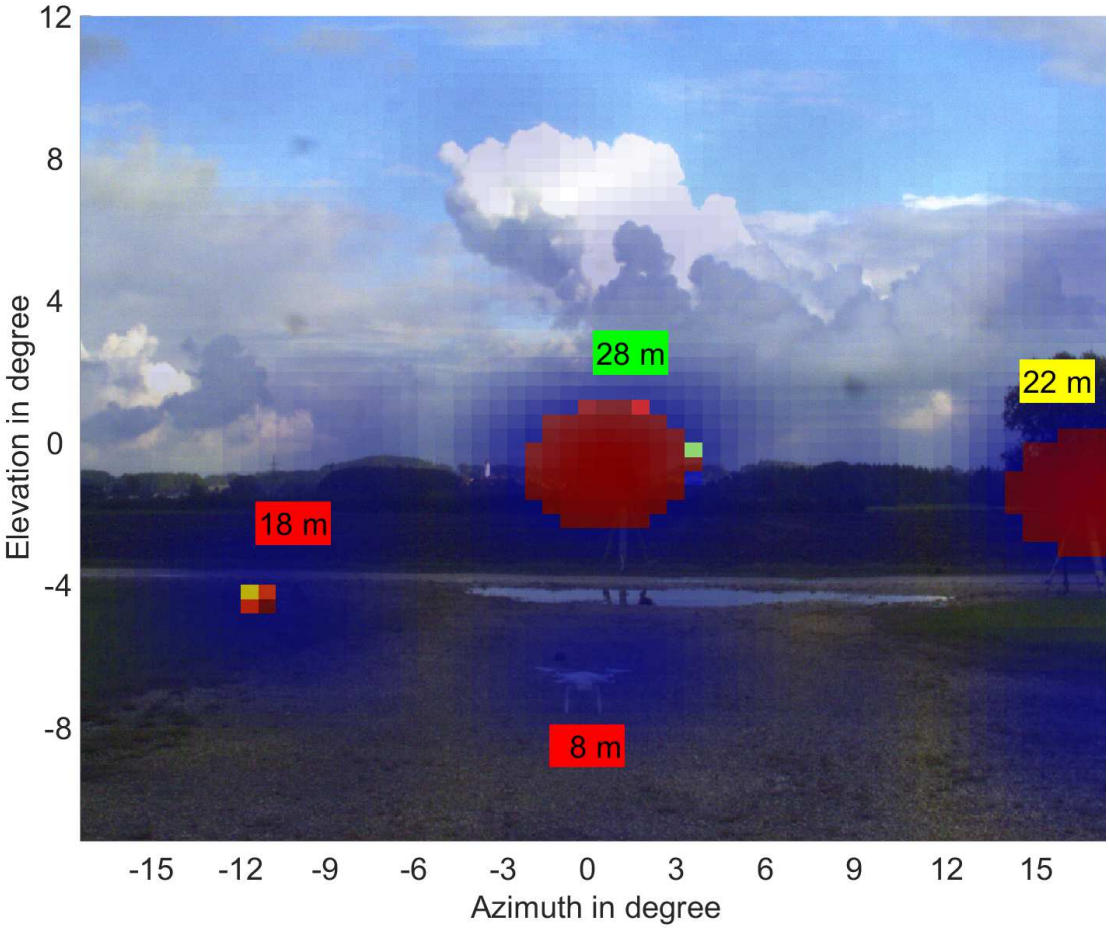

FIGURE 4.33: Camera and radar image overlaid. The color and the level of opaqueness is proportional to the amplitude of the reflection. The targets' ranges are displayed in boxes with different colors. The field of view is limited by the camera.

4.10.2 Scene Imaging

In order to show the full imaging capabilities of the radar system and the 3D-FFT beamforming processing, two scenarios have been used.
The first scene is shown in Fig. 4.34 subsection A. The MIMO radar is positioned at an elevated level, around 20 m from the ground, inside a building and pointing, through a window, towards the ground level.
Range-elevation section views of the 3D radar image captured, along two different Azimuth angles, are presented. In Fig. 4.34 subsection B, a cut at an angle of $\theta = -21°$ is performed. As it can be seen from this picture, a good representation of the scenario capture by camera on the left is achieved. The tree on the left, circled in red, representing the main object in the scenario, is clearly identified. As a matter of fact, the reflections from the tree can be seen starting from the ground level, -25 m below the radar's boresight (Y-Position), at a distance of 25 m from the radar (Z-Position), and propagate all the way up to almost 4 m above the radar's boresight. Additionally, at 55 m from the radar (Z-Position), reflections from the building with the square windows, at the back, can also be noticed. Furthermore, aliasing reflections coming from the walls

of the building where the radar is situated on, are present on the upper part of Fig. 4.34 subsection B. These are due to the fact that the building's walls are outside of the field of view of the radar, therefore the reflections are folding, due to the sampling theorem, inside the captured data.
In Fig. 4.35, instead, a cut at an angle of $\theta = +10°$ is performed. In this case, the tree on the left is not visible anymore, however, the main object of the scenario becomes the tree on the right, circled in red. As it can be seen from Fig. 4.35 subsection B, the reflections from the tree can be seen starting from the ground level, -12 m below the radar's boresight (Y-Position), at a distance of 45 m from the radar (Z-Position), and propagate all the way up to almost 6 m above the radar's boresight.

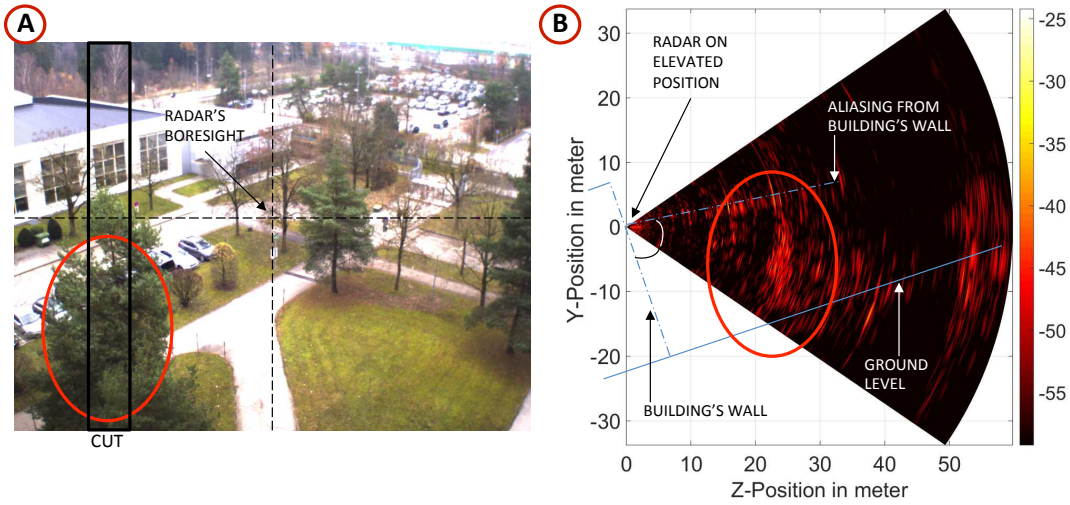

FIGURE 4.34: Imaging scenario captured with in-built camera, on the left (A). Range-elevation section view of the 3D radar image capture, cut at $\theta = -21°$, on the right (B). The left tree, circled in red, is the main object in the scene.

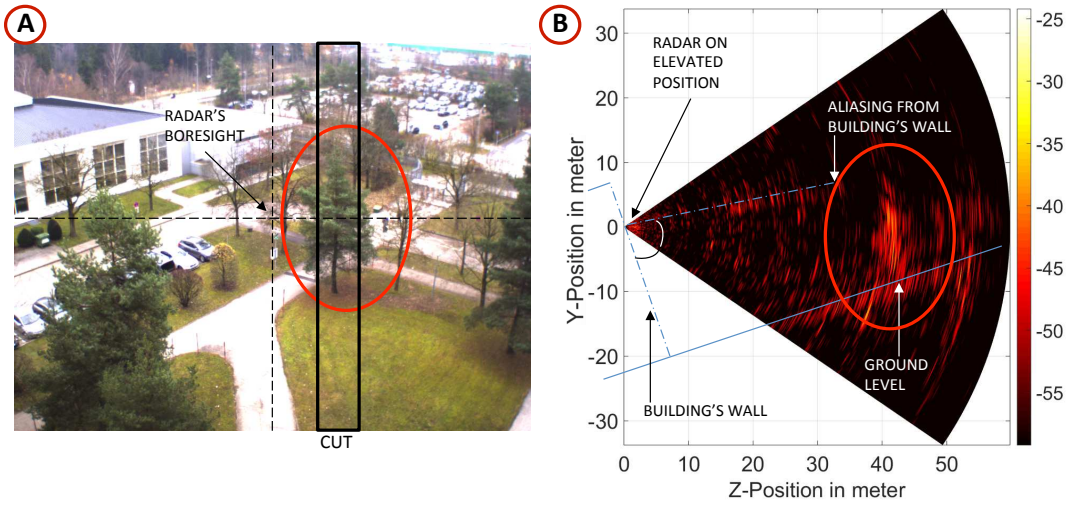

FIGURE 4.35: Imaging scenario captured with in-built camera, on the left (A). Range-elevation section view of the 3D radar image capture, cut at $\theta = +10°$, on the right (B). The right tree, circled in red, is the main object in the scene.

The second scene used is shown in Fig. 4.36 subsection A. The MIMO radar is positioned at a slightly elevated position. As it can be noticed from Fig. 4.36 subsection B, the

two hills, representing the main objects in the scene, are clearly identifiable at distances of 18 m and 33 m from the radar (Z-Position), and are both around 4 m below the radar's boresight. Additionally, as it was previously with the example of the trees, the information on the size of the object is sensed, since, from the reflections, it can be understood that the hills are 1.5 m high.

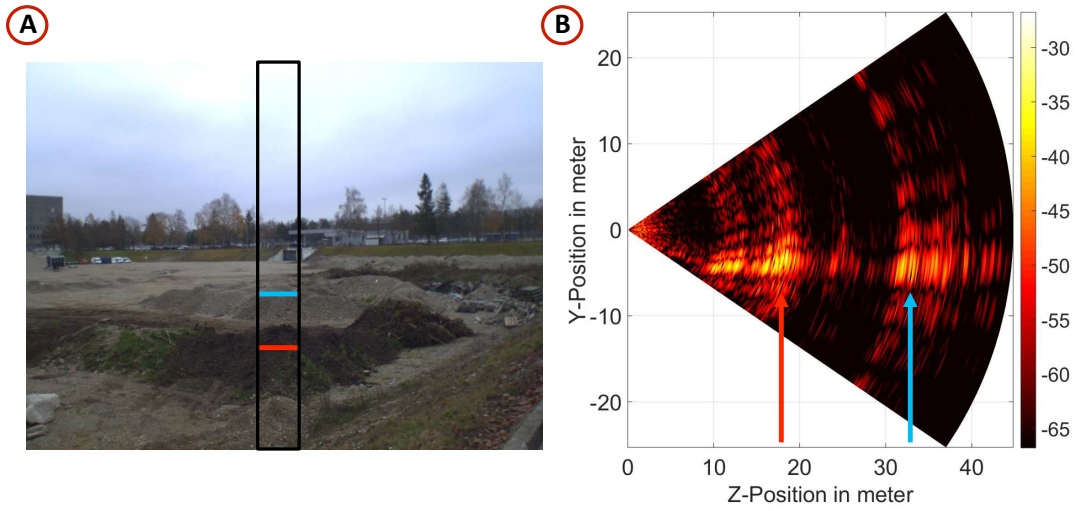

FIGURE 4.36: Imaging scenario captured with in-built camera, on the left (A). Range-elevation section view of the 3D radar image capture, cut at $\theta = 0°$, on the right (B). The two hills represent the main objects in the scene.

These two examples proposed, demonstrate the full capabilities of the 3D MIMO radar demonstrator in correctly reconstructing 3D imaging representations of the captured scenes, including range, Azimuth and elevation information of all objects.

4.10.3 Moving Targets Algorithms and Applications

Measurements have been conducted in order to analyse the performance of the presented MIMO radar demonstrator, in scenarios with moving targets, like in the case of flying UAVs or people walking. In this section, radar captures are shown, together with the description of the algorithms which allow to see a moving target and perform a tracking operation on it. Finally, a scenario where the MIMO radar and the tracking capabilities are used together with a jamming unit, for the tracking and jamming of a small UAV, is presented.

4.10.3.1 Averaging on Consecutive Measurements

As previously described, the radar system performs, through the 3D-FFT beam-forming processing, a 3D sensing of the environment. The 3D image captured by the radar is represented as a 3D matrix in Azimuth, elevation and range and contains the magnitudes of the reflections of all scatterers present in the scene. However, the image also includes static targets which are of no interest in these kind of applications, where

moving targets need to be seen. Therefore, a moving target detection algorithm is implemented by dynamically averaging consecutive radar images. Considering M_k as the 3D matrix which contains Azimuth, elevation and range information of the targets, with $k = 1 \dots N_{Measures}$ and $N_{Measures}$ the number of measurements, then the operation can be seen as

$$M_{k+1} = M_k - \sum_{n=1}^{k} \frac{M_{k-n}}{2^n} \tag{4.12}$$

and it is implemented in the radar processing just before the 3D-FFT block, shown in 4.13. The result achieved is that static reflections in the radar image, starting from the second radar measurement, will be almost entirely removed. Therefore, only reflections which are linked to a different range, Azimuth or elevation position, from one measurement to the next, as in the case of the ones coming from moving targets, will remain. Thus, this prevents static targets, which could possibly have high RCS values, from appearing in the radar image and highlights moving targets. Additionally, a scaling of the dynamic range of the amplitude peaks can then be applied based on the value associated with the highest peak, which will be linked to the RCS of the moving target.
The algorithm here proposed represents a sort of simple change detection algorithm, which works good in conditions of little static object scintillation which could arise, for example, from tree leaves movement due to wind and rain, or particular cases of ground clutter.

4.10.3.2 UAV Detection

The first scenario with a moving target analyzed is that of a UAV flying in opposite direction from the radar, starting from 22 m away and flying to a distance of 35 m, keeping always the same altitude and speeds from 1 m/s up to 4 m/s. A total of six consecutive captures are taken, from the in-built camera displayed on the left, and, simultaneously, the radar sensor displayed on the right. The results are shown in Fig. 4.37, for the first three captures (22-30 m), and Fig. 4.38, for the last three captures (31-35 m). The UAV target is circled in red and it is safe to assume that the nominal RCS of the UAV is in the order of $\sigma \approx 0.15\ m^2$. The radar images shown as Azimuth-range section views of the 3D radar image captures, cut at $\phi = 0°$, are obtained through the use of the averaging algorithm, for the detection of moving targets, previously explained in 4.10.3.1. As it can be seen from these radar captures, displayed in subsections (B), (D) and (F), the reflections from static targets have bene completely removed and mostly only a peak, belonging to the moving UAV, is visible in the image. Through an analysis of Fig. 4.37 and Fig. 4.38, it can be seen that the UAV is moving away from the radar, keeping a fairly central Azimuth angle, and the radar system is able to clearly detect the UAV in all six radar captures. The range and Azimuth values are correct and match the corresponding images captured by the camera. It can be noticed, that the reflected signals belonging to the UAV, get weaker the more the target is moving away from the radar, with the strongest peak reported at -73 dB, in the case of Fig. 4.37, subsection

A, and the lowest at -77 dB, in the case of Fig. 4.38, subsection F.
An important aspect that needs to be pointed out, is the advantage of having a multifunctional system which performs the capture of the scenario through both an optical system and a radar sensor.
It can be clearly seen, by having a closer look to subsections (A), (C) and (E), especially in Fig. 4.38, that the UAV slowly becomes difficult to identify, or actually completely disappears. For example, in Fig. 4.38, subsection (E), the UAV cannot be seen at all. This highlights the intrinsic problematic connected to an only optical based sensor, which poorly performs in low light conditions and is hardly able to identify targets which are at long distances, if not by changing the lenses, and imposing a restriction on the field of view and an increase in the overall costs.
On the other hand, the radar, thanks to its good performance properties in all weather conditions and its material penetration, long range and 3D sensing capabilities, outperforms the camera sensor. As shown in subsections (B), (D) and (F) of Fig. 4.37 and Fig. 4.38, the UAV is always visible, even when it cannot be seen anymore from the camera, and additionally, the position of the targets is also sensed.
However, from the radar images, it is not possible to classify the nature of the target.
Therefore, the proposed multifunctional system, based on both a camera and radar sensor, through the presented application, is proven to have a good performance in detecting even moving objects, with low nominal RCS values, as a UAV, at medium range distances. The camera sensor enables a user to classify the nature of the target, by looking at the corresponding camera image.

4.10.3.3 Tracking on Consecutive Measurements

In order to track a target acquired by the MIMO radar demonstrator, and continuously sense and log its coordinates, information which can be used in conjunction with an alert triggered based system or for steering a camera or antenna towards it, a basic tracking algorithm has been implemented. The same tracking algorithm can be used on the measurements performed for the previous experiment, described in 4.10.3.2.
The target tracking algorithm operates on the M_k and M_{k+1} matrixes, previously described in equation (4.12), therefore, in conjunction with the averaging algorithm, and it is implemented in the radar processing just after the target identification block which follows the 3D-FFT operation, shown in 4.13.
This means that it operates on two consecutive measurements. First, the most significant targets are extracted by applying a threshold above the noise floor. This is repeated for the next measurement and consecutively a comparison between the two sets of potential targets is calculated. For the comparison, the euclidean norm of the coordinates between all targets of M_k and all targets of M_{k+1} is calculated. By applying a constraint for the norm's value, which is similar to creating a virtual sphere around the target from snapshot M_k, only targets which fulfil the constraint are considered as targets. The algorithm has to be adapted to the expected speed of the targets. This way, it can be avoided that single event reflections appear as targets.
Finally, an option based target selection is applied. For example, either the target closest to the radar, the furthest, the one which is at specific range or Azimuth values or

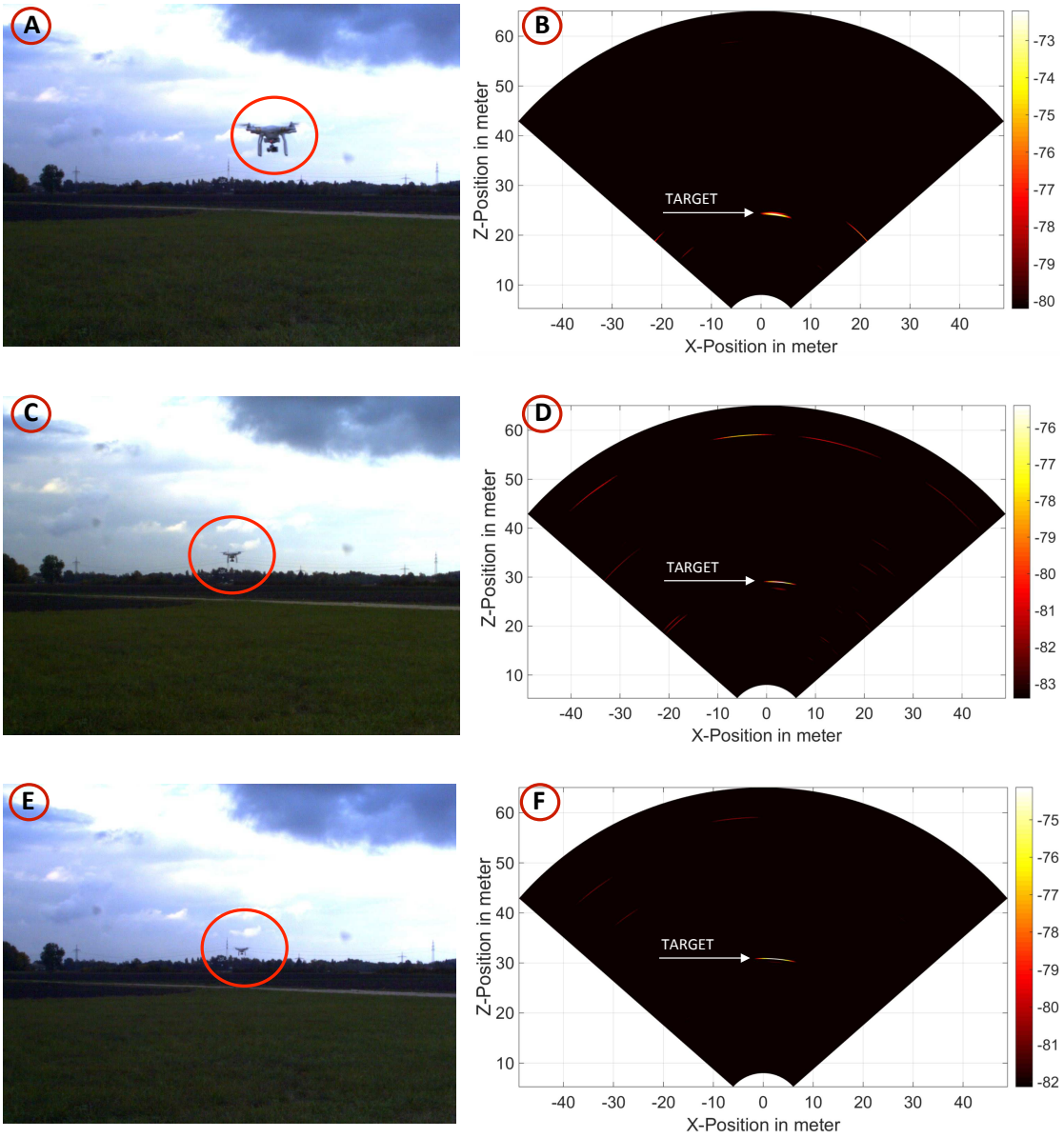

FIGURE 4.37: Images captured with in-built camera, on the left, in (A), (C) and (E). The scene presents a UAV flying from a distance of 22 m to a distance of 30 m. Corresponding Azimuth-range section views of the 3D radar image captures, cut at $\phi = 0°$, are shown on the right, in (B), (D) and (F).

simply the target with the strongest reflection, can be selected.

After acquisition, selection and tracking of a target, the 3D coordinates (range, Azimuth and elevation) are continuously logged (optionally into a file). In the radar images which have the tracking procedures enabled, white crosses are displayed for each tracked position of a target. A large cross in the figures represents the strongest reflecting target. Additionally, the tracking algorithm will display the last two tracking positions, for better readability of the plot, and in order to create a trace. Finally, the second most strong reflecting target is displayed with a smaller sized white cross.

Examples to show the performance of the tracking algorithm in various scenarios are shown. At first for the case of the tracking of a walking person and, afterwards, to

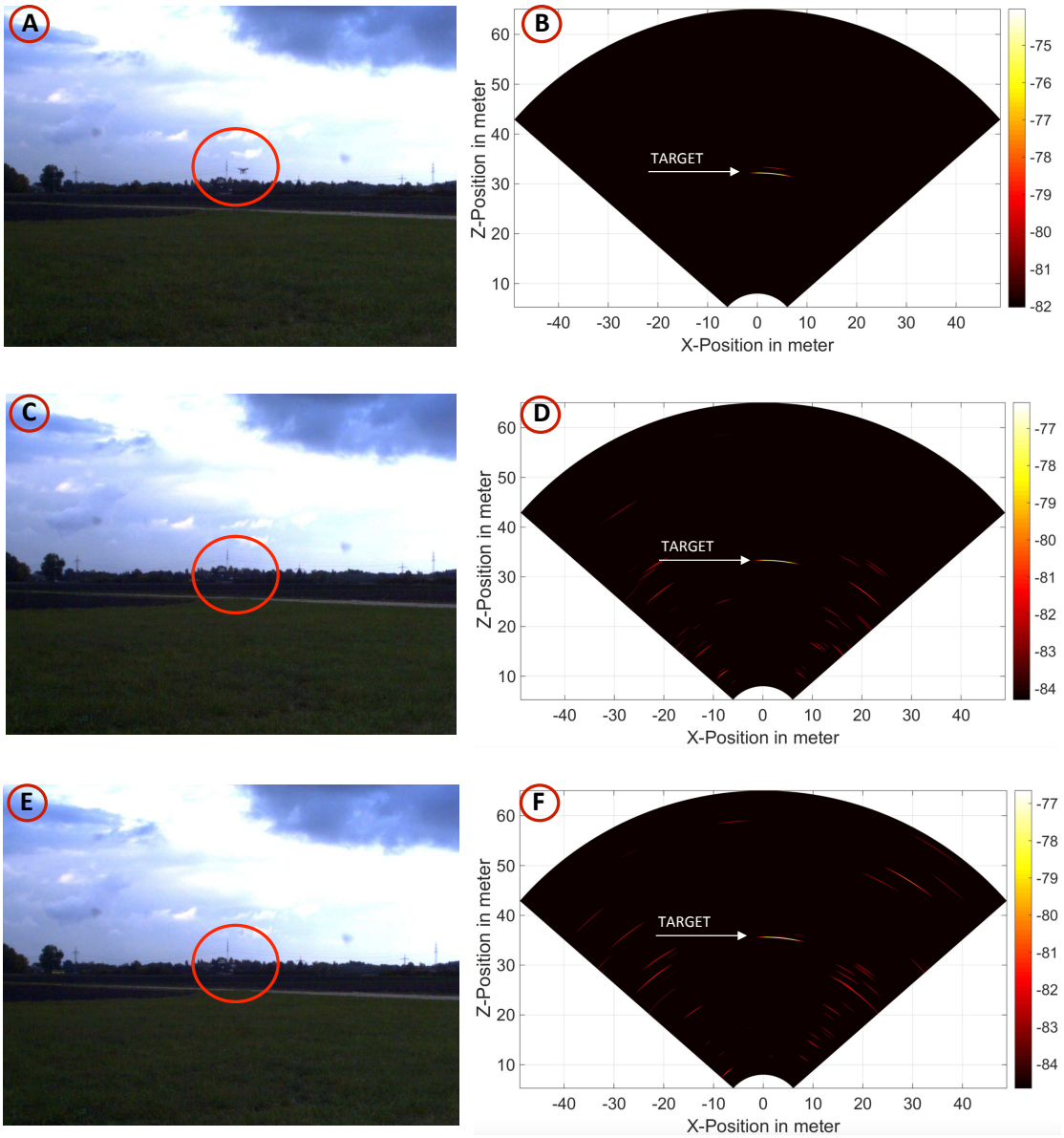

FIGURE 4.38: Images captured with in-built camera, on the left, in (A), (C) and (E). The scene presents a UAV flying from a distance of 31 m to a distance of 35 m. Corresponding Azimuth-range section views of the 3D radar image captures, cut at $\phi = 0°$, are shown on the right, in (B), (D) and (F).

show how the tracking can be used, in real-time, to pilot the in built two-axis gimbal, described in Fig. 4.3. Finally, an example of UAV jamming application is analyzed, where the target which is closest to the radar is selected and its coordinates sent to an external servo controller board, which then points a directional antenna towards the target, which is transmitting a jamming signal.

4.10.3.4 Person Detection and Tracking

The second scenario with a moving target analyzed is that of a person moving towards the radar, starting from 55.6 m away and walking to a distance of 24.9 m, at an elevation

angle close to $\phi = 0°$, an Azimuth angle which is increasing from $\theta = 11.6°$ to $\theta = 27.5°$, and an average speed of 1.4 m/s. A total of six consecutive captures are taken, simultaneously, from the in-built camera, displayed on the left, and the radar sensor, displayed on the right. The results are shown in Fig. 4.39, for the first three captures (55.6-46 m), and Fig. 4.40, for the last three captures (40.9-24.9 m). The target (person) is circled in red and it is safe to assume that the nominal RCS of a person is in the order of $\sigma \approx 1\ m^2$. The radar images shown as Azimuth-range section views of the 3D radar image captures, cut at $\phi = 0°$, are obtained through the use of both the averaging algorithm, for the detection of moving targets, previously explained in 4.10.3.1, and the tracking procedures described in 4.10.3.3.

As it can be seen from these radar captures displayed in subsections (B), (D) and (F), due to the averaging algorithm, the reflections from static targets have bene completely removed and mostly only a peak, belonging to the walking person, is visible in the image. Additionally, the white crosses visible in the image, are displayed by the tracking procedures for each tracked position of a target. A large cross in the figures represents the position of the strongest reflecting target, whereas a smaller cross represents the second most reflecting target. In the images, additionally to the white cross at the position of the strongest and tracked target, and in order to keep a trace of the target, other crosses are visible. These represent the old position, or trace, of the target. Through an analysis of Fig. 4.39 and Fig. 4.40, it can be seen that the person is walking closer to the radar, moving from left to right, therefore increasing the Azimuth angle with respect to the radar's position, and the radar system is able to clearly detect the person and its position in all six radar captures. The range and Azimuth values are correct and match the corresponding images captured by the camera. Additionally to previously presented radar images, in these images, the target's range (R) and Azimuth (A) values, for better readability of the plot, are displayed in the bottom left part of the picture.

As in the case of the previously analyzed scenario with the UAV in section 4.10.3.2, the advantages of having a multifunctional system which performs a capturing with both a camera and a radar system, are now analyzed.

The presented scene, represents a fairly simple scenario that can be captured by a camera sensor. The light conditions are good and there are not so many objects in the scene, despite fields, trees in the background and a person walking on a road from left to right, moving closer to the camera. Therefore, in all subsections (A), (C) and (E) of Fig. 4.39 and Fig. 4.40, the target can be seen.

However, in the case of fog, rain, snow or simply during night time, the identification would not be possible.

Therefore, the proposed multifunctional system, based on both a camera and radar sensor, through the presented application, is proven to have a good performance in detecting moving objects, with low nominal RCS values, as a walking person, at medium range distances. Additionally, thanks to the tracking capability, the coordinates of the most reflecting object in the scene are captured and a trace is made for its previous positions.

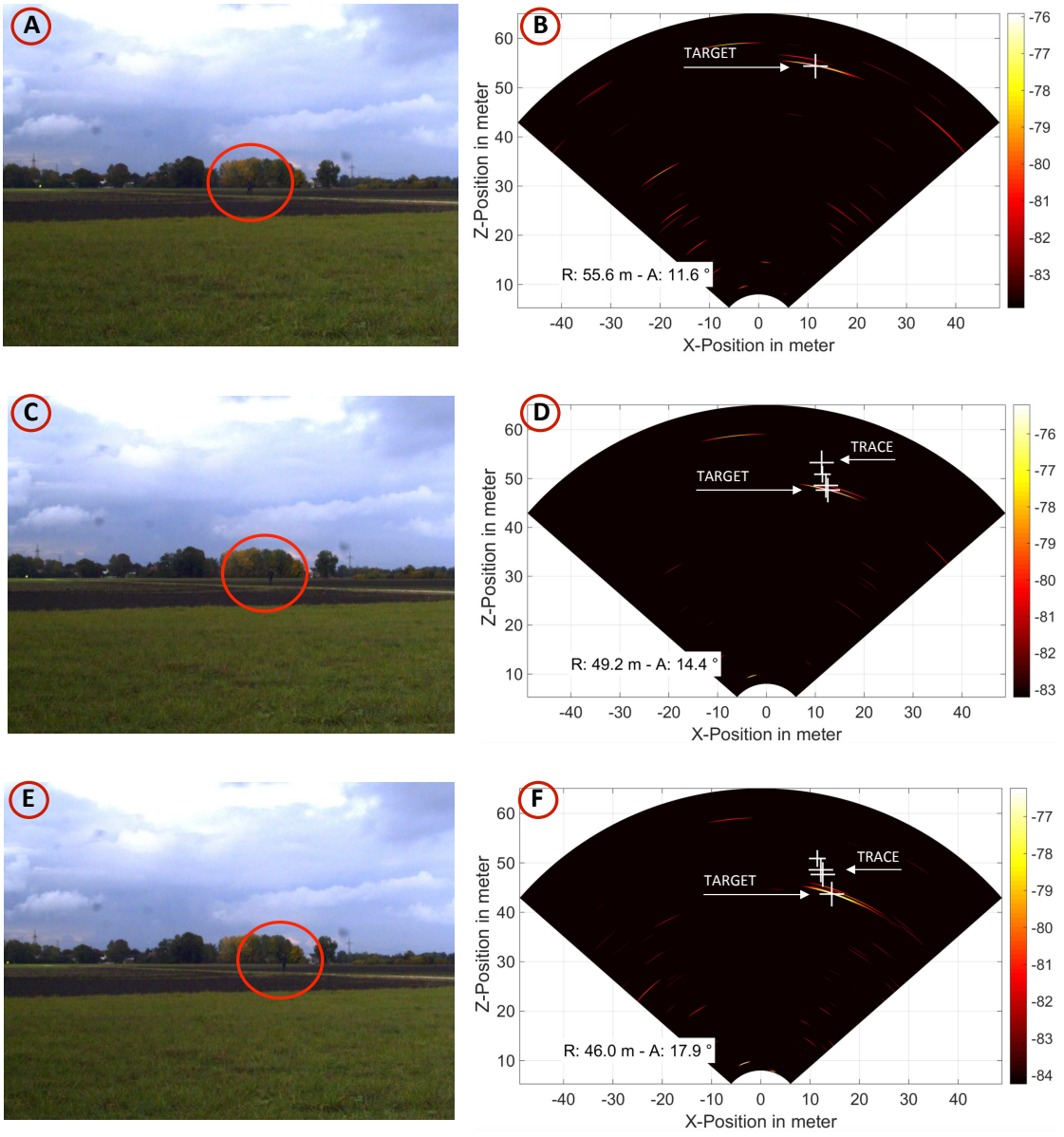

FIGURE 4.39: Images captured with in-built camera, on the left, in (A), (C) and (E). The scene presents a person walking from a distance of 55.6 m and Azimuth angle of $\theta = 11.6°$, to a distance of 46 m and Azimuth angle of $\theta = 17.9°$. Corresponding Azimuth-range section views of the 3D radar image captures, cut at $\phi = 0°$, are shown on the right, in (B), (D) and (F).

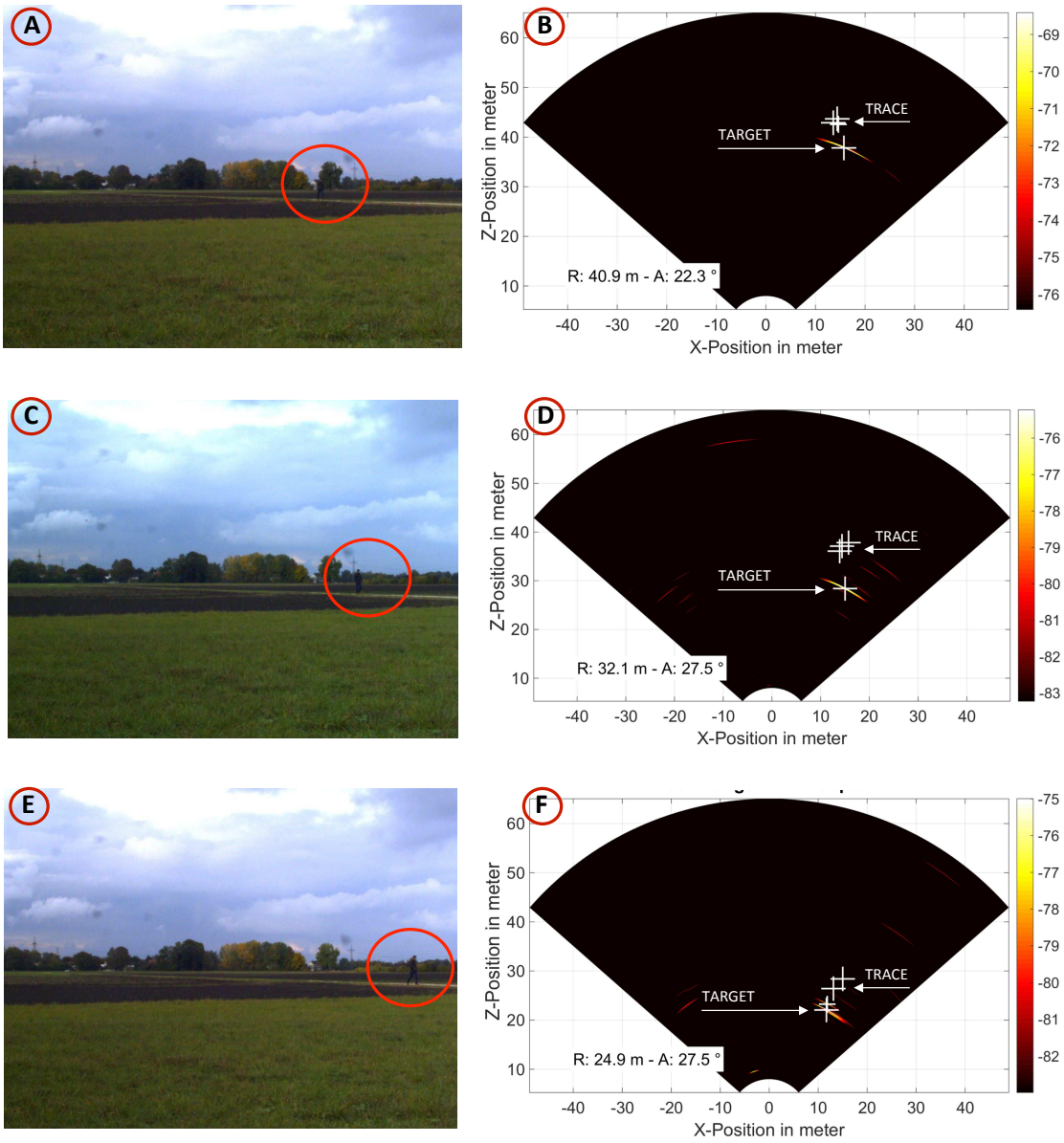

FIGURE 4.40: Images captured with in-built camera, on the left, in (A), (C) and (E). The scene presents a person walking from a distance of 40.9 m and Azimuth angle of $\theta = 22.3°$, to a distance of 24.9 m and Azimuth angle of $\theta = 27.5°$. Corresponding Azimuth-range section views of the 3D radar image captures, cut at $\phi = 0°$, are shown on the right, in (B), (D) and (F).

4.10.3.5 UAV Tracking and Jamming

This section presents an anti-UAV system which consists of combining the MIMO radar with a directional jammer working at 2.4 GHz [164]. The tracking algorithm evaluates the movement of a target in the scene captured by the radar. If a potential threat is identified, the directional antenna, mounted on a two-axis gimbal, is steered to the target. With the use of a directional antenna, the control signal of the UAV can be superimposed by a strong jamming signal which makes controlling of the UAV impossible.
If a UAV loses its control signal, it might keep its position and hover at the same location or it might have an integrated "coming home" function, which would return it to its take-off point via Global Positioning System (GPS). Another possibility would be that it performs an emergency landing at its current position. Even if the drone would move further or back to its base station, the radar would track it and continue blocking the communication. This way, it is possible to secure critical infrastructure against most of the commercially available drones using WiFi frequencies, for control and payload transmission.
Many systems for UAV detection exist, which use different techniques. One of them, consists in the detection of the rotor sound with a microphone array [165]. This approach however is limited to rather quiet environments. This makes it impractical for the aspired use in urban environments where voices, fans, engines and other noise sources are present. Another way to detect a UAV is via its emitted signals [166]. Its control and video links can be targeted with a directional antenna. The drawback of the RF link detection is that the UAV's signals are used for the detection. If the UAV follows a preprogrammed GPS path, it will be invisible for the system. Camera based systems, like described in [167], can detect a drone in good weather conditions, but have poor performance in foggy or dark environments. In contrast, a radar system can also detect a UAV if there is no control signal or if the sight conditions are poor. To prevent a UAV from entering a certain zone, conventional rifles, High Energy Lasers (HEL), Electromagnetic Pulse (EMP) guns and RF jammers can be used. There are several products available which detect drones and provide countermeasures, but as they are designed for military use, the prices are rather high.

A cost effective and efficient approach, based on the MIMO radar demonstrator presented in this chapter, an RF jammer and a directional antenna in the 2.4 GHz band is now described. Since the UAV detection is based on radar technology, it can be operated in all weather conditions. Additionally, the system is independent of RF signals sent by the UAV, which means that also UAVs with a preprogrammed GPS path can be detected. The 3D target coordinates delivered by the radar and the tracking algorithm are used to steer a directional antenna in the direction of the target. By sending a jamming signal through the antenna, any communication link of the UAV can be blocked. In this way, the system can jam only the UAV instead of all the surroundings. The use of a directed antenna makes it possible to jam UAVs at longer distances, as compared to omni-directional antennas [168]. Thus, the system is able to prevent most of the consumer UAVs from entering a certain area. The possible application of the proposed system is to shield a predefined area against the approaching of unwanted UAVs. Examples

of situations where the system is helpful are long-term surveillance of security areas or temporary protection of mass events.

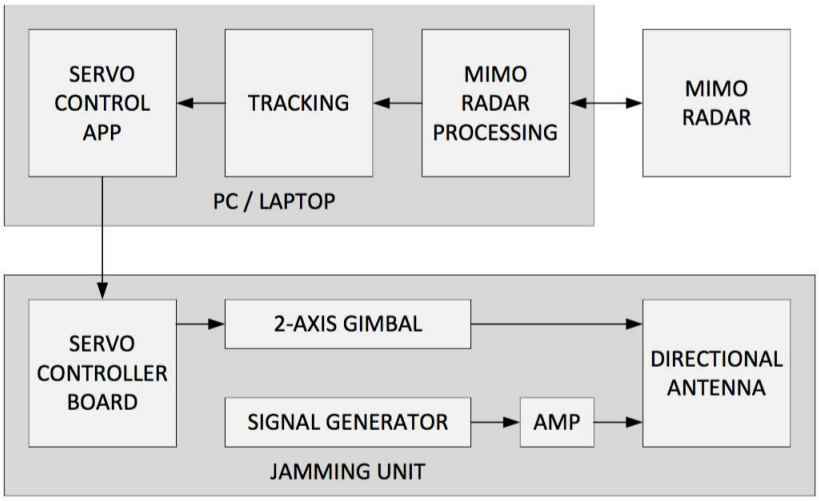

FIGURE 4.41: Block diagram of the MIMO radar and jamming system.

A block diagram of the proposed system is shown in Fig. 4.41. The MIMO radar system is the same as discussed in this chapter, in 4.3, and it is based on the same 3D-FFT beam-forming processing. Additionally, it includes the averaging and tracking capabilities, discussed in 4.10.3.1 and 4.10.3.3, respectively. However, in addition to the previous system, a jamming unit is used, together with a servo controller board and application running on the PC or laptop. The jamming unit consists of a Commercial Off The Shelf (COTS) signal generator with a built in modulator, connected to an optional amplifier and a directional antenna. The directional antenna is a COTS 2.4 GHz antenna with 9 dBi gain. As it can be seen in Fig. 4.42, the antenna is mounted on a two-axis gimbal which can steer in both directions, azimuth and elevation. The servo motors receive their PWM signals from a servo controller board which is connected to the laptop via USB. The servo controller application (APP), receives the coordinates from the tracking algorithm and generates signals for the servo controller board.

A COTS signal generator is used to create the jamming signal. With an additional amplifier a maximum output power of 30 dBm can be reached. With the built-in modulator, a band limited noise signal (5 MHz) is modulated on a carrier that can be placed in the range of 2.4 GHz to 2.5 GHz. The overall jamming signal has a bandwidth of 10 MHz for an AM modulation, which is sufficient to block one WiFi channel. The jamming signal is directly routed to the directional antenna which is steered according to the tracking algorithm. An illustration of this is shown in Fig. 4.43, where a UAV, the corresponding remote controller (RC) and the radar and jamming unit can be seen. The outer circle shows the coverage of the jamming unit using a directional antenna, the inner one with an omni-directional antenna. The maximum range can be roughly estimated by using the FSPL equation, previously introduced in (2.3).
In the scenario, two links exist. One from the remote controller to the UAV and one from the jammer to the UAV. For both, the link budget is calculated. On the one hand, if the remote control with 20 dBm output power is assumed to be at 20 m distance

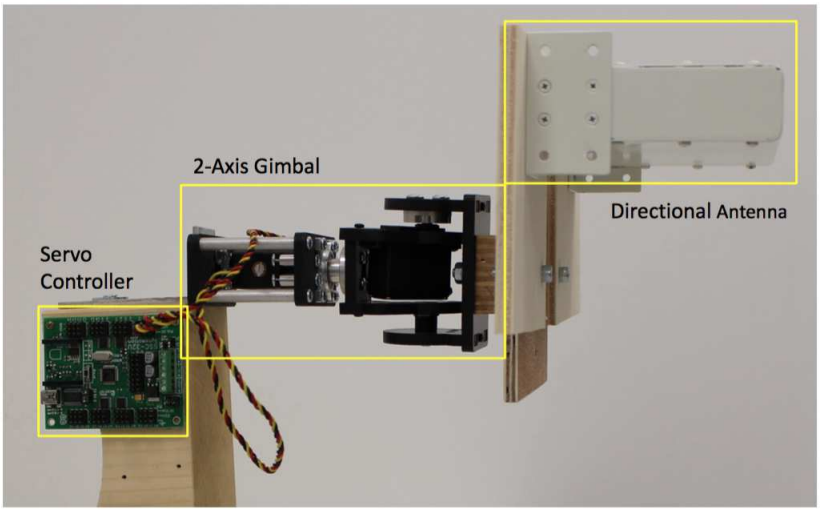

FIGURE 4.42: Prototype of the jamming unit consisting of a servo controller, a 2-axis gimbal and a directional antenna.

from the UAV and both transmit and receive antennas are omni-directional, then the resulting signal strength is about -46 dBm. On the other hand, if the jammer sends a band-limited noise signal with 30 dBm via an antenna with 1 dBi gain, the signal will have an amplitude of about -42 dBm in 250 m distance. Since the jamming signal power that reaches a UAV at 250 m is higher than the control link power, even when the remote controller is near by, the UAV will not be manoeuvrable anymore. Considering that the maximum range of the radar is about 250 m, a 16 dBi antenna is sufficient.

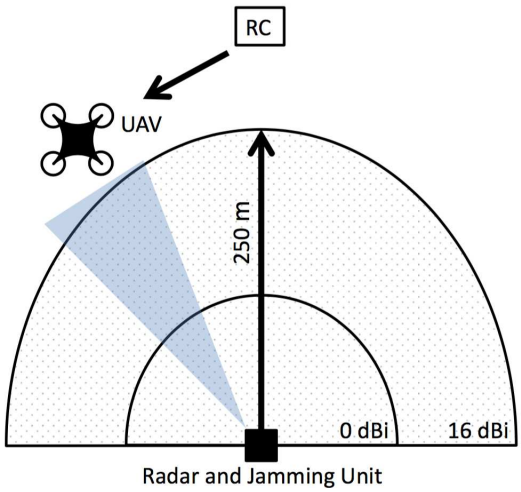

FIGURE 4.43: The use of a directional antenna allows to jam at longer distances also when the remote control (RC) is close by. In the given scenario a maximum range of 250 m is reached with a 16 dBi antenna.

In order to verify the performance of the system, an outdoor test is performed. As it can be seen in Fig. 4.44, subsection A, the test setup consists of a MIMO radar, a jammer and a processing unit. As target, a COTS UAV [169] is used and manoeuvred in an area which could be a security zone, for example. The UAV is controlled via a smartphone application, which uses the 2.4 GHz WiFi band and is flown in the field of view of the

radar.

As described in the previous chapter, the MIMO radar system is constantly observing a field of view of 100° and the update rate of the system is about 3 s. If a potential target enters the security zone and is detected, the tracking algorithm starts. After two consecutive measurements, information about moving targets can be extracted, as described before in 4.10.3.3. Fig. 4.44, subsection B, shows an Azimuth-range view generated by the MIMO radar. As for the cases analyzed before, a suppression of the static targets is done through the averaging algorithm implemented and moving targets are highlighted. The white crosses mark the track of the identified target. A big cross in the figure represents the strongest reflecting target, which is the UAV, at about 60 m distance from the radar. Additionally, the tracking algorithm shows the two last tracking positions for better readability of the plot.

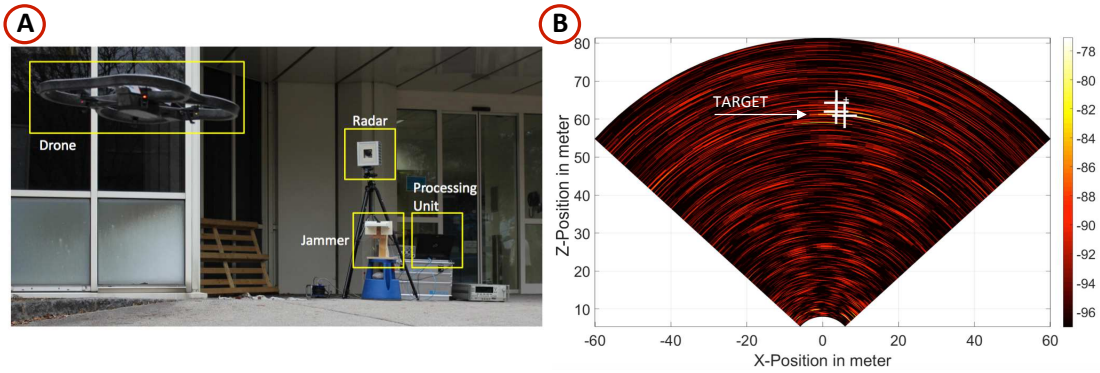

FIGURE 4.44: Measurement setup consisting of the 3D MIMO radar, jammer and processing unit with a drone hovering in the foreground, on the left (A). On the right (B), an Azimuth-range view of a drone approaching at 60 m, as captured by the MIMO radar, is shown. The white crosses represent the tracked target.

The determined coordinates of the target are sent to a conversion program written in *C* code and implemented in a MEX file launched in the MATLAB environment, which does the coordinate transformation between the radar and the servo controller board for the two-axis gimbal. The program translates the coordinates to serial packets, containing information about the desired pulse width of both the servo motors. After this process, the coordinates are sent via USB to the servo controller board, which creates the PWM signals for the servo motors. Consecutively, the directional antenna is steered in the direction of the target by the servos. When the position is reached, the jamming signal is fed to the antenna and blocks the communication between the smartphone and the drone. The control signal is immediately lost and the drone cannot be manoeuvred anymore. Fig. 4.45 shows the UAV control GUI, as captured by the smartphone display, in the moment when the jammer is active. As the radar is still tracking the UAV, the directional antenna follows the UAV in case it moves from its position. The UAV used in this test is programmed so that it hovers and keeps its position when the signal is lost. Overtaking control is not possible until the jammer is switched off.

The system can be used in scenarios where many people are present and do not even notice the operation, since the jamming signal is spatially confined. The proposed system has a higher output power than allowed by EU regulations. Therefore, it is meant to

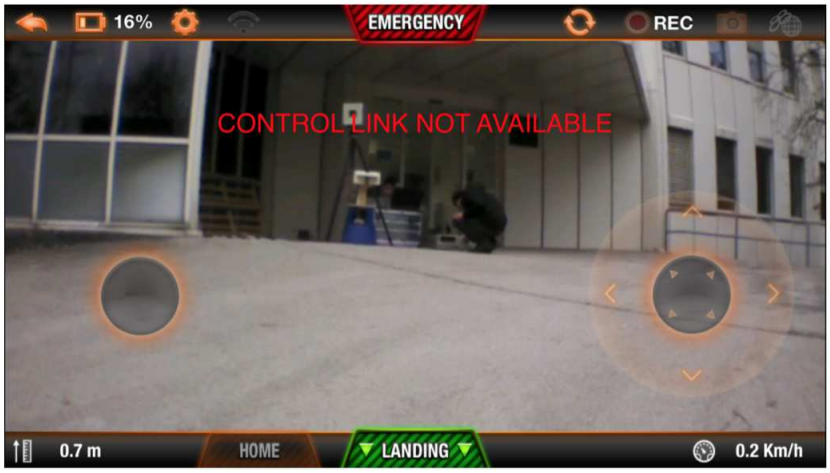

FIGURE 4.45: Screenshot of the drone control GUI while jammer is active. Control link is lost and can only be retaken by deactivating the jammer and reconnecting to the WiFi.

be used by authorities and governmental institutions which have permission to operate devices above the law constraints applying for civil users.

4.11 Chapter's Conclusions

An innovative and successful implementation of a complete 3D imaging MIMO radar, based on a 16x16 antenna array, an advanced ZYNQ based digital architecture and a fast 3D-FFT beam-forming radar processing, has been presented. The goal to achieve a portable, but also, compact and faster system has been reached, by overall miniaturisation and improvement in all aspects of the previous demonstrator from Chapter 3, from the RF front-end, to the digital architecture and the radar processing algorithms. One of the most important aspects which allowed a faster radar capturing to be achieved, is the implementation of a digital architecture into a single board, including the ADCs, and the development of a complete processing which conjointly elaborates the radar data between three domains, which are the FPGA and ARM firmware's and 3D-FFT beam-forming processing running on the PC.
Additionally, the architecture has been brought even further, with the integration of multifunction capabilities, achieved through the use of additional sensors and/or actuators, such as a camera or a two-axis gimbal, for the tracking of targets.
A detailed hardware and software architecture's description has been presented, together with a description of the 3D-FFT beam-forming based DOA estimation and the MIMO cycle timing. The performance and resolutions of the multifunctional system have been verified by measurements in both an anechoic chamber and outdoors, in multi-target environments, highlighting the synergies among the two functionalities. The advantages of a MIMO radar system over a camera based system are highlighted, as well as the advantages of having both sensors operating into a unique system.
The results presented, show the full capabilities of the system in detecting multiple targets, corner cubes, UAVs and people, even in situations where the targets are moving,

and correctly achieving a 3D reconstruction of the surroundings. This yields a complete sensing of range, Azimuth and elevation of the targets, and it is shown how to combine this information with a camera image.
Furthermore, a low-cost approach to prevent commercial UAVs from entering a security area is also shown, presenting the combination of the MIMO radar with tracking capabilities and a directional jammer connected to a two-axis gimbal, which demonstrated an effective solution against flying targets.

Therefore, the outcome of this chapter, is a demonstration that the developed 3D FMCW MIMO radar demonstrator has been proved to be suitable for detection of various types of targets in a multitude of applications. Additionally to applications for the surveillance of wide-zones and critical infrastructures, with this demonstrator here presented, thanks to its size and fast sensing of 3D information from targets, a new range of applications can be addressed, as for example, all those situations where high-resolution 3D imaging sensors are required to have a small size factor, because the space limitation is critical. This includes, but it is not limited to, applications of situational awareness, detection and object classification in flying platforms, landing aid for helicopters in brown-out/ white-out situations and autonomous flying operations.

The RF and digital hardware architectures here presented, represent a step closer towards the implementation of a nearly real-time capable 3D imaging radar. However, the orthogonality of the signal is still achieved by adoption of a TDM scheme, thus, creating a delay for each switching of every transmit antenna. In the next chapters, a completely new type of radar architecture will be introduced, where the orthogonality is achieved by means of orthogonal coding between transmit signals and the waveforms adopted are not going to be the FMCW radar signals generated in the DDS and PLL unit anymore, but digitally created OFDM signals.

Chapter 5

OFDM Radars Concepts and Parametrization

5.1 Chapter's Introduction

The previous chapters presented concepts, architecture's and algorithm's implementations for the signal processing of FMCW based MIMO radars, operating with TDM schemes.
In this chapter, a new radar architecture is introduced, which is based on the concepts and theory of OFDM signals, well known in communication's systems, therefore, gaining the name of OFDM radar.
An OFDM signal is composed of a set of sub-carriers that are mathematically orthogonal in the time domain, i.e., each carrier has an integer number of cycles over a symbol period [170], [171], [172]. Consequently, the spectrum of each carrier has a null at the center frequency of the other carriers in the system, and thus a higher level of spectral efficiency can be achieved. The composition from a multitude of orthogonal sub-carriers, makes OFDM radars particularly suitable for real-time MIMO radar applications. The allocation of orthogonal coded waveforms to the different transmit channels of the radar allows the simultaneous operation of all transmit channels of a MIMO radar, in an interference-free manner.
Compared to MIMO radars based on a TDM architecture, which have to operate their transmitters sequentially, this is a big advantage of OFDM MIMO radars regarding real-time performance. Digital beamforming methods for image reconstruction with high angular resolutions can be applied in a similar way as to FMCW MIMO radars. The RF front-end circuitry of OFDM radars, however, differs from the one of other types of radars. OFDM radars are based on the transmission and reception of broadband vector-modulated signals. Direct cross-talk from transmit antennas to receive antennas for FMCW radars results in very low beat frequencies that can be filtered out at an early stage using analogue high-pass filters. Pulse radars can avoid this effect by activating the receive path after the pulse has been sent. Since both of these methods cannot be applied to OFDM radars, the whole analogue and digital signal processing chain of the receivers has to be dimensioned with a high dynamic range, so that weak reflections can

be detected even in the presence of these strong cross-talk signals.
To cope with such highly dynamic signals, a front-end and antenna array design that minimizes the TX-RX crosstalk, therefore, is inevitable, as well as a signal processing that minimizes the inherent Crest factor of the OFDM signals [173], [174]. As it will be discussed in Chapter 6, specific waveforms which have a constant envelope and can address a solution to these problematic, are proposed in this thesis.
Finally, the use of OFDM radar waveforms which can carry information, paves the way for the implementation of systems which are able to operate both as radar's and communication's system [175]. Moreover, due to the fact that MIMO radars are being integrated in every vehicle and because they all operate at the same frequency bands, in proximity to each other and mostly at the same time, interference occurs [176]. With an OFDM architecture, the use of digitally created OFDM radar signals and coding techniques, the problematics of future radars' interference could be mitigated.

The aim of this chapter is to present a brief introduction to the basics of OFDM based radars, focusing the attention on the waveforms parameter's characterization. In order to give a better understanding of the influence of the parameters chosen in the waveform's design of OFDM radars, an example of system concept is created and analyzed, which aims at addressing specific applications. As previously discussed in Chapter 1, the ideas for the creation of an OFDM based MIMO radar, derived from the research and collaboration of Airbus and other partners, within a German's government sponsored project, named "FAST - Fast Actuators Sensors and Transceivers". The tasks include the implementation of situational awareness, anti-collision, and imaging technologies for flying vehicles, such as airplanes, helicopters, but also air-taxis and UAVs. However, in a real-time capable manner, which is why OFDM has been chosen as the preferred architecture, together with the possibility to flexibly allocate the carriers and the carrier's contents. Therefore, considering these applications, a set of requirements that should be met has been studied and identified, and presented in [56]: the system shall be affordable for civil operators, have near-field obstacle detection range of up to 250 m that guarantees minimum 10 seconds warning time, shall be integrated on flying platforms and not be impaired by any weather conditions. In this type of flying platform's operation scenarios, moving objects with a speed in the range of 0-23 m/s are to be expected and the sufficient performance parameters to be achieved are range resolution in the range of 3 meters, angular resolution of 7° (achieved by the chosen antenna configuration) and a Doppler resolution in the range of 0.5 to 1 m/s. The chosen system's frequency is f_C = 17 GHz according to the airborne radar band.
Taking into consideration the performances required, the decision of the system parameters is then based on the chosen hardware capabilities and on the impairments in the OFDM system, including Doppler shifts, dispersive fading, timing and frequency offsets. The proposed system parametrization in this chapter is, therefore, given according to the real-time multichannel system requirements, as specified above. However, the procedure can flexibly be adapted to different needs.

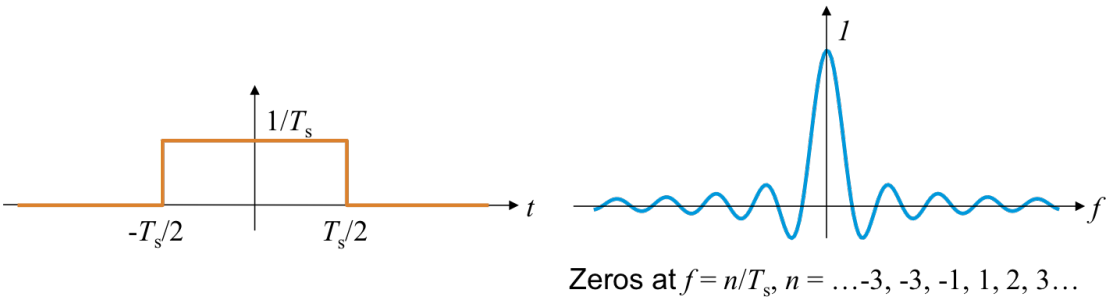

FIGURE 5.1: Generation of OFDM carriers. The basis is a rect-function with symbol duration T_s, displayed on the left. The spectrum of the rect-function, which is the sinc-function, is displayed on the right.

5.2 OFDM Theory

Generally, an OFDM signal can be regarded as a time-limited form of multi-carrier modulation [175], and it is composed of symbols and sub-carriers. The available and/or required spectrum in OFDM is covered by the multiple orthogonal sub-carriers, which are all de-correlated due to their pulse duration T_s being inverse to the sub-carrier's distance $\Delta f = 1/T_s$ [177]. Considering N and M as the number of sub-carrier and the number of symbols, respectively, the transmit pulse, or OFDM frame, which covers the whole bandwidth B, is defined as $N_{FRAME} = N \times M$ and has a duration of $T_{TOT} = M \times T_s$. Let $s(n)_{n=0}^{N-1}$ be one of the complex symbols to be transmitted through the OFDM modulation, then the modulated OFDM signal can be expressed as

$$s(t) = \sum_{n=0}^{N-1} s_n e^{j2\pi f_n t} = \sum_{n=0}^{N-1} s_n \phi_n(t) \quad \text{for} \quad 0 \leq t \leq T_s \tag{5.1}$$

where $f_n = f_0 + k\Delta f$ and

$$\phi_n(t) = \begin{cases} e^{j2\pi f_n t} & \text{if } 0 \leq t \leq T_s \\ 0 & \text{otherwise} \end{cases} \tag{5.2}$$

for $n = 0, 1, \ldots, N-1$. The rect-function, whose corresponding spectrum is the sinc-function, as shown in Fig. 5.1 on the left and right, respectively, can be considered the basis and can be seen expressed as $\frac{1}{T_s} rect\left(\frac{t}{T_s}\right)$. Consequently, the generation of a set of orthogonal basis functions can be obtained, by shifting sinc-functions in frequency domain by multiplication with the complex carriers [178]. This is represented in Fig. 5.2, where an example of OFDM symbol composed of four orthogonal subcarriers, with spacing Δf, is shown.

In order for the receiver to demodulate the OFDM signal, the symbol duration must be long enough, such that $T_s \Delta f = 1$, which is called the orthogonality condition.
To deal with the delay spread of the channel, a cyclic extension, knows as cyclic prefix (CP), is usually used in OFDM systems [179]. The introduction and removal of the cyclic prefix, essentially also converts the linear convolution OFDM channel to a circular convolution channel. Furthermore, since the eigen functions of a circular convolution

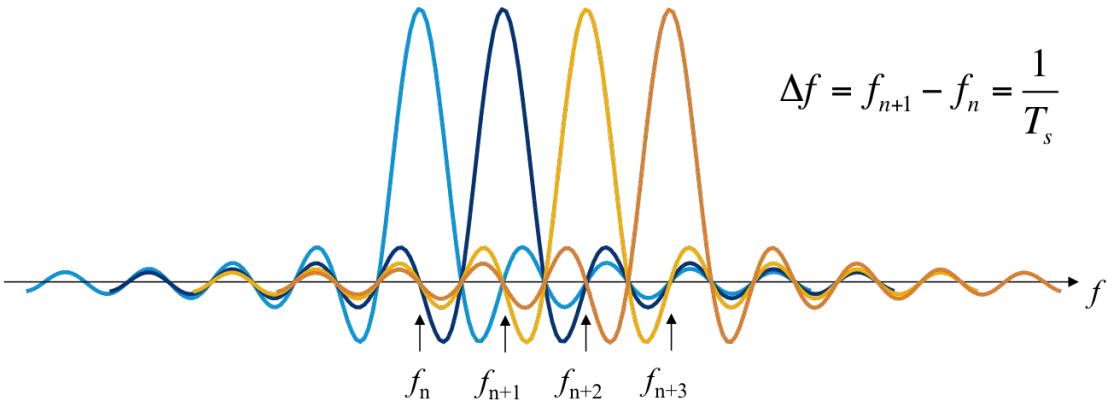

FIGURE 5.2: Example of OFDM symbol composed of four orthogonal subcarriers with spacing Δf

channel are the DFT kernels, the OFDM receiver can be simplified. Let T_{CP} denote the length of a cyclic prefix that is inserted at the beginning of an OFDM symbol, extracted from the end of the symbol. Thus, the OFDM signal $s(t)$ can be extended into $\bar{s}(t)$ by

$$\bar{s}(t) = \begin{cases} s(t) & \text{if } 0 \leq t \leq T_s \\ s(t - T_s) & \text{if } T_s \leq t \leq T_s + T_{CP} \end{cases} \tag{5.3}$$

With the cyclic extension, the actual OFDM symbol duration is increased from T_s to $T_{OFDM} = T_s + T_{CP}$. For an OFDM signal consisting of N subchannels, the signal bandwidth is about $(N+1)\Delta f$ and the total transmission rate of the OFDM signal is $\frac{N}{T}$ symbol/sec, thus the bandwidth efficiency is

$$\begin{aligned} \eta &= \frac{N/T}{(N+1)\Delta f} \\ &= \frac{1}{1+\frac{1}{N}} \frac{1}{1+\frac{T_{CP}}{T_s}} \end{aligned} \tag{5.4}$$

Since for most practical OFDM systems, $N >> 1$ and $T_{CP} << T_s$, then $\eta \approx 1$.

Considering $D(n,m)$ as the data matrix that is to be transmitted from the OFDM system, $m = 0, 1, \ldots, M-1$, representing the symbols, then the complete transmit OFDM frame can be represented in time domain as

$$x(t) = a_{TX}(n,m) \sum_{n=0}^{N-1} \sum_{m=0}^{M-1} d_{TX}(mN+n) \exp(j2\pi f_n t) rect\left(\frac{t - mT_s}{T_s}\right) \tag{5.5}$$

where $mT_s \leq t \leq (m+1)T_s$, $a_{TX}(n,m)$ is the attenuation of each component in the signal, and $d_{TX}(m,n)$ represents the complex modulation element, which is the arbitrary data modulated with any digital modulation technique.

As it can be noticed by the expression of the time discrete signal in equation (5.5), the complex baseband OFDM can simply be seen as the Inverse Discrete Fourier Transform (IDFT) on N input modulation symbols. Practically, this means that for each time

interval of length T, the OFDM symbol is created through an IDFT operation and, equivalently, a DFT operation at the receiver, for demodulation. If a power of 2, number of carrier is chosen, then the whole transmit and receive system can be represented by an IFFT and FFT processing.

5.2.1 OFDM Radar

In the presence of a reflecting object at the distance R from the radar, with the relative velocity of v_{rel}, which results in the Doppler frequency of f_D, the received OFDM symbol in time domain becomes

$$y(t) = \sum_{n=0}^{N-1} \sum_{m=0}^{M-1} d_{RX}(m,n) \exp(j2\pi f_n t) rect\left(\frac{t - mT_s}{T_s}\right) \tag{5.6}$$

where $mT_s \leq t \leq (m+1)T_s$ and $d_{RX}(m,n)$ can be expressed as

$$d_{RX}(m,n) = a_{TX}(n,m) d_{TX}(mN+n) \exp\left(-j2\pi f_n \frac{2R}{c_0}\right) \exp\left(j2\pi f_D T_{TOT}\right) \tag{5.7}$$

where c_0 is the speed of light and T_{TOT} represents the total transmit OFDM frame duration, including the cyclic prefix in each symbol. Considering f_C as the carrier's frequency, then f_D can be expanded to

$$f_D = \frac{2v_{rel}}{\lambda} = \frac{2v_{rel}}{c_0} f_C \tag{5.8}$$

Equation (5.7) represents the received complex symbol [180], [181], which is obtained at the radar's receiver, at the output of the OFDM demultiplexer. It can be noticed, that the received complex symbol d_{RX} contains the information of the transmitted symbol d_{TX}, together with the distortions due to the transmission over the channel, such as delay and Doppler shifts.

After transmission, the OFDM radar's received waves from objects that reflected the signals, together with the information on both transmitted and received signals, can now be used. One possible approach, it to calculate the radar profiles by simply correlating the received time domain signal $y(t)$ with the transmitted time domain signal $x(t)$ according to the integral

$$\phi_{yx} = \int y(t) x(t-\tau) dt \tag{5.9}$$

where τ represents the time variable of the radar range profile. The proposed approach, is justified with the pulse-like structure of the time domain OFDM signal. After correlation, typical beam-forming techniques can be applied on the resulting data, in order to

extract the information of range and Doppler, from a target, together with its Azimuth and elevation angles.

An innovative OFDM radar's receiver processing and a four-dimensional FFT-based beam-forming technique are presented in this thesis, and will be later described in Chapter 6. The proposed architecture allows for the estimation of range, Azimuth, elevation and speed of the targets, in one OFDM frame.

5.3 OFDM Radar Waveform's Parametrization

In this section, a description of how the parameters obtained for an OFDM radar waveform directly influence the performance of the OFDM radar system [182], is given. This section covers concepts such as the radar's bandwidth and resolution properties, from a practical point of view, in accordance with the requirements described at the beginning of this chapter.

5.3.1 Signal Bandwidth and Range

The total signal bandwidth plays a significant role in determining the number of subcarriers N and the subcarrier spacing Δf. Usually, when considering an implementation of an OFDM radar system [183], the bandwidth is a fixed parameter, since it is most likely limited by the performance of the analogue to digital converters. This is true for the cases where the OFDM signal is generated from a digital board and, obviously, not for the cases where the signal is generated from an expensive, big and hardly portable laboratory signal generator, which is out of the scope of the targeted low cost and compact radar applications of this thesis. As an example, the ADCs which have been used in the MIMO radar demonstrator presented in Chapter 4, have 14 bit conversion at up to 125 MSPS. Therefore, the achievable bandwidth, in this case, would fall in the range of 50 MHz. Therefore, this is the bandwidth that is considered, from now on, for the system concepts presented in this chapter, but also for the following chapters, where models, simulations and a complete 3D OFDM MIMO radar demonstrator, based on the digital board and ADCs of the radar in Chapter 4, are shown.
Having said this, it is important to remember from Chapter 2, that the achievable range resolution of a radar system depends purely on the total bandwidth occupied by the transmitted radar signal and it is expressed as $\Delta R = \frac{c_0}{2B}$, according to equation 2.14.
Higher bandwidth means higher resolution (decreasing Δr). For the previous mentioned example, considering a bandwidth of 50 MHz, the range resolution would translate to $\Delta R = 3$ m.

5.3.2 Doppler Shift

The motion of an antenna positioned on an airborne radar produces Doppler shifts of incoming received waves over a multi-path channel, as well as moving targets do, for a

static mounted radar. The Doppler effect, connected to the speed of the moving targets and the direction in which they are moving, is a critical factor in the parametrization of the OFDM radar's waveform. As a matter of fact, it represents the starting point for the characterization of the other parameters. Before defining the number of subcarriers and symbols in the OFDM frame, a consideration must be given on what is the maximum speed of the targets that need to be acquired. After a limit is set, defined as v_{max}, according to the equation previously defined in 5.8, the maximum associated Doppler shift which is intended to be captured by the radar, is calculated and defined as f_D. Considering the maximum relative velocity of 23 m/s or 83.8 km/h as per system specification [56], the maximum capturable Doppler shift is calculated as

$$f_{D_{max}} = \frac{2v_{max}f_C}{c_0} \tag{5.10}$$

For the considered system, therefore, it means that targets can be captured, in an environment where the Doppler shift value is maximum $f_{D_{max}} = 2.6$ kHz.

5.3.3 Subcarrier Spacing and Number of Subcarriers

The subcarrier spacing must be kept at a level so that synchronization is achievable and the Doppler shift does not cause a significant disturbance to the orthogonality between the subcarrier. According to [184], a good OFDM system design rule, that ensures orthogonality, is to assume a spacing 10 times larger than the previously defined maximum Doppler shift frequency, meaning $\Delta f > 10 f_{D_{max}}$. Which means that it must be that $\Delta f > 26$ kHz. The exact value for the subcarrier spacing is decided upon considerations on the number of subcarriers, which should be the product of the smallest possible prime numbers, preferably an integer power of 2, to use the highly efficient FFT butterfly algorithm. With the already fixed parameters, a number of subcarriers $N = 1024$ could be chosen. Therefore, the redefined minimum spacing that is tolerable due to the Doppler constraint and chosen for the system concept is $\Delta f = B/N$, which translates to 48.8 kHz. The total OFDM period, being the inverse of the subcarriers spacing, is easily deducted and it's $T_s = 20.48\ \mu s$.

5.3.4 Radar Range Ambiguity

The maximum range at which a target can be located, so as to guarantee that the leading edge of the received backscatter from that target is received before transmission begins for the next symbol, is called maximum unambiguous range. Considering the OFDM symbol duration and periodic structure, it can be calculated, recalling from Chapter 2, that the maximum unambiguous measurement distance is $r_{umax} = c_0 T_s/2 = 3.07$ km.

5.3.5 Multipath Propagation and Maximum Detectable Range

Transmission over a multi-path channel causes the received signals to be affected by inter-symbol interference (ISI) which is a type of distortion caused when consecutive

transmitted symbols interfere with each other at the receiver. ISI is only completely eliminated in OFDM by the use of a cyclic prefix. The duration of the CP must encompass the longest delay that is expected to be present in the channel [185]. The longest delay in the so called radar channel corresponds to the round trip radio path for the maximum range of interest, considering that there is a factor of 2 involved, since the signals travel twice the distance between radar device and scattering object.
Based on the maximum detectable distance that the OFDM radar is intended for, the 250 m of the detectable target as per requirements [56], in order to keep the symbols isolated, the CP has to satisfy the relation

$$T_{CP} = \frac{2d_{max}}{c_0} \tag{5.11}$$

with d_{max} the maximum detectable distance. For the considered system concept, (5.11) becomes T_{CP} >1.66 μs. It is common practice in OFDM system to the choose $T_{CP} = T_s/8$ [184], which translate into $T_{CP} = 2.56$ μs and so, $d_{max} = 768$ m.

5.3.6 Total OFDM Symbol Duration

Therefore, the total OFDM period is $T_{ofdm} = T_s + T_{CP} = 23.04$ μs, according to the equation previously anticipated in (5.3).

5.3.7 Doppler Resolution

The Doppler resolution is related to the total OFDM period and the number of symbols transmitted according to

$$\Delta v_{max} = \frac{\lambda}{2T_{ofdm}} \tag{5.12}$$

which, considering the OFDM period previously defined, and the carrier's frequency of 17 GHz, translates to $\Delta v_{max} = 383$ m/s. Additionally, considering the fact that the Doppler can be both positive and negative, it is better expressed as $\Delta v_{max} = \pm 191,5$ m/s. Consequently, this corresponds to around $\pm 689,32$ km/h which is more than the given requirements. Taking into account that twice the Doppler of the relative velocity occurs for a reflected wave, the Doppler resolution in terms of velocity resolution is dependent on the number evaluated symbols M, and amounts to

$$\Delta v = \frac{\lambda}{2MT_{ofdm}} \tag{5.13}$$

Therefore, by considering 512 symbols, a value of $\Delta v = 0.74$ m/s is obtained. Theoretically, an evaluation of an even greater number of OFDM symbols would result in a finer velocity resolution. However, this becomes in the long run impractical, as moving

TABLE 5.1: Model Parameters Summary

Symbol	Parameter	Value
f_c	Carrier Frequency	17 GHz
N	Number of subcarriers	1024
Δf	Subcarrier spacing	48,82 kHz
T	Elementary OFDM symbol duration	20,48 us
T_{CP}	Cyclic prefix duration	2,56 us
T_{OFDM}	Transmit OFDM symbol duration	23,04 us
B	Total signal bandwidth	50 MHz
Δ_r	Range resolution	3 m
r_{max}	Maximum unambiguous range	3072 m
v_{max}	Maximum unambiguous velocity	$\pm$ 191,48 m/s
M	Number of evaluated symbols	512
Δ_v	Velocity resolution	0,74 m/s

objects must remain within one range resolution cell during the evaluation. On the other hand, by evaluating over $M = 512$ symbol, with a total duration of 11.79 ms, an object traveling at the maximum unambiguous velocity would have travelled only 2,25 m, which is still within the resolution cell size of 3 m. Therefore, an appropriate performance for practical flying platform's applications is guaranteed and 2,69 km/h is perfectly in line with requirements.

5.3.8 Summary

The OFDM system parameters of the previous subchapters and summarized in Table 5.1, are an example set that fit the real-time OFDM radar system requirements [56]. It has to be noticed, that the above parameters are obtained considering, as a starting point, a bandwidth of 50 MHz, limited by the ADCs inside the digital board presented in Chapter 4. Obviously, it would be better if the ADCs could be upgraded to devices with higher MSPS, giving higher achievable bandwidths and so, increasing the range resolution of the radar. However, a trade-off would now arise concerning the cost efficiency of the OFDM radar system.

5.4 OFDM Signals in a MIMO Radar Architecture

The definition of the OFDM radar's waveform parameters represents the first step towards the achievement of an OFDM radar system. However, in order to include MIMO capabilities and, therefore, obtain a MIMO OFDM radar architecture, the orthogonality between the transmit antennas must be considered.
Several ways exist, in order to obtain orthogonality in a MIMO radar architecture [81]. One example, is the use of a TDM scheme [137], as done in the systems of Chapter 3 and 4, switching between the transmit antenna elements in a round-robin sequence, with only one active antenna at a time. Many MIMO radars up to date, use this orthogonality scheme [123]-[139]. However, this approach has the drawback of introducing a switching

time in between captures.
Additionally, like in the case of OFDM MIMO radars, the orthogonality can be achieved in frequency domain, separating transmit waveforms into orthogonal frequency sub-bands, and applying orthogonal coding schemes, to the different transmit signals.
The allocation of orthogonal coded waveforms to the different transmit channels of the radar, allows the simultaneous operation of all transmit channels in an interference-free manner.
In the next Chapter, an OFDM based MIMO radar system architecture is presented, which encompasses a set of novel adaptive orthogonal waveforms with constant envelope and a radar receiver processing, which includes a 4D-FFT beam-forming technique, for the estimation of targets and the generation of radar images. The waveforms and overall architecture have been implemented into a simulation model, tested and analyzed, according to the parameters for the OFDM waveform described in this chapter.

Chapter 6

LFM based Orthogonal-Coded 4D OFDM MIMO Radar

6.1 Chapter's Introduction

This chapter follows up on the concepts introduced in Chapter 5, for the implementation of a MIMO radar system, which is based on OFDM signals. The previously done parametrization of the OFDM radar's waveform, forms the basis for the simulation results which will be introduced in this chapter, linked to innovative concepts, which aim at addressing the intrinsic problematic of orthogonality among transmitters in a MIMO architecture, the processing of the signals at the OFDM receiver and the extraction of the targets' information.
In this section, a novel design and receiver processing of nearly orthogonal waveforms based on linear frequency modulated, or LFM, signals for MIMO OFDM radars [186], is presented. The design, implementation and results of a complete system, capable of detection and imaging of radar targets, are here described. The orthogonality of sounding signals is critical for multi-channel radar applications since the interference between signals can significantly limit the radar's ability for observation of weak targets in presence of stronger targets and background clutter. The orthogonal waveforms are designed by coding consecutive complex LFM signals in a frame so that they can be sent to the different transmit antennas of the radar, allowing the simultaneous operation of all transmit channels. The orthogonality in the proposed architecture, is achieved by applying several coding techniques, at a symbol level: Golay complementary, Frank Zadoff Chu, Walsh-Hadamard, Space-Time, Discrete Fourier Transform (DFT) and Costas based sequences. Moreover, a radar receiver processing, based on a complex frame based multiplication in frequency domain between transmit and received waveforms, is presented, together with a unique 4D-FFT beam-forming algorithm. This allows for a fast and complete sensing of range, azimuth, elevation and Doppler, in one frame. The performance of the proposed waveforms, is evaluated through the analysis of their cross ambiguity functions and imaging capabilities, while the general performance of the radar's receiver processing is shown through the use of multiple radar images. The flexibility in generating such

orthogonal coded waveforms and the proposed general receiver architecture, pave the way for an adaptive radar.

6.2 State of the Art and Applications

The orthogonal waveforms used by the MIMO radar systems must be carefully designed to avoid the self-interference and to achieve a high range resolution [187]-[188]; low aperiodic autocorrelation ensures high range resolution, high signal to noise ratio (SNR) and high resolution of multiple targets. Orthogonal coding signals, including orthogonal phase coding and orthogonal discrete frequency coding signals, have attracted attention in the design of MIMO radar waveforms and architectures. An LFM signal by itself is a very common waveform for radar sounding. It can provide high range resolution due to pulse compression, while having low computational costs. Thus, it is well suited for real-time digital signal processing. Some orthogonal waveforms for MIMO FMCW radar operation are discussed in [189],[147].
OFDM signals have been proven to be appropriate as radar signals [56]-[58], whereas their composition from a multitude of orthogonal sub-carriers, makes them particularly suitable for real-time MIMO radar applications.
As discussed at the end of Chapter 5, several ways exist, in order to obtain orthogonality in a MIMO radar architecture [81]. In the case of OFDM MIMO radars, the orthogonality can be achieved in frequency domain, separating transmit waveforms into orthogonal frequency sub-bands, and consequently applying orthogonal coding schemes, to the different transmit signals.
The allocation of orthogonal coded waveforms to the different transmit channels of the radar, allows the simultaneous operation of all transmit channels in an interference-free manner.
The OFDM based MIMO radar system architecture here presented, encompasses a set of novel adaptive orthogonal waveforms and an innovative radar receiver processing, which includes a 4D FFT beam-forming technique, for the estimation of targets and the generation of radar images.
The radar waveforms start as periodically repeated complex LFM signals, which are then orthogonally coded through several coding techniques. Hence, the waveforms can be sent, at the same time, to the different transmit elements of the MIMO radar, allowing the simultaneous operation of all transmit channels. Unlike other approaches which operate through sub-carrier interleaving [190]-[191], in all the proposed waveforms, the orthogonality is achieved at a symbol level. Thus, all subcarriers in an OFDM frame are used and the energy utilization is increased compared to the previously proposed methods. The design and implementation of the radar waveforms are shown, together with a comparison of their respective cross Ambiguity Functions (AF) and imaging capability, to evaluate their orthogonality performance.
The individual target-modified components from individual transmit waveforms can be extracted from the received super-positioned signals at the receiver, with the new proposed radar receiver processing, here presented. The design comprises a complex frame based multiplication in frequency domain, between transmit and received waveforms,

conjoint with a 4D-FFT beam-forming algorithm.
This yelds a fast and complete sensing of range, azimuth, elevation and Doppler, or speed of a target, in one frame, allowing for the evaluation of all of the proposed waveforms and the general system's performance.

The proposed orthogonal waveform's design and overall OFDM MIMO radar architecture is simple, reliable and can be easily configured on the fly, thus making the proposed system attractive for an adaptive radar, which is capable of adaptively changing its waveform, based on the radar channel which is used in. Thus, the system paves the way for the realization of an adaptive real-time and low cost device, which can target a multitude of applications: ground and air based surveillance systems, radar plus communication operations and, especially, situation awareness in cars or miniaturized flying platforms, UAVs and air-taxis, for operation in unknown areas or degraded visual conditions.

6.3 Basic OFDM

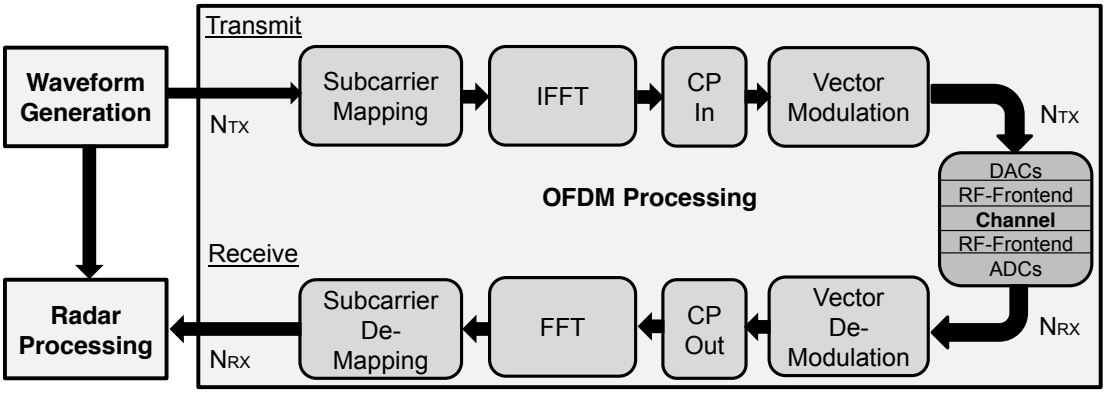

FIGURE 6.1: Top level view of the complete system architecture.

The OFDM radar transmit and receive architecture is represented in Fig. 6.1. The OFDM processing block in this image shows a typical OFDM system structure [192], while the two blocks depicted on the left of this picture, are the waveform generation, which is responsible for creating the novel constant envelope waveforms, and the radar processing, which processes the received radar signals and extracts the targets' information. These two, will be better described in the next sections. As in a conventional OFDM system, at the transmit side, the waveforms to be sent, go through subcarrier mapping, IFFT processing, cyclic prefix addition and vector modulation [56]. The signals are then passed through Digital-to-Analogue Converters (DACs), the Radio-Frequency (RF) frontend for the frequency up-conversion and, subsequently, transmitted from the transmit antennas over the channel. After being recaptured by the receiver antennas, the signals are down-converted and sampled from the ADCs. Similarly to the transmit paths, at the receiver side, the received signals undergo vector demodulation, cyclic prefix removal, FFT processing and subcarrier demapping. Afther this, the radar processing of the signals, consisting in beamforming and image generation techniques, is

applied.
In the next chapter, the various waveforms, which are mapped into the symbols and subcarriers of the OFDM frame, are discussed.

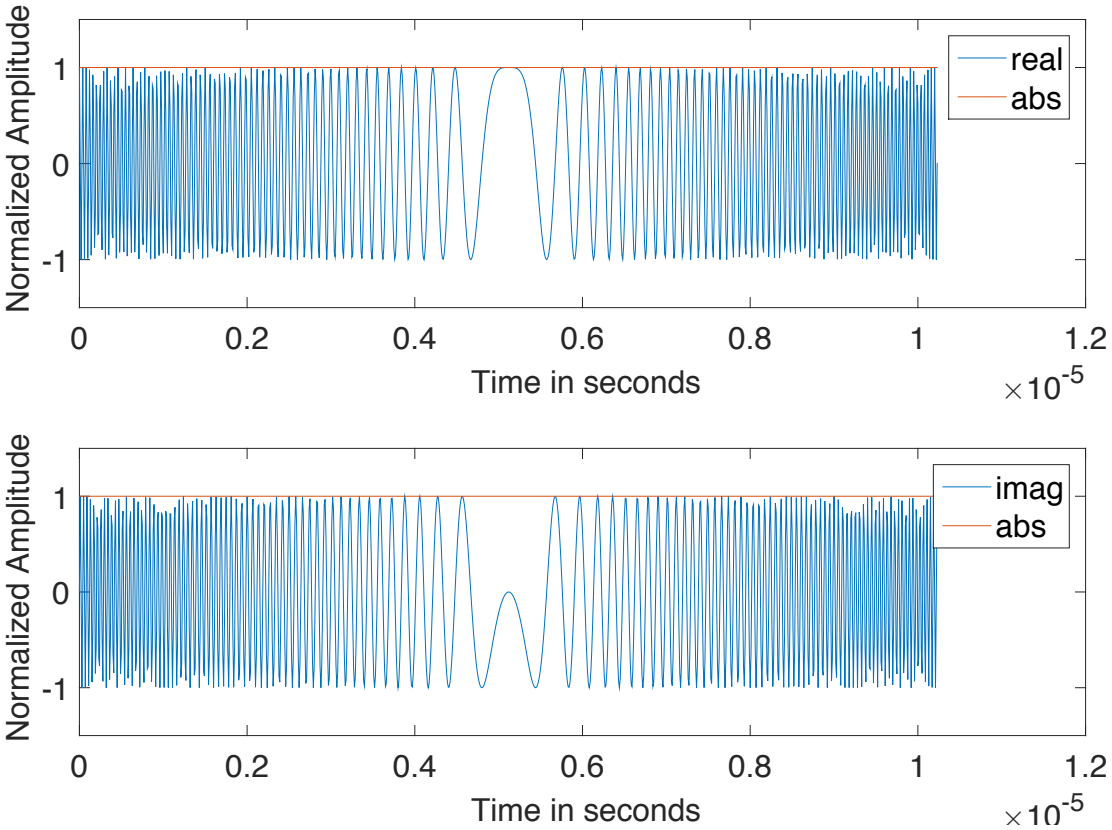

FIGURE 6.2: Time domain view of an LFM signal. The real and imaginary part are represented in the upper and lower part of the image, respectively.

6.4 OFDM LFM-Based Waveforms Generation

As shown in Fig. 6.1, the initial step of the MIMO OFDM radar architecture, is the generation of the transmit waveforms. In the system here described, novel LFM based waveforms with different orthogonal coding schemes, are proposed. The waveform, or frame, transmitted from each antenna can be seen as a concatenation of several symbols, where each symbols is an LFM signal which is coded according to the chosen scheme. An LFM signal is expressed as

$$s(t) = rect(\frac{t}{T_p})exp(j2\pi(f_c t + \frac{1}{2}\alpha t^2)) \tag{6.1}$$

where f_c is the carrier frequency, α is the chirp rate denoted as radar bandwidth per pulse width, i.e. W/T_p, W, T_p being the radar bandwidth and radar pulse width, respectively. A time domain view of an LFM signal is shown in Fig. 6.2, where the real, imaginary and absolute representations of the chirp are illustrated, denoting the constant nature of this waveform.

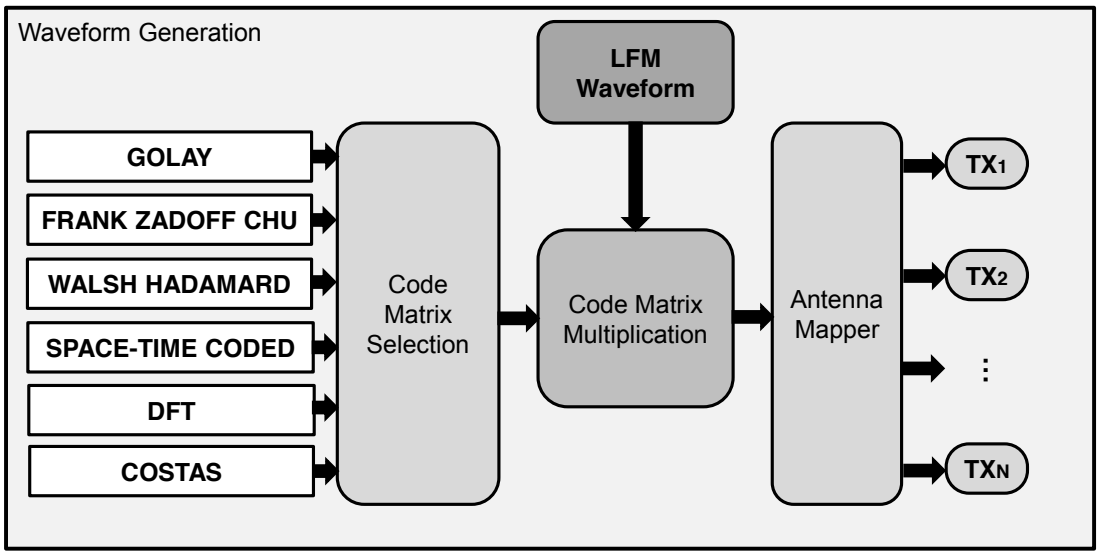

FIGURE 6.3: Schematic representation of the orthogonal waveforms generation architecture.

In Fig. 6.3, the waveform generation architecture is presented. As it can be seen, a set of different coding schemes has been created in order to achieve the orthogonality across transmit antennas. The waveform transmitted on the i-th transmit antenna, is expressed as

$$x^i(t) = \sum_{m=1}^{M} c_m^i P(t - mT_p)s(t) \tag{6.2}$$

where $P(t-mT_p)$ is the pulse train, T_p denotes the pulse's width, c_m^i is the coded signature, M is the number of symbols transmitted and $s(t)$ is the LFM signal. The proposed coding schemes, c_m, are: Golay complementary pairs, Frank Zadoff Chu sequences, Walsh Hadamard codes, Space-Time, DFT based matrixes and Costas sequences. As depicted in Fig. 6.3, after the codes are generated, a code matrix selection block decides which code is to be applied. The selected code is then fed to a code matrix multiplication block, which then multiplies the LFM waveform with the selected code, according to (6.2). The orthogonality is achieved through a multiplication at a symbol level. Each LFM waveform, representing a symbol of the transmitted OFDM frame, is multiplied with an element of the chosen sequence.
The result of these operations, is the generation of N_{TX} orthogonal waveforms $x^i(t)$, where N_{TX} represents the number of transmit antenna elements in the MIMO radar system. Each of the N_{TX} waveforms, or frames, consists of $L_{FRAME} = N$ x M x $N_{SAMPLES}$ elements, where N, M and $N_{SAMPLES}$ represent the number of subcarriers, symbols and samples, respectively. Subsequently, as shown in Fig.6.1, the orthogonal waveforms will then undergo the typical OFDM architecture and be processed in the radar processing block.

In the following chapters, a description will be given for each of the proposed LFM based waveforms, together with a benchmarking and comparison of their orthogonal properties, through analysis of their cross ambiguity functions. The cross ambiguity function of $x^i(t)$ and $x^j(t)$, is defined as

$$\chi(\tau,\nu) = \int x^i(t)x^j(t-\tau)^* e^{i2\pi\nu t}dt \tag{6.3}$$

which can be expanded as

$$\begin{aligned}\chi(\tau,\nu) = \int \sum_{m=1}^{M} c_m^i P(t-mT_p)s(t)\cdot \\ \sum_{n=1}^{N} d_n^{j*} P(t-\tau-mT_p)s^*(t-\tau)e^{i2\pi\nu t}dt\end{aligned} \tag{6.4}$$

which is then,

$$\begin{aligned}\chi(\tau,\nu) = \sum_{m=1}^{M}\sum_{n=1}^{N}(c_m^i d_n^{j*})\cdot \\ (\int s(t)s^*(t-\tau)P(t-mT_p)P(t-\tau-mT_p)e^{i2\pi\nu t}dt)\end{aligned} \tag{6.5}$$

For each code, the cross ambiguity function is provided, in order to evaluate the performance of the orthogonality properties [193]-[194]. The construction of orthogonal waveforms, is to be done considering not only the performance at a transmit level, but also at a receiver level. The reason is to be found in the fact that, the orthogonality has to be preserved even after the targets' induced delay and Doppler effects on the waveforms, in order to extract the targets' parameters. The cross ambiguity function study, allows to analyze the channel induced orthogonality properties of each waveform. For example, it can be used to understand how good the orthogonality properties are preserved for targets with arbitrary Doppler values, either fast moving or almost static. Cross ambiguity functions capture the inherent cross antenna interference posed at the receiver, for arbitrary delay and Doppler values, without considering thermal noise and clutter effects.
The analysis of the ambiguity functions is performed within an OFDM MIMO radar simulation model, purposely created in order to test the performance of the waveforms and the overall radar system architecture. The chosen waveform parameters have been calculated in Chapter 5 and are shown in Table 5.1. Therefore, the evaluation is performed with $N = 1024$ subcarriers and $M = 512$ symbols.

6.4.1 Golay Complementary Pair

Golay complementary series, have the property that the sum of their respective autocorrelation series, is zero everywhere except for the center term [195],[196]. In other words, the two complementary codes, when transmitted consecutively, yield sidelobes with opposite polarity that add up to zero when the range profiles from the two Golay complementary codes are summed up. The Golay sequences are generated through the linear combination of monomials that spawn the Boolean functions of the desired length. A Boolean function is a function f from $Z_2^m = (x_1, x_2, \ldots x_m)|x_i\varepsilon(0,1)$ to Z_2.

The Boolean variable x_i can attain only the values $0, 1$, which may actually correspond to binary phase codes, if the phase modulation technique is to be utilized in the implementation.
Golay codes are generated through a specific combination of the monomials, which is formulated as a Boolean function

$$f(x_1, x_2, \ldots, x_m) = \frac{q}{2} \sum_{i=0}^{m-2} x_{\pi(i)} x_{\pi(i+1)} + \sum_{i=0}^{m-1} g_i x_i + g' \tag{6.6}$$

where $g_i \varepsilon (0, 1, \ldots, q-1)$, $q = 2^h$ is the constellation size, π here is a permutation of $0, 1, \ldots, m-1, 2^m$ being the length of the Golay code, and x_i are the monomials. The x_i represent the c_m^i sequences expressed in (6.2). The number of Golay codes that can be generated using the function in (6.6), is $\frac{m!}{2} q^{m+1}$ which represents the maximum number of orthogonal sequences, thus the maximum number of transmit antennas that can be used. The utilization of Golay phase codes when generating the OFDM frame, will result into a reduction of the noise floor along the zero-range Doppler cut of the ambiguity function.
Fig. 6.4 presents the cross ambiguity function of two LFM based signal stream employing Golay Complementary Pair sequences for orthogonality coding. The parameters chosen for generating the cross AF are m= 2 and q=2. In Fig. 6.5, the cross energy from the cross ambiguity function across the zero delay axis, in subfigure A, and along the zero Doppler axis, in subfigure B, can be seen.

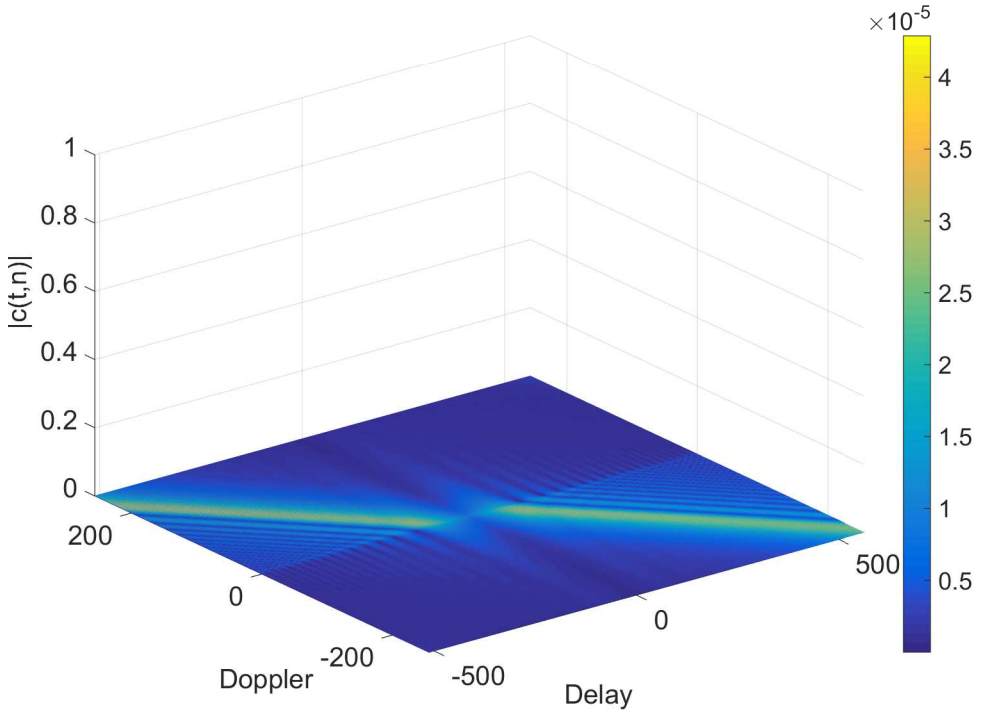

FIGURE 6.4: Cross Ambiguity Function of Golay Complementary Pair based LFM waveforms.

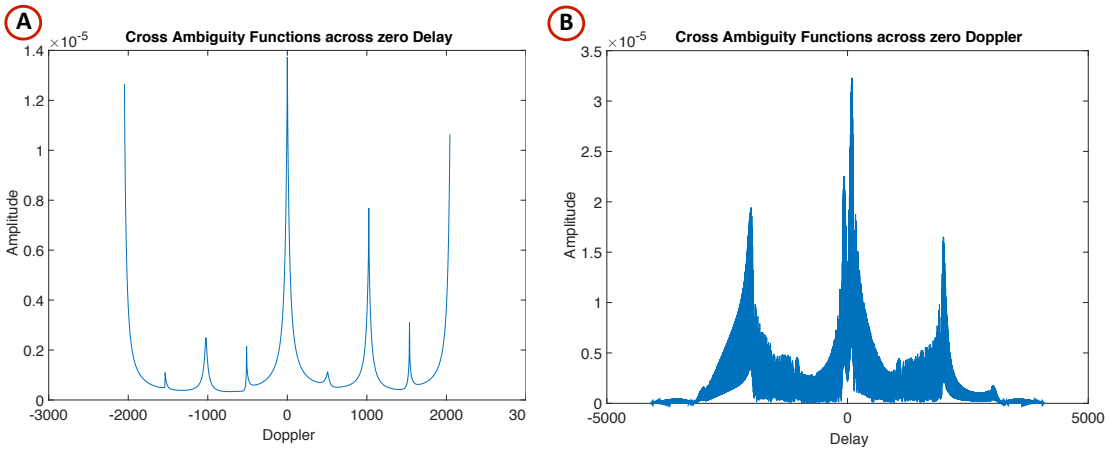

FIGURE 6.5: Cross Ambiguity Function of Golay Complementary Pair based LFM waveforms, across zero Delay, on the left in A, and across zero Doppler, on the right in B.

6.4.2 Frank Zadoff Chu Sequence

Frank Zadoff Chu (FCZ) sequences, are complex-valued constant envelope sequences whose cyclically shifted versions of the sequence imposed on a signal, result in zero correlation with one another at the receiver [197],[198]. These sequences, exhibit the useful property that cyclically shifted versions of themselves, are orthogonal to one another, provided, that is, that each cyclic shift, when viewed within the time domain of the signal, is greater than the combined propagation delay and multi-path delay-spread of that signal between the transmitter and receiver. The complex Zadoff Chu sequence, $x_u(n)$, with length N_{ZC}, parametrized by u, is given by

$$x_u(n) = \exp\left(-j\frac{\pi u n(n+1)}{N_{\text{ZC}}}\right) \tag{6.7}$$

where $0 < u < N_{ZC}$ and the gross common divider of (N_{ZC}, u) is 1. The term $x_u(n)$, represents the c_m^i sequences expressed in (6.2), where n and u are m and i, respectively.

Fig. 6.6 presents the cross ambiguity function of two LFM based signal stream employing Zadoff-Chu sequences for orthogonality coding. The parameters chosen are N_{zc}= 521, with u chosen to be 5 and 12 respectively for both codes. In Fig. 6.7, the cross energy from the cross ambiguity function across the zero delay axis, in subfigure A, and along the zero Doppler axis, in subfigure B, can be seen.

6.4.3 Walsh Hadamard Matrix

A Hadamard matrix A of order n, is an $n \times n$ matrix of 1s (ones) and -1s (minus ones), in which $HH^T = nI_n$, where I_n is the $n \times n$ identify matrix [199]. Equivalently, a Hadamard matrix is an $n \times n$ matrix of 1s and -1s in which any two distinct rows agree in exactly $n/2$ positions and, thus, disagree in exactly $n/2$ positions. Starting from a

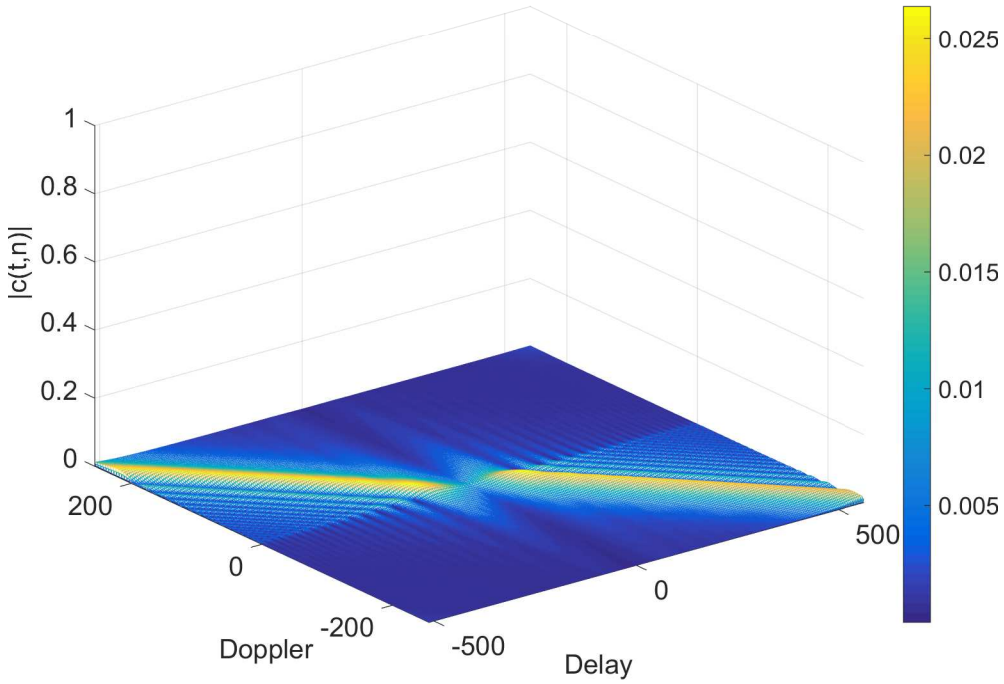

FIGURE 6.6: Cross Ambiguity Function of Zadoff Chu sequence based LFM waveforms.

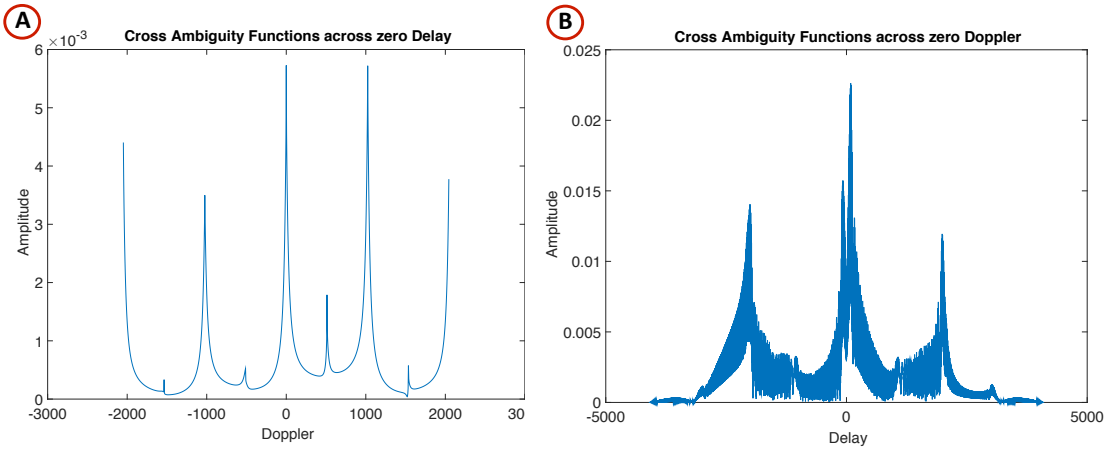

FIGURE 6.7: Cross Ambiguity Function of Zadoff Chu sequence based LFM waveforms, across zero Delay, on the left in A, and across zero Doppler, on the right in B.

basic kernel A, the orthogonal code can be extended over multiple transmit antennas by cascading it, as seen from the following equation

$$A = \begin{bmatrix} 1 & 1 \\ 1 & -1 \end{bmatrix}$$
$$B = \begin{bmatrix} A & A \\ A & -A \end{bmatrix} \tag{6.8}$$

Any two rows in the cascaded matrix, will be orthogonal between each other and will be used as the code for modulating across the symbols. Any individual rows in the cascaded matrix, representing the spread spectrum sequences generated by the Walsh-Hadamard functions, are chosen for the orthogonal code c_m^i, expressed in (6.2). The orthogonality is achieved by transmitting different Walsh-Hadamard codes, through the various transmit antennas. Since the basic information waveform is LFM, the ambiguity properties of LFM and the range compression property of the waveform are retained, while maintaining full resolution properties and diversity order provided by the MIMO radar.

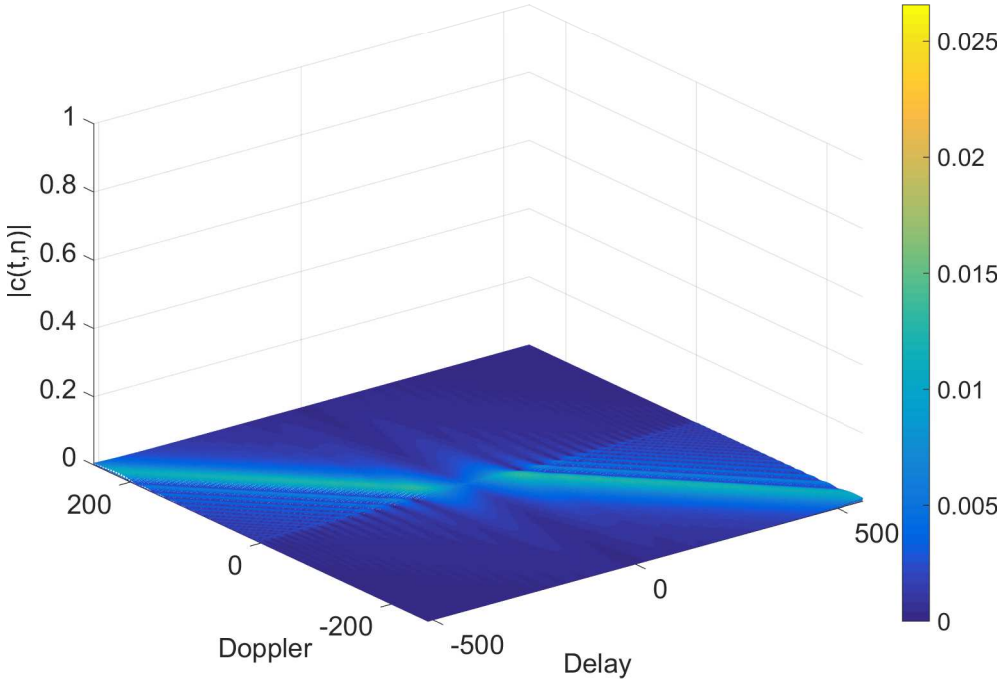

FIGURE 6.8: Cross Ambiguity Function of Walsh-Hadamard based LFM waveforms.

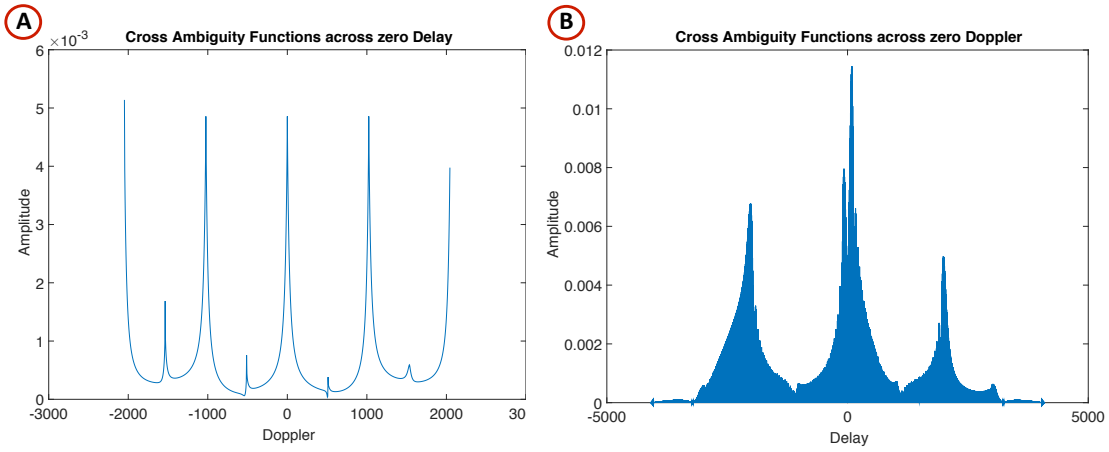

FIGURE 6.9: Cross Ambiguity Function of Walsh-Hadamard based LFM waveforms, across zero Delay, on the left in A, and across zero Doppler, on the right in B.

Fig. 6.8 presents the cross ambiguity function of two LFM based signal streams, employing Walsh Hadamard sequences for orthogonality coding. For the Walsh Hadamard,

the parameters are generated by cascading the basic kernel 9 times and selecting the first 2 rows. In Fig. 6.9, the cross energy from the cross ambiguity function across the zero delay axis, in subfigure A, and along the zero Doppler axis, in subfigure B, can be seen.

6.4.4 Space-Time Coded

Data is encoded using a Space-Time Block Code (STBC) and the encoded data is split into N_{TX} streams which are simultaneously transmitted using N_{TX} transmit antennas. Space-time block codes are designed to achieve the maximum diversity order, for a given number of transmit and receive antennas subject to the constraint of having a simple decoding algorithm. The classical mathematical framework of orthogonal designs is applied to construct STBC. It is shown that space-time block codes constructed in this way, only exist for few sporadic values of N_{TX}. In the case of STBC in particular, the data stream to be transmitted is encoded in blocks, which are distributed among spaced antennas and across time. This means that the STBC is designed in such a way that the vectors representing any pair of columns taken from the coding matrix is orthogonal. The result of this is a simple, linear, optimal decoding at the receiver [200],[201],[202],[203]. In [201], it is shown that no orthogonal code with rate 1 exists from more than two transmit antennas. Although this has an implication in communication systems, it does not have a limitation for radar application purposes. The transmit waveform over two symbols in a frame, from two TX antennas, can be expressed as

$$x^1 = \begin{bmatrix} \underline{s}_1 \\ -\underline{s}_2^* \end{bmatrix}$$
$$x^2 = \begin{bmatrix} -\underline{s}_2 \\ \underline{s}_1^* \end{bmatrix} \tag{6.9}$$

where $\underline{s}_1$ and $\underline{s}_2$, are the transmitted signals on the N subcarriers by the transmit antenna 1 and 2, respectively, on symbol 1, whereas $-\underline{s}_2^*$ and $\underline{s}_1^*$, are the transmitted signals on the same N subcarriers by the transmit antennas 1 and 2, respectively, on the following symbol, i.e. symbol 2. The symbols $\underline{s}_1$ and $\underline{s}_2$, are either the up-chirp and the down-chirp or two up-chirps with different chirp rate, respectively. In the case of $N > 2$ transmitters, a generalization can be found in [201].

Fig. 6.10 presents the cross ambiguity function of LFM based Space-Time coded signal streams for orthogonality coding. For the case of two antennas, the Space-Time code is the Alamouti code [203], which is used here for generating the cross ambiguity function. In Fig. 6.11, the cross energy from the cross ambiguity function across the zero delay axis, in subfigure A, and along the zero Doppler axis, in subfigure B, can be seen.

6.4.5 DFT Codes (Time-Coded)

In this time-coded approach, consecutive symbols from a particular transmit antenna, are coded by the DFT sequence, for e.g. $1, \omega, \omega^2, \ldots \omega^{N-1}$. The orthogonal code of

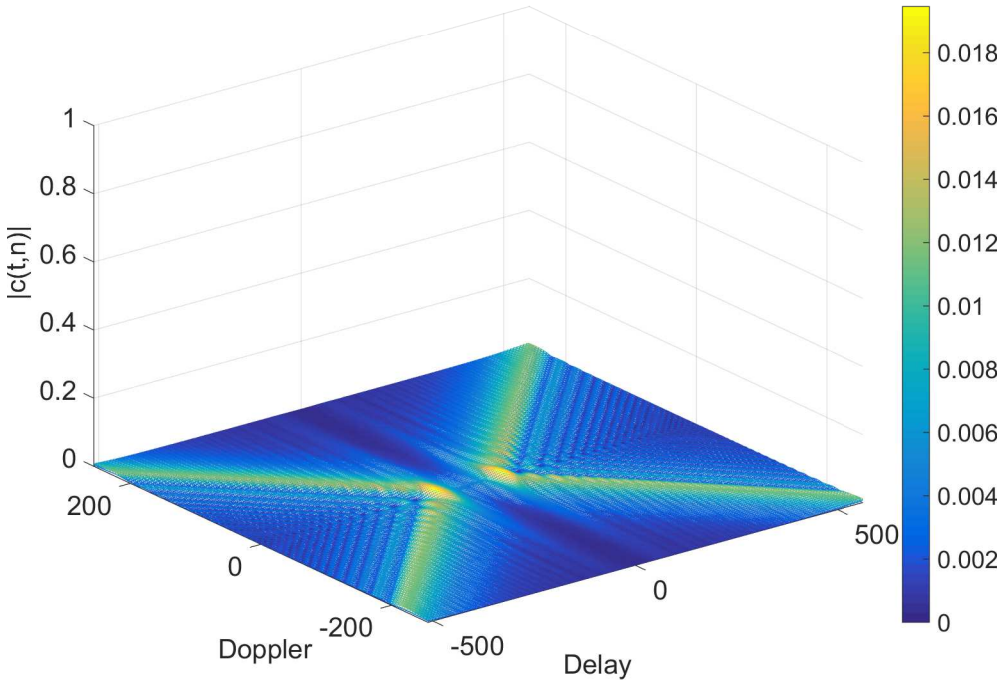

FIGURE 6.10: Cross Ambiguity Function of Space-Time Code based LFM waveforms.

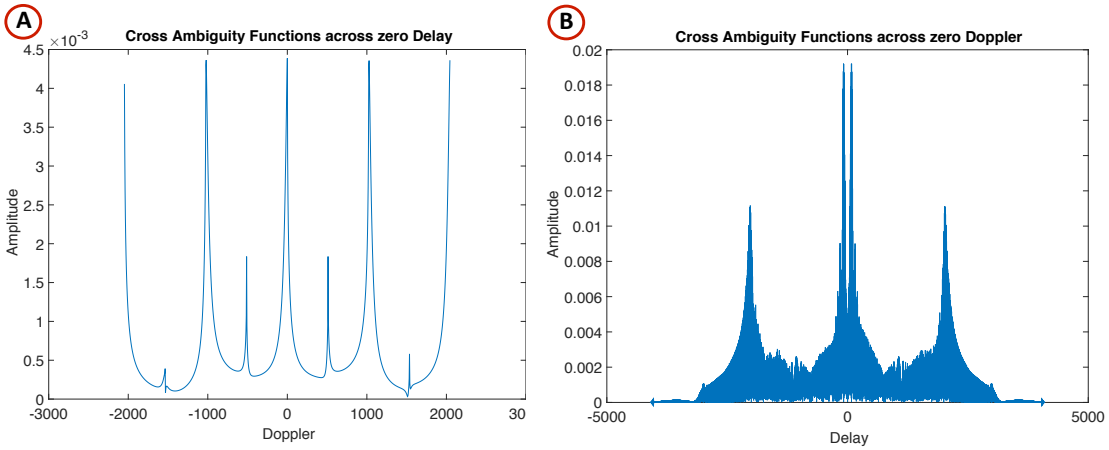

FIGURE 6.11: Cross Ambiguity Function of Space-Time Code based LFM waveforms, across zero Delay, on the left in A, and across zero Doppler, on the right in B.

length N, can be expressed by the following matrix

$$C = \begin{bmatrix} 1 & 1 & \dots & 1 \\ 1 & \omega & \dots & \omega^{N-1} \\ \vdots & \ddots & \dots & \vdots \\ 1 & \omega^{N-1} & \dots & \omega^{(N-1)(N-1)} \end{bmatrix} \tag{6.10}$$

where each row represents the orthogonal code applied for each transmit waveform. The matrix in equation (6.10), represents the c_m^i sequences expressed in (6.2), where the

indexes m and i run across the columns and rows of C, respectively.

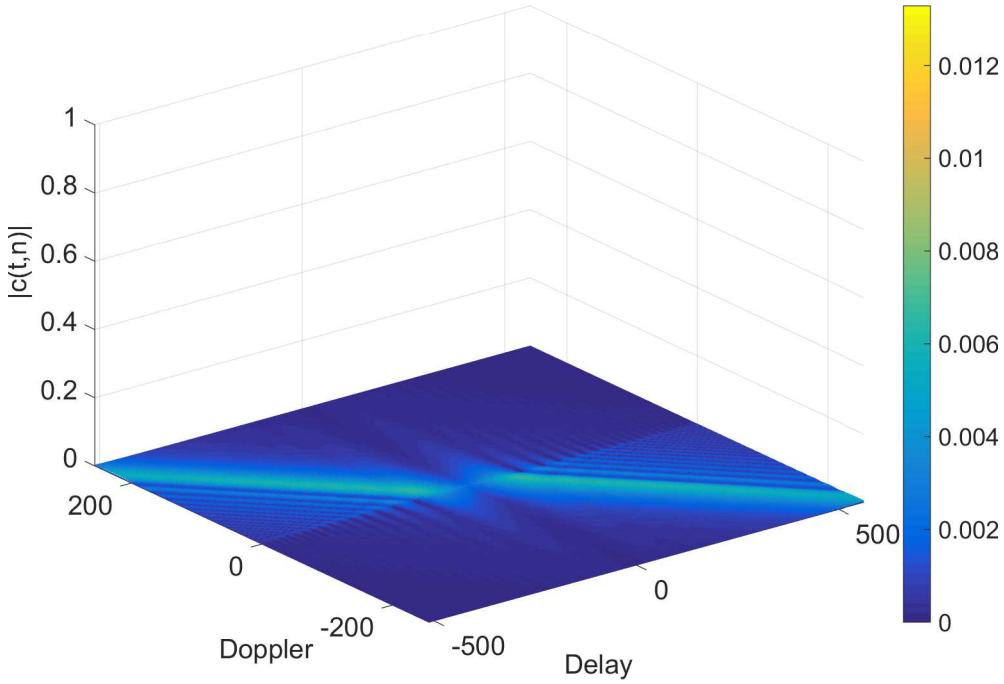

FIGURE 6.12: Cross Ambiguity Function of DFT based LFM waveforms.

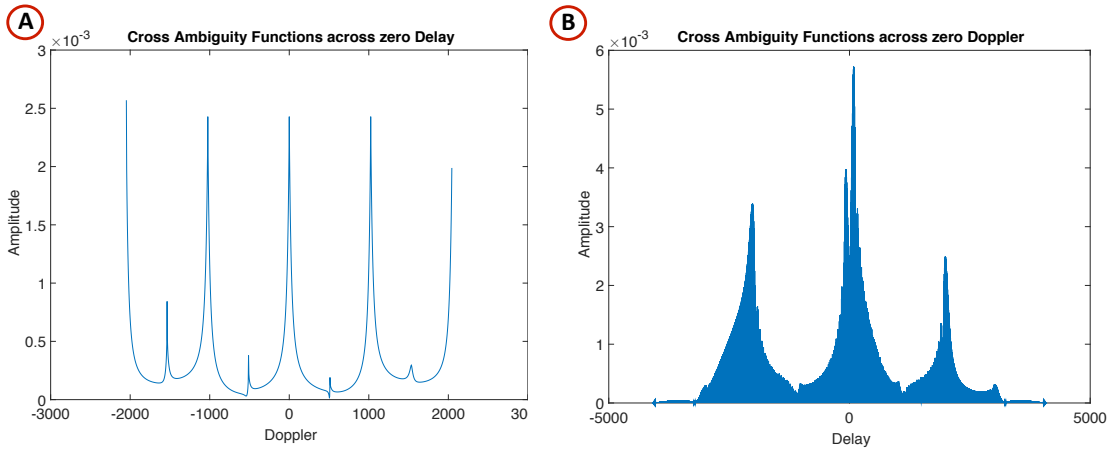

FIGURE 6.13: Cross Ambiguity Function of DFT code based LFM waveforms, across zero Delay, on the left in A, and across zero Doppler, on the right in B.

Fig. 6.12 presents the cross ambiguity function of LFM based time coded signal streams for orthogonality coding. For this time coded waveform, the parameters chosen are selected with $N = 512$, where the first two rows represent the orthogonal codes for the transmit waveforms. In Fig. 6.13, the cross energy from the cross ambiguity function across the zero delay axis, in subfigure A, and along the zero Doppler axis, in subfigure B, can be seen.

6.4.6 Costas Sequence

Costas codes are a variant of pulse compression waveforms, largely studied for their attractive time-frequency properties [204], [205]. Costas codes are Doppler tolerant frequency hopping waveforms, that exhibit near-ideal range-Doppler ambiguity functions. There are several methods for constructing Costas codes, with no one able to generate all codes. One of the methods for generating Costas codes, consists in the use of the Welch-Costas construction. The Welch-Costas construction, is based on the idea of finding primitive roots to a Galois field. The number of elements N in the Galois field, is one less than some prime number q. The primitive roots i of the Galois field, are defined as the integers $1 \leq i \leq N$ that satisfy, generating all of the integers i between 1 and N. The sequence of integers generated by a given value of i corresponds to the Costas code of length $N = q - 1$, with parameter q. This can be expressed as

$$c_m^i = exp(j2\pi f_m^i t) \tag{6.11}$$

where

$$f_m^i = mod(i^m, q) \tag{6.12}$$

where $0 < m < q - 1$, q is prime and i is relatively prime to q. The f_m term, represents the frequency hopping pattern of the Costas code.

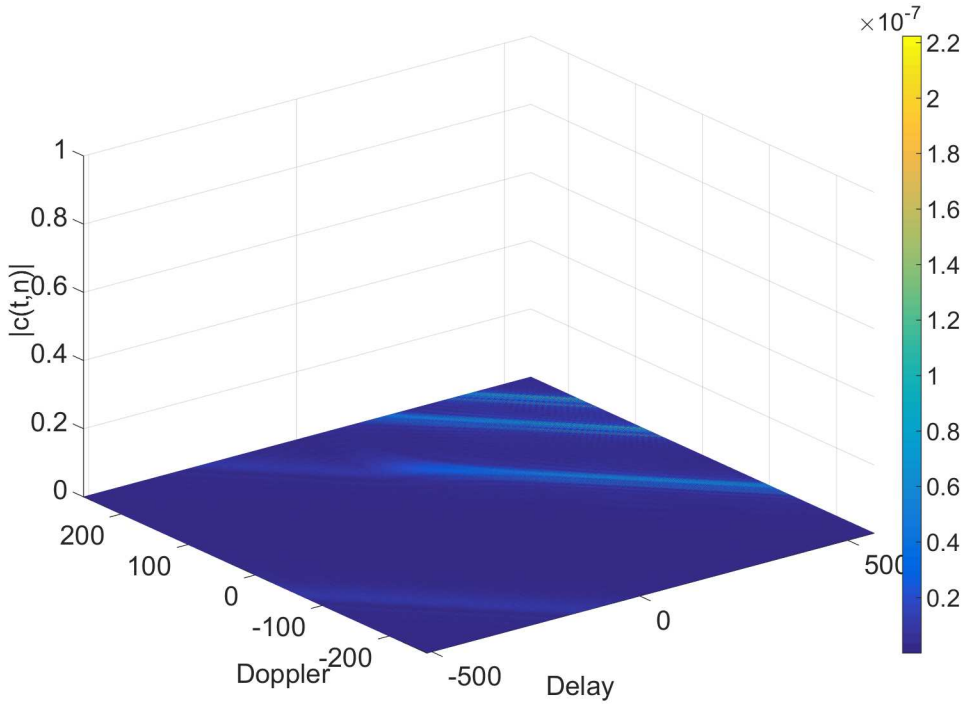

FIGURE 6.14: Cross Ambiguity Function of Costas sequence based LFM waveforms.

Fig. 6.14 presents the cross ambiguity function of LFM based Costas sequence streams for orthogonality coding. For the Costas waveform, the parameters chosen are selected with $q = 509$, $N = 508$ and $i = [2, 3]$, where 2 and 3 are selected for the different transmit waveforms. In Fig. 6.15, the cross energy from the cross ambiguity function

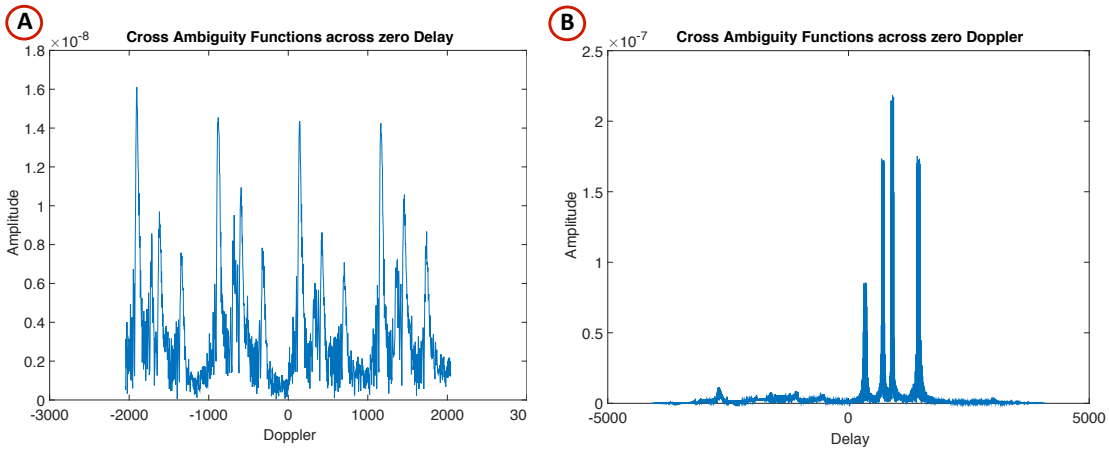

FIGURE 6.15: Cross Ambiguity Function of Costas sequence based LFM waveforms, across zero Delay, on the left in A, and across zero Doppler, on the right in B.

across the zero delay axis, in subfigure A, and along the zero Doppler axis, in subfigure B, can be seen.

6.4.7 Performance Overview

Additionally to the cross ambiguity function, analysis is also performed through the Woodward's ambiguity function, which is common for all the proposed LFM based waveforms and shown in Fig. 6.16. The Woodward's ambiguity function, introduced in [206], depicts the performance of a radar waveform in accurately measuring both the range and speed of a target [207]. It derived from the optimization of the multi-dimensional matched filter approach, obtained by cross correlation, or convolution, of an unknown received signal, reflected from targets, with the complex conjugate of the time-reversed version of the known signal transmitted from the radar. Fig. 6.16 depicts the Woodward ambiguity function of a basic LFM waveform, which has a closed form expression as follows,

$$|\chi(\tau,\nu)| = (1-\frac{\tau}{T})sinc(\pi T(\nu \mp B(\frac{\tau}{T}))(1-\frac{\tau}{T})) \tag{6.13}$$

where $|\tau| \leq T$ and 0 elsewhere. As it can be seen from Fig. 6.16, LFM waveforms have excellent delay-Doppler properties, which make them suitable for radar applications.
In table 6.1, a comparison between the performances in terms of cross energy along zero delay axis, along zero Doppler axis and overall cross energy of the different waveforms, is given.

From table 6.1 and the cross ambiguity plots 6.4-6.15, it can be observed that Costas sequence based LFM modulation has the best cross ambiguity properties, in the overall order of 10^{-16}. Performance wise, they are followed by Golay Complementary Pair based LFM waveforsm, in the order of 10^{-11} and by Space-Time coded LFM waveforms, which reach a value of 1.2×10^{-6}. Finally, following up, are the DFT, Zadoff-Chu and Walsh-Hadamard coded LFM based waveforms, with almost same ambiguity performance levels, set at 4.8×10^{-6}.

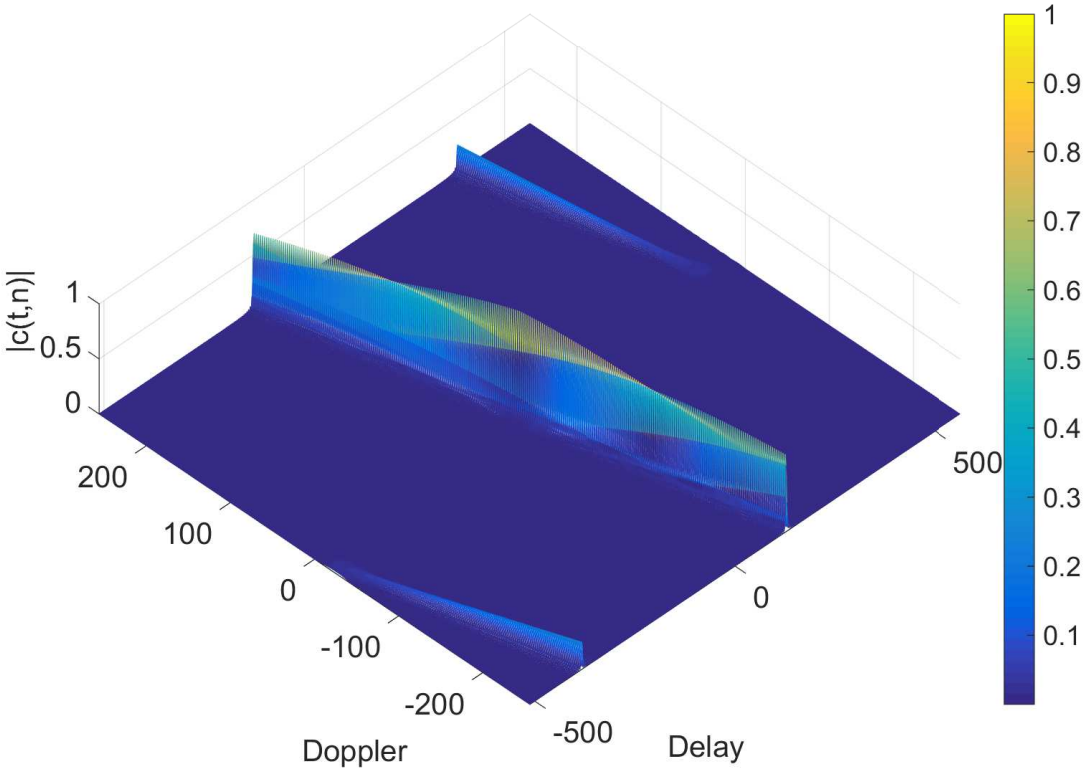

FIGURE 6.16: Woodward Ambiguity Function of the proposed LFM based waveforms.

TABLE 6.1: Cross Ambiguity Function Parameter Summary

Coded Waveform	Zero Doppler Axis	Zero Delay Axis	Overall
Golay	4.01×10^{-12}	1.86×10^{-11}	1.75×10^{-11}
Zadoff-Chu	9.44×10^{-7}	8.86×10^{-6}	4.85×10^{-6}
Walsh-Hadamard	9.44×10^{-7}	2.15×10^{-6}	4.85×10^{-6}
Space-Time Coded	2.35×10^{-7}	5.36×10^{-7}	1.20×10^{-6}
DFT Coded	9.44×10^{-7}	4.86×10^{-6}	4.85×10^{-6}
Costas	2.04×10^{-17}	1.69×10^{-16}	1.68×10^{-16}

6.5 Proposed Radar Receiver Processing

In the following chapters, a description is given for the novel radar receiver processing. As previously shown in Fig. 6.1, the radar processing takes place after the signals from all receivers have gone through the OFDM basic receiver processing, which can be seen as N_{RX} frames of length L_{FRAME}. This matrix of data represents the input to the block, together with the N_{TX} frames of length L_{FRAME}, which represent the transmit waveforms from the waveform generator block in the same figure.

In Fig. 6.17, the novel radar processing architecture is presented. The block is comprised of two important processing steps: a frame based complex multiplication and a 4D-FFT beamforming technique.

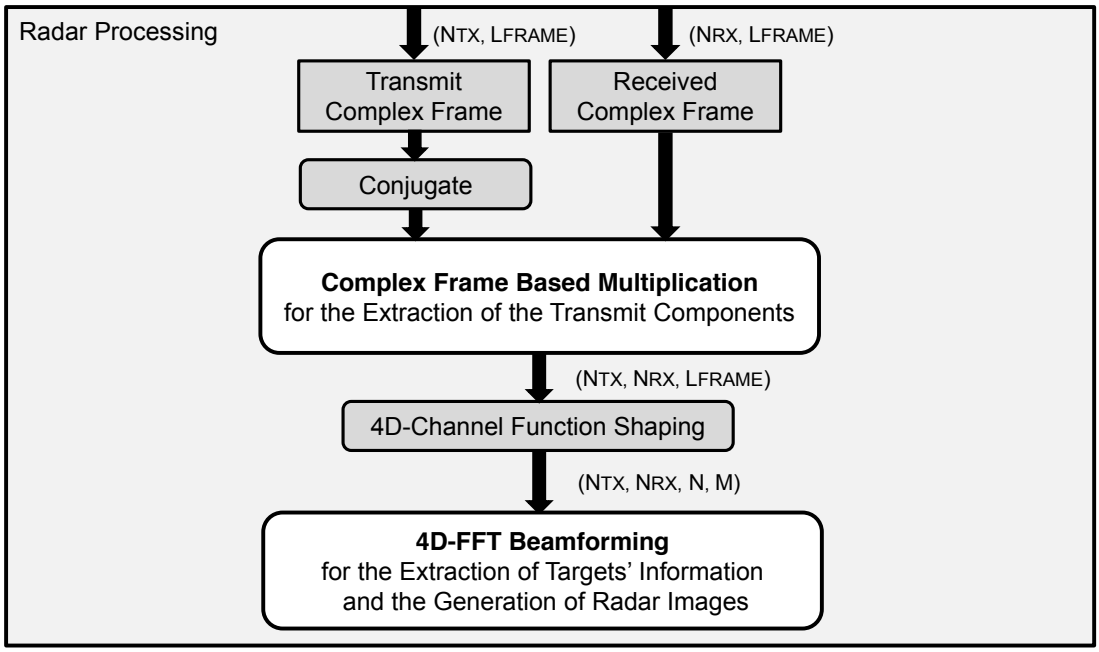

FIGURE 6.17: Receiver processing architecture.

6.5.1 Complex Frame-Based Multiplication

The N_{TX} transmit waveforms from different transmit antennas are separated at each of the N_{RX} receivers, by means of a frame-based complex multiplication in frequency domain, between the received complex signal and the conjugate of the original transmit signal. The signal from the i-th transmit antenna is received at the receiver as

$$y(t) = x^i(t) * h^i(t) + \sum_{j=1, j\neq i}^{I} x^j(t) * h^j(t) \tag{6.14}$$

where $h^i(t)$ and $h^j(t)$ are the channel, therefore targets, response from i-th and j-th transmit antenna to the receiver, respectively, and $*$ denotes the convolution operation. The sum, $\sum_{j=1,j\neq i}^{I} x^j(t) * h^j(t)$, denotes the interference term. The demodulation done in order to extract the response from the i-th transmit antenna, is performed by deconvolution with the conjugate of the i-th transmit signal as

$$x^i(t) * y(t) = x^i(t) * x^i(t) * h^i(t) + x^i(t) * \sum_{j=1, j\neq i}^{I} x^j(t) * h^j(t) \tag{6.15}$$

Due to the orthogonality property of the coded sequence, the output of this demodulation operation is proportional to the channel/target response $h^i(t)$. The deconvolution operation is achieved in frequency domain, which translates then to a multiplication operation, due to the property of OFDM signals.
After extraction of the transmit components from each receiver, a set of $N_{TX} \times N_{RX}$ signals of length L_{FRAME} is reconstructed, which will be processed to obtain the targets' information. The results of these operations are then fed to a 4D channel function shaping block, which reshapes the data into a 4D matrix, since the signals can be seen

as frames of M symbols of N subcarriers each. Therefore, the data can be organized into a 4D matrix which has dimensions (N_{TX}, N_{RX}, N, M).

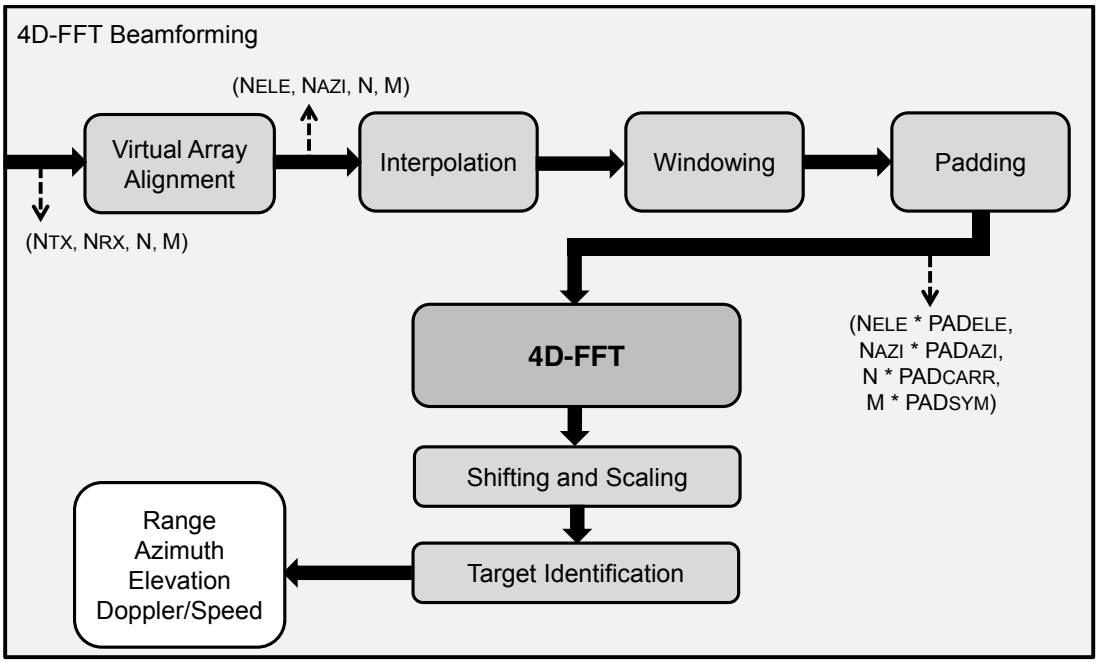

FIGURE 6.18: 4D-FFT beamforming architecture.

6.5.2 4D-FFT Based Beamforming and Targets Parameters Estimation

The second important step of the receiver processing is the 4D-FFT algorithm, which is presented in Fig. 6.18. As it can be seen in this image, the first step of the processing is the virtual array alignment block. For evaluation purposes and to better clarify the operational steps, an example array comprising 2 transmit and 16 receive elements has been created. The array can be easily edited in the simulation environment. The chosen array is shown in Fig. 6.19, where both the TX and RX antennas' position is illustrated, in red and blue, respectively. In Fig. 6.20, instead, the so called virtual array is illustrated.

According to the MIMO principle, received signals from different transmitters are combined in such a manner that virtual radiating elements can be generated to form a virtual array. The equivalent virtual array can be calculated as the discrete convolution of the overall RX and TX element positions. Thus, the total number of virtual elements is N_{TX} x N_{RX}. The size of the 4D data matrix scales according to the virtual array size, where the horizontal axis can be denoted as azimuth and the vertical axis can be denoted as elevation, thus yielding a 4D radar signal matrix with size $N_{ELE} \times N_{AZI} \times N \times M$, where N_{ELE} and N_{AZI} are the number of virtual elements in the vertical/elevation and horizontal/azimuth axis, respectively. Therefore, each element in Fig. 6.20, effectively represents an $N \times M$ OFDM frame or waveform. The next optional step is the interpolation of the missing (or zero) elements, which might be required or not according to

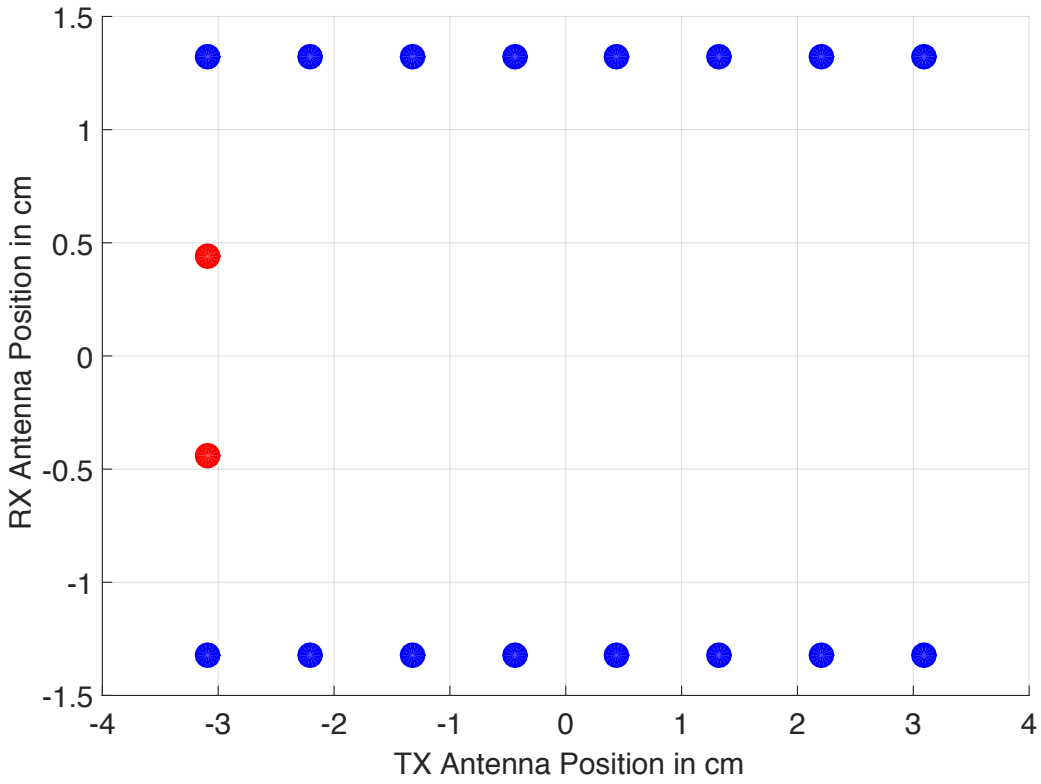

FIGURE 6.19: 2x16 antenna array. The RX array configuration is shown in blue, while the TX array in red.

the chosen antenna array configuration and resulting virtual array matrix. Other two additional steps in the processing, are the windowing and padding operation of the radar data matrix. Various windowing functions can be applied before the FFT, as decribed in [138]. According to which matrix dimension the window is applied to, it might affect the resolution, defined as the 3 dB beam-width of the main lobe of a radar target, in either range, azimuth or elevation directions. One of the most commonly selected window functions, and used throughout our simulations, is the Hamming window, which has a minimal influence on the resolutions.

The zero padding operation is introduced just after the application of the window function and consists, as the name suggests, into the concatenation, or padding, of zeros at the end of the radar signals, in time domain. Taking advantage of the fact that at the end of a windowed signal, the signal itself smoothly goes to zero, it can be understood that zero padding must be applied after windowing, in order to avoid a sharp transitioning of the signal to zero. The use of zero padding operations on the radar data matrix, allows to achieve two important things. First of all, the radar matrix can be increased, so that along each of the dimensions, a power of 2 number of samples is reached. This is of crucial importance, considering the fact that the FFT operations, implemented in either simulation environments or FPGA architectures, are based on radix-2 FFT algorithms. Hence, if this is achieved, an improvement in the timing for the FFT operations and, therefore, the generation of the radar images, is to be expected, thanks to the increase in efficiency of the algorithmic operations. Secondly, the increase in the dimension of

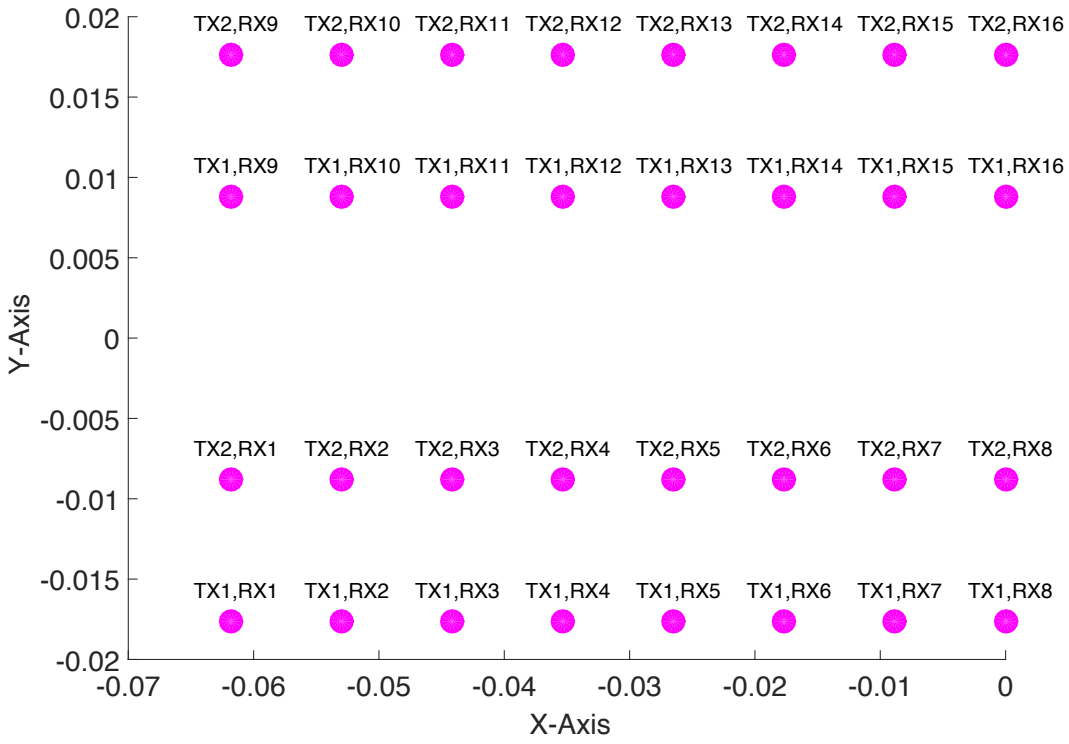

FIGURE 6.20: Virtual antenna array. It is the results of the convolution between the TX and RX arrays.

the radar matrix itself, along the dimensions where the padding is applied, means that longer FFTs need to be applied on the resulting data matrix, which translates into an increase in the number of frequency bins available, after the FFT operation, with finer spacing in between. However, this increase does not affect the resolution capabilities of the radar system itself, but rather just helps into creating a radar image which looks smoother. Thus, it makes it easier to identify targets, without the need for additional interpolation operations.
As shown in 6.18, after the padding operation, the size of the 4D data matrix scales according to the padding factor which has been chosen in the previous step. Therefore, a 4D data matrix of size $(N_{ELE} \times PAD_{ELE}) \times (N_{RX} \times PAD_{AZI}) \times (N \times PAD_{CARR}) \times (M \times PAD_{SYM})$ is obtained and will be used throughout the rest of the processing. PAD_{ELE}, PAD_{AZI}, PAD_{CARR} and PAD_{SYM} represent the padding factor for the elevation, azimuth, subcarriers and symbols dimensions, respectively. For optimum performance, each dimensioń length should be a power of two, as mentioned before.

The 4D reconstruction of the radar scenario is done with a 4D-FFT on the 4D radar signals matrix, resulting from the previous operations. The 4D-FFT can be seen as an operation that computes in-place the one-dimensional fast Fourier transform along each dimension of the 4D radar signals matrix, in this order:

1. The first FFT goes along the first dimension of the 4D matrix, which represents the elevation components of the virtual array, and yields the elevation information of the targets.

2. The second FFT goes along the second dimension of the 4D matrix, resulting from the operation in step 1, which represents the azimuth components of the virtual array, and yields the azimuth information of the targets.

3. The third FFT goes along the third dimension of the 4D matrix, resulting from the operation in step 2, which represents the carrier components and yields the range information of the targets.

4. The fourth FFT goes along the fourth dimension of the 4D matrix, resulting from the operation in step 3, which represents the symbol components and yields the Doppler, or speed, information of the targets.

Hence, a complete sensing of range, azimuth, elevation and speed of the targets is achieved in this manner, which represent the 4 dimensions of the resulting 4D data matrix, after the 4D-FFT. Moreover, it is important to understand that in this way, the compensate and integrate properties of the N-Dimensional FFT are exploited to yield better target estimates. For illustration of target range estimates, the FFT method across the first 3 dimensions (symbols, azimuth angles, elevation angles) presents a Doppler-compensated, azimuth-angle compensated, elevation-angle compensated, received signal integrated along symbols M, along horizontal virtual elements/azimuth angles N_{AZI} and along vertical virtual elements/elevation angles N_{ELE}. Subsequently, this transformed data is transformed by the fourth FFT along the range dimension for a particular Doppler value, azimuth angle and elevation angle parameters (these parameters can be provided by the peak identification operations along those dimensions), to enable better estimation of the target's range parameter. Equivalently, the same operations in the other dimensions lead to better Doppler estimation, azimuth angle and elevation angle estimates owing to the data integration property of the FFT in their respective dimensions.
As shown at the bottom of Fig. 6.18, the last two steps of the algorithm are the shifting and scaling of the resulting data matrix, after the 4D-FFT processing, and the target identification. The shifting and scaling procedures consists of various mathematical operation, among which coordinates transformations, for the plotting of the 4D radar images into a 2D metric coordinates system, with respect to the radar defined as origin. X and Z are the axis used to represent the range and the cross-range in meters, respectively, in the case of range-Azimuth radar images. Finally, the target identification consists in peak analysis functions which yield the most significant targets in a radar's image, based on thresholding.

6.6 Performance and Results

The following section presents the performance analysis for the proposed constant envelope orthogonal waveforms, simulated in a complete OFDM MIMO radar model, based on the architecture presented in the previous chapter. Furthermore, the capabilities of the 4D-FFT radar processing in generating a 4D estimation in multi-target scenarios are shown, through several radar images.

TABLE 6.2: Target Parameters Summary

Target Number	Range	Azimuth	Elevation	Speed	RCS
1	50 m	0°	10°	5 m/s	10 dB
2	150 m	-15°	10°	15 m/s	10 dB
3	350 m	30°	10°	-15 m/s	10 dB

For the simulation of different targets and scenarios, a OFDM MIMO radar simulation model has been created for testing purposes. The parameters chosen for the OFDM model are the ones from Table 5.1. Moreover, the number of TX and RX antennas of the simulated system, have been chosen to be 2 and 16, respectively. This is due to the fact that, as it will be described in the Chapter 7, an OFDM MIMO radar demonstrator has been implemented, with a digital architecture based on the ZYNQ-based board described in Chapter 4, which has 2 DACs and 16 ADCs, therefore allowing to capture with a 2×16 antenna array.

The point scatter channel model is used for modeling of the wave propagation in a channel. Depending on the distance R and the relative velocity v_{rel} of each target, a complex exponential with a phase rotation caused by range and Doppler effects, is added to the transmit signals. Considering the case of K targets at position $\underline{r}_k \, \varepsilon \, R^{3x1}$ and relative radial velocity $\underline{v}_k \, \varepsilon \, R^{3x1}$, the received signal at any receive antenna from transmit antenna i, is expressed as

$$y(t) = \sum_{i=1}^{I} (\sum_{k=1}^{K} \sqrt{\frac{G_T G_R \lambda^2 \sigma_k}{(4\pi)^3 ||\underline{r}_k||^4}} exp(-j\frac{2\pi f_c}{c} \underline{u}_k^T \underline{r}_k) \cdot exp(-j\frac{2\pi f_c}{c} \underline{u}_k^T \underline{v}_k) a_R(\underline{u}_k)) a_T^i(\underline{u}_k) s^i(t) \tag{6.16}$$

where G_T and G_R are the transmit antenna and receive antenna gains, respectively. The term σ_k, denotes the radar cross section, or RCS, of the k-th target, $\underline{u}_k$ is the k-th directional vector and $a_R(\underline{u}_k)$ and $a_T(\underline{u}_k)$, are the receiver and transmit steering antenna components, respectively, provided by the antenna positions.

The results are presented for an exemplary scenario with three point targets with the parameters shown in Table 6.2, in conditions of Signal to Interference plus Noise Ratio (SINR) of -10 dB and then also 10 dB. The speed value illustrated in the table, is positive or negative, according to whether the target is moving away or towards the radar, respectively.

Each of the images is generated with the OFDM frame parameters in Table 5.1. For easier understanding of the results, slices of the 4D images are presented in the following chapters, in the form of 2D images. Doppler-range images are provided, obtained by slicing the 4D images at the different Azimuth and elevation values for the three targets and then superimposing the radar data. Furthermore, the range-Azimuth 2D section views are presented, obtained by slicing the 4D images at the different elevation and Doppler frequency values for the three targets and then superimposing the radar data. For the example scenario provided with 3 targets, in both cases, the result is a superimposition of three 4D radar images slices into one 2D image.

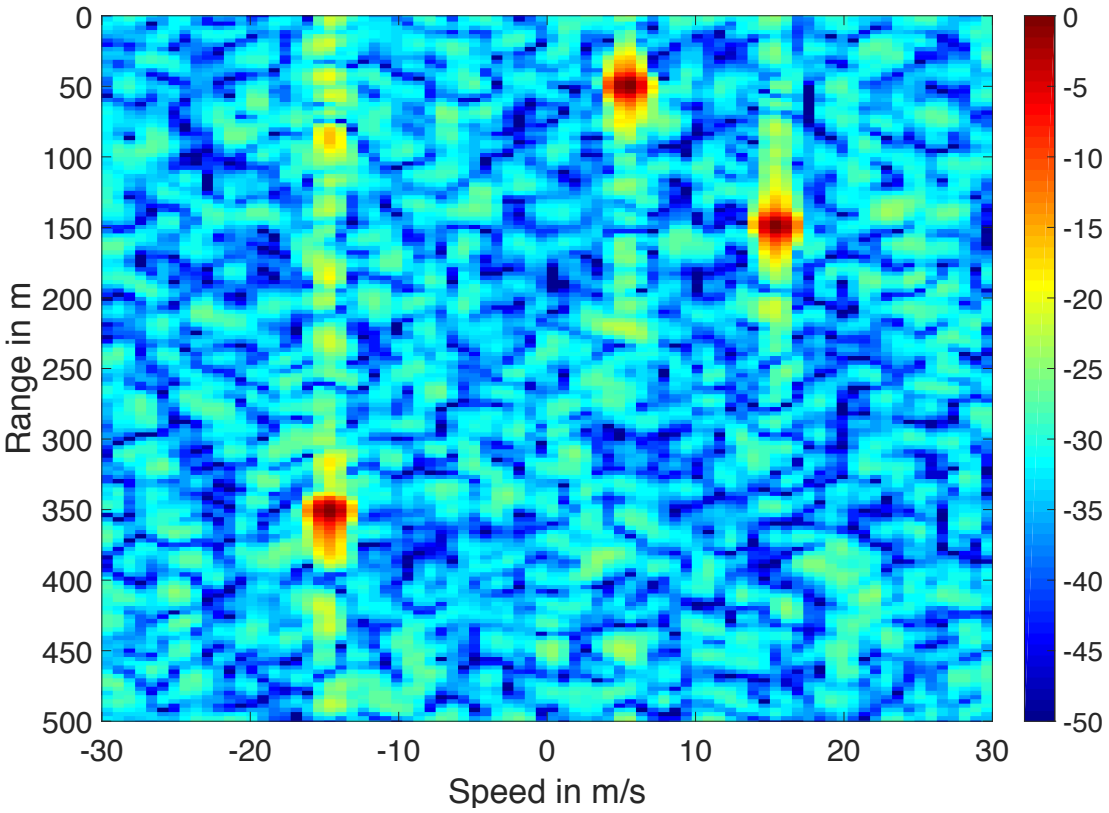

FIGURE 6.21: Range-Doppler map of Golay Complementary Sequence at -10 dB SINR.

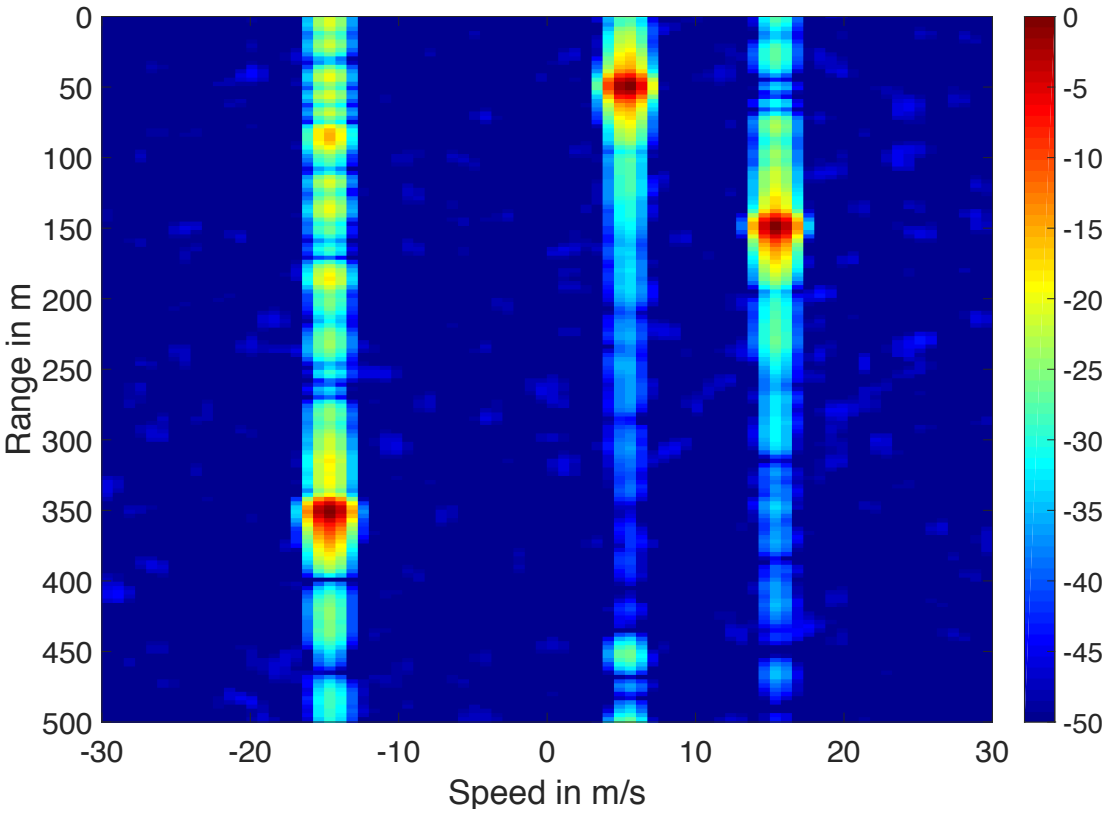

FIGURE 6.22: Range-Doppler map of Golay Complementary Sequence at 10 dB SINR.

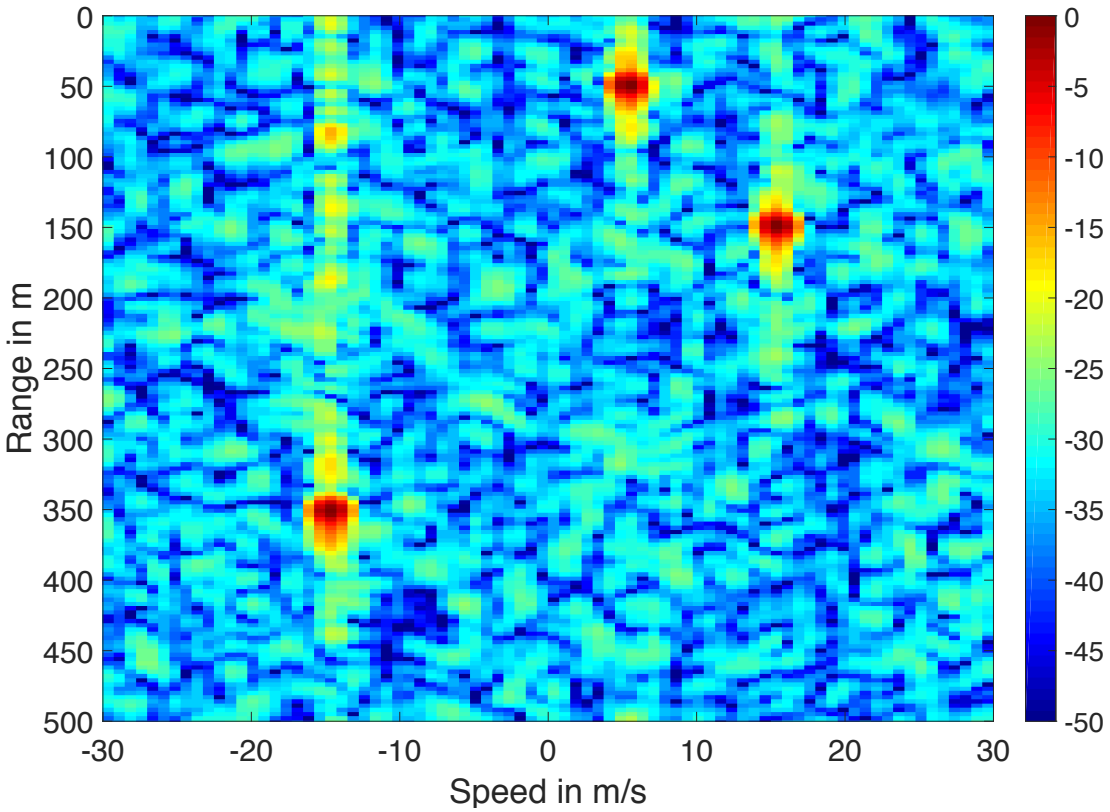

FIGURE 6.23: Range-Doppler map of Zadoff-Chu Sequence at -10 dB SINR.

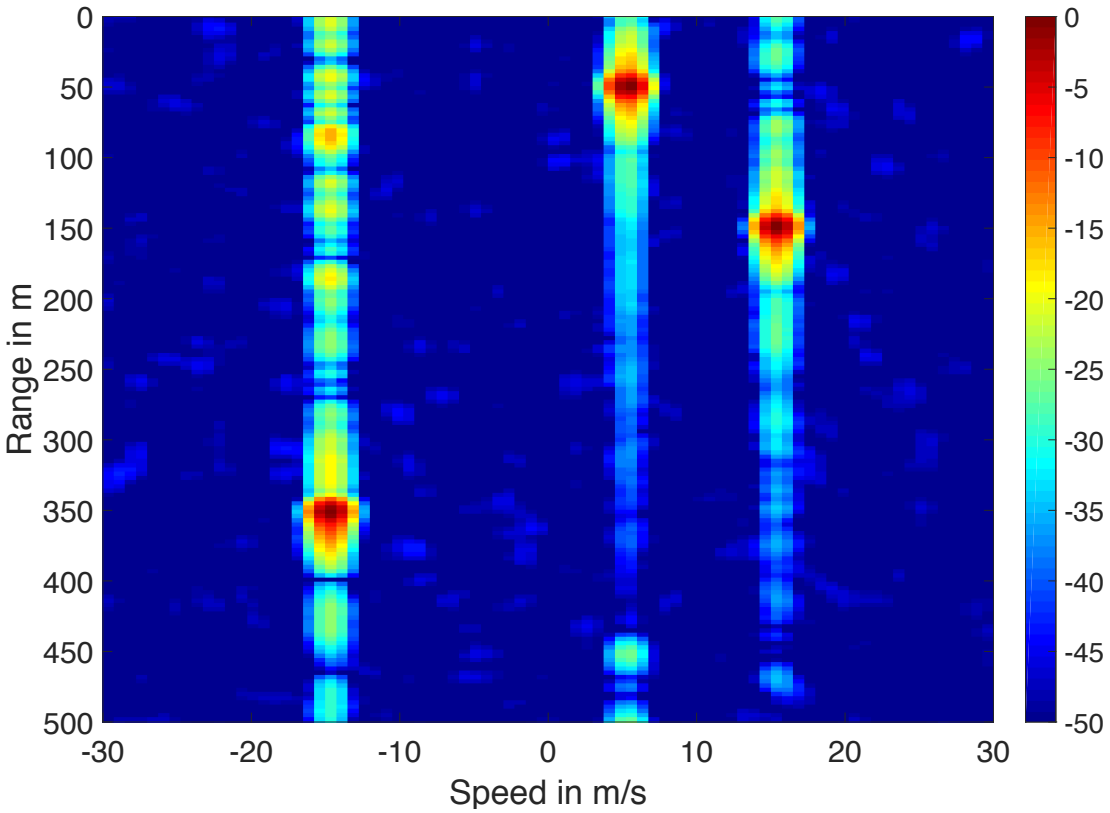

FIGURE 6.24: Range-Doppler map of Zadoff-Chu Sequence at 10 dB SINR.

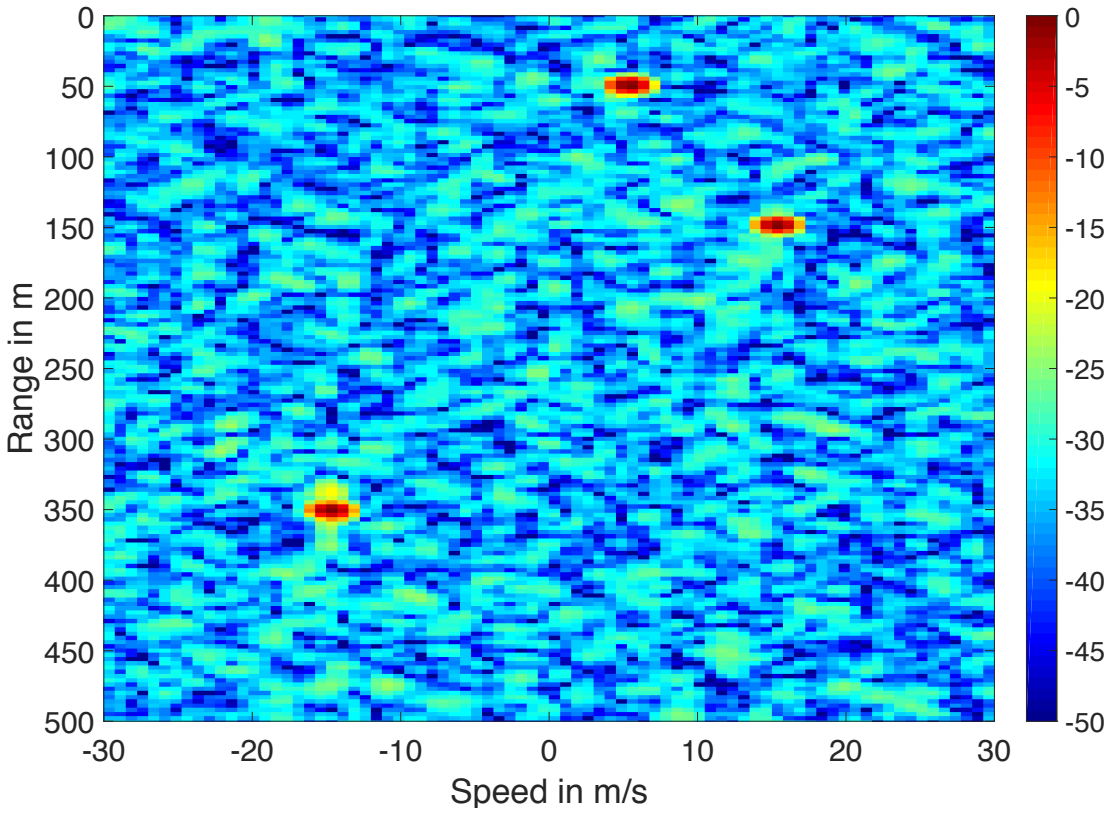

FIGURE 6.25: Range-Doppler map of Space-Time based LFM waveforms at -10 dB SINR.

The first images presented are the Doppler-range radar captures. The colorbar on the right of these images, represents normalized power values in dB. As it can be seen from Figures 6.21-6.32, for all of the proposed waveforms, the three targets are identifiable in all images, at ranges of 50 m, 150 m and 350 m, and speeds of 5 m/s, 15 m/s and -15 m/s, respectively, matching the values in Table 6.2. By comparing Figures 6.22, 6.24, 6.26, 6.28, 6.30 and 6.32, it is clear that under conditions of SINR = 10 db, in all images, all three targets can be uniquely identified with the Space-Time, Walsh-Hadamard and DFT based LFM waveforms among the best in terms of general signal to noise ratio, for both slow and fast moving targets, with peaks reaching values of around 40 dB from the maximum. The situation for the Costas based LFM waveform, is almost the same with just a slight decrease in the signal to noise ratio, with respect to the previously mentioned waveforms, with the noise reaching at times peaks of 33 dB from the maximum. Performance wise, following up, are the Zadoff Chu and Golay complementary sequences based waveforms. However, in the case of these last two, a spread is visible in the range direction at values of around 25 dB from the maximum, which is directly affected by the speed of the moving target, as it is worse at -15 m/s, or 15 m/s, rather than at 5 m/s. This, which is not visible in the first four waveforms compared, would make it marginally more difficult to identify very weak targets which are moving at the same speed. The same effect can be seen present in the Space-Time, Walsh-Hadamard and DFT based waveforms, even though hardly noticeable at more than 30 dB from the maximum. By comparing now Figures 6.21, 6.23, 6.25, 6.27, 6.29 and 6.31, it can be seen that under conditions of SINR = -10 dB, the identifiability

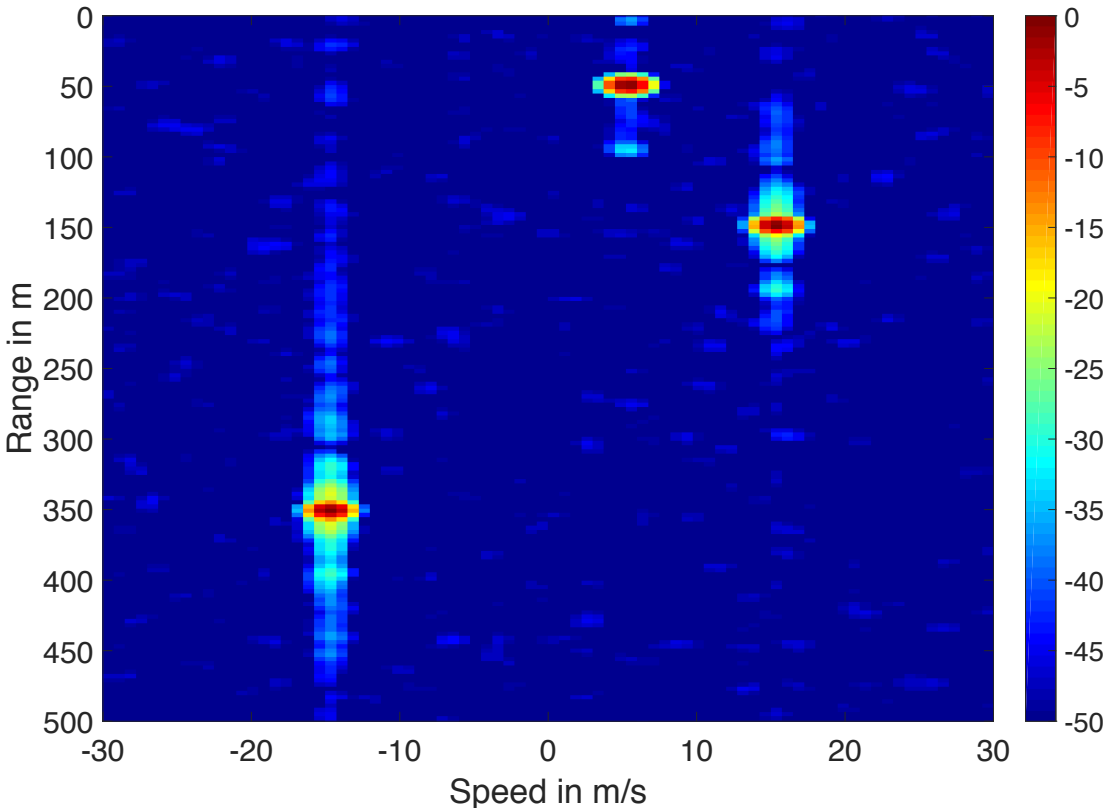

FIGURE 6.26: Range-Doppler map of Space-Time based LFM waveforms at 10 dB SINR.

performance is proportionally similar to what has been previously described. The Space-Time, Walsh-Hadamard and DFT based LFM waveforms, now together with Costas at the same level, perform the best in terms of general signal to noise ratio, for both slow and fast moving targets, with values of around 20 dB from the maximum. The spread in range is now completely masked by the background noise, in the case of these four waveforms, and is still noticeable in the case of Zadoff Chu and Golay complementary sequences based LFM waveforms.

Subsequently, two-dimensional range-Azimuth radar captures are shown in Figures 6.33-6.44. By comparing Figures 6.34, 6.36, 6.38, 6.40, 6.42 and 6.44, it can be seen that under conditions of SINR = 10 dB, the targets can always be identified, with all types of LFM waveforms. Yet again, as in the case of the range-Doppler images, all three targets can be uniquely identified the best with the Space-Time, Walsh-Hadamard, DFT and Costas sequences based waveforms. The three targets are present at ranges of 50 m, 150 m and 350 m and Azimuth values of 0°, -15° and 30°, respectively, matching the values in Table 6.2. Moreover, even in the case of the Zadoff Chu based waveform, the targets are uniquely identifiable, even though a decrease in the value of the reflected power of around 1 dB can be noticed for the farthest most targets. In the case of the Golay complementary sequence based waveform, the targets are also visible, but a slight decrease in the general signal to noise ratio is visible, compared to first four waveforms mentioned, with noise peaks reaching values of around 7 dB from the maximum. If a comparison is now made across Figures 6.33, 6.35, 6.37, 6.39, 6.41 and 6.43, it can

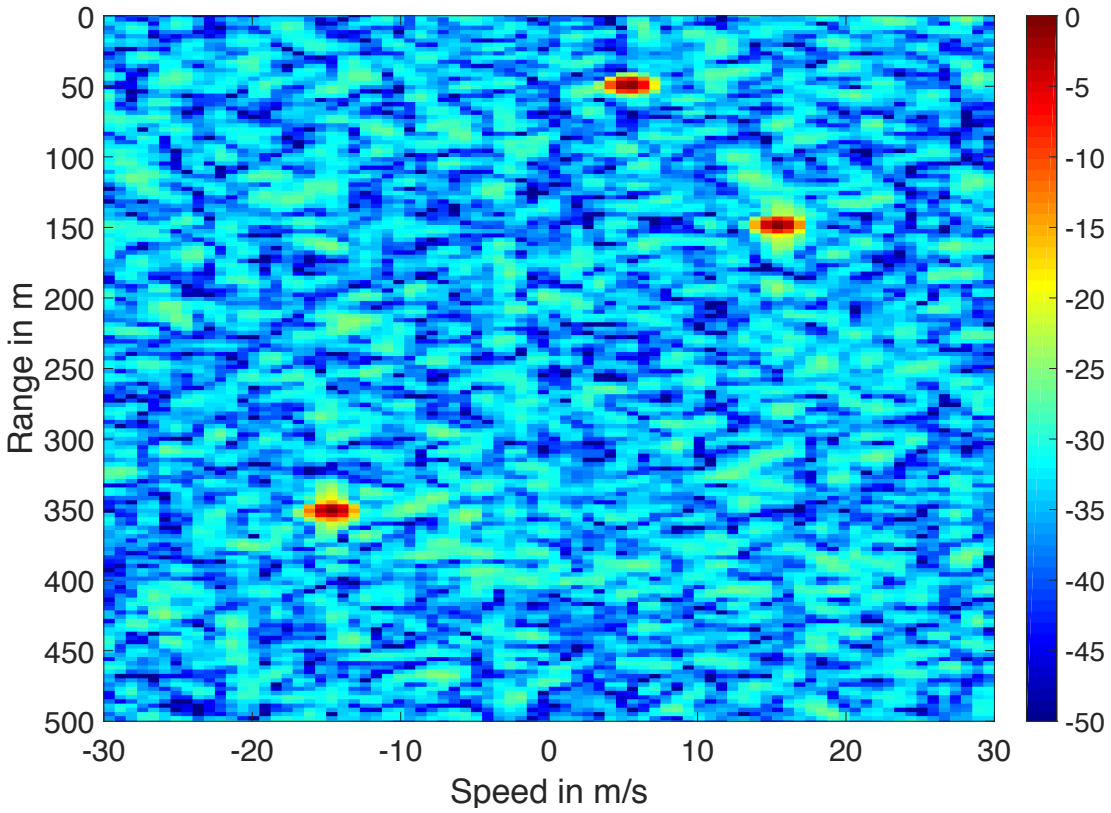

FIGURE 6.27: Range-Doppler map of Walsh-Hadamard based LFM waveforms at -10 dB SINR.

be seen that under conditions of SINR = -10 dB, the situation is different. In this case, all three targets can be uniquely identified the best with the Walsh-Hadamard and Costas based LFM waveforms, with a signal to noise ratio which is more than 15 dB. Different from before, Zadoff Chu based waveforms perform also good in high noise channels, slightly worse than Walsh-Hadamard and Costas code based waveforms, with noise peaks reaching values of 7 dB from maximum. DFT and Space-Time sequences based LFM waveforms are almost similar, with the first one better off in terms of general signal to noise ratio, but sensibly worse compared to the Zadoff Chu ones. Lastly, in the case of Golay complementary pairs based LFM waveforms, in a channel with these noise characteristics, the three targets are not identifiable.

Finally, in order to highlight the full capabilities of the presented system, a complete set of range-elevation results at 10 dB SINR, for all of the LFM based OFDM radar waveforms analyzed, is shown in Fig. 6.45, and a 3D view of the 4D radar data structure is presented, in Fig. 6.46, for the Costas sequence based LFM waveform, at 10 dB SINR. For the above mentioned results, a new scenario has been set up and the same parameters of Table 6.2 have been used. However, in order to show the performance with different elevation values, the elevation is now set to 0°, 20° and -10°, for the targets at 50 m, 150 m and 350 m, respectively. The purpose, is to show how all four targets' parameters are extracted correctly, as it can be seen in all of the plots from Fig. 6.45, as well as in the 3D plot shown in Fig. 6.46, where even the speed (S), which extracted value from the fourth dimension, is included in the label for each target. Additionally, in each label

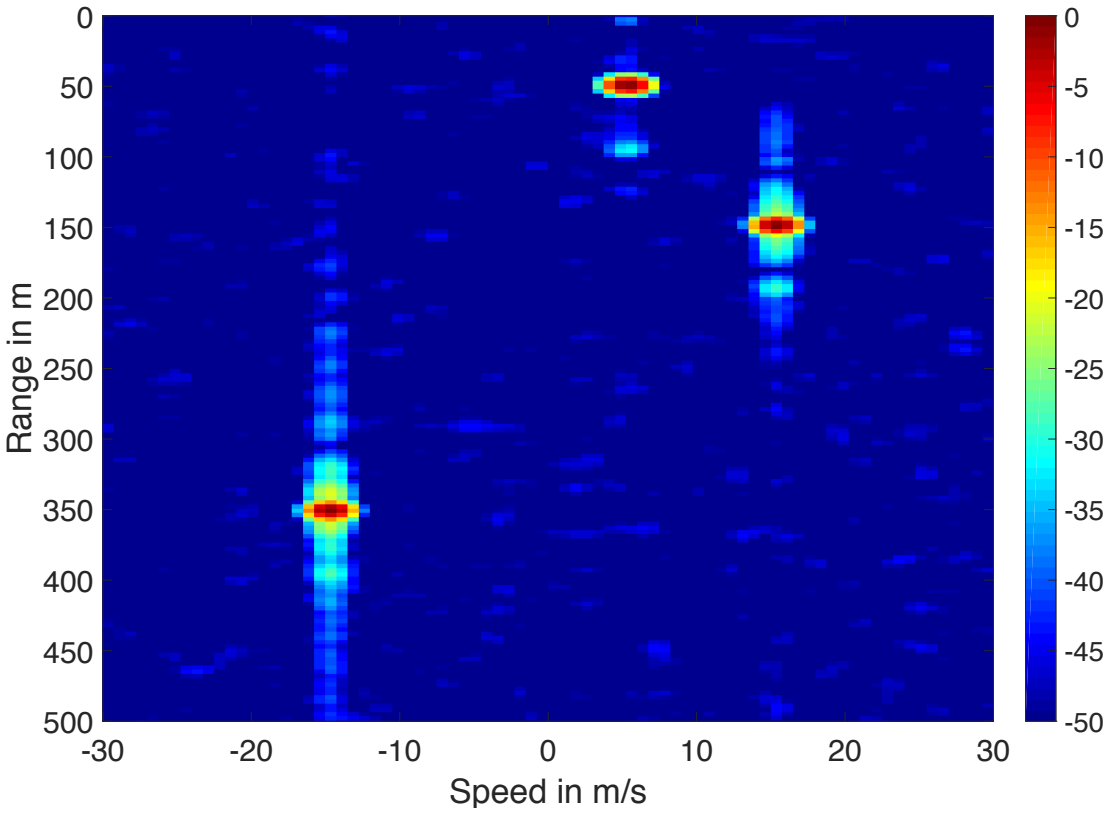

FIGURE 6.28: Range-Doppler map of Walsh-Hadamard based LFM waveforms at 10 dB SINR.

of the image, the extracted values for range (R), Azimuth (A) and elevation (E) are also displayed. The values in this image, are presented as normalized from 0 to 1, where 1 represents the strongest reflecting target.

6.7 Chapter's Conclusions

A successful implementation and thorough analysis of novel LFM based orthogonal-coded waveforms and a complete MIMO OFDM radar architecture, together with its innovative receiver processing and 4D-FFT beamforming technique, is presented. The orthogonal waveforms are designed by coding consecutive complex LFM signals in a frame so that they can be sent simultaneously to the different transmit channels of the radar. The orthogonality is achieved by applying several coding techniques, at a symbol level. The waveforms are first compared through the analysis of their respective cross ambiguity functions, to evaluate their orthogonality performance. Consecutively, the MIMO OFDM system architecture and evaluation model is presented, highlighting the receiver processing based on a complex frame based multiplication in frequency domain between transmit and received waveforms, which allows for the extraction of the individual target-modified components from individual transmit waveforms. Together with the 4D-FFT beamforming processing, this yields a fast and complete sensing of range, azimuth, elevation and speed of a target, in one frame. This allows for the evaluation

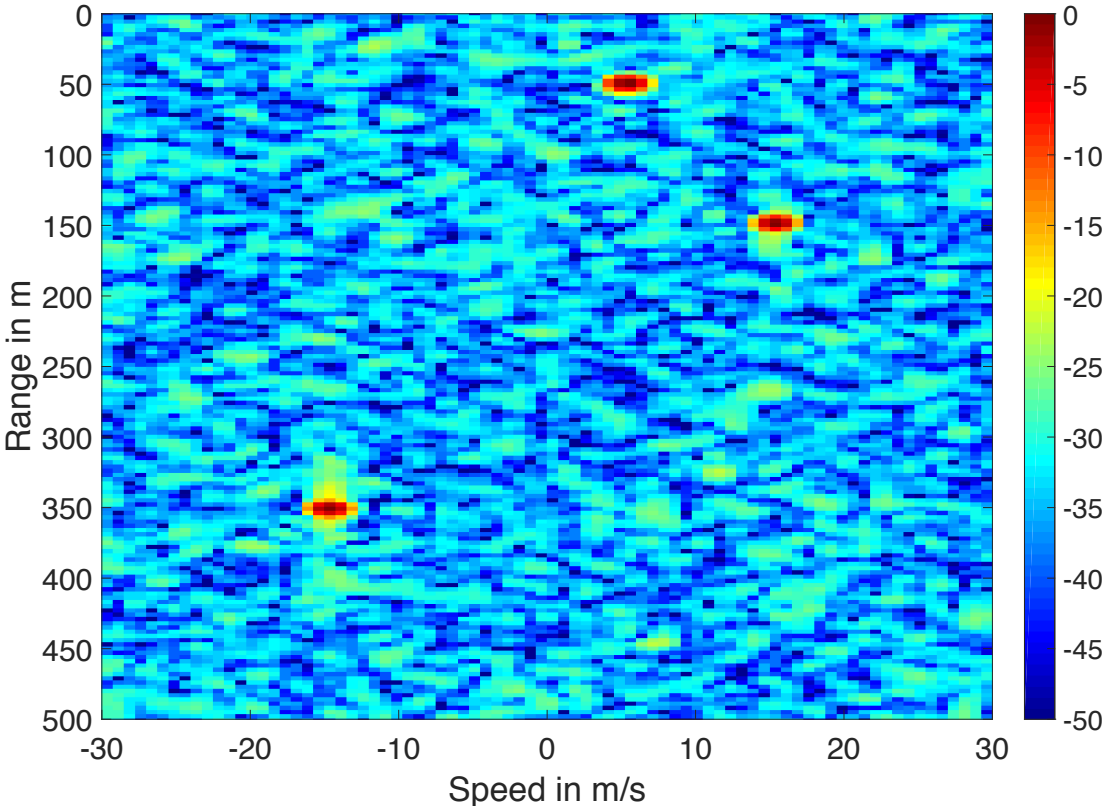

FIGURE 6.29: Range-Doppler map of DFT based LFM waveforms at -10 dB SINR.

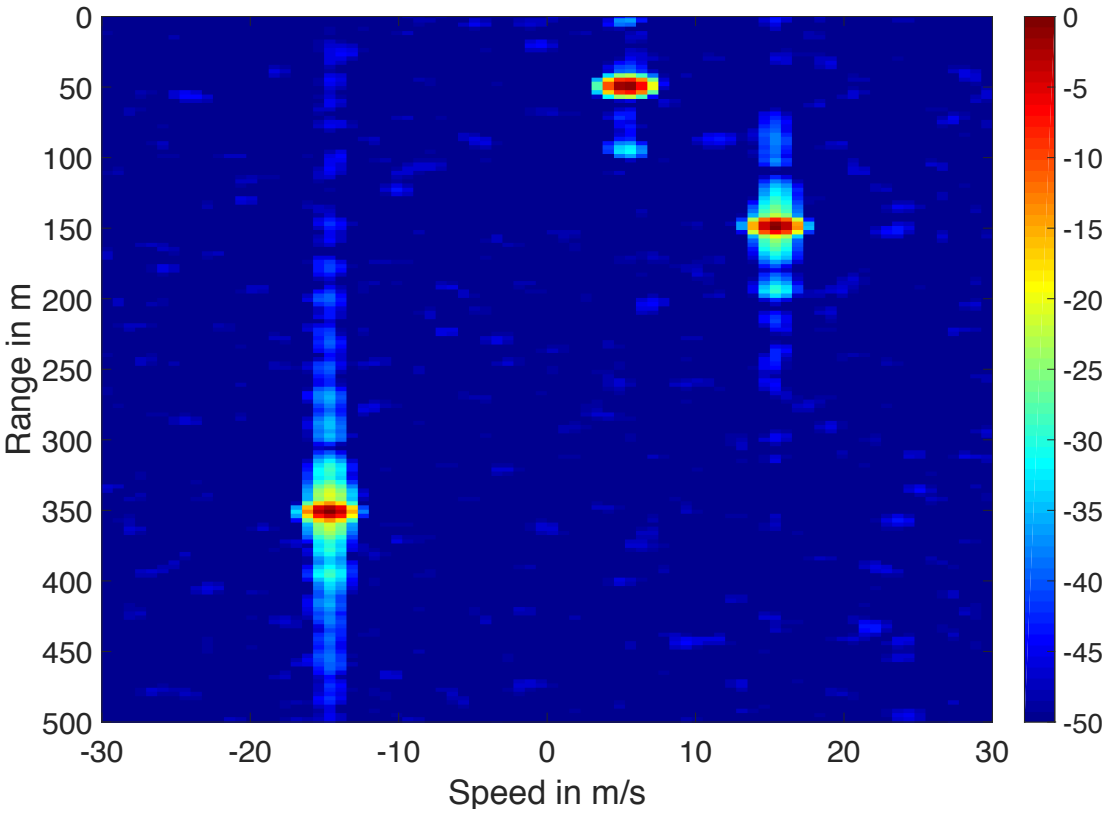

FIGURE 6.30: Range-Doppler map of DFT based LFM waveforms at 10 dB SINR.

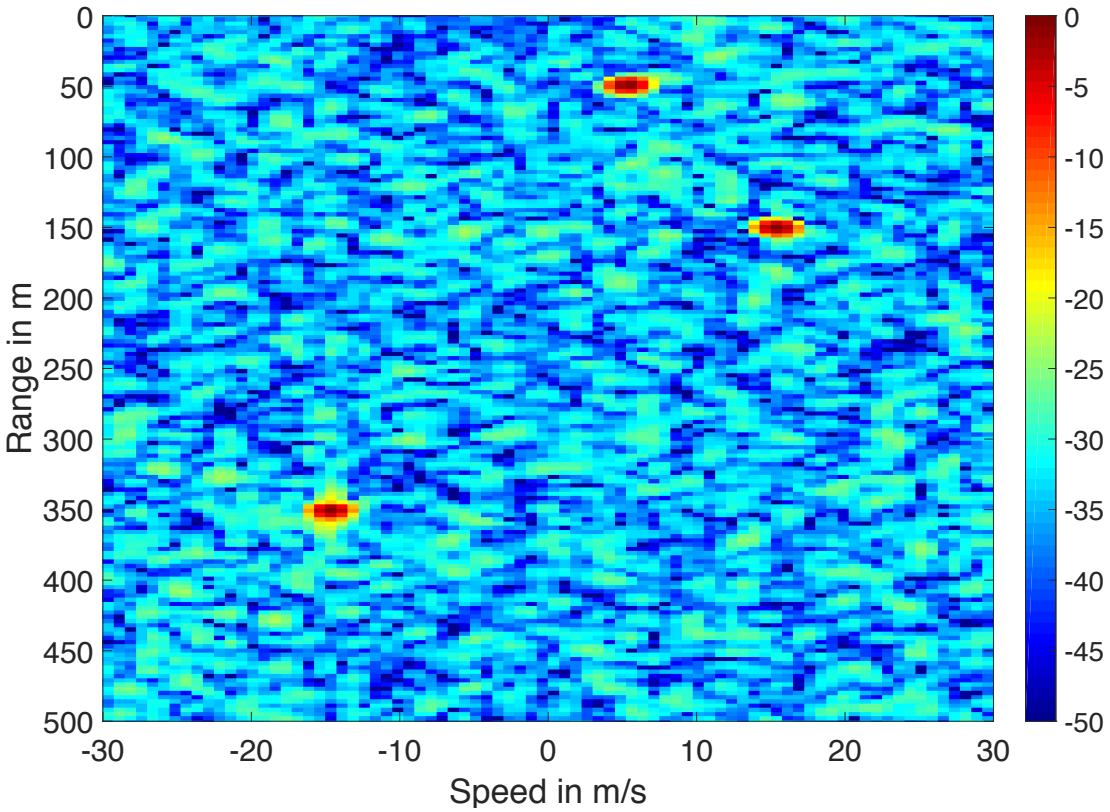

FIGURE 6.31: Range-Doppler map of Costas sequence at -10 dB SINR.

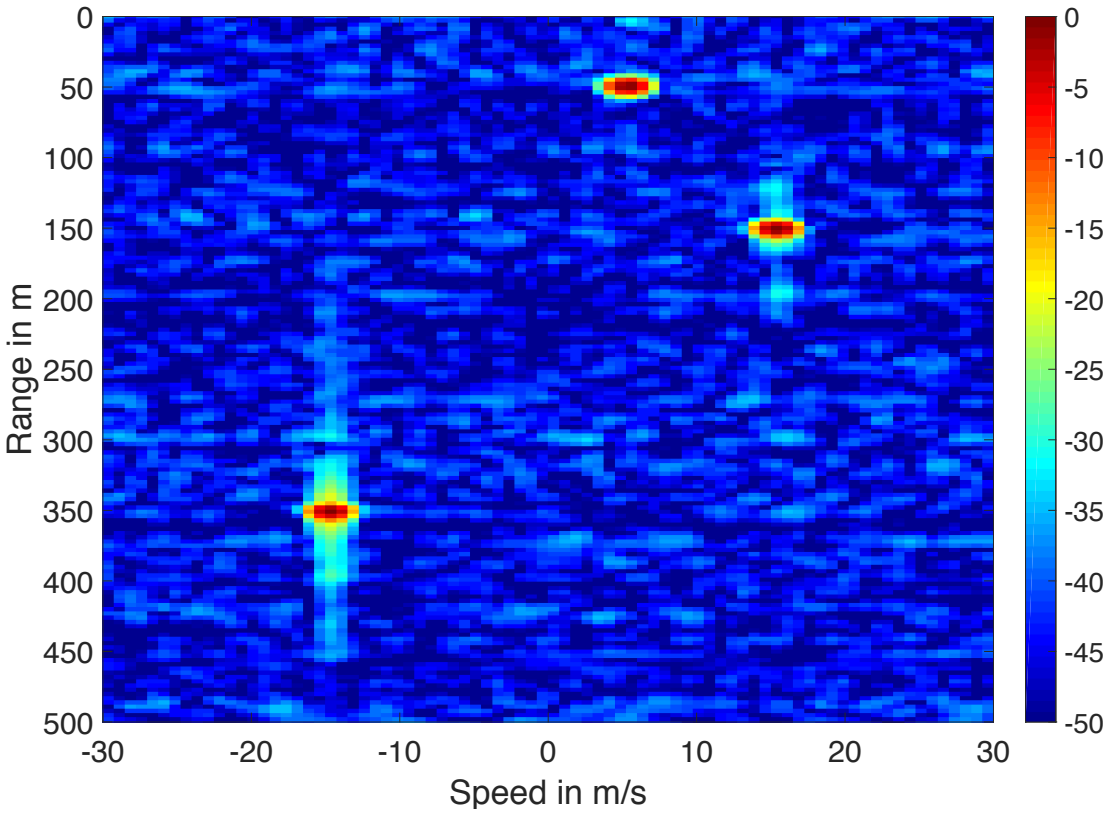

FIGURE 6.32: Range-Doppler map of Costas sequence at 10 dB SINR.

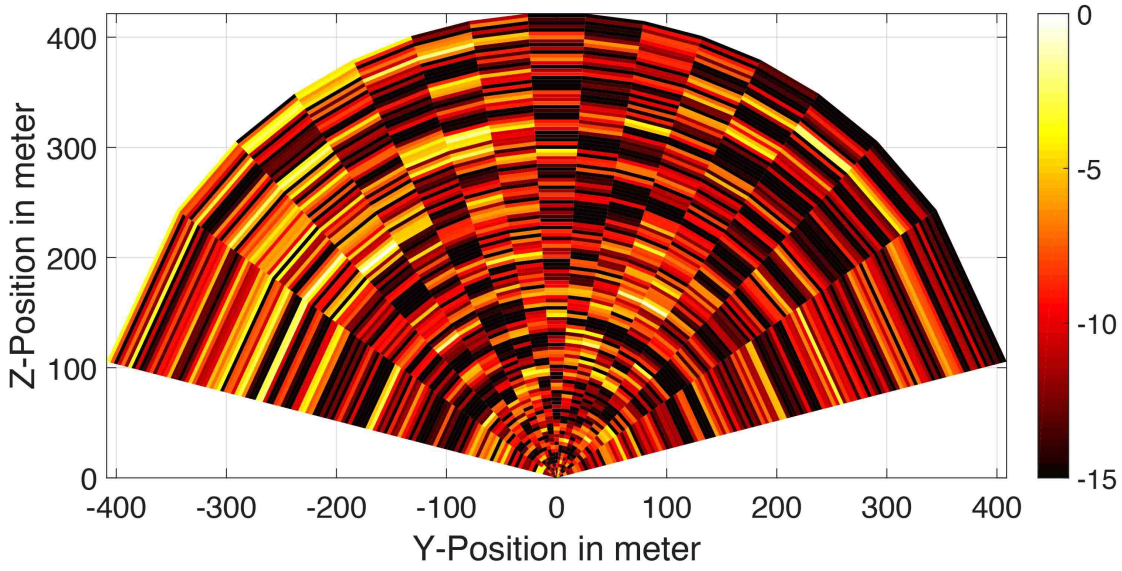

FIGURE 6.33: Range-Azimuth plot of Golay Complementary pair waveform at -10 dB SINR.

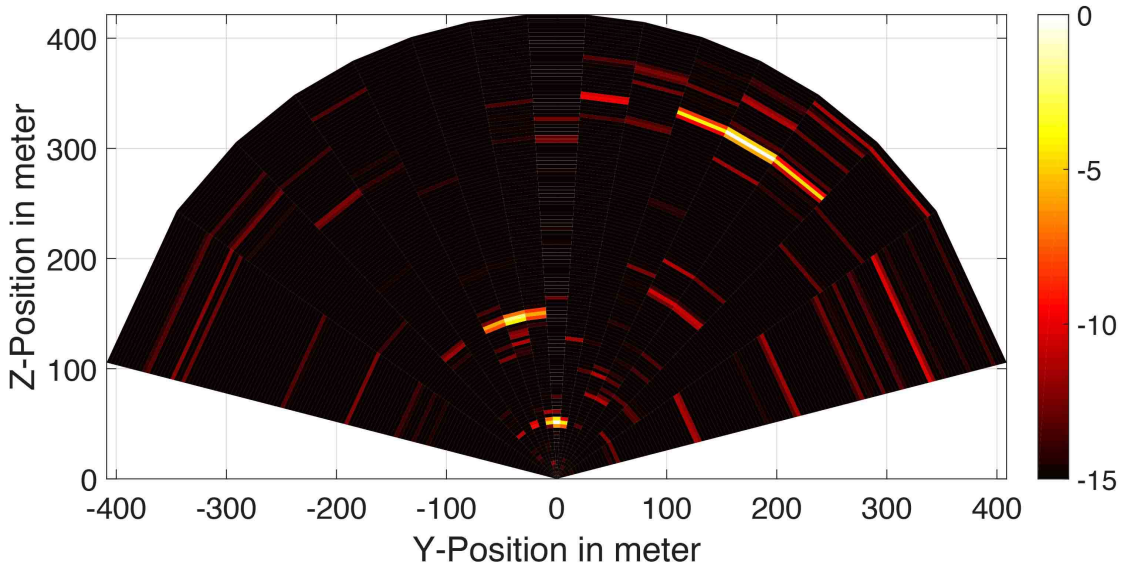

FIGURE 6.34: Range-Azimuth plot of Golay Complementary pair waveform at 10 dB SINR.

of all the proposed waveforms and the general system's imaging performance, shown through several radar images.

Through the analysis which has been carried out, it is possible to discern that all of the proposed waveforms are proven to be appropriate radar signals, with some having better performance than others. In particular, the study shows the importance in drawing conclusions based on, not only investigation of the ambiguity functions, but also the radar images which are obtained with the waveforms. Therefore, the implementation of the MIMO OFDM system, radar receiver processing and 4D-FFT beamforming are crucial in the characterization of the performance.

By comparison of the cross ambiguity functions, it is clear that the Costas sequence LFM based radar waveforms achieve the best orthogonality properties. This is directly

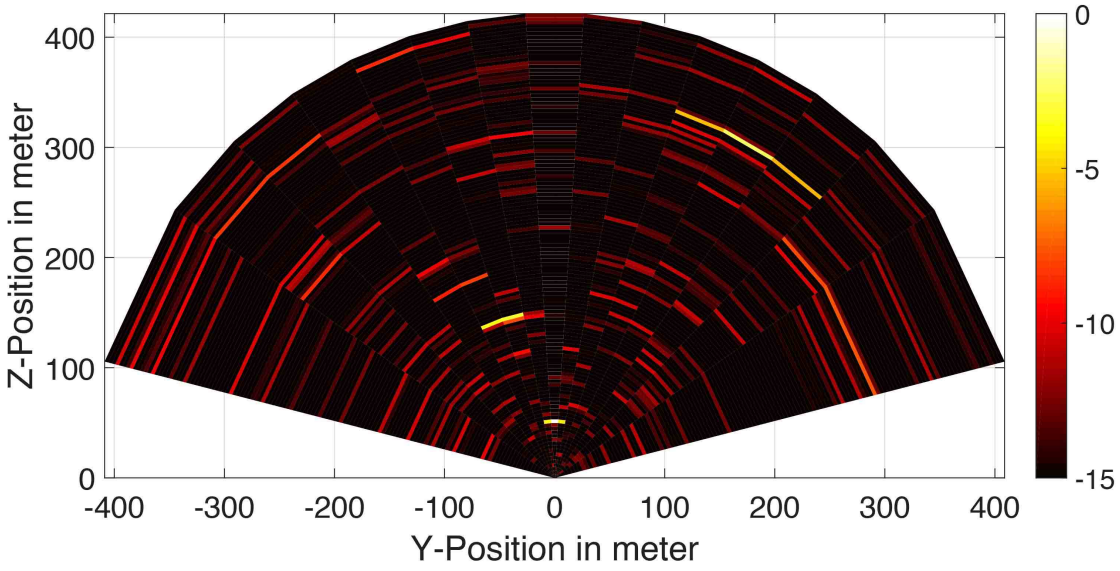

FIGURE 6.35: Range-Azimuth plot of Zadoff Chu sequence at -10 dB SINR.

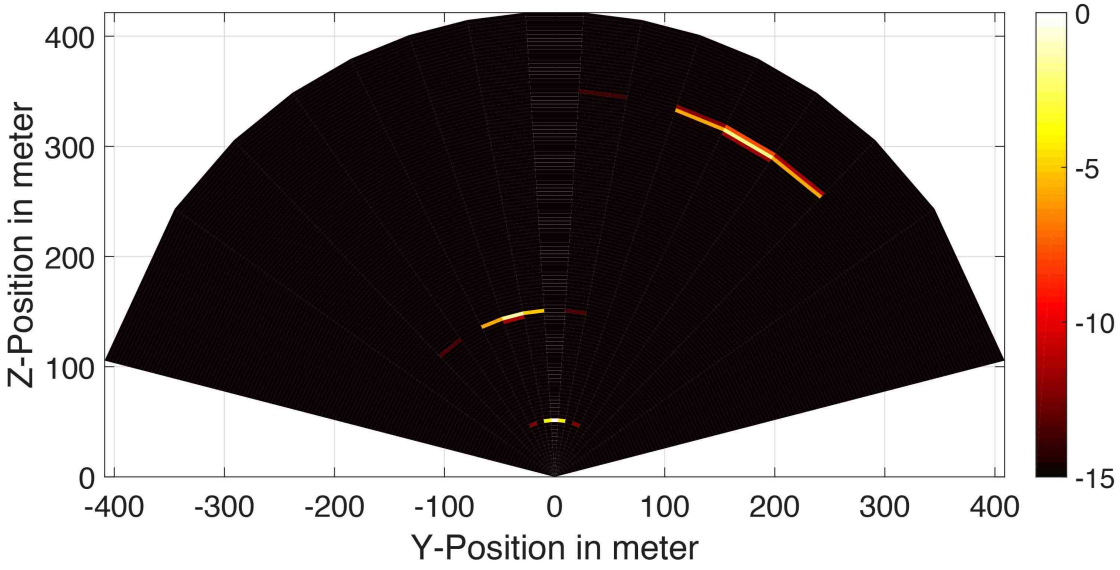

FIGURE 6.36: Range-Azimuth plot of Zadoff Chu sequence at 10 dB SINR.

proven and perceived by the results given in the Azimuth-range radar plots, where, in both conditions of higher and lower noise, the targets are uniquely identifiable. Although the ambiguity function of Walsh-Hadamard based waveforms seems to indicate a worse orthogonality performance of these radar signals compared to Costas based LFM waveforms, from the radar images it can be clearly seen that they perform equivalently, in Azimuth-range radar plots, and even slightly better in allowing to identify targets, from the Doppler-range images. Surprisingly, even though from the ambiguity function it would seem that Golay based waveforms would perform as good as the Costas based, from a comparison of the radar image cuts, it can be seen that these waveforms perform slightly worse than Costas and Walsh-Hadamard based ones, for target identification in both Doppler-range and Azimuth-range plots. Space-Time and DFT code based LFM

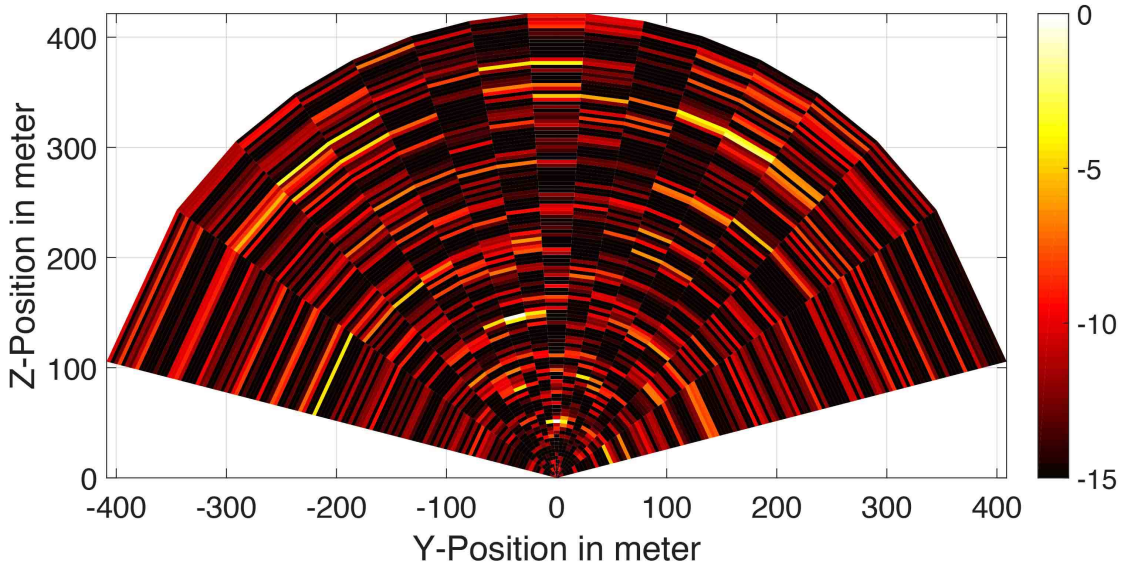

FIGURE 6.37: Range-Azimuth plot of Space-Time based LFM waveform at -10 dB SINR.

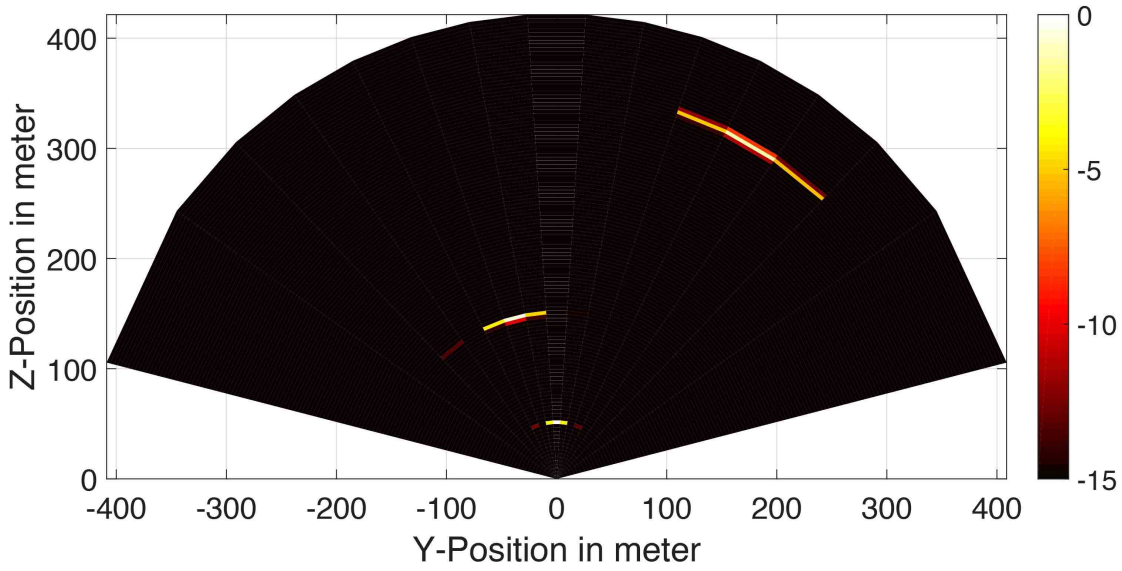

FIGURE 6.38: Range-Azimuth plot of Space-Time based LFM waveform at 10 dB SINR.

waveforms perform very similarly to Walsh-Hadamard based ones in all scenarios analyzed, despite for the target identification in the Azimuth-range images in high noise environments, where they have a slightly worse outcome. As from the performed analysis, the ambiguity function of Zadoff-Chu based LFM waveforms indicates a marginally worse orthogonality performance, as compared to Golay based ones. However, although the signal to noise ratio is the same in the Doppler-range images, from the Azimuth-range radar images it can be seen that Zadoff-Chu based LFM waveforms achieve better target identifiability performance.

The proposed orthogonal waveform's design and overall OFDM MIMO radar architecture is proven to give successful results. Being simple, reliable and easily configurable on the fly, the proposed system is attractive for an adaptive radar, which is capable

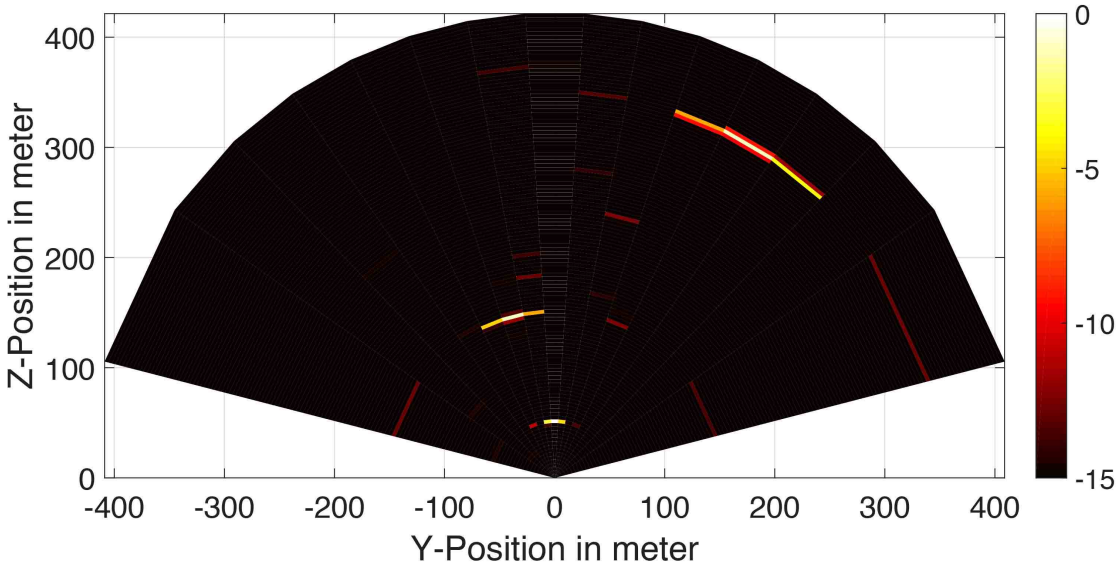

FIGURE 6.39: Range-Azimuth plot of Walsh-Hadamard based LFM waveform at -10 dB SINR.

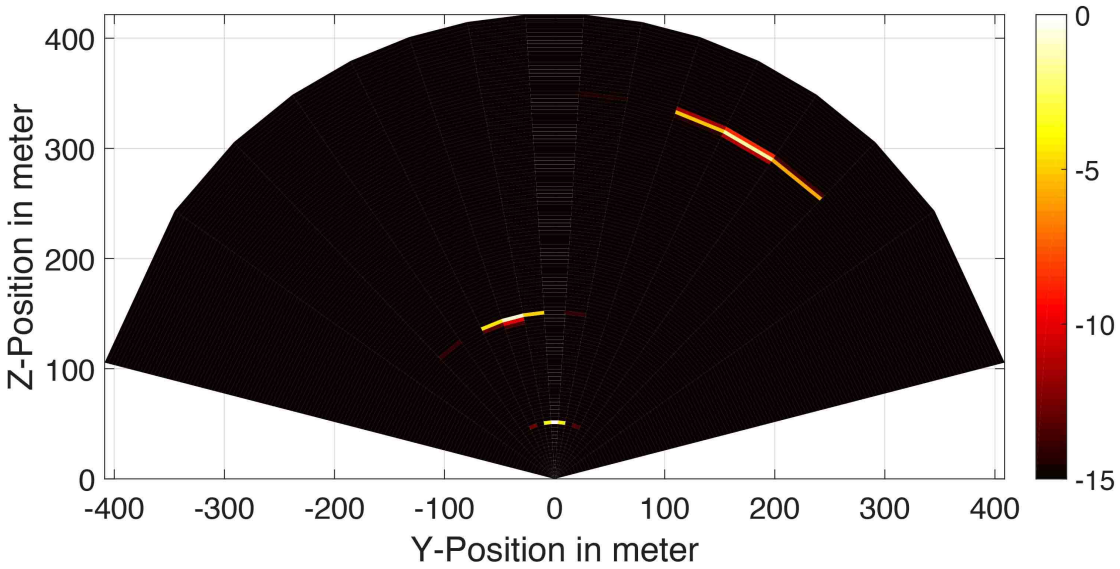

FIGURE 6.40: Range-Azimuth plot of Walsh-Hadamard based LFM waveform at 10 dB SINR.

of adaptively changing its waveform, based on the radar channel which is used in. For example, the system could be initialized with Costas based LFM waveforms, since they have been proven to have the best cross ambiguity properties and Azimuth-range performance. Consecutively, after probing of the environment, the radar system can be reconfigured to use Walsh-Hadamard based LFM waveforms, in the case that an accurate Doppler estimation is required. Additionally, for example, Space-Time coded LFM and DFT coded LFM waveforms can be used in fast changing environment since less number of symbols are required per frame to achieve orthogonality, whereas other coded waveforms are advantageous in case of stationary targets with low RCS.

The system, with these novel orthogonal waveforms, patented in [208],[209],[210] and

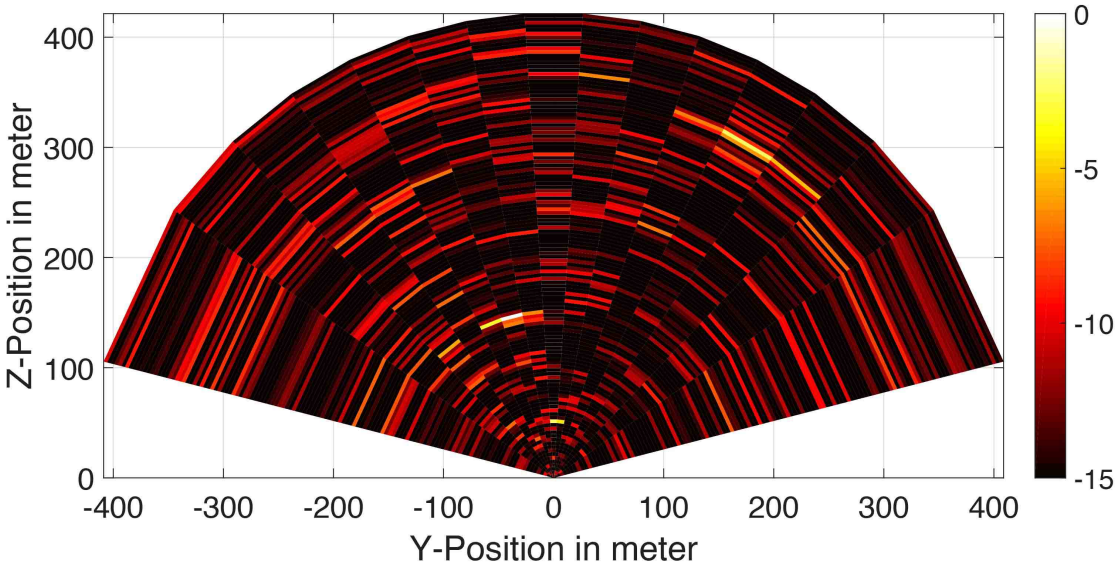

FIGURE 6.41: Range-Azimuth plot of DFT based LFM waveform at -10 dB SINR.

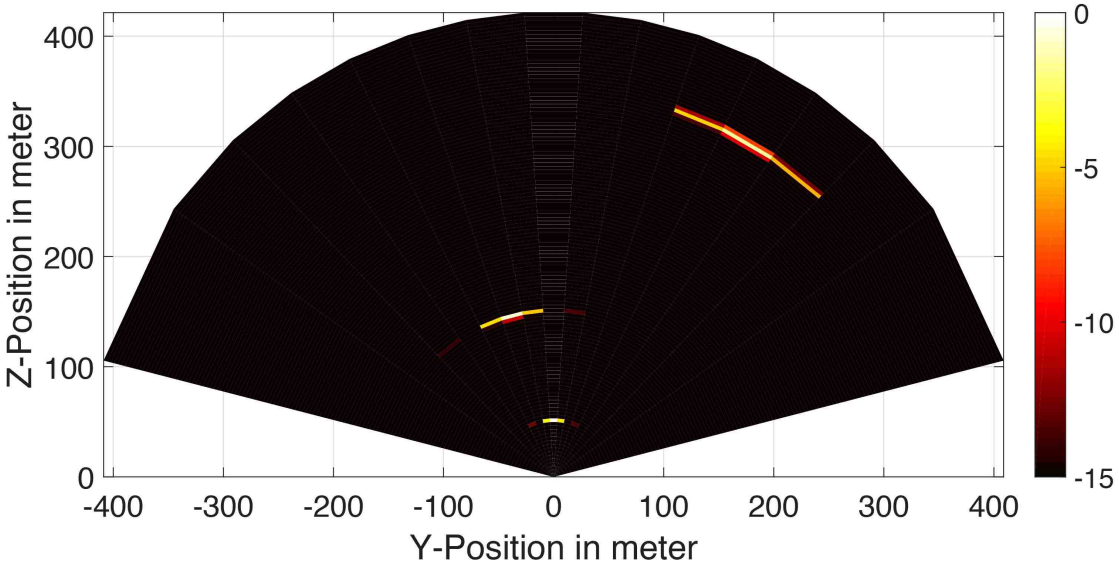

FIGURE 6.42: Range-Azimuth plot of DFT based LFM waveform at 10 dB SINR.

receiver architecture, patented in [211], paves the way for realization of an adaptive real-time and low cost device, which can target a multitude of applications, especially for the situation awareness in miniaturized flying platforms, air taxis and both air and ground based radar systems.

In the next chapter, the concepts which have been introduced up until here, regarding the OFDM MIMO radar architecture, will be concretized into the implementation of a complete radar demonstrator, which has been tested and analyzed outdoors.

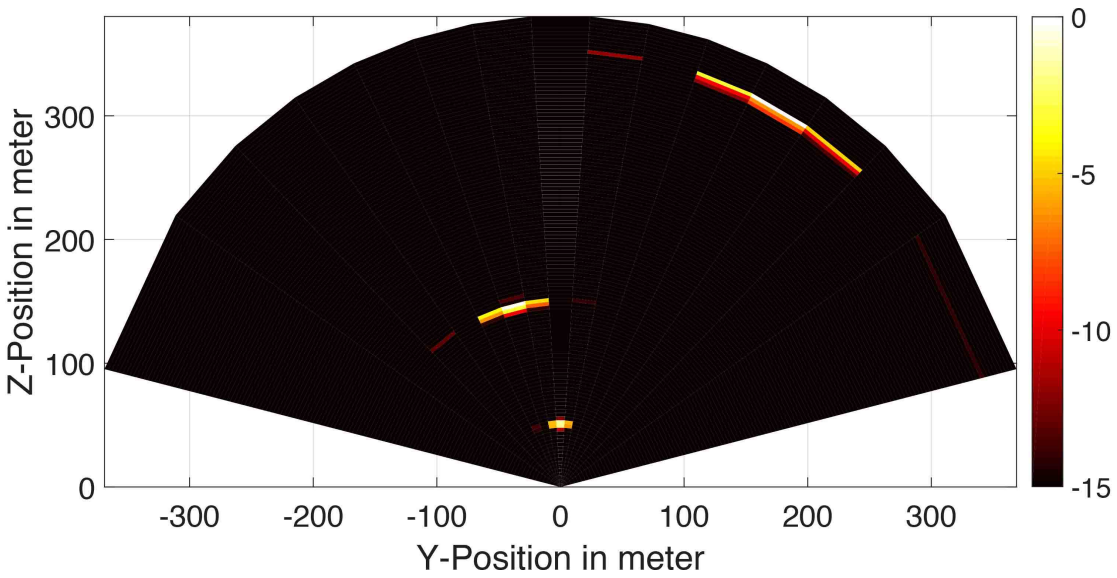

FIGURE 6.43: Range-Azimuth plot of Costas sequence at -10 dB SINR.

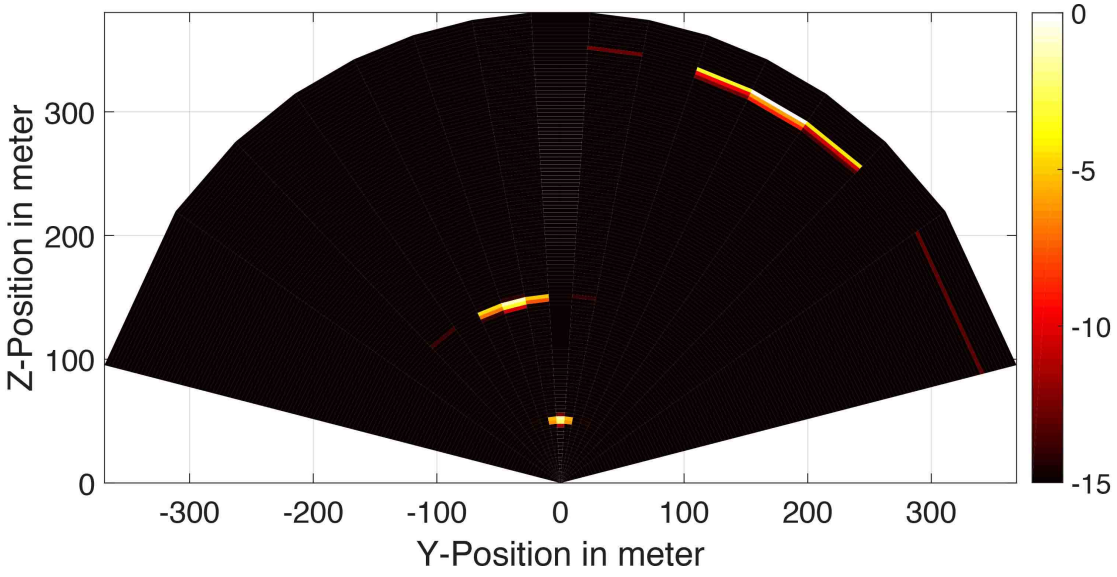

FIGURE 6.44: Range-Azimuth plot of Costas sequence at 10 dB SINR.

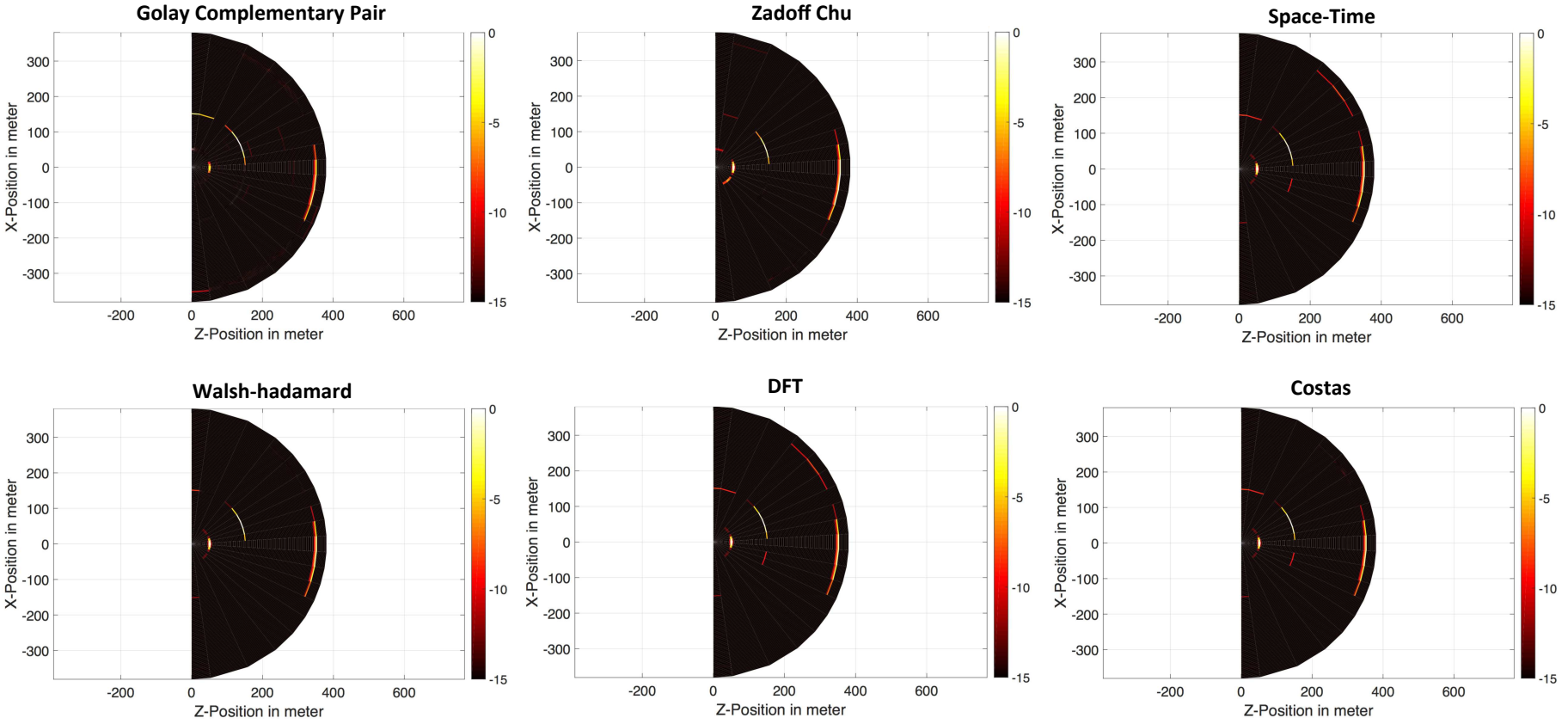

FIGURE 6.45: Range-elevation plots of all of the proposed LFM based OFDM radar waveforms at -10 dB SINR.

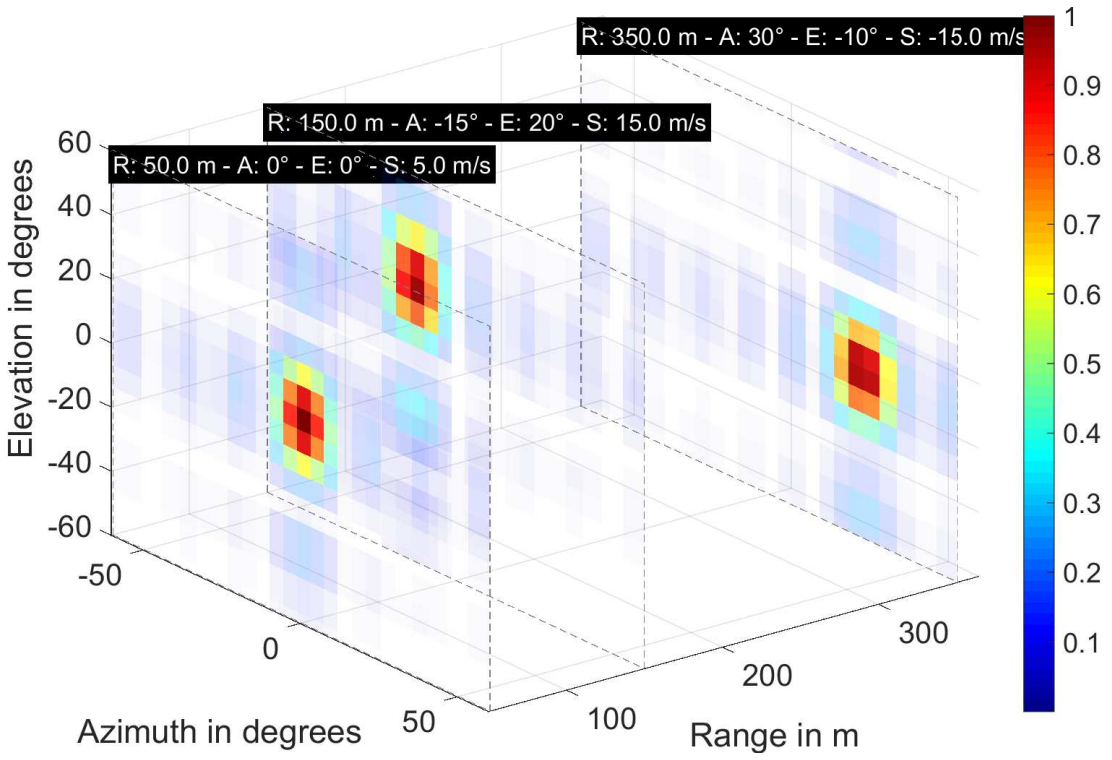

FIGURE 6.46: 3D radar image of Costas sequence based LFM waveform at 10 dB SINR.

Chapter 7

3D Imaging OFDM MIMO Radar Demonstrator

7.1 Chapter's Introduction

In Chapter 5, an introduction to OFDM systems is given, together with the characterization of the OFDM waveform's parameters, for a specific application, intended into addressing the use of MIMO radar's in flying platform scenarios.
In Chapter 6, a novel type of MIMO OFDM radar architecture which includes orthogonal waveforms and a 4D-FFT beam-forming based radar's receiver processing is given.
In this final chapter, the previously introduced concepts and architectures are conjoint and a 3D imaging OFDM MIMO system demonstrator presented in [212].
The OFDM MIMO system is based on one of the novel orthogonal waveforms of Chapter 6, which is the Walsh Hadamard code based complex LFM waveform. The radar architecture is based on the use of OFDM signals which are simultaneously transmitted from all transmit antennas and the orthogonality is applied at a symbol level [211].
Furthermore, the system shares a lot of the hardware which has been previously described in Chapter 4.
The radar system is verified through measurements and the results are presented, through radar image captures. The proposed architecture, paves the way for a low cost, miniaturized and real-time capable, adaptive OFDM MIMO radar systems.

7.2 System Structure

The top-level system structure is presented in the form of a block diagram in Fig. 7.1. The system in based on the hardware architecture of the MIMO radar demonstrator which has been shown in Chapter 4, however, the transmit part and the digital architecture implemented in the ZYNQ board, have been completely changed and adapted to a MIMO OFDM radar system, as the one presented in Chapter 6, in Fig. 6.1. The receive antennas are the wide-band resonant slot patch antenna elements previously used.

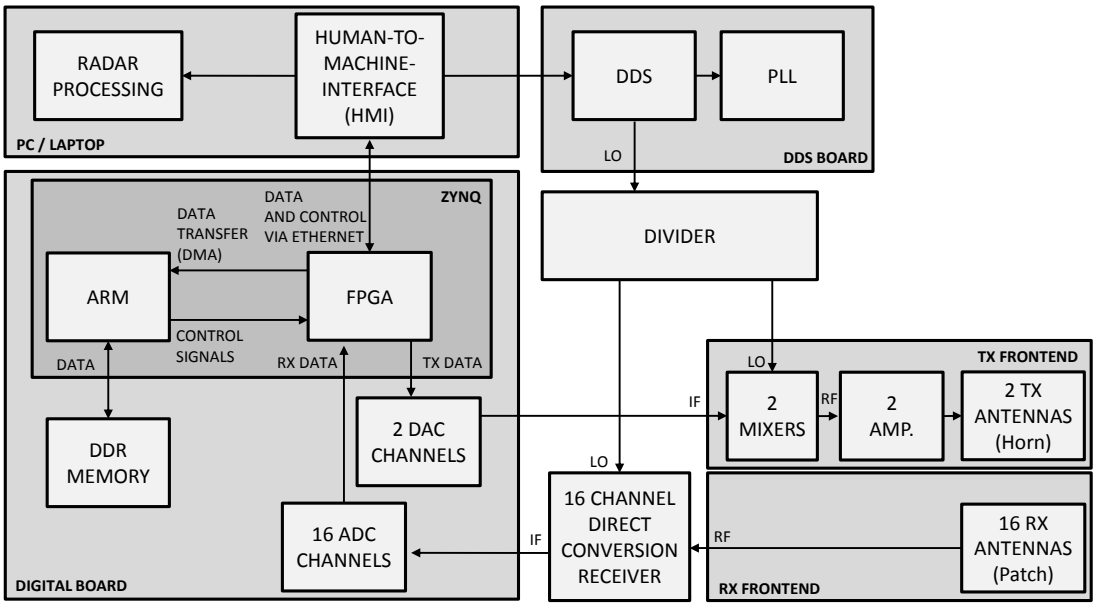

FIGURE 7.1: OFDM MIMO radar top-level block diagram

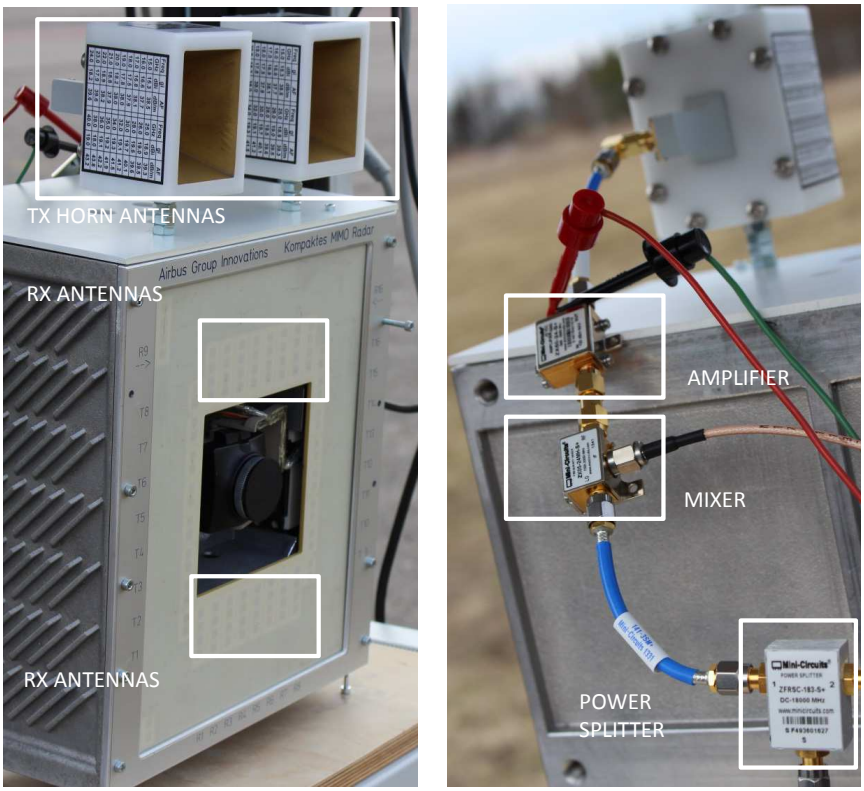

FIGURE 7.2: Front-view (left) and back-view (right) of the OFDM MIMO radar.

Additionally, the same 16-channel analog receiver board, shown in Fig. 6.17, is used, the same 3D printed chassis is used, as seen in Fig. 7.2, and for the hardware realization of the radar signal processing, the same Xilinx Zynq Z-7045 SoC based proprietary platform, comprising two ARM CPU cores, an FPGA unit and the 16 ADC channels, is used, as previously shown in Fig. 4.8. Differently from before, for the transmit RF part of the MIMO OFDM demonstrator, new COTS components have been used. This includes power dividers, couplers, mixers, amplifiers, filters and horn antennas. The used components can be seen in Fig. 7.2. In this picture, it can be noticed that the two horn antennas are added on top of the chassis. Moreover, the DDS and PLL unit, is not used in a chirp generating mode for providing the FMCW signals for transmit and de-ramping, but only for the generation of a continuous waveform. Therefore, this unit acts as a wide-band local oscillator, or simply LO, board for the generation of the up-conversion and down-conversion carrier frequency, now set at 15 GHz. The reason for this is that the radar signals are now generated digitally and not from a dedicated board, hence, there is a need for a continuous wave signal for the conversion to and from baseband. This can be seen in Fig. 7.1, where it can be noticed that the signals from the DDS and PLL unit go through a divider, where the two exits are connected to the up-mixing stage where the mixers are, and to the down-mixing stage, where the 16 channel receiver is.
Since the OFDM transmit signals are generated digitally from the ZYNQ board, now the two DACs available are effectively used. As a matter of fact, it is important to remember from Fig. 4.9, that the ZYNQ based digital platform used, provides two AD9129 14-bit DAC units, useful for the generation of digital waveforms.
The 16 ADC signal inputs and ADC clock inputs are shown in Fig. 4.8, subsection D, where also the 2 DAC signal outputs and the DAC clock input can be seen.
The DAC outputs are connected directly to the two mixers, which up-convert the radar signals, from baseband, to radar band, as shown in Fig. 7.1.
The OFDM radar transmit waveforms, are pre-saved in the internal memory of the FPGA, read-out and continuously streamed through the DACs. Moreover, the board serves as the interface between the 16 ADCs which are integrated on the board and the laptop performing the acquisition of digital data. As a matter of fact, it can be remembered from Chapter 4, that the 16 ADC input ports on the digital board, are directly connected to the 16 IF output ports of the receiver's board.
The resulting signals are digitized by 16 ADCs, the data is stored in the FPGA and then transferred to the DDR memory of the system via DMA transfer. From the digital board, the data is transferred to the laptop via Ethernet, where the OFDM radar's beam-forming and image generation processing is done.

7.3 The Digital Architecture

A schematic view of the implemented digital architecture for the signal processing of the OFDM radar signals, from sampling to image generation, is presented in Fig. 7.3.

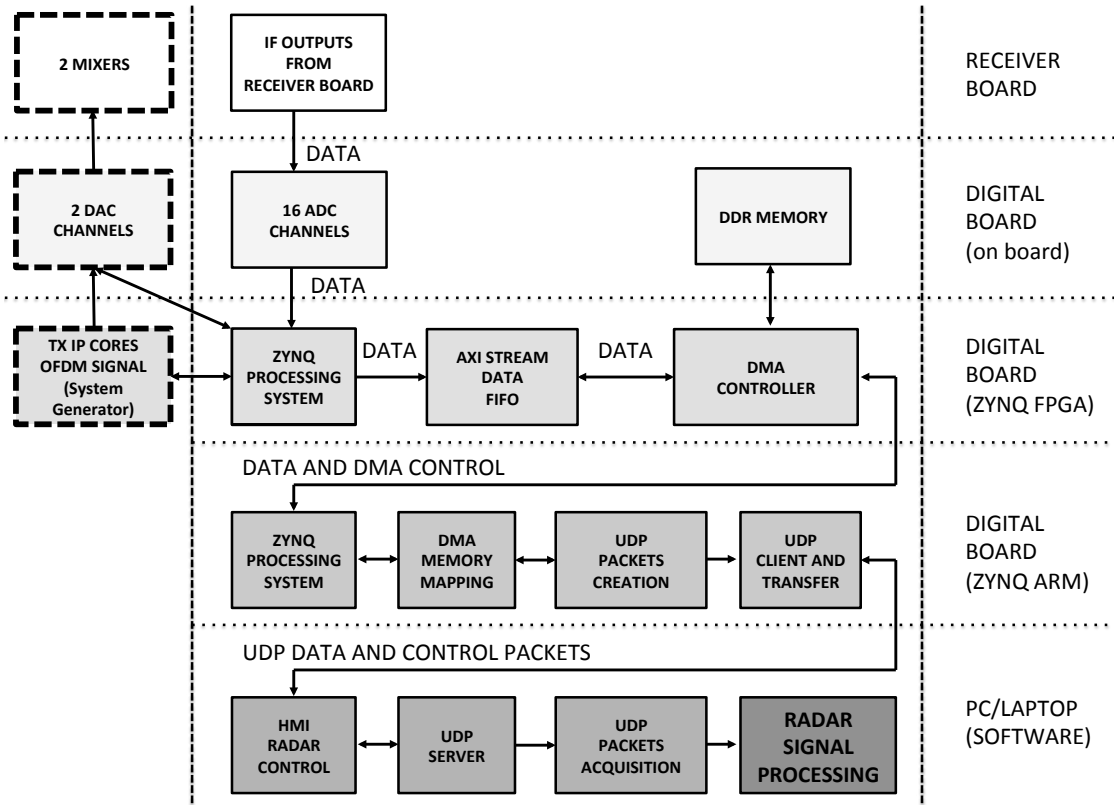

FIGURE 7.3: Schematic view of the digital architecture for the OFDM radar processing, from the sampling of the radar signals, to the radar image generation.

It is based on the previously presented architecture from Chapter 4, in Fig. 4.10, however, the internal processing is adapted to an OFDM architecture. Therefore, the TDM scheme is not used anymore, since the transmit antennas are transmitting the orthogonally coded OFDM signals simultaneously. Additionally, as it can be seen, the two available DACs have been interfaced to the FPGA's logic. The radar signal processing adopted is the one described in Chapter 5, with the frame based complex multiplication of the transmitted and received OFDM radar signals, together with the 4D-FFT beamforming.

As it can be seen from Fig. 7.3, the complex architecture consists of several interfaces and domains, which are continuously crossed with a flow of both data and control signals. The architecture is a fusion between physical interfaces, VHDL firmware components, ARM drivers and applications, *C* code blocks and applications, MEX functions and MATLAB code programs.

From the HMI radar control interface, a user can start the processing of the OFDM radar signals. However, in order to understand how the radar data and control signals flow, throughout the design, it is important to start from the basic concepts of how the data is sampled and processed.

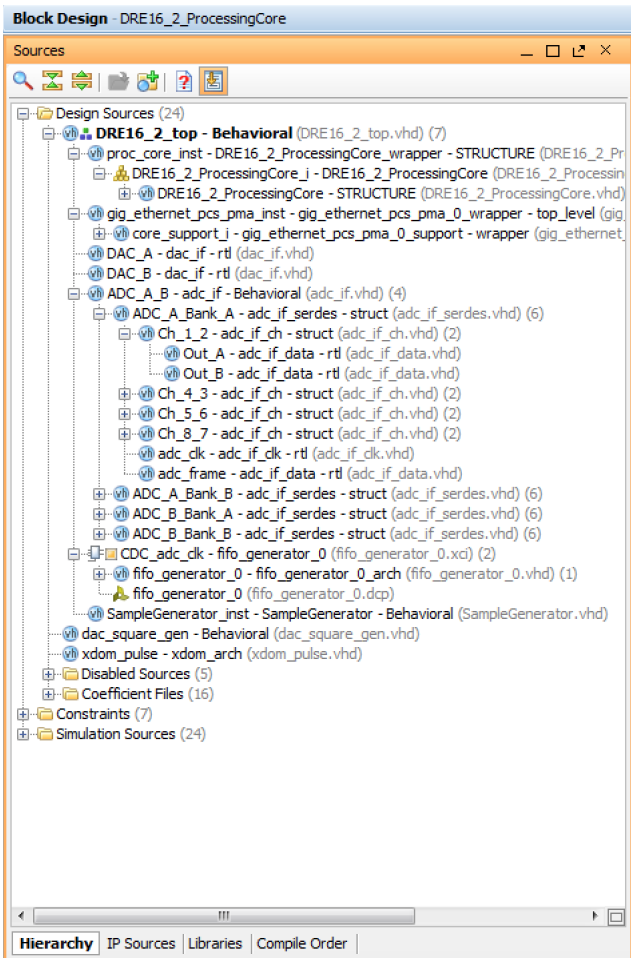

FIGURE 7.4: Picture from the Xilinx Vivado tool, depicting the main blocks implemented in the VHDL firmware for the radar processing.

7.3.1 The FPGA Processing

It can be recalled from Chapter 4, that the first step is the interfacing of the two LTM9011 ADC chips on the digital board and, therefore, the 16 ADC inputs, which stream the radar signals data, sampled from the signals arriving from the receiver board. This, among other functionalities, is achieved in the implemented firmware for the ZYNQ board, as it can be seen from Fig. 7.4, which depicts the main components of the VHDL based firmware, such as the ADCs, DACs and FIFOs, and Fig. 7.5, which illustrates a schematic view of the complete firmware architecture, from a top level view. The main components which can be seen from Fig. 7.5, are the FIFOs, the ZYNQ processing system, the DMAs and the AXI components and peripherals.
After initial setup of the ADC chips' interfaces and serial/deserializing operations, the 16 ADC channels are connected to LogiCORE IP AXI4-Stream FIFO cores, which allow a memory mapped access to a AXI4 stream interface. For the storing of the ADC samples, a DMA module is used, which allows the transferring of data from the ADCs, to the external DDR memory. The AXI-lite bus allows the ZYNQ processor to communicate with the AXI DMA controller to setup, initiate and monitor data transfers. This is done through master-to-slave (AXI_MM2S) and slave-to-master (AXI_S2MM) buses,

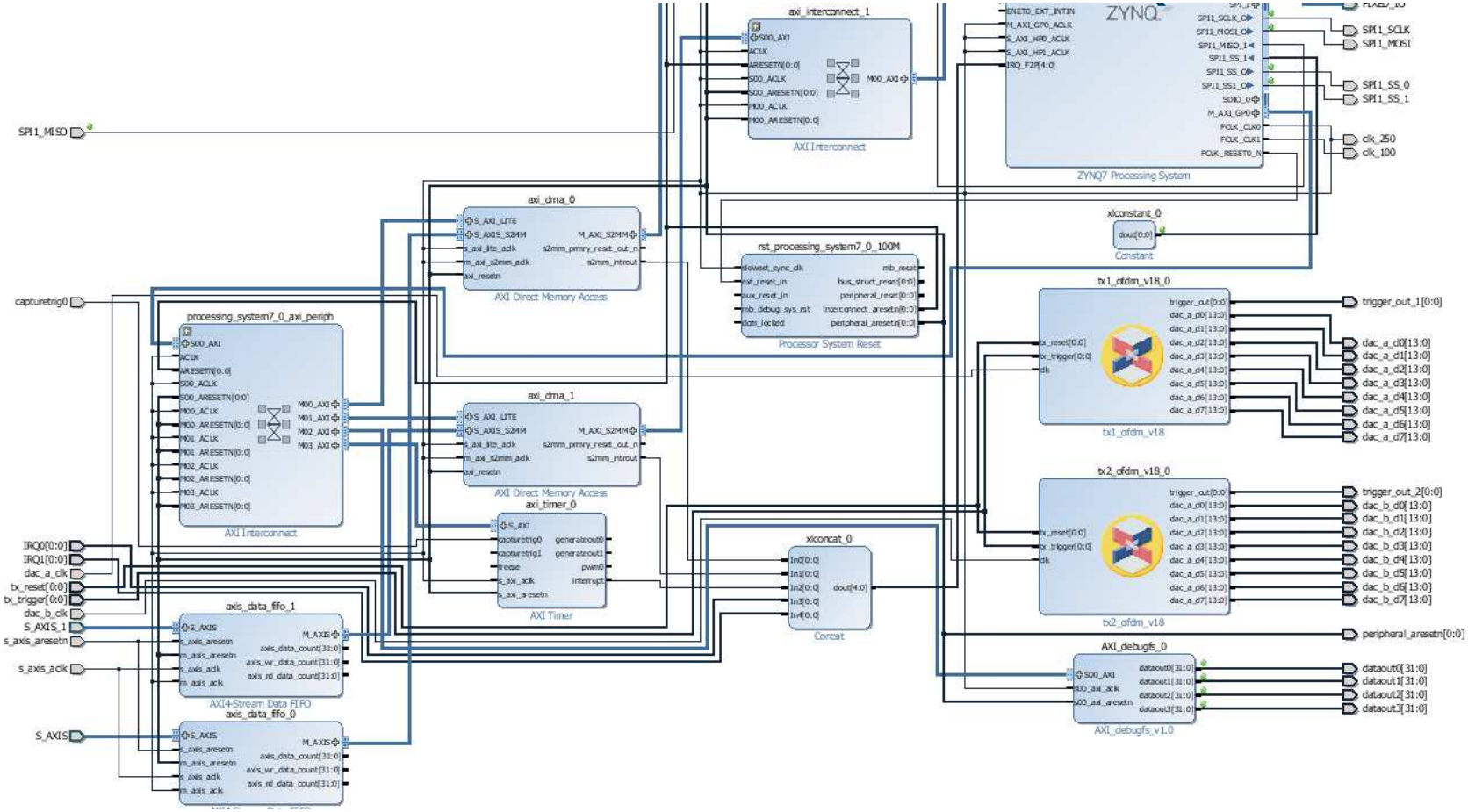

FIGURE 7.5: Schematic view of the VHDL firmware for the radar processing, implemented in the Xilinx Vivado tool.

which are memory-mapped AXI4 buses, which provide the DMA access to the DDR memory.
With the above mentioned operations, it is possible to store the samples of the OFDM MIMO radar signals inside an external DDR memory, which is necessary due to the size of the transferred data, which would not, otherwise, fit inside the internal FPGA memory. The content of the OFDM radar signals present inside the DDR memory is then transferred, through the ARM processor and through an Ethernet interface, to the PC, where the radar beam-forming and image processing is done.

The second step involves the interfacing of the two DAC AD9129 chips, which are are high performance 14-bit RF converters, supporting data rates up to 2.85 GSPS. After initial setup of the DAC chips' interfaces and parallelizing operations, the two DAC channels are fully operational and interfaced to the FPGA chip, thanks to the implemented firmware. More specifically, the two DAC interfaces are connected to two blocks which feed them the OFDM transmit signal to be sent from the two transmit antennas. Important part of the connection, is the implementation of an 8 input channel interface, with specific clock and data format requirements, necessary for the DAC to operate.
The two blocks can be noticed in the lower right part of Fig. 7.5, identifiable by the Xilinx logo on them, and represent two components which have been generated in Xilinx System Generator and imported as IP cores in the Xilinx Vivado software [213]. Eight of the nine outputs of these blocks, which are the signals named *dac_a_d*0 to *dac_a_*7 and *dac_b_d*0 to *dac_b_*7, for the $tx1\_ofdm$ and $tx2\_ofdm$ blocks, for the TX1 and the TX2 antenna, respectively, are directly connected to the inputs of the DACs' parallel interfaces in the VHDL firmware. Since eight input paths are required for the interface, and since the DACs are configured to operate with a sampling of 2.5 GSPS, set in the boot-up sequence, each signal data path needs to be clocked at 312.5 MHz. Additionally, the data provided, as per the DAC's architecture, needs to be in a 14 bit format. A description of the OFDM radar waveforms used and how they are linked to the DACs, is now explained.

7.3.2 Walsh Hadamard coded LFM based OFDM Waveform

The proposed radar system is based on an OFDM architecture, which means that from each transmit antenna, an OFDM waveform is transmitted.
Each of the waveforms, or frames, transmitted from each of the N_{TX} antennas, consists of $N \times M$ samples, where N and M represent the number of subcarriers and number of symbols, respectively. For the generation of each waveform, a MATLAB based radar processing script is used, which generates the vectors, representing the frames to be sent to the DACs.
In the proposed system demonstrator, an LFM based signal is chosen as a base radar signal, visible in Fig. 6.2, which has been coded according to Walsh-Hadamard sequences, as previously presented in Chapter 6.4.3. It can be recalled, that the coding is based on a Hadamard matrix H of order n, which is an $n \times n$ matrix of ones $(+1)$ and minus ones (-1) in which $H^T H = nI_n$, where I_n is the $n \times n$ identity matrix and $H^T H$ is

TABLE 7.1: 3D OFDM MIMO Radar's Parameters Summary

Symbol	Parameter	Value
f_c	Carrier Frequency	15 GHz
N	Number of subcarriers	450
N_{FFT}	Number of subcarriers	1024
Δf	Subcarrier spacing	100 kHz
T_p	Cyclic prefix duration	64 us
T_{OFDM}	Transmit OFDM symbol duration	10,24 us
B	Total signal bandwidth	30 MHz
Δ_r	Range resolution	5 m
r_{max}	Maximum unambiguous range	1500 m
M	Number symbols	512

the transpose of H. Since the system is based on two TX antenna elements, the coding matrix can be represented as

$$A = \begin{bmatrix} 1 & 1 \\ 1 & -1 \end{bmatrix} \tag{7.1}$$

The two rows in the matrix, representing the spread spectrum sequences generated by the Walsh-Hadamard functions, are chosen for the orthogonal code c_m^i, expressed in (6.2) and are used as the code for modulating across the M symbols of each transmit antenna. The coding scheme architecture has been previously described in Fig. 6.3, where it has been shown how the coding is applied, at a symbol level, by means of a multiplication with the original LFM signal.

7.3.3 The OFDM Waveform's Parameters

A summary of the implemented OFDM frame parameters is presented in Table 7.1. The total signal bandwidth plays a significant role in the parametrization of the OFDM frame and in particular in determining the number of subcarriers N and the subcarrier spacing Δf. In this system demonstrator, the bandwidth is a fixed parameter, limited by the ADCs used in the chosen digital board. As previously explained, these converters support 14 bit conversion at up to 100 MSPS. The achievable bandwidth, consequently, is 50 MHz. However, due to the presence of low-pass filters implemented in each of the 16 receive channels of the receiver board, illustrated in Fig. 6.17, as it can be seen from the receiver board's frequency response in Fig. 4.7, an attenuation of about 4-5 dB can be noticed, at about 30 MHz. Therefore, the maximum operational bandwidth is set to 30 MHz, instead of the 50 MHz, which have been previously though possible to be achieved.
Hence, the achievable range resolution of the OFDM MIMO radar system is $\Delta R = c_0/2B = 5m$, according to equation (2.14). The chosen system's frequency is $f_c = 15$ GHz, according to the airborne radar band and this is the value imposed in the DDS and

PLL unit, for the generation of the CW signal for the up-conversion and down-conversion from and to baseband, as shown in Fig. 7.1. Moreover, based on considerations regarding the speed of the objects which need to be identified and the Doppler resolution required, the remaining OFDM parameters can be calculated, according to what has been previously done in Chapter 6.

After the coding has been applied and the parameters have been set, the two waveforms, for each antenna, are processed according to an OFDM architecture, as the one previously shown in Fig. 6.1. Therefore, the transmit bit-streams go through various OFDM stages, which are, the subcarrier mapping, the IFFT processing with FFT size $N_{FFT} = 1024$, the cyclic prefix attachment and the vector modulation. The resulting signal is shown in Fig. 7.6. In this image, one of the Walsh-Hadamard orthogonally coded LFM waveforms is shown. In particular, the plots shown are a time-domain view of the chirp signal, a magnitude of the FFT view and a double and single sided power spectral density view, in the upper left, upper right, lower left and lower right parts of the figure, respectively. From the single sided power spectral density plot, it can be seen that the resulting bandwidth of the chosen radar's waveform is 30 MHz.

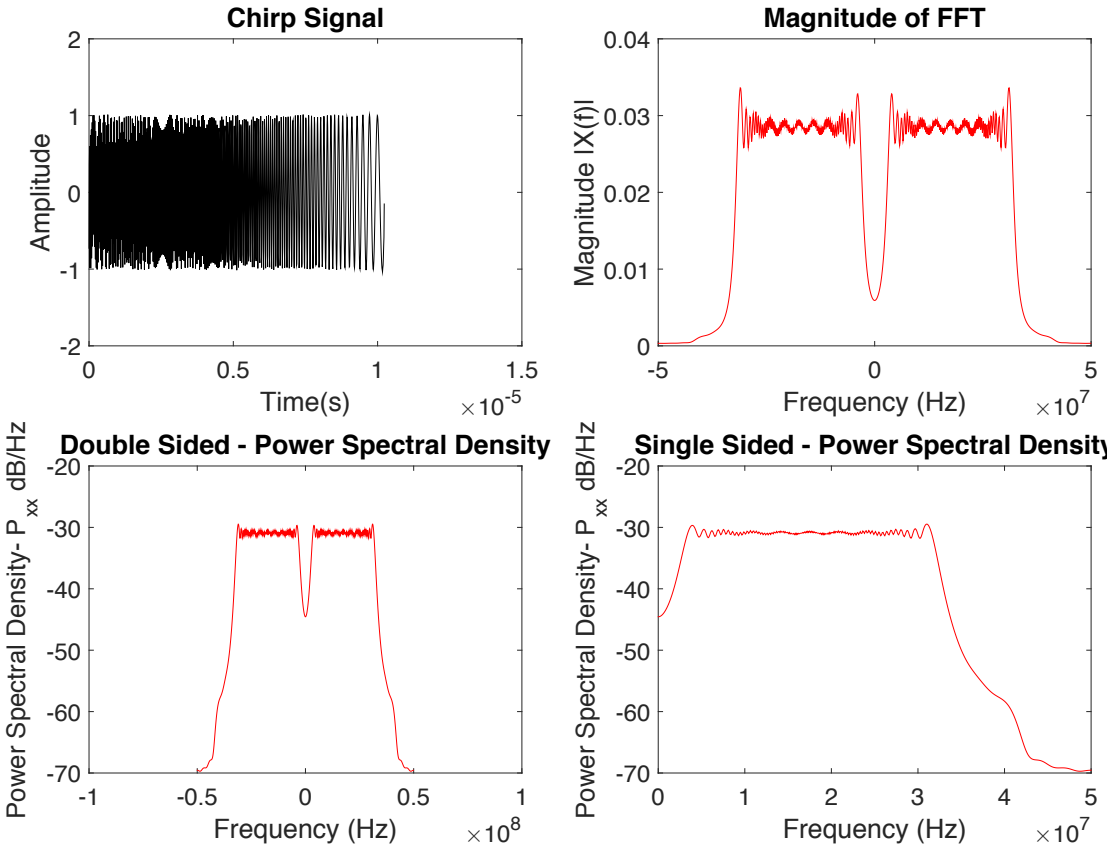

FIGURE 7.6: Walsh Hadamard coded LFM based OFDM radar waveform: chirp signal's time-domain view in the upper left, magnitude of the FFT view in the upper right, double and single sided power spectral density, in the lower left and lower right, respectively.

The two Walsh-Hadamard orthogonally coded LFM based OFDM radar waveforms,

which after the OFDM processing consist of $N_{FFT} \times M$ samples each, are then upsampled, in order to match the DAC's sampling clock, and parallelized into a set of eight vectors, in order to match the DAC's eight channel input interface. Considering that the DAC's chips operate at 2.5 GSPS, this means that a factor of interpolation of 25 needs to be used. Therefore, each of the resulting waveforms, before parallelization, consists of $N_{FFT} \times M \times 25 = 26214400$ samples.

The architecture involves saving the values and further process the waveforms in the Xilinx System Generator software, in order to link them to the internal Read Only Memory (ROM) inside the FPGA unit.

However, it can be noticed that it is not possible to directly do so, since 26214400 samples of 14 bit each, would result into a total memory consumption, per single waveform, of 43.75 MB or 87.5 MB for both, which is beyond the FPGA's internally available 2 MB memory, after implementation of the rest of the logic.

Nevertheless, it can be from equation 7.1, that by taking advantage of the coding scheme applied at a symbol level, the waveforms can be greatly simplified. For the waveform going to antenna TX1, considering the first row of matrix A in the equation, it means that the signal is multiplied by ones, and can be simply seen as a repetition of the first symbol, M times. Therefore, if the signal is to be stored into a memory, only the first symbol needs to be stored and then read out, $M = 512$ times. This means that only the first $N_{FFT} \times 1 \times 25 = 25600$ samples are stored, resulting into a memory consumption of 0.04 MB.

Considering now the second waveform, the one intended to be sent from antenna TX2, and looking at the second row of matrix A in equation 7.1, a periodic pattern, repetition of multiplications by ones and minus ones, can be noticed. Therefore, the signal can be simplified and only the first two symbols need to be considered and repeated. Therefore, if the signal is to be stored into a memory, only the first two symbols need to be stored and then read out, $\frac{M}{2} = 256$ times. This means that only $N_{FFT} \times 2 \times 25 = 51200$ samples are stored, resulting into a memory consumption of 0.08 MB.

In order to give a symmetrically ordered structure to the system, for both signals, the first two symbols are considered. Therefore, for each waveform, $N_{FFT} \times 2 \times 25 = 51200$ samples are considered and read out 256 times. Consequently, the total memory consumption, considering both waveforms, is of 0.16 MB.

The final step, is to format the waveforms according to the parallel structure of the DACs. Eight vectors are created, per waveform, in this manner: the first vector is created by selecting every 8-th sample, starting from sample 1 of the waveform, until the last sample; the second vector is created by selecting every 8-th sample, starting from sample 2 of the waveform, until the last sample; and so son until the 8-th vector, which is created by selecting every 8-th sample, starting from sample 8 of the waveform, until the last sample. The same is repeated for the second waveform.

Therefore, eight vectors of $\frac{51200}{8} = 6400$ samples are created, for each waveform. Each of these eigth vectors is going to be saved into a ROM block of the FPGA, through the use of a Xilinx System Generator based implementation.

7.3.4 Xilinx System Generator Model

A Xilinx System Generator model has been implemented, as shown in Fig. 7.7, which represents the block diagram for the generation of the samples, for one of the TX OFDM radar waveforms. The DACs' interfaces require eight parallel 14 bit data inputs, clocked at an 8-th of the operational sampling clock set for the DAC chips. Therefore, since the data must be provided in this format, the OFDM radar waveform needs to be formatted accordingly, as it has been previously described. As it can be seen in Fig. 7.7, there are nine data outputs, out of which the first eight, named *out*0 to *out*7, represent the connections to the DACs' interfaces. The same procedure is applied for the second antenna. An inside look, of the block named $Subsystem\_TX$, is shown in Fig. 7.8.

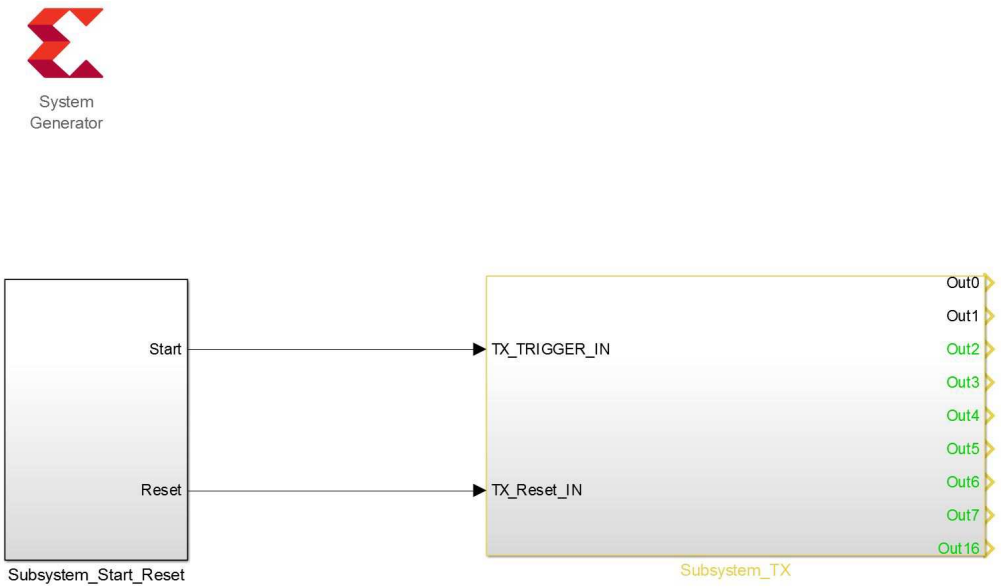

FIGURE 7.7: Top-level view of the implemented System Generator based architecture, for the generation of the OFDM radar waveform's values, to be stored and sent to the DACs.

Each of the LFM based OFDM transmit radar signals which have been created in MATLAB, has been divided into a stream of eight parallel vectors of 6400 samples each. Each of these vectors is stored in a look-up-table, which is continuously read out from a Xilinx System Generator ROM Block. There are a total of 8 block ROMs implemented. The block ROM uses dedicated, on-chip, hardware resources and represents the most area-efficient ROM implementation. The memory contents are specified through a block parameter. The block has one input port for the memory address and one output port for data out. It can be initialized to a $1 \times n$ vector that matches the depth of the ROM and the signal connected to the address port must be unsigned with no fractional bits. In this case, the ROM depth is set to $n = 6400$ and MATLAB is used to set the initial value vector, which corresponds one of the eight vectors, one per block ROM, as depicted in Fig. 7.8.

As it can be noticed on the upper left side of this image, an address generator logic has been implemented, in order to created the address values for the block ROMs. As previously explained, it has been possible to simplify each waveform by simply storing the

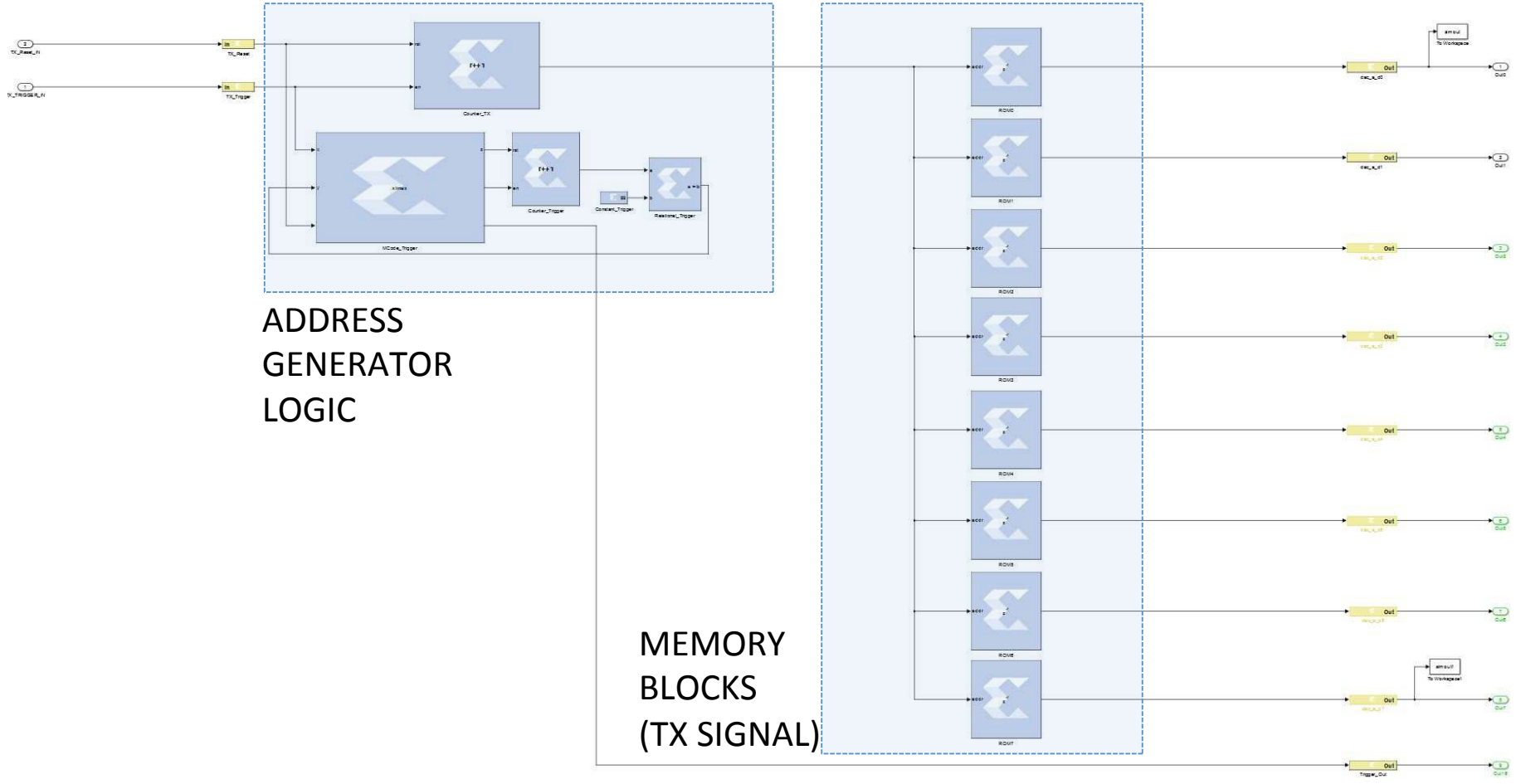

FIGURE 7.8: Inside view of the *Subsystem_TX* block of the implemented System Generator based architecture from Fig. 7.7. The ROM memories which store the values of the OFDM radar waveform are visible on the right side of the image.

first two symbols of each. This needs to be taken into account by the address generator logic, which needs to provided address values for the correct read out of the two stored symbols, for a total of $\frac{M}{2} = 256$ times.
Moreover, the signals running in the Xilinx System Generator model and the output ports of the block ROMs, as it can be recalled, need to be clocked at an 8-th of the operational sampling clock set for the DAC chips, of 2.5 GSPS. Therefore, the data is read out from each ROM with a clock of 312.5 MHz. The same model is created also for the second waveform. The eight data outputs of Fig. 7.7, named $out0$ to $out7$, correspond to the 14 bit outputs of the ROMs.
Finally, the integrated Xilinx Vivado software provides for an automatic generation of VHDL code directly from the System Generator blocks, so that the design can be compiled to an HDL netlist ready to be processed by a synthesis tool and automatically implemented with the Xilinx Vivado software. Therefore, the design visible in Fig. 7.7, is compiled for each of the two waveforms and the resulting modules are imported into the Xilinx Vivado software as custom IP cores.
The two imported blocks can be noticed in the lower right part of Fig. 7.5. The signals named dac_a_d0 to dac_a_7 and dac_b_d0 to dac_b_7, for the $tx1\_ofdm$ and $tx2\_ofdm$ blocks, for the TX1 and the TX2 antenna, respectively, are directly connected to the inputs of the DACs' parallel interfaces in the VHDL firmware. These are the 14 bit signal outputs, clocked at 312.5 MHz, which were named $out0$ to $out7$ in Fig. 7.7, which represent the memory saved waveforms.

After sampling and conversion of each waveforms from each of the two DAC chips, the analogue signals are sent through the RF transmit front-end, which converts the IF baseband signals from the digital unit into the selected RF radar band at 15 GHz and, finally, to the antenna array, shown in Fig. 7.2.

7.3.5 The Transmitted OFDM Radar Waveforms

In Fig. 7.9, the spectrum of the LFM based OFDM radar waveform sent from antenna TX1 is shown. The picture represents a screenshot taken directly from the spectrum analyzer, after connecting the end cable just before the signal is fed to one of the horn antennas. As it can be seen from this image, the transmit radar signal, has the typical shape of an OFDM signal, where a large number of finely spaced orthogonal sub-carrier signals are spread on several parallel frequencies. The total occupied bandwidth is, as per specifications, of 30 MHz, spanning between 5 MHz and 35 MHz. In the middle of the image, the carrier's frequency of 15 GHz can be seen, as well as an unoccupied bandwidth between -5 MHz and 5 MHz, which has been implemented in order not to propagate the DC components. Additionally, in this image, the effects of a low-pass filter, integrated just before the up-mixing of the signal, can be seen. The filter matches the characteristics of the one integrated in the receive channels of the receiver's board, illustrated in Fig. 6.17.

In Fig. 7.10, a zoom in of the spectrum from Fig. 7.9 is shown. In this image, it is possible to clearly identify a subset of the N_{FFT} components which have been mapped to the different frequencies, with a spacing of 100 KHz.

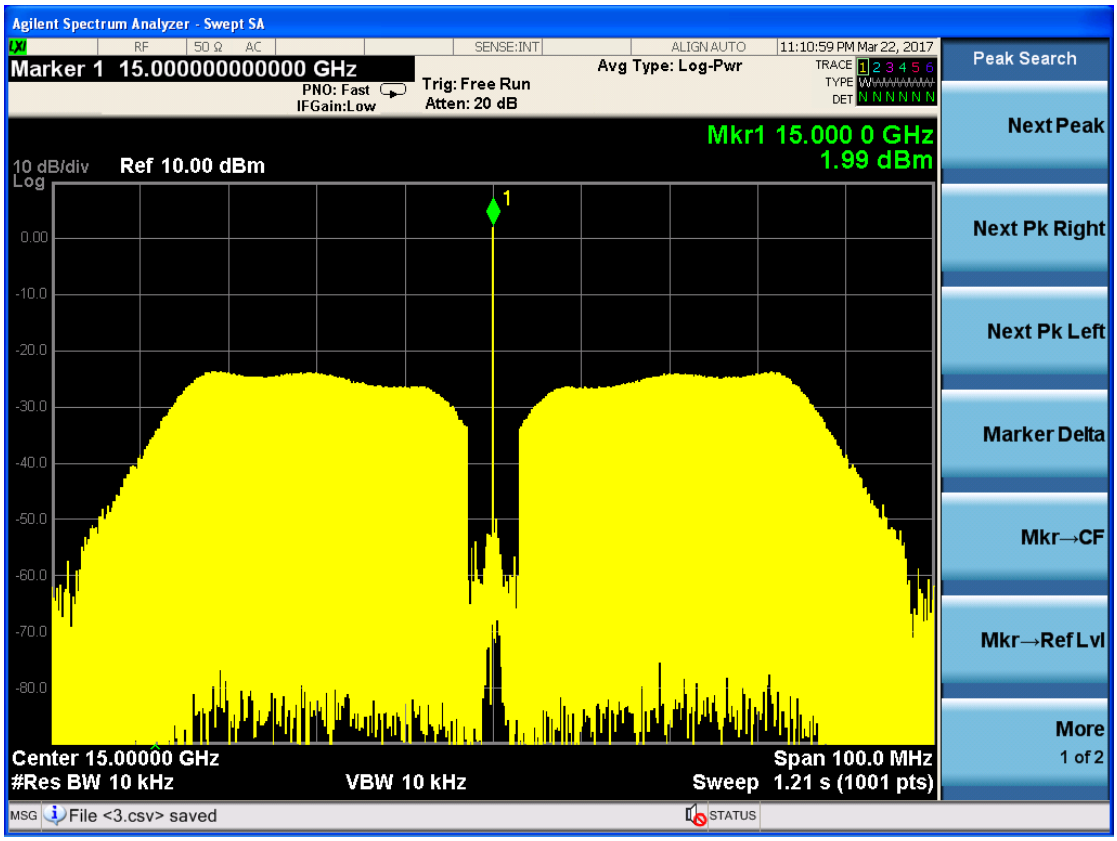

FIGURE 7.9: Spectrum of the LFM based OFDM radar waveform sent from antenna TX1, captured with a spectrum analyzer.

After transmission, the signals are reflected off from scattering objects in environment and the received signals are processed in a dual way. The RF radar band OFDM signals are received from the RX patch antennas, down-converted to IF through the 16 channel receiver board, captured by the ADCs, processed by the FPGA unit and saved into the external DDR memory, as previously explained in subchapter 7.3.1.

7.3.6 The ARM Processing

The software architecture which has been implemented in the ARM processed, is similar to the one which has been previously described in Chapter 4. The data is managed inside the ARM core, through the use of kernel drivers and user applications, which are written in *C* code, for the Linux based operating system, provided by Xilinx directly through the PetaLinux SDK. As it can be seen from Fig. 7.3, the ARM system is responsible for two main functionalities, which are the reading of the data from the DDR memory and the transferring of the OFDM radar data, through UDP, to the PC or laptop, for further radar and image processing.
Through a mapping of the DMA device memory directly into the user process's address space and various DMA I/O operations, the data inside the DDR memory can be accessed from the Linux operating system.
Consequently, from another kernel based driver which acts as a UDP client, the DDR

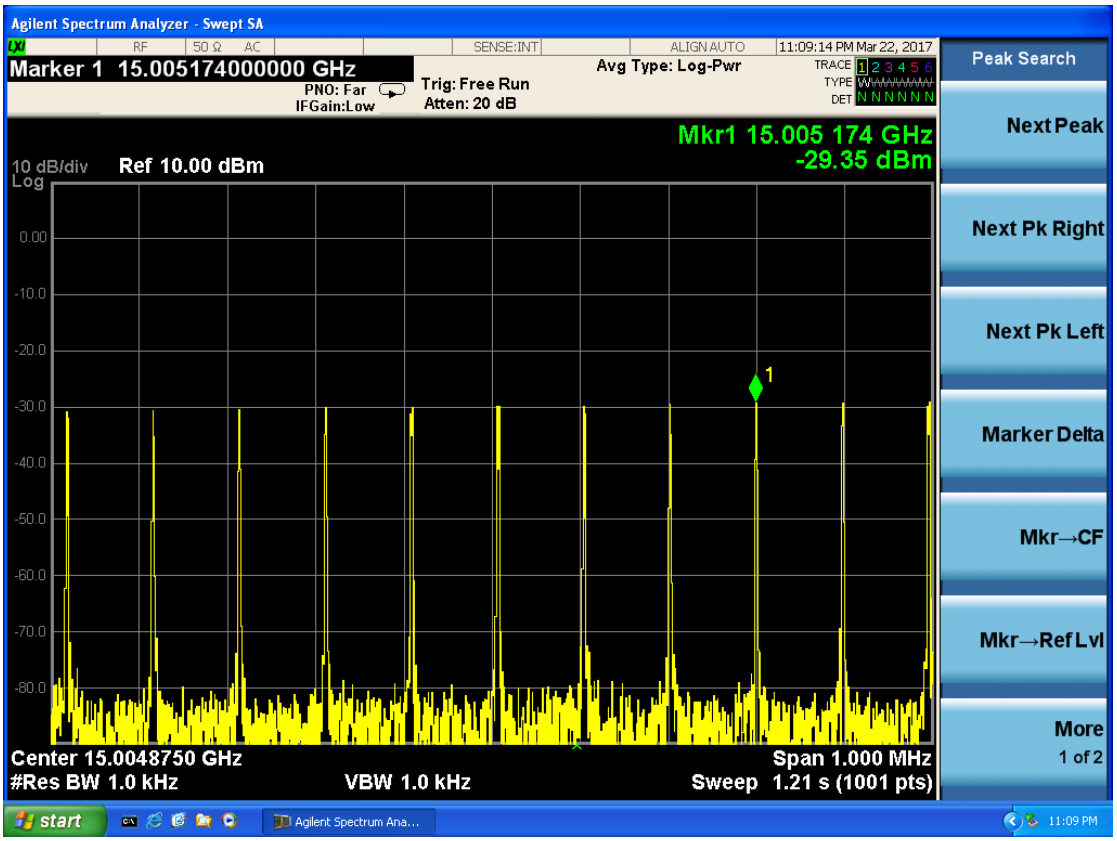

FIGURE 7.10: Zoom in of the spectrum of the LFM based OFDM radar waveform sent from antenna TX1, shown in Fig. 7.9

accessed data is read and encapsulated into UDP packets and sent to a UDP server running on the PC, connected through Ethernet connection
Differently from the process shown in Chapter 4, the procedures are not repeated for each and every antenna, as this architecture is not based on a TDM structure. However, the whole procedure is repeated in the case that multiple measurements have been requested. In this case, the content of the DDR memory is transferred to the PC, an acknowledgment packet is received, the content is cleared, the FPGA and ARM routines are re-launched and a new transfer is initialized.

7.3.7 The Software Processing

The PC or laptop, has a MATLAB based OFDM radar processing program running at all times, which includes both the HMI radar control system and the UDP server. The UDP server, implemented through the use of MEX files, has the ability to send commands, through UDP packets, to the digital board and also to receive the OFDM radar data which is sent from the UDP client running on the ARM unit.
The commands are given from the HMI radar control system, which can be the start or stop of the radar capture, and how may measurements to take.
After the data has been completely received, an acknowledgment UDP packet is sent to

the ARM unit, which redirects the signal to the FPGA. Everything is reset, all register values and memories, including the DDR memory, are cleared. In the case that multiple measurements have been selected, a new radar capture is initialized and a new transfer is done towards the PC, process which is repeated until all measurements have been correctly transferred.
Once the UDP server acquires the OFDM radar data, it saves it into a 3D radar data matrix, which has dimensions $N_{RX} \times N_{Samples}$, which corresponds to the number of RX antennas and the number of samples for each signal. This is repeated a number $N_{Measures}$ of times, corresponding to the number of measurements taken. It is easy to understand that, as per architecture implementation, the number of samples $N_{Samples}$ corresponds to the two symbols which have been transmitted consecutively. Therefore, it is possible to assume $N_{Samples} = 2 * N_{FFT}$, where N_{FFT} represents the number of mapped frequencies, along the available bandwidth. Moreover, the number of measurements to be taken, corresponds in this case to $N_{Measures} = \frac{M}{2}$, since each transmitted waveforms incorporates already two symbols.
However, due to the size of the FFT buffers implemented, described in Chapter 7.3.1, a maximum limit of 10000 samples can be processed in the current implemented architecture of this OFDM MIMO radar demonstrator. Considering that each received symbol has a length of $N_{FFT} = 1024$ samples, this means that even though the number of symbols has been previously envisioned to be $M = 512$, in reality only 9 of the symbols are processed at a time. From now on, the term M will be denoting the number of received and processed symbols M_r, instead of the transmitted ones, which means that it will be assumed that $M = M_r = 9$.
For simplicity, the whole data can be seen as a matrix with dimensions $N_{RX} \times L_{FRAME}$, where $L_{FRAME} = N_{FFT} \times M_r$, which mean that $L_{FRAME} = 1024 \times 9 = 9216$.
It is important to notice that after the demodulation operations at the OFDM receiver processing, the size of L_{FRAME} is going to be reshaped according to N, the number of subcarriers originally mapped in the OFDM transmit processing.
The OFDM radar data matrix is then passed to the MATLAB based radar processing routines, which apply various OFDM signal processing and digital beam-forming procedures, in order to generate radar images of the captured scenario and targets.

7.4 The Radar Processing

A total of 16 signals are read from the UDP server, or optionally loaded from a previous file measurement, into a MATLAB matrix of 16×9216 elements, corresponding to the number of receive antennas and the size of the FFT used for the OFDM transmit generation multiplied by the total number of symbols processed, respectively.
Similarly to the OFDM transmit path, the 16 received signals go through various OFDM stages implemented in the MATLAB model, which are, the vector de-modulation, the cyclic prefix removal, the FFT processing and the sub-carrier de-mapping, as previously shown in Fig. 6.1. The resulting data, after the FFT demodulation, reshapes according to the 450 subcarriers which have been originally mapped in the transmit OFDM processing. Therefore, the resulting data becomes a matrix which has a dimension of

16×4050, where 4050 represents the number of subcarriers, multiplied by the number of symbols.
Consequently, the OFDM radar data is processed according to the receiver's processing architecture introduced in Chapter 6.5, and the radar processing algorithms based on the 4D-FFT beamforming approach, explained in 6.5.2 and shown in Fig. 6.18.
It is important to remember that at this point, the received signals have only $M_r = 9$ of the originally sent 512 symbols, therefore this needs to be taken into account. The transmit waveform, consisting of N_{TX} frames of length $L_{FRAME} = N \times M$, is preloaded, before the radar's receiver processing starts, and only the first 9 symbols are considered, therefore $M = M_r = 9$. As previously described in Fig. 6.1, the radar processing takes place after the signals from all receivers have gone trough the OFDM basic receiver processing, which can be seen as N_{RX} frames of length $L_{FRAME} = N_{FFT} \times M$, with $M = M_r = 9$, here as well. This matrix of data represents the input to the block, together with the N_{TX} frames, which represent the preloaded transmit waveforms from the waveform generator block in the same figure.
Through the frame-based complex multiplication in frequency domain, between the received complex signals and the already loaded conjugate of the original transmit signals, as described in Chapter 6.5.1, the N_{TX} transmit waveforms from the different transmit antennas can be separated at each of the N_{RX} receivers. This, is due to the the output of this demodulation operation, which is proportional to the channel/targets' response. After extraction of the transmit components from each receiver, a set of $N_{TX} \times N_{RX}$ signals of length L_{FRAME} is reconstructed. The output of this operation, is then fed to a 4D channel function shaping block, which reshapes the data into a 4D matrix which has dimensions (N_{TX}, N_{RX}, N, $M = M_r$), which in this case is (2, 16, 450, 9).

The second important step of the receiver processing is the 4D-FFT algorithm, which has been introduced in Chapter 6.5.2. As it can be recalled, the first step of the processing is the virtual array alignment block. Similarly to the example proposed in the previous chapter, also in the OFDM MIMO radar here proposed, the antenna array is composed of 2 transmit and 16 receive elements.
However, due to the position of the antenna elements, the virtual array results into two single horizontal lines of 16 elements, and not the virtual array which has been shown in the previous chapter.
The chosen array is shown in Fig. 7.11, where both the TX and RX antennas' position is illustrated, in red and blue, respectively. In Fig. 7.12, instead, the virtual array is illustrated.
Thus, the total number of virtual elements is N_{TX} x $N_{RX} = 2 \times 16$. The size of the 4D data matrix scales according to the virtual array size, where the horizontal axis can be denoted as Azimuth and the vertical axis can be denoted as elevation, thus yielding a 4D radar signal matrix with size $N_{ELE} \times N_{AZI} \times N \times M$, where N_{ELE} and N_{AZI} are the number of virtual elements in the vertical/elevation and horizontal/azimuth axis.
Consequently, as previously shown in Fig 6.18, the next steps are the interpolation of the missing elements, the windowing and padding of the radar signals and the 4D-FFT beam-forming operation. Hence, after the 4D-FFT operation, a complete sensing of range, Azimuth, elevation and speed of the targets is achieved in this manner, which represent the 4 dimensions of the resulting 4D data matrix.

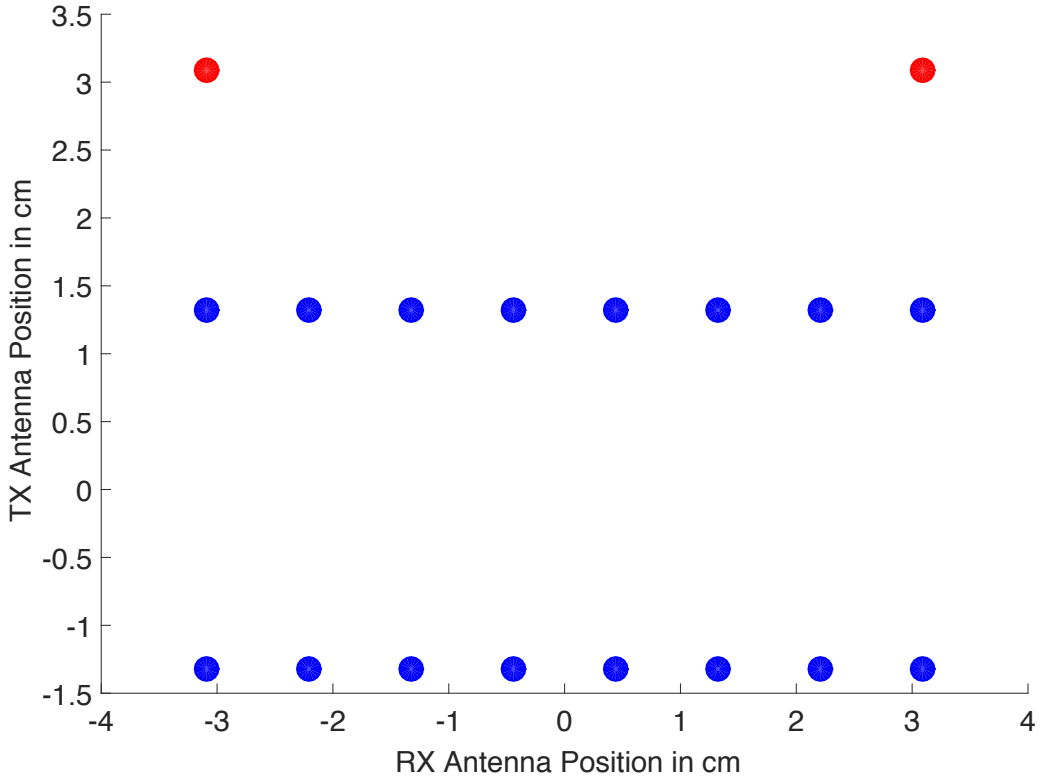

FIGURE 7.11: 2x16 antenna array. The RX array configuration is shown in blue, while the TX array in red.

Finally, the last two steps of the algorithm are the shifting and scaling of the resulting data matrix, after the 4D-FFT processing, and the targets' identification.

7.5 System Results

In order to verify the system, measurements have been conducted. A corner reflector with a nominal radar cross section of 36 m^2 has been centrally placed at 25 meters from the radar, as illustrated in Fig. 7.13. As it can be seen in the image, the scene represents a near ideal environment with a flat terrain, limited by a wire fence at 50 meters. The system is then activated and a radar capture is started. The radar signals captured are sent to the radar processing unit running on a laptop, which through the 4D-FFT based beam-forming, generates the 3D radar images. In Fig. 7.14, a generated radar image can be seen, which represents a cut of the 3D radar image and represents a Azimuth-range view of the captured scene. In the figure, targets are identified by bright colours and brighter colours represent stronger reflections. The corner reflector can be uniquely identified at 25 meters. Additionally, reflections from the fence can be seen at 50 meters.
Finally, in order to show the full 3D capabilities of the OFDM MIMO radar demonstrator here presented, in Fig. 7.15 a cut of the 3D radar image at the range cell where the target is, at 25 meters, is shown in the form of an Azimuth-elevation view of the captured

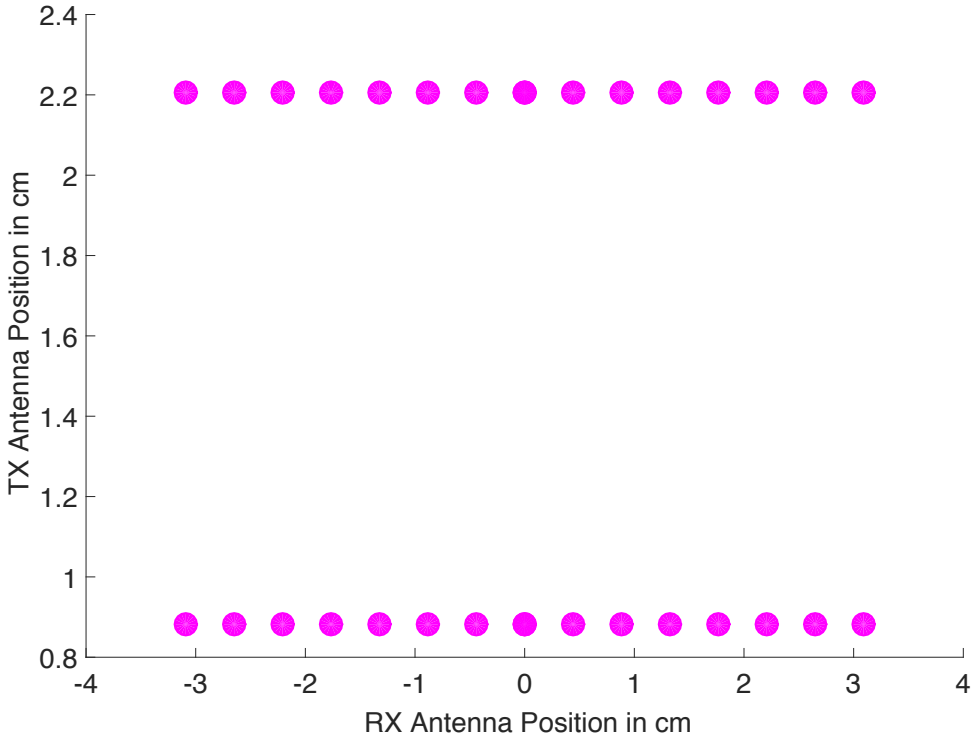

FIGURE 7.12: Virtual antenna array. It is the results of the convolution between the TX and RX arrays.

scene. In this image as well, the target can be seen and identified at a central Azimuth angle and at an elevation angle which is slightly lower than the bore-sight of the radar, at around -2 degrees, as expected from the scene captured in Fig. 7.13. Additionally, the side-lobes can also be seen in this image.

7.6 Chapter's Conclusions

A 3D imaging OFDM MIMO radar system demonstrator has been implemented, as a first step towards a real-time low-cost multichannel OFDM radar system which is both compact and cost efficient. Moreover, one of the novel OFDM radar waveform techniques, introduced in Chapter 6, which relies on the transmission of periodically repeated complex LFM chirps with a Walsh-Hadamard orthogonality coding approach applied at symbol level, has been integrated into a MIMO OFDM radar demonstrator and tested [211]. Results, shown through radar captures, of test targets obtained through the 4D FFT beamforming of the received radar signals, allowed to verify the performance of the system demonstrator, but also to verify the good capabilities of the radar's OFDM receiver processing and beam-forming algorithms proposed in Chapter 6. Since the waveforms can be easily saved into the internal FPGA memory, it means that multiple waveforms can be used, as an approach towards a radar which could in real-time adapt its transmit waveform, according to the different scenarios of operation.

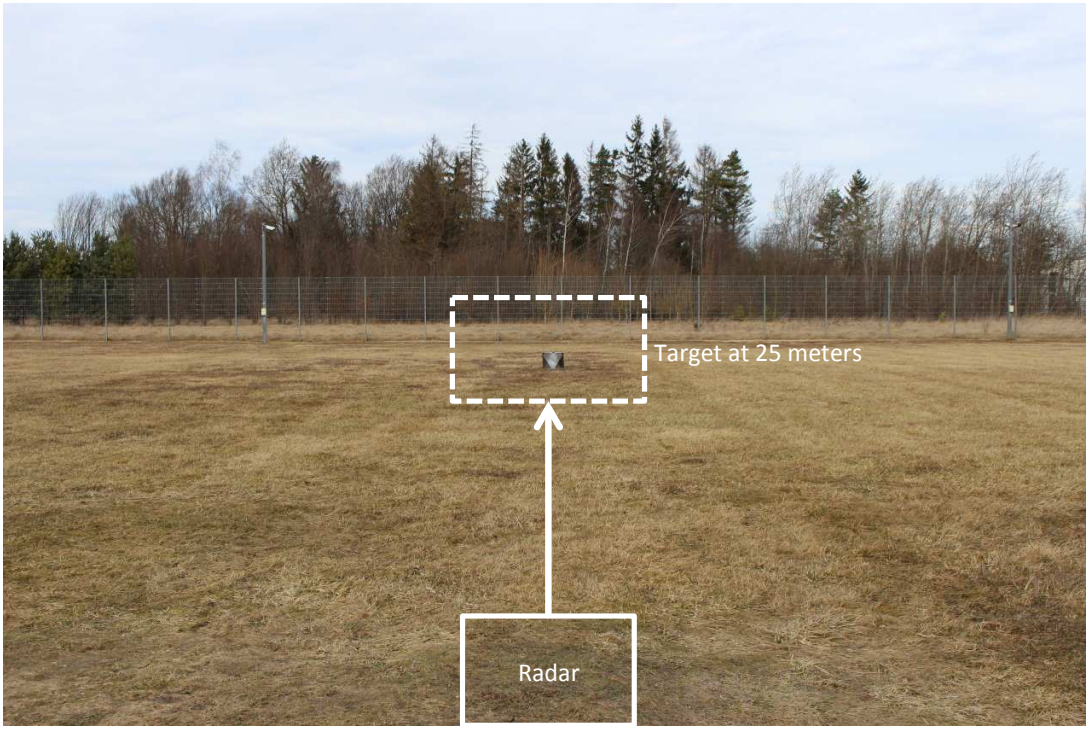

FIGURE 7.13: Scenario captured by the radar, with a corner cube centrally positioned at 25 m and wire fence at 50 m.

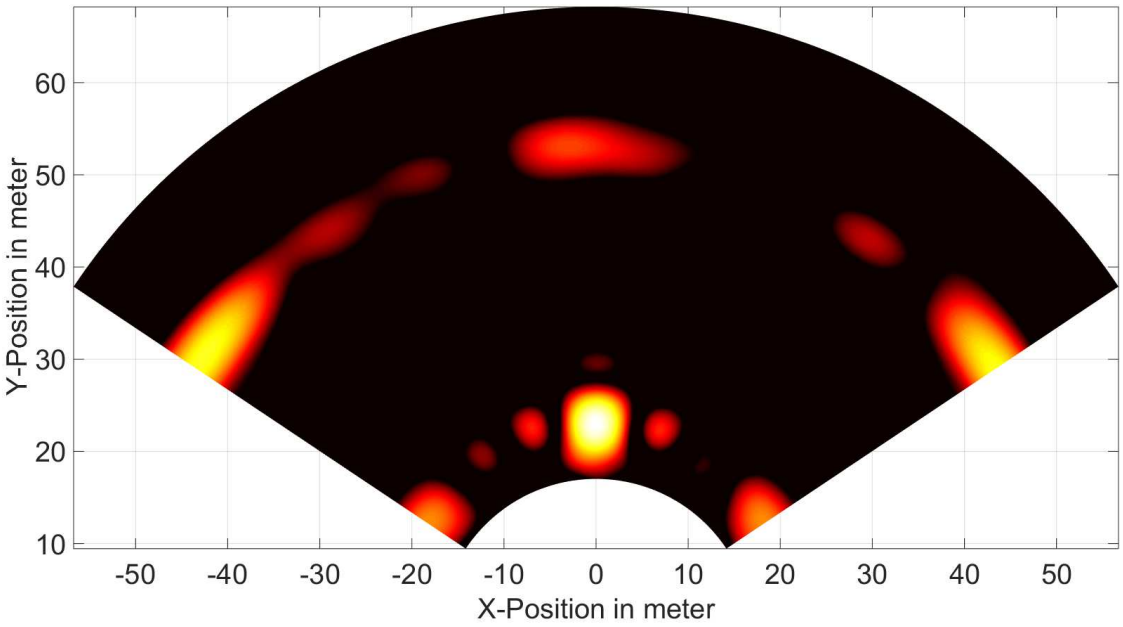

FIGURE 7.14: Azimuth-range view of the scene shown in Fig. 7.13.

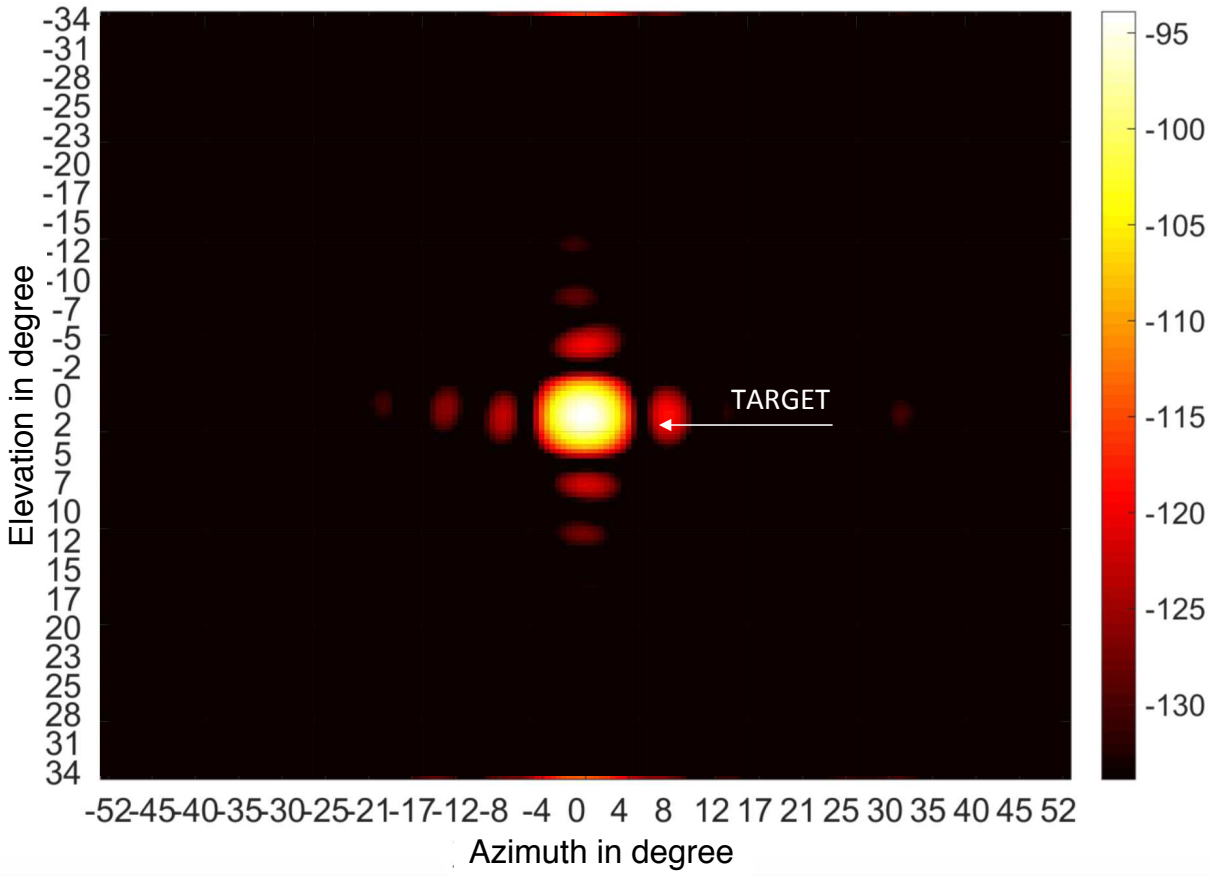

FIGURE 7.15: Azimuth-elevation view of the scene shown in Fig. 7.13.

Chapter 8

Conclusions

8.1 Final Remarks

In this thesis, a comprehensive research, implementation and analysis of innovative architectures, algorithms and complete demonstrator systems, based on MIMO imaging radar technology and both FMCW and OFDM waveforms, has been discussed. A key topic of the work has been the achievement of compact MIMO radar systems, capable of performing a fast 3D beam-forming and radar image processing, for a complete sensing of range, Azimuth, elevation, and, in the case of the real-time capable OFDM based radar system, also the speed of the targets. The system's architectures and parameters have been shaped in order to address several civil and military applications, such as the surveillance and detection of targets, both air and ground based, in wide-zones and environments with critical infrastructures, and for the situational awareness, anti-collision and imaging technologies, both in cars and in flying platforms, such as helicopters, UAVs and air-taxis. These applications are in accordance to the ones required by both the European project "ZONeSEC" and the German project "FAST", for which part of the research has been focused to.

All of the MIMO radar system demonstrators here presented, have been thoroughly described from an in-depth analysis at a sub-system level. As a matter of fact, pictures and measurements have been presented for many of the sub-systems components which compose the final demonstrators.
Furthermore, all of the radar system's hardware and digital architectures have been thoroughly tested, in simulation environments or on the field measurements, with the results shown in the form of radar images in 2D or 3D views, which allow to clearly identify the static or moving targets present in the captured scenes. A complete set of Azimuth-range, range-elevation, Azimuth-elevation and Doppler-range 2D radar images have been presented. Additionally, 3D radar images, radar images superimposed to camera images and, finally, 4D images with a 3D data view and speed added as a label, have been shown. This yields a complete evaluation of the performance and resolution parameters.
Essentially, the work and achievements can be primarily divided into four main parts.

The first achievement, which results have been published in a journal in [120], has been the implementation of a complete 3D MIMO imaging radar demonstrator which operates with a 24x24 MIMO 2D antenna array configuration and a TDM scheme. The radar sensor working frequency range spans between 16 GHz and 17 GHz, transmitting and processing FMCW signals with an operational bandwidth of 1 GHz. A complete system integration of the RF front-end, the digital system and the software architecture for digital signal processing has been accomplished. Moreover, the radar system is intended to be flexible as much in its hardware as it is in its software, and a modular approach based on conventional low cost PCBs is used for the transmit and receive boards, which allows to flexibly add or remove boards.
For the hardware realization of the digital signal processing part, three FPGA based cards have been used, each equipped with an 8 channel ADC board. The hardware is matched with a custom built VHDL coded firmware for the radar processing. Additionally an FFT and delay and sum based beam-forming technique is performed on the raw data acquired via Ethernet, in order to generate complete 3D images of the radar captured scenario.
A careful evaluation of the radar's resolutions and separation capabilities along the Azimuth angles, elevation angles and range, has been carried out. Several radar measurements have been carried out with static targets in the form of corner reflectors, in both an anechoic chamber and in outdoor radar test fields.
Additionally, test scenarios for the evaluation of the radar's maximum range and analysis of the imaging performance of the radar in the presence of multiple targets are presented.
The first 3D MIMO radar system presented, has been found to be well suited in targeting applications, such as, the ground based surveillance of stationary wide-zones and high security or hazardous infrastructures. The portability and compact size factor aid in this, allowing the radar to be easily and flexibly moved.
However, the system, as per built-architecture, allows for the estimation of static targets only.
Therefore, a study and comprehensive research on the hardware and digital architectures of this demonstrator, allowed to find stages where improvements could be made, in order to address applications which require an even more compact and faster device, such as those linked to the detection of targets in flying platforms.

The second achievement, which dedicated journal is awaiting for publication in May 2018 [140] and two conference papers have been presented [152],[164], has been the implementation and testing of a second 3D FMCW MIMO radar demonstrator, which represents the engineering of the improvement related ideas coming from extensive research on the first demonstrator. This improved radar system has been developed with a much smaller RF front-end, which integrates 16 TX and 16 RX antennas with a smarter antenna array configuration, together with all the circuitry needed, from the amplifiers to the filters and mixers, all combined into a single planar PCB. Furthermore, the digital hardware architecture used, has been changed to a single proprietary ZYNQ Z-7020 SoC based board, which combines an ARM Cortex-A9 dual-core processor with an FPGA and, additionally, 16 ADCs. Moreover, a metallic 3D printed housing, which accomplishes also

the task of cooling the electronics, has been built and assembled to house all the components. Thus, a more compact and portable system is achieved, compared to the first radar described. A complete description of the hardware and software radar processing architectures, implemented in a cross domain between FPGA, ARM and PC, has been provided.
Similarly to the first radar system presented, the orthogonality of the TX signals is obtained through a TDM scheme and FMCW signals which space from 16 GHz to 17 GHz, with an operational bandwidth of 1 GHz, are used.
However, compared to the previous radar, a 3D-FFT beam-forming based radar processing is implemented, which allows for a much faster estimation of the targets' range, Azimuth and elevation parameters, which is here accomplished in 3 s instead of the 11 s of the first demonstrator. This yielded the possibility to capture radar images with a faster refresh rate, thus opening up the MIMO radar demonstrator to a multitude of additional radar applications, such as the case of moving targets environments. This is also due to new algorithms for the averaging on consecutive measurements and for the tracking of targets, which have been introduced.
Finally, the system is integrated with additional sensors and actuators, introducing multiple functions, which are integrated in a single system. With regard to this aspect, the MIMO radar system is tested in combination of a camera and a gimbal for target tracking.
This compact version of a 3D FMCW MIMO radar demonstrator is tested and analysed in several scenarios. In an anechoic chamber and in outdoor test fields, for the detection of targets, both static and moving, represented by corner reflectors, UAVs and people. Additionally, to show the advantages of the second functionality, the MIMO radar system, combined with a camera and a gimbal for target tracking, is tested in multiple scenarios. First, the imaging capabilities of the radar, integrated with the camera imaging capabilities, are tested in a scenario without corner reflectors. Second, the target tracking capabilities of the system are analyzed, and the detection is performed in the presence of UAVs and people. Finally, a scenario where a jamming system is used against small UAVs, is also shown.

The third achievement, which dedicated journal is awaiting for acceptance [186] and a conference paper has been presented [56], has been the research and implementation of nearly orthogonal OFDM MIMO radar waveforms, processing algorithms and systems, based on a new architecture, which is the OFDM structure, applied to radars
The design and processing of several orthogonal waveforms based on LFM signals for MIMO OFDM radars has been described, together with the results of a complete system, capable of detection and imaging of radar targets. The orthogonal waveforms are designed by coding consecutive complex LFM signals in a frame so that they can be sent to the different transmit channels of the radar, allowing the simultaneous operation of all transmit channels. This is achieved by applying several coding techniques, at a symbol level: Golay complementary, Frank Zadoff Chu, Walsh-Hadamard, Space-Time, Discrete Fourier Transform (DFT) and Costas based sequences. Moreover, a novel radar receiver processing based on a complex frame based multiplication in frequency domain between transmit and received waveforms has been presented, together with a unique 4D-FFT based beam-forming algorithm.

The introduction of this beam-forming technique allowed for a fast and complete estimation of the targets' range, Azimuth, elevation and Doppler in a frame. The performance's analysis of the proposed waveforms has been evaluated by their cross ambiguity functions and, also to test the general performance of the system and its receiver processing, multiple radar images in the form of 2D and 3D plots are shown.
Through the analysis which has been carried out, it has possible to discern that all of the proposed waveforms have been proven to be appropriate radar signals, with some having better performance than others, especially for the case of Costas and Walsh-Hadamard based LFM waveforms.
Due to its simplicity and easy on the fly configuration, the proposed system is attractive for an adaptive OFDM MIMO radar, which is capable of adaptively changing its waveform, based on the radar channel which is used in, therefore paving the way for adaptive real-time and low cost device. This is of crucial importance for applications linked to the situation awareness in miniaturized flying platforms, air taxis and both air and ground based radar systems. The novel orthogonal waveforms have been patented in [208],[209],[210] and receiver architecture, together with the 4D-FFT beam-forming, has been patented in [211].

The final achievement, which dedicated conference paper has been published [212], has been the implementation of the previously introduced concepts and architectures for OFDM radars, into a 3D imaging OFDM MIMO system demonstrator. The demonstrator shares the hardware of the compact and improved 3D FMCW MIMO radar system, which had the single board based RF front-end, receiver board and ZYNQ based digital architecture. However, new COTS components have been used for the TX front-end, which include power dividers, couplers, mixers, amplifiers, filters and horn antennas. Furthermore, the digital processing is completely changed and adapted to be operating with an OFDM radar's architecture, including the introduced novel radar's receiver processing and the 4D-FFT based beam-forming. One of the novel LFM based OFDM waveforms introduced, where the orthogonality between transmit elements is achieved by means of a Walsh-Hadamard based coding scheme, has been integrated into the digital architecture, allowing for the generation of a completely digitally generated waveform, simply read out from an internal memory in the ZYNQ board. The radar system is verified through measurements and the results are presented, through radar image captures achieved outdoors. Therefore, due to the successful implementation of this novel OFDM architecture, the developed system paves the way for low cost, miniaturized and real-time capable, adaptive OFDM MIMO 3D radar systems.

8.2 Future Perspectives

The research carried out in this thesis has unlocked new architectures and algorithms for the processing of radar signals in classic FMCW or new OFDM based systems. Thanks to the many radar image captures provided, from different targets in different scenarios, a thorough analysis of these MIMO radar systems is possible.
In the case of the FMCW demonstrators, it can be understood that a high level of

performance has been achieved in the digital architecture, especially due to the implementation of FFT based beam-forming algorithms. A step further would be to include part of the radar software processing, directly into the FPGA or ARM units, sharing the computational requirements of the MATLAB based model and allowing for a faster capturing of the radar scenarios. However, the biggest improvements which can be achieved, are mainly to be found in the even further miniaturization of the RF front-end, intrinsically connected to a reduction of the overall system's costs. This would allow for a faster adoption into the automotive and aerospace industries, where radars are becoming essential sensors for performing 360 degree evaluations of the surroundings of cars or flying platforms, and therefore, are needed in high quantities.
Finally, the results from this thesis can be used to further improve existing systems or, as anticipated, even set the basis for low cost, miniaturized and real-time capable, adaptive radar systems. This kind of systems would represent an ideal device for autonomous cars of flying platforms. It would be possible to scan an area in real-time and based on the channel characteristics, change the waveforms which are being used, in order to always adopt the ones which are more performant. Furthermore, due to the nature of the OFDM architecture, an OFDM based MIMO radar can also be integrated with communication capabilities. In this case the device could perform sensing of range, Azimuth, elevation and speed of targets and, at the same time, create a data link for communication with these targets, be it cars, UAVs or aircrafts. A data link which could be adapted based on the channel and targets' parameters, sort of an adaptive OFDM communication system with integrated radar and channel sounding capabilities. In this context, systems equipped with these radar and communication sensor could autonomously drive or fly, in complex scenarios, and in real-time exchange or broadcast radar estimations or pure data, such as video streams.

Bibliography

[1] MathWorks Automotive adaptive cruise control using FMCW technology. URL https://de.mathworks.com/help/phased/examples/automotive-adaptive-cruise-control-using-fmcw-technology.html.

[2] M. A. Richards. *Fundamentals of radar signal processing*. Tata McGraw-Hill Education, 2005.

[3] C. Hülsmeyer. Verfahren, um entfernte metallische gegenstände mittels elektrischer wellen einem beobachter zu melden. *German Patent*, 165, 1904.

[4] W. Wiesbeck et. al. Radar 2020: The future of radar systems. In *Geoscience and Remote Sensing Symposium (IGARSS), 2015 IEEE International*, pages 188–191. IEEE, 2015.

[5] C. T. Capraro et al. Knowledge-based radar signal and data processing: a tutorial review. *IEEE Signal Processing Magazine*, 23(1):18–29, 2006.

[6] C. Alabaster. *Pulse Doppler Radar*. The Institution of Engineering and Technology, 2012.

[7] R. J. Mailloux. *Phased array antenna handbook*, volume 2. Artech House Boston, 2005.

[8] J. C. Curlander and R. N. McDonough. *Synthetic aperture radar*. John Wiley & Sons New York, NY, USA, 1991.

[9] M. Schneider. Automotive radar-status and trends. In *German microwave conference*, pages 144–147, 2005.

[10] A. Farina and F. A. Studer. Radar data processing. volume 2-advanced topics and applications. *NASA STI/Recon Technical Report A*, 86, 1986.

[11] X. Jianjuan H. You and G. Xin. *Radar data processing with applications*. John Wiley & Sons, 2016.

[12] J. M. Loomis. Army radar requirements for the 21st century. In *2007 IEEE Radar Conference*, pages 1–6, April 2007. doi: 10.1109/RADAR.2007.374182.

[13] C. Rusch, S. Beer, T. Zwick, and T. Klein. 77 ghz cw-radar concept with passive components in ltcc. In *2012 42nd European Microwave Conference*, pages 281–284, Oct 2012. doi: 10.23919/EuMC.2012.6459291.

[14] D. Maskell G. Woods and M. Mahoney. A high accuracy microwave ranging system for industrial applications. *IEEE Transactions on Instrumentation and Measurement*, 42(4):812–816, 1993.

[15] S. Kingsley and S. Quegan. *Understanding radar systems*, volume 2. SciTech Publishing, 1999.

[16] H. Meikle. *Modern radar systems*. Artech House, 2008.

[17] L. Bowden. The story of iff (identification friend or foe). *IEE Proceedings A (Physical Science, Measurement and Instrumentation, Management and Education, Reviews)*, 132(6):435–437, 1985.

[18] N. J. Willis. *Bistatic radar*, volume 2. SciTech Publishing, 2005.

[19] G. T. Ruck. *Radar cross section handbook*, volume 2. Plenum Publishing Corporation, 1970.

[20] M. E. Russell. Future of rf technology and radars. In *Radar Conference, 2007 IEEE*, pages 11–16. IEEE, 2007.

[21] Jung-Chih Chiao, Yiton Fu, Iao Mak Chio, Michael DeLisio, and Lih-Yuan Lin. Mems reconfigurable vee antenna. In *Microwave Symposium Digest, 1999 IEEE MTT-S International*, volume 4, pages 1515–1518. IEEE, 1999.

[22] G. M. Rebeiz. *RF MEMS: theory, design, and technology*. John Wiley & Sons, 2004.

[23] C. A. Wiley. Synthetic aperture radars. *IEEE Transactions on Aerospace and Electronic Systems*, (3):440–443, 1985.

[24] C. Pell. Phased-array radars. *IEE Review*, 34(9):363–367, 1988.

[25] H. Hommel and H. Feldle. Current status of airborne active phased array (aesa) radar systems and future trends. In *Radar Conference, 2004. EURAD. First European*, pages 121–124. IEEE, 2004.

[26] A. G. Seabridge I. Moir and M. Jukes. *Military avionics systems*. John Wiley & Sons, 2006.

[27] E. Fishler et al. Mimo radar: An idea whose time has come. In *Radar Conference, 2004. Proceedings of the IEEE*, pages 71–78. IEEE, 2004.

[28] R. S. Blum A. M. Haimovich and L. J. Cimini. Mimo radar with widely separated antennas. *IEEE Signal Processing Magazine*, 25(1):116–129, 2008.

[29] DW Bliss and KW Forsythe. Multiple-input multiple-output (mimo) radar and imaging: degrees of freedom and resolution. In *Signals, Systems and Computers, 2004. Conference Record of the Thirty-Seventh Asilomar Conference on*, volume 1, pages 54–59. IEEE, 2003.

[30] F. C. Robey et al. Mimo radar theory and experimental results. In *Signals, Systems and Computers, 2004. Conference Record of the Thirty-Eighth Asilomar Conference on*, volume 1, pages 300–304. IEEE, 2004.

[31] E. Fishler et al. Performance of mimo radar systems: Advantages of angular diversity. In *Signals, Systems and Computers, 2004. Conference Record of the Thirty-Eighth Asilomar Conference on*, volume 1, pages 305–309. IEEE, 2004.

[32] A. Hassanien and S. A. Vorobyov. Phased-mimo radar: A tradeoff between phased-array and mimo radars. *IEEE Transactions on Signal Processing*, 58(6):3137–3151, 2010.

[33] P. Stoica J. Li and X. Zheng. Signal synthesis and receiver design for mimo radar imaging. *IEEE Transactions on Signal Processing*, 56(8):3959–3968, 2008.

[34] R. K. Raney. Radar fundamentals: technical perspective. *Principles and applications of imaging radar*, 2:9–130, 1998.

[35] R. Sullivan. *Radar foundations for imaging and advanced concepts*. The Institution of Engineering and Technology, 2004.

[36] I. Faulconbridge. *Radar fundamentals*. Argos Press, 2002.

[37] A. W. Rihaczek. Principles of high-resolution radar. *Norwood, MA: Artech House, 1996.*, 1996.

[38] R. G. Wiley. Electronic intelligence: the analysis of radar signals. *Dedham, MA, Artech House, Inc., 1982. 250 p*, 1982.

[39] S. Samkov I. Y. Immoreev and T. H. Tao. Short-distance ultra wideband radars. *IEEE Aerospace and Electronic Systems Magazine*, 20(6):9–14, 2005.

[40] D. H. Mooney W. H. Long and W. A. Skillman. Pulse doppler radar. *Radar Handbook*, 2, 1990.

[41] E. C. Farnett and G. H. Stevens. Pulse compression radar. *Radar handbook*, 2: 10–1, 1990.

[42] Alain Faure and Noel Suinot. Pulse compression radar, May 23 2000. US Patent 6,067,043.

[43] B. Mencia-Oliva et al. Low-cost cw-lfm radar sensor at 100 ghz. *IEEE transactions on microwave theory and techniques*, 61(2):986–998, 2013.

[44] A. W. Doerry. Generating nonlinear fm chirp waveforms for radar. Technical report, Sandia National Laboratories, 2006.

[45] C. X. Hua and J. Oksman. A new algorithm to optimize barker code sidelobe suppression filters. *IEEE Transactions on Aerospace and Electronic Systems*, 26 (4):673–677, 1990.

[46] E. E. Hollis. Comparison of combined barker codes for coded radar use. *IEEE Transactions on Aerospace and Electronic Systems*, (1):141–143, 1967.

[47] B. L. Lewis and F. F. Kretschmer. Linear frequency modulation derived polyphase pulse compression codes. *IEEE Transactions on Aerospace and Electronic Systems*, (5):637–641, 1982.

[48] W. A. Holm. Continuous wave radar. In *Principles of Modern Radar*, pages 397–421. Springer, 1987.

[49] Z. Li and K. Wu. 24-ghz frequency-modulation continuous-wave radar front-end system-on-substrate. *IEEE Transactions on Microwave Theory and Techniques*, 56(2):278–285, 2008.

[50] A. J. Hymans and J. Lait. Analysis of a frequency-modulated continuous-wave ranging system. *Proceedings of the IEE-Part B: electronic and communication engineering*, 107(34):365–372, 1960.

[51] J. P. Reilly F. E. Nathanson and M. N. Cohen. Radar design principles-signal processing and the environment. *NASA STI/Recon Technical Report A*, 91, 1991.

[52] V. Winkler. Range doppler detection for automotive fmcw radars. In *Microwave Conference, 2007. European*, pages 1445–1448. IEEE, 2007.

[53] T. Baker Jr Charles. Moving target indicator radar, October 29 1957. US Patent 2,811,715.

[54] D. K. Barton. Modern radar system analysis. *Norwood, MA, Artech House, 1988, 607 p.*, 1988.

[55] A. Meta and P. Hoogeboom. Signal processing algorithms for fmcw moving target indicator synthetic aperture radar. In *Geoscience and Remote Sensing Symposium, 2005. IGARSS'05. Proceedings. 2005 IEEE International*, volume 1, pages 4–pp. IEEE, 2005.

[56] A. Ganis et al. A system concept for a 3d real-time ofdm mimo radar for flying platforms. In *2016 German Microwave Conference (GeMiC)*, pages 201–204, March 2016. doi: 10.1109/GEMIC.2016.7461590.

[57] T. Zwick C. Sturm and W. Wiesbeck. An ofdm system concept for joint radar and communications operations. In *Vehicular Technology Conference, 2009. VTC Spring 2009. IEEE 69th*, pages 1–5. IEEE, 2009.

[58] S. Sen and A. Nehorai. Adaptive design of ofdm radar signal with improved wideband ambiguity function. *IEEE Transactions on Signal Processing*, 58(2): 928–933, 2010.

[59] Telecommunication Union. International telecommunication union. *Yearbook of Statistics 1991–2000*, 2001.

[60] K. Q. Abernathy. Why the world radiocommunication conference continues to be relevant today. *Fed. Comm. LJ*, 56:287, 2003.

[61] G.S.N. Raju. *Radar engineering.* IK International Pvt Ltd, 2010.

[62] H. J. Liebe. Mpm—an atmospheric millimeter-wave propagation model. *International Journal of Infrared and millimeter waves*, 10(6):631–650, 1989.

[63] H. J. Liebe. An updated model for millimeter wave propagation in moist air. *Radio Science*, 20(5):1069–1089, 1985.

[64] Naval air systems command and Naval air warfare center. *Electronic warfare and radar systems engineering handbook*. Naval air warfare center, 1997.

[65] P. W. Rosenkranz H. J. Liebe and G. A. Hufford. Atmospheric 60-ghz oxygen spectrum: New laboratory measurements and line parameters. *Journal of quantitative spectroscopy and radiative transfer*, 48(5-6):629–643, 1992.

[66] G. A. Hufford H. J. Liebe and M. G. Cotton. Propagation modeling of moist air and suspended water/ice particles at frequencies below 1000 ghz. In *In AGARD, Atmospheric Propagation Effects Through Natural and Man-Made Obscurants for Visible to MM-Wave Radiation 11 p (SEE N94-30495 08-32)*, 1993.

[67] T. Manabe H. J. Liebe and G. A. Hufford. Millimeter-wave attenuation and delay rates due to fog/cloud conditions. *IEEE transactions on antennas and propagation*, 37(12):1617–1612, 1989.

[68] G. Grimmestad H. Liebe and J. Hopponen. Atmospheric oxygen microwave spectrum–experiment versus theory. *IEEE Transactions on Antennas and Propagation*, 25(3):327–335, 1977.

[69] D. Sedgwick. Self-driving cars will boost demand for collision-avoidance sensors. URL http://europe.autonews.com/article/20141017/COPY/310179999/self-driving-cars-will-boost-demand-for-collision-avoidance-sensors.

[70] Research in China. Global and china automotive radar industry report, 2015-2020. URL https://www.electronics.ca/store/automotive-radar-industry.html.

[71] L. Wood. Automotive radar market 2017. URL http://www.prnewswire.co.uk/news-releases/.

[72] S. Smith. Automotive radar market size to grow to 6.61 billion usd by 2021. URL http://www.prnewswire.com/news-releases/.

[73] John Markoff. No longer a dream: Silicon valley takes on the flying car. URL https://www.nytimes.com/2017/04/24/technology/flying-car-technology.html?mcubz=0.

[74] Sarwant Singh. Flying cars are close to moving from fiction to reality. URL https://www.forbes.com/sites/sarwantsingh/2017/06/05/flying-cars-from-fiction-to-reality/#4925203e4b46.

[75] AIRBUS. URL http://www.airbus.com/.

[76] Dipartimento Politecnico di Ingegneria e Architettura. URL http://www2.diegm.uniud.it/diegm/.

[77] Università degli Studi di Udine (University of Udine). URL www.uniud.it.

[78] J. A. Post and M. J. Bennett. Alternatives for military space radar. Congress of the United States, Congressional Budget Office, 2007.

[79] M. Soumekh. *Synthetic aperture radar signal processing*, volume 7. New York: Wiley, 1999.

[80] E. Brookner. Phased-array radars. *Scientific American*, 252(2):94–102, 1985.

[81] J. Li and P. Stoica. Mimo radar signal processing, 2009.

[82] B. J. Donnet and I. D. Longstaff. Mimo radar, techniques and opportunities. In *Radar Conference, 2006. EuRAD 2006. 3rd European*, pages 112–115. IEEE, 2006.

[83] B. J. Donnet and I. D. Longstaff. Combining mimo radar with ofdm communications. In *Radar Conference, 2006. EuRAD 2006. 3rd European*, pages 37–40. IEEE, 2006.

[84] A. A. Kishk X. H. Wu and A. W. Glisson. Mimo-ofdm radar for direction estimation. *IET Radar, Sonar & Navigation*, 4(1):28–36, 2010.

[85] Y. Zhang and J. Wang. Ofdm-coded signals design for mimo radar. In *Signal Processing, 2008. ICSP 2008. 9th International Conference on*, pages 2442–2445. IEEE, 2008.

[86] ZONeSEC. URL https://www.zonesec.eu/.

[87] Xilinx inc. URL https://www.xilinx.com/.

[88] FAST Fast Actuators Sensors and Transceivers. URL https://de.fast-zwanzig20.de/.

[89] European Aviation Safety Agency. Annual safety review 2016. Technical report, EASA, 2016.

[90] Mathworks, . URL https://www.mathworks.com/.

[91] T. S. Rappaport et al. *Wireless communications: principles and practice*, volume 2. prentice hall PTR New Jersey, 1996.

[92] Radartutorial.eu, . URL http://www.radartutorial.eu/01.basics/Free-Space%20Path%20Loss.en.html.

[93] H. Stockman. Communication by means of reflected power. *Proceedings of the IRE*, 36(10):1196–1204, 1948.

[94] A. C. Balanis. Antenna theory: A review. *Proceedings of the IEEE*, 80(1):7–23, 1992.

[95] Radartutorial.eu, . URL http://www.radartutorial.eu/01.basics/The%20Radar%20Range%20Equation.en.html.

[96] W. L. Stutzman and G. A. Thiele. *Antenna theory and design*. John Wiley & Sons, 2012.

[97] E. F. Knott. *Radar cross section measurements*. Springer Science & Business Media, 2012.

[98] Radartutorial.eu, . URL http://www.radartutorial.eu/01.basics/Maximum%20Unambiguous%20Range.en.html.

[99] H. Sauvageot. *Radar meteorology*. Artech House Publishers, 1992.

[100] W. S. Burdic. *Radar signal analysis*. Prentice-Hall, 1968.

[101] D. Kissinger. Radar fundamentals. In *Millimeter-Wave Receiver Concepts for 77 GHz Automotive Radar in Silicon-Germanium Technology*, pages 9–19. Springer, 2012.

[102] M. Lesturgie. Some relevant applications of mimo to radar. In *Radar Symposium (IRS), 2011 Proceedings International*, pages 714–721. IEEE, 2011.

[103] E. Fishler et al. Spatial diversity in radars—models and detection performance. *IEEE Transactions on Signal Processing*, 54(3):823–838, 2006.

[104] K. W. Forsythe and D. W. Bliss. Mimo radar: Concepts, performance enhancements, and applications. *MIMO Radar Signal Processing*, pages 65–121, 2009.

[105] A. M. Haimovich H. Godrich and R. S. Blum. Target localization accuracy gain in mimo radar-based systems. *IEEE Transactions on Information Theory*, 56(6): 2783–2803, 2010.

[106] E. Fishler et al. Statistical mimo radar. In *12th Conf. on Adaptive Sensor Array Processing*, pages 16–18, 2004.

[107] B. Friedlander. On the relationship between mimo and simo radars. *IEEE Transactions on Signal Processing*, 57(1):394–398, 2009.

[108] C. Y. Chen and P. P. Vaidyanathan. Mimo radar space–time adaptive processing using prolate spheroidal wave functions. *IEEE Transactions on Signal Processing*, 56(2):623–635, 2008.

[109] D. J. Rabideau and P. Parker. Ubiquitous mimo multifunction digital array radar. In *Signals, Systems and Computers, 2004. Conference Record of the Thirty-Seventh Asilomar Conference on*, volume 1, pages 1057–1064. IEEE, 2003.

[110] M. I. Skolnik. *Radar Handbook - Third Edition*. McGraw-Hill Education, 2008.

[111] Y. Qu et al. Performance analysis of beamforming for mimo radar. *Progress In Electromagnetics Research*, 84:123–134, 2008.

[112] J. Ender and J. Klare. System architectures and algorithms for radar imaging by mimo-sar. In *Radar Conference, 2009 IEEE*, pages 1–6. IEEE, 2009.

[113] Texas Instruments SandeepRao. Mimo radar - application report -swra554 - may 2017. URL http://www.ti.com.cn/cn/lit/an/swra554/swra554.pdf.

[114] G.F. Masters and S. F. Gregson. Coordinate system plotting for antenna measurements. URL http://www.nsi-mi.com/images/Technical_Papers/2007/AMTA07-0092-GFM_SFG.pdf.

[115] I. V. Komarov and S. M. Smolskiy. *Fundamentals of short-range FM radar*. Artech House, 2003.

[116] Aircraft101. Radar fundamentals (part ii). URL https://basicsaboutaerodynamicsandavionics.wordpress.com/2016/08/11/radar-fundamentals-part-ii/.

[117] A. G. Stove. Linear fmcw radar techniques. In *IEE Proceedings F (Radar and Signal Processing)*, volume 139, pages 343–350. IET, 1992.

[118] Y. Huang et al. Fmcw based mimo imaging radar for maritime navigation. *Progress In Electromagnetics Research*, 115:327–342, 2011.

[119] P. Lacomme. *Air and spaceborne radar systems: An introduction*. Number 108. William Andrew, 2001.

[120] A. Ganis et al. A portable 3d imaging fmcw mimo radar demonstrator with a 24x24 antenna array for medium range applications. *IEEE Transactions on Geoscience and Remote Sensing*, vol. 56(no. 1):298–312, Jan. 2018.

[121] R. Feger et al. A 77-ghz fmcw mimo radar based on an sige single-chip transceiver. *IEEE Transactions on Microwave Theory and Techniques*, 57(5):1020–1035, 2009.

[122] J. Li and P. Stoica. Mimo radar with colocated antennas. *IEEE Signal Processing Magazine*, 24(5):106–114, 2007.

[123] A. Schiessl S. S. Ahmed and L.-P. Schmidt. Novel fully electronic active real-time millimeter-wave imaging system based on a planar multistatic sparse array. In *Microwave Symposium Digest (MTT), 2011 IEEE MTT-S International*, pages 1–4. IEEE, 2011.

[124] X. Zhuge and A. G. Yarovoy. A sparse aperture mimo-sar-based uwb imaging system for concealed weapon detection. *IEEE Transactions on Geoscience and Remote Sensing*, 49(1):509–518, 2011.

[125] J. Klare et al. Artino: A new high resolution 3d imaging radar system on an autonomous airborne platform. *IGARSS 2006*, 2006.

[126] J. Klare et al. First experimental results with the imaging mimo radar mira-cle x. In *Synthetic Aperture Radar (EUSAR), 2010 8th European Conference on*, pages 1–4. VDE, 2010.

[127] W. Mayer et al. A compact 24 ghz sensor for beam-forming and imaging. In *Control, Automation, Robotics and Vision, 2006. ICARCV'06. 9th International Conference on*, pages 1–6. IEEE, 2006.

[128] A. Ziroff M. Harter and T. Zwick. Three-dimensional radar imaging by digital beamforming. In *Radar Conference (EuRAD), 2011 European*, pages 17–20. IEEE, 2011.

[129] R. Janaswamy and D. Schaubert. Analysis of the tapered slot antenna. *IEEE Transactions on Antennas and Propagation*, 35(9):1058–1065, 1987.

[130] T. Spreng et al. Wideband 120 ghz to 140 ghz mimo radar: System design and imaging results. In *Microwave Conference (EuMC), 2015 European*, pages 430–433. IEEE, 2015.

[131] MACOM. *GaAs SPDT Switch DC - 20 GHz*, masw-008322, rev-3 edition, 2013.

[132] Xilinx Inc. *Virtex-5 Family Overview*, ds100, rev-5.1 edition, Aug. 2015.

[133] 4DSP. *FMC108 high pin count FMC ADC 8-channel 14-bit ADC - 250 MSPS*, fmc108 data-sheet, rev-1.1 edition, June 2014.

[134] Freescale Semiconductor. *MPC8640 and MPC8640D Integrated Host Processor Hardware Specifications*, mpc8640d, rev-4 edition, May 2014.

[135] Analog Devices. *AD9510 Datasheet*, rev. c edition, 2016.

[136] Wikipedia. Serial peripheral interface bus. URL https://en.wikipedia.org/wiki/Serial_Peripheral_Interface_Bus.

[137] A. Zwanetski and H. Rohling. Continuous wave mimo radar based on time division multiplexing. In *Radar Symposium (IRS), 2012 13th International*, pages 119–121. IEEE, 2012.

[138] F. J. Harris. On the use of windows for harmonic analysis with the discrete fourier transform. *Proceedings of the IEEE*, 66(1):51–83, Jan 1978. ISSN 0018-9219. doi: 10.1109/PROC.1978.10837.

[139] T. Spreng et al. Uwb near-field mimo radar: Calibration, measurements and image reconstruction. In *Radar Conference (EuRAD), 2013 European*, pages 33–36. IEEE, 2013.

[140] E. Miralles, A. Ganis, and et al. Multifunctional and compact 3d fmcw mimo radar system with rectangular array for medium range applications. *IEEE Aerospace and Electronic Systems Magazine*, (Paper accepted and awaiting for publication in May 2018), 2018.

[141] Xilinx Inc. *7 Series FPGAs Data Sheet: Overview*, ds180 (v2.4) edition, March 28 2017.

[142] G. Fasano et al. Multi-sensor-based fully autonomous non-cooperative collision avoidance system for unmanned air vehicles. *Journal of Aerospace Computing, Information, and Communication*, 5(10):338–360, 2017/07/22 2008. doi: 10.2514/1.35145. URL https://doi.org/10.2514/1.35145.

[143] J. S. Dittrich and E. N. Johnson. Multi-sensor navigation system for an autonomous helicopter. In *Proceedings. The 21st Digital Avionics Systems Conference*, volume 2, pages 8C1–1–8C1–19 vol.2, 2002. doi: 10.1109/DASC.2002.1052941.

[144] D. L. Hall and J. Llinas. An introduction to multisensor data fusion. *Proceedings of the IEEE*, 85(1):6–23, Jan 1997. ISSN 0018-9219. doi: 10.1109/5.554205.

[145] Z. Ji and D. Prokhorov. Radar-vision fusion for object classification. In *2008 World Automation Congress*, pages 1–6, Sept 2008.

[146] S. Kemkemian, M. Nouvel-Fiani, P. Cornic, and P. Garrec. A mimo radar for sense and avoid function: A fully static solution for uav. In *11-th INTERNATIONAL RADAR SYMPOSIUM*, pages 1–4, June 2010.

[147] G. M. Brooker. Understanding millimetre wave fmcw radars. In *1st International Conference on Sensing Technology*, pages 152–157, 2005.

[148] A. J. Kirschner, J. Guetlein, S. Bertl, and J. Detlefsen. A millimetre-wave mimo radar system for threat detection in patrol or checkpoint scenarios. In *IET International Conference on Radar Systems (Radar 2012)*, pages 1–6, Oct 2012. doi: 10.1049/cp.2012.1573.

[149] R. Streubel and B. Yang. Fusion of stereo camera and mimo-fmcw radar for pedestrian tracking in indoor environments. In *2016 19th International Conference on Information Fusion (FUSION)*, pages 565–572, July 2016.

[150] G. C. Tavik, C. L. Hilterbrick, J. B. Evins, J. J. Alter, J. G. Crnkovich, J. W. de Graaf, W. Habicht, G. P. Hrin, S. A. Lessin, D. C. Wu, and S. M. Hagewood. The advanced multifunction rf concept. *IEEE Transactions on Microwave Theory and Techniques*, 53(3):1009–1020, March 2005. ISSN 0018-9480. doi: 10.1109/TMTT.2005.843485.

[151] E. Miralles et al. Low cost multipurpose rf system approach: Integration of a mimo radar and a communications frontend on a single pcb. In *2016 European Radar Conference (EuRAD)*, pages 137–140, Oct 2016.

[152] J. Mietzner, A. Ganis, and et al. Compact 3d mimo radar – antenna array design and experimental results. In *Proc. European Microwave Week (EuMW)*, Nuremberg, Germany, Oct. 2017.

[153] F. Croq and A. Papiernik. Large bandwidth aperture-coupled microstrip antenna. *Electronics Letters*, 26(16):1293–1294, Aug 1990. ISSN 0013-5194. doi: 10.1049/el:19900832.

[154] Rosenberger. Mini-smp. URL http://www.rosenberger.com/us_en/pdf/products/rf_coax_connectors/Mini-SMP.pdf.

[155] Linear Technology. *LTM9011-14/LTM9010-14/LTM9009-14 - 14-Bit, 125Msps/105Msps/80Msps Low Power Octal ADCs*, 9009101114fc edition, .

[156] Analog Devices. *11-/14-Bit, 5.7 GSPS, RF Digital-to-Analog Converter AD9119/AD9129*, rev. b edition.

[157] Xilinx Inc. *AXI4-Stream FIFO v4.1 - LogiCORE IP Product Guide*, pg080 edition, April 6 2016.

[158] Xilinx Inc. *AXI DMA v7.1 - LogiCORE IP Product Guide*, pg021 edition, October 5 2016.

[159] Xilinx Inc. *AXI Reference Guide*, ug761 (v13.1) edition, March 7 2011.

[160] Xilinx Inc. *PetaLinux SDK User Guide - Application Development Guide*, ug981 (v2013-10) edition, November 25 2013.

[161] Matt Johnston. Dropbear ssh. URL https://matt.ucc.asn.au/dropbear/dropbear.html.

[162] J. Corbet and A. Rubini. *Linux Device Drivers, 2nd Edition*. O'Reilly Media, June 2001.

[163] Mathworks. Introducing mex files, . URL https://www.mathworks.com/help/matlab/matlab_external/introducing-mex-files.html.

[164] T. Multerer, A. Ganis, and et al. Low-cost jamming system against small drones using a 3d mimo radar based tracking. In *Proc. European Microwave Week (EuMW)*, Nuremberg, Germany, Oct. 2017.

[165] Squarehead Technology. http://www.sqhead.com/acoustic-camera/, .

[166] Dedrone. http://www.dedrone.com/de/dronetracker/.

[167] N. P. Santos, V. Lobo, and A. Bernardino. A ground-based vision system for uav tracking. In *OCEANS 2015 - Genova*, pages 1–9, May 2015. doi: 10.1109/OCEANS-Genova.2015.7271349.

[168] M. Kratky J. Farlik and J. Casar. Detectability and jamming of small uavs by commercially available low-cost means. In *2016 International Conference on Communications (COMM)*, pages 327–330, June 2016. doi: 10.1109/ICComm.2016.7528287.

[169] Parrot Sa. Parrot uav. URL https://www.parrot.com/.

[170] R. van Nee and R. Prasad. *OFDM for wireless multimedia communications*. Artech House, Inc., 2000.

[171] Y. S. Cho et al. *MIMO-OFDM wireless communications with MATLAB*. John Wiley & Sons, 2010.

[172] B. R. Saltzberg A. Bahai and M. Ergen. *Multi-carrier digital communications: theory and applications of OFDM*. Springer Science & Business Media, 2004.

[173] N. Lehmann et al. Evaluation of transmit diversity in mimo-radar direction finding. *IEEE transactions on signal processing*, 55(5):2215–2225, 2007.

[174] M. Ström and M. Viberg. Low papr waveform synthesis with application to wideband mimo radar. In *Computational Advances in Multi-Sensor Adaptive Processing (CAMSAP), 2011 4th IEEE International Workshop on*, pages 5–8. IEEE, 2011.

[175] G. L. Stuber, J. R. Barry, S. W. McLaughlin, Ye Li, M. A. Ingram, and T. G. Pratt. Broadband mimo-ofdm wireless communications. *Proceedings of the IEEE*, 92(2):271–294, Feb 2004. ISSN 0018-9219. doi: 10.1109/JPROC.2003.821912.

[176] G. M. Brooker. Mutual interference of millimeter-wave radar systems. *IEEE Transactions on Electromagnetic Compatibility*, 49(1):170–181, 2007.

[177] H. Liu and G. Li. *OFDM-based broadband wireless networks: design and optimization*. John Wiley & Sons, 2005.

[178] H. Schulze and C. Lüders. *Theory and applications of OFDM and CDMA: Wideband wireless communications*. John Wiley & Sons, 2005.

[179] J. Heiskala and J. Terry Ph D. *OFDM wireless LANs: A theoretical and practical guide*. Sams, 2001.

[180] T. Zwick C. Sturm, E. Pancera and W. Wiesbeck. A novel approach to ofdm radar processing. In *Radar Conference, 2009 IEEE*, pages 1–4. IEEE, 2009.

[181] Christian C. Sturm, T. Zwick, W. Wiesbeck, and M. Braun. Performance verification of symbol-based ofdm radar processing. In *Radar Conference, 2010 IEEE*, pages 60–63. IEEE, 2010.

[182] M. Braun et al. Parametrization of joint ofdm-based radar and communication systems for vehicular applications. In *Personal, Indoor and Mobile Radio Communications, 2009 IEEE 20th International Symposium on*, pages 3020–3024. IEEE, 2009.

[183] Y. L. Sit et al. The ofdm joint radar-communication system: An overview. In *Proc. Int. Conf. Advances in Satellite and Space Communications (SPACOMM 2011)*, pages 69–74, 2011.

[184] J. D. Parsons. *The Mobile Radio Propagation Channel, 2 ed.* John Wiley and Sons Ltd, 2000.

[185] B. Sklar. Rayleigh fading channels in mobile digital communication systems (pt i and 11). *IEEE Communications Magazine*, vol. 35:pp. 90–109, 1997.

[186] A. Ganis, A. Santra, and et al. Design, processing and analysis of lfm based orthogonal-coded 4d mimo ofdm radar. *IEEE Transactions on Aerospace and Electronic Systems*, (Paper sent and waiting for acceptance), 2017.

[187] C. Y. Chen and P. P. Vaidyanathan. Mimo radar waveform optimization with prior information of the extended target and clutter. *IEEE Transactions on Signal Processing*, 57(9):3533–3544, Sept 2009. ISSN 1053-587X. doi: 10.1109/TSP.2009.2021632.

[188] J. Li M. Xue and P. Stoica. Mimo radar waveform design. In *Waveform Design and Diversity for Advanced Radar Systems :*. IET Press, 2012.

[189] A. G. Stove. Linear fmcw radar techniques. *IEE Proceedings F - Radar and Signal Processing*, 139(5):343–350, Oct 1992. ISSN 0956-375X. doi: 10.1049/ip-f-2.1992.0048.

[190] C. Sturm, E. Pancera, T. Zwick, and W. Wiesbeck. A novel approach to ofdm radar processing. In *2009 IEEE Radar Conference*, pages 1–4, May 2009. doi: 10.1109/RADAR.2009.4977002.

[191] Y. L. Sit and T. Zwick. Mimo ofdm radar with communication and interference cancellation features. In *2014 IEEE Radar Conference*, pages 0265–0268, May 2014. doi: 10.1109/RADAR.2014.6875596.

[192] M. Natkaniec. Wireless ofdm systems: How to make them work? *IEEE Communications Magazine*, 41(2):16–18, Feb 2003. ISSN 0163-6804. doi: 10.1109/MCOM.2003.1179493.

[193] *Ambiguity Functions of Matched Illumination Radar Signals*, Dec. 2013. India, IRSI 2013, Bangalore.

[194] C. Y. Chen and P. P. Vaidyanathan. Mimo radar ambiguity properties and optimization using frequency-hopping waveforms. *IEEE Transactions on Signal Processing*, 56(12):5926–5936, Dec 2008. ISSN 1053-587X. doi: 10.1109/TSP.2008.929658.

[195] R. Sivaswamy. Multiphase complementary codes. *IEEE Transactions on Information Theory*, 24(5):546–552, Sep 1978. ISSN 0018-9448. doi: 10.1109/TIT.1978.1055936.

[196] J. A. Davis and J. Jedwab. Peak-to-mean power control in ofdm, golay complementary sequences and reed-muller codes. In *Proceedings. 1998 IEEE International Symposium on Information Theory (Cat. No.98CH36252)*, pages 190–, Aug 1998. doi: 10.1109/ISIT.1998.708788.

[197] B. M. Popovic. Generalized chirp-like polyphase sequences with optimum correlation properties. *IEEE Transactions on Information Theory*, 38(4):1406–1409, Jul 1992. ISSN 0018-9448. doi: 10.1109/18.144727.

[198] S. Beyme and C. Leung. Efficient computation of dft of zadoff-chu sequences. *Electronics Letters*, 45(9):461–463, April 2009. ISSN 0013-5194. doi: 10.1049/el.2009.3330.

[199] Yang-Seok Choi, P. J. Voltz, and F. A. Cassara. On channel estimation and detection for multicarrier signals in fast and selective rayleigh fading channels. *IEEE Transactions on Communications*, 49(8):1375–1387, Aug 2001. ISSN 0090-6778. doi: 10.1109/26.939860.

[200] B. Vucetic and J. Yuan. *Space-Time Coding*. John Wiley & Sons, Inc., New York, NY, USA, 2003. ISBN 0470847573.

[201] V. Tarokh, H. Jafarkhani, and A. R. Calderbank. Space-time block codes from orthogonal designs. *IEEE Transactions on Information Theory*, 45(5):1456–1467, Jul 1999. ISSN 0018-9448. doi: 10.1109/18.771146.

[202] V. Tarokh, H. Jafarkhani, and A. R. Calderbank. Correction to "space-time block codes from orthogonal designs". *IEEE Transactions on Information Theory*, 46 (1):314–314, Jan 2000. ISSN 0018-9448. doi: 10.1109/TIT.2000.1282193.

[203] S. M. Alamouti. A simple transmit diversity technique for wireless communications. *IEEE Journal on Selected Areas in Communications*, 16(8):1451–1458, Oct 1998. ISSN 0733-8716. doi: 10.1109/49.730453.

[204] J. P. Costas. A study of a class of detection waveforms having nearly ideal range doppler ambiguity properties. *Proceedings of the IEEE*, 72(8):996–1009, Aug 1984. ISSN 0018-9219. doi: 10.1109/PROC.1984.12967.

[205] N. Levanon. Multifrequency radar signals. In *Record of the IEEE 2000 International Radar Conference [Cat. No. 00CH37037]*, pages 683–688, 2000. doi: 10.1109/RADAR.2000.851916.

[206] P. M. Woodward. *Probability and Information Theory: With Applications to Radar*. Number Bd. 3 in Electronics and Waves. Elsevier Science & Technology, 1953. URL https://books.google.de/books?id=RA0nAAAAMAAJ.

[207] G. San Antonio, D. R. Fuhrmann, and F. C. Robey. Mimo radar ambiguity functions. *IEEE Journal of Selected Topics in Signal Processing*, 1(1):167–177, June 2007. ISSN 1932-4553. doi: 10.1109/JSTSP.2007.897058.

[208] A. Ganis and A. Santra. Multiple input multiple output, mimo, radar system. Indian Patent INA201641043847 and European Patent EP17181032, Filed, 22 December 2016.

[209] A. Ganis and A. Santra. Multiple input multiple output, mimo, radar system. Indian Patent INA201641043881 and European Patent EP17181029, Filed, 22 December 2016.

[210] A. Ganis and A. Santra. Multiple input multiple output, mimo, radar system. Indian Patent INA201641043893 and European Patent EP17181035, Filed, 22 December 2016.

[211] A. Santra A. Ganis and V. Ziegler. A multiple input multiple output, mimo, radar system. Indian Patent INA201641043912 and European Patent EP17181041, Filed, 22 December 2016.

[212] A. Ganis and et al. Imaging mimo ofdm radar based on a complex dss-lfm waveform. In *Proc. IET Radar Conference 2017*, Belfast, 2017.

[213] Xilinx Inc. System generator for dsp. URL https://www.xilinx.com/products/design-tools/vivado/integration/sysgen.html.